MULTIPHASE TRANSPORT IN DEFORMABLE PHASE-CHANGING POROUS MATERIALS

A Dissertation

Presented to the Faculty of the Graduate School

of Cornell University

in Partial Fulfillment of the Requirements for the Degree of

Doctor of Philosophy

by

Ashish Dhall

January 2011

MULTIPHASE TRANSPORT IN DEFORMABLE PHASE-CHANGING POROUS MATERIALS

Ashish Dhall, Ph.D.

Cornell University 2011

The primary aim of this work is mathematical modeling of transport phenomena during processing of food materials. Quantitative information from such models can be used to design food processes that deliver microbiologically and chemically safe products with optimized food quality and process efficiency. Most factors characterizing food safety and quality can, in principle, be expressed as functions of the state and the history of a product. Thus, the emphasis is on accurate prediction of the final state of a food material– temperature, moisture (and, if present, concentration of other species such as air, fat etc.), and stresses and strains for deformable food materials, and its evolution during a process.

For the purpose of mathematical modeling, most solid foods can be treated as porous materials comprising of a solid polymer matrix with water (and, if present, air, fat, oil etc.) occupying its pore space. During a food process such as frying, drying or baking, energy and mass (water and other species) transport takes place altering the state of the product. Thus, mathematically, food process is just single- or multi-phase transport in rigid or deformable porous media, with or without phase transitions. As porous media transport is widely studied across application areas, some of the physics can be borrowed from other materials (mainly, soils, wood and polymers), while some physics is specific to food materials and processes. This dissertation is a compilation of a series of modeling efforts (both theory development and applications), exploring various aspects of porous media transport.

The first chapter deals with modeling of nongray radiative heat exchange in an infrared oven. The purpose is to characterize the nature and intensity of infrared radiation reaching the food material in an oven. Although the focus of this study is radiation heat transport outside food (unlike other chapters, which focus on internal transport), the study can help to elucidate the complexities involved in determining energy boundary conditions which are a necessary input to most transport models within food materials.

Chapters 2 to 4 deal with multiphase transport in rigid porous materials. Chapter 2 (joint work with Dr. Amit Halder) focuses on development of a comprehensive theoretical framework for materials in which, besides mass transfer between the fluids in pore space, significant mass transfer may occur between the solid matrix and the pore space. In chapter 3, the theory developed in the previous chapter is applied to model multiphase (moisture and fat) transport in meat and the simulation results are validated against double-sided contact heating of hamburger patties. Chapter 4 deals with a non-food application, hot air drying of channeled ceramic substrates. The focus is on breakdown of the local equilibrium between liquid water and water vapor (where vapor pressure is not given by moisture sorption isotherm), a phenomena also observable and significant in food materials with large pore sizes such as bread.

Finally, deformation through solid momentum balance is added to the analysis in the final 2 chapters– theoretical development with example applications in chapter 5 and detailed analysis of transport in meat (single-sided contact heating of hamburger patties) in chapter 6. Modeling framework accounting for different driving forces causing deformation (moisture change and gas pressure) is developed. Stress generation due to transition of food from a soft and rubbery state to rigid and glassy state is discussed.

BIOGRAPHICAL SKETCH

Ashish Dhall was born at Ambala Cantonment in the state of Haryana, India. He attended 8 different schools in Jammu and Kashmir, Punjab, and Chandigarh, before joining Indian Institute of Technology, Bombay in July 1999 for his undergraduate education. Ashish took ”Transport Phenomena” and ”Modeling and Simulation” courses at IIT and has been enamored with the subjects since then. In December 2004, he completed the Dual Degree Program (Bachelor’s and Master’s degrees) majoring in Chemical Engineering with ”Process Systems Design and Engineering” as Master’s specialization. His Master’s thesis was titled ”CFD Analysis of a Batch Rotary Kiln”. After IIT, he joined Fluent India Private Limited as a Trainee Applications Engineer working with the Academic Support Team. Following a short stint of 9-months at Fluent, Ashish left Indian shores for the first time in August 2005 to pursue graduate studies at Department of Biological and Environmental Engineering at Cornell University, Ithaca, New York.

To my parents, Neelam and Prem Chander Dhall

ACKNOWLEDGEMENTS

I thank my advisor, Prof. Ashim Datta for his constant support and guidance throughout the PhD program. I owe the successful completion of this dissertation to his incredible patience and the encouragement I got from him. He always taught me to think big and, at the same time, to never forget the details. I would like to thank Prof. Subrata Mukherjee and Prof. Claude Cohen for serving on my Special Committee. Help from Late Prof. Kenneth Torrance on modeling of radiation oven is sincerely acknowledged. My thanks also goes to Dr. Jacob George, Dr. William Woods, Gary Squier and others at Corning Inc. for their help with the ceramic substrate study.

I would specially like to thank past and present Datta group members – Dr. Vineet Rakesh, Dr. Amit Halder, Shruti Thussu, Peyman Taherkhani, Diana Mitrea and Alex Warning, people with whom I have worked for the past 5 years and shared joys and sorrows of grad life. My thanks also goes to Haolin Zhu for all the discussions and help on solid mechanics. Lastly, I would mention my family – my parents, my brother, my wife and her parents for being the reason I am here completing this degree and looking forward to future beyond Cornell.

TABLE OF CONTENTS

LIST OF TABLES

LIST OF FIGURES

CHAPTER 1

RADIATIVE HEAT EXCHANGE MODELING INSIDE AN OVEN

The complete authorship of this work should be read as Ashish Dhall, Ashim K. Datta, Kenneth E. Torrance and Marialuci F. Almeida.

1.1 Abstract

The 3-D non-gray radiative heat exchange in a near-infrared commercial oven is modeled. The spectrum is divided into into four gray bands to model the narrow wavelength range in which the halogen heat source radiates, the wavelength dependence of the food surface emittance, and the absorption coefficient of the heat source cover glass. The model is used to estimate the heating of a cuboidal food sample for 1 minute at different cyclic settings of a halogen radiant heat source. The model predictions agree with the experimental data, and capture the cover-glass and the food-surface temperature and heat flux histories very well. The band-wise distribution of energy absorption by the food reveals the separate contributions from the source and the oven walls. Comparison of the heating rates between the measured non-gray food-surface and the different gray food-surface emittance values establishes the necessity of the non-gray treatment.

Nomenclature

a	Absorption coefficient, m^{-1}
A	Area, m^2
c_p	Specific heat, $\mathrm{J/kg \cdot K}$
$f(t)$	Fraction of total lamp power emitted at time t
E_λ	Irradiance as a function of wavelength, W/m^2
$F_{(0-n\lambda_i T)}$	Band energy ratio
h_c	Convective heat transfer coefficient, $\mathrm{W/m^2 \cdot K}$
$I(\mathbf{r}, \mathbf{s})$	Intensity of radiation at a location $\mathbf{r}$ in direction $\mathbf{s}$, $\mathrm{W/m^2}$
$I_b(\mathbf{r})$	Blackbody emission at a location $\mathbf{r}$, $\mathrm{W/m^2}$
I_0	Radiation intensity at a surface, $\mathrm{W/m^2}$
k_c	Thermal conductivity, $\mathrm{W/m \cdot K}$
n	Refractive index
$P(t)$	Power of the lamps at time t, W
q	Heat flux, $\mathrm{W/m^2}$
$\mathbf{r}$	Position vector
r_d	Interfacial reflectivity at a surface
$\mathbf{s}$	Direction
T	Temperature, K
t	Time, s
$\mathbf{u}$	Velocity of air, $\mathrm{m/s}$

Greek Letters

ϵ	Emittance
λ	Wavelength, m
ρ	Density, $\mathrm{kg/m^3}$
σ	Stefan-Boltzmann's constant, $5.67 \times 10^{-8}\ \mathrm{W/m^2 \cdot K^4}$
Ω	Solid Angle, rad

Subscripts

air	Surrounding air properties
avg	Average
c	Solid
in	Incoming
out	Outgoing
$surf$	Surface
r	Radiation
s	Source
w	Wall
λ	At given wavelength, or per unit wavelength

1.2 Introduction

The infrared heating of food in an oven is a classic process. More recently, infrared heating has been combined with other modes of heating such as microwave or forced hot air. Different regions of the infrared spectrum, such as the near-infrared (halogen),

have been introduced[1–5]. The low penetration depth of infrared waves leads to rapid surface heating which has been exploited to produce effects such as the pre-drying of sheeted foods (chips, tortillas etc.) and the surface browning of meat products (to seal the meat juice) that are not possible with other modes of heating. The exchange of radiation between an infrared source and the food inside an oven is a complex process. Surface properties of the food are an important factor in determining the amount of energy absorbed and these properties can vary with radiation wavelength. The radiation surface properties can also vary with food composition, temperature, and surface conditions. The complex radiation exchange process determines the temperature-time history and therefore the final quality of a heated food such as crust formation and color development[6,7]. A better understanding of the effects of various food and oven parameters on infrared heating should lead to improved optimization of this heating, contributing to better quality of infrared-heated food, novel uses of infrared energy in food processing, less energy usage, and increased automation of food processing through appropriate combinations of infrared with other modes of heating such as microwave.

Fundamentals-based analyses of the food heating process that allow for complexities such as the variation in radiative properties (i.e., reflection, absorption) and the effects of source wavelength do not exist, generally speaking[8]. Studies have been either qualitative or were very simple analyses of the radiative exchange assuming black or gray surfaces; complete radiative exchange analyses are complex and have not been performed[9–15]. Models of infrared exchange in non-food applications such as computer graphics imaging, microelectronics, and paper and wood processing are more complete but do not include the combinations of geometry, radiative properties, and other physical parameters that typically describe food heating[16–19].

The present study 1) develops a thermal radiative exchange model for a 3-D cavity

that uses wavelength-dependent (non-gray) radiative properties for the heat source, the oven and the food materials, and predicts the oven wall temperatures, food temperatures, and time-varying heat fluxes; 2) experimentally validates the predicted temperatures and heat fluxes; and 3) performs sensitivity analyses with the model for the input food and oven parameters. The paper starts with a description of the problem, the governing equations, and the boundary conditions for thermal radiative exchange. Then, input parameters are discussed, followed by a description of experimental measurements. In the last two sections of the paper, validation results and sensitivity analyses are presented.

1.3 Mathematical Model

The physical geometry is sketched in Figure 1.1. Radiative heat exchange occurs inside an oven (a 3-D enclosure) which has two halogen lamps in a top cavity and one halogen lamp in a bottom cavity (not used in this study). The food is placed inside the oven just above the floor.

The lamp cavities are covered by transparent glass plates. The halogen lamps emit infrared radiation with the spectrum shown in Figure 1.2. Most of the short wavelength radiation emitted by the lamps (approximately 71%[20]) is transmitted by the cavity glass; the longer wavelength radiation as well as that emitted by the oven walls, is absorbed by the glass. The food surface properties can vary with wavelength. The lamp is cycled on-off by the heating control system. During this process, the lamp maintains its emission spectrum, while the heat flux magnitude changes with cycling. Thus, we model the lamp as an essentially constant temperature source with a time-varying heat flux. The emitted flux is assumed to originate from two small heated strips in the top surface of the lamp cavity, as shown in Figure 1.1. The emitted radiant intensity is used with the radiative

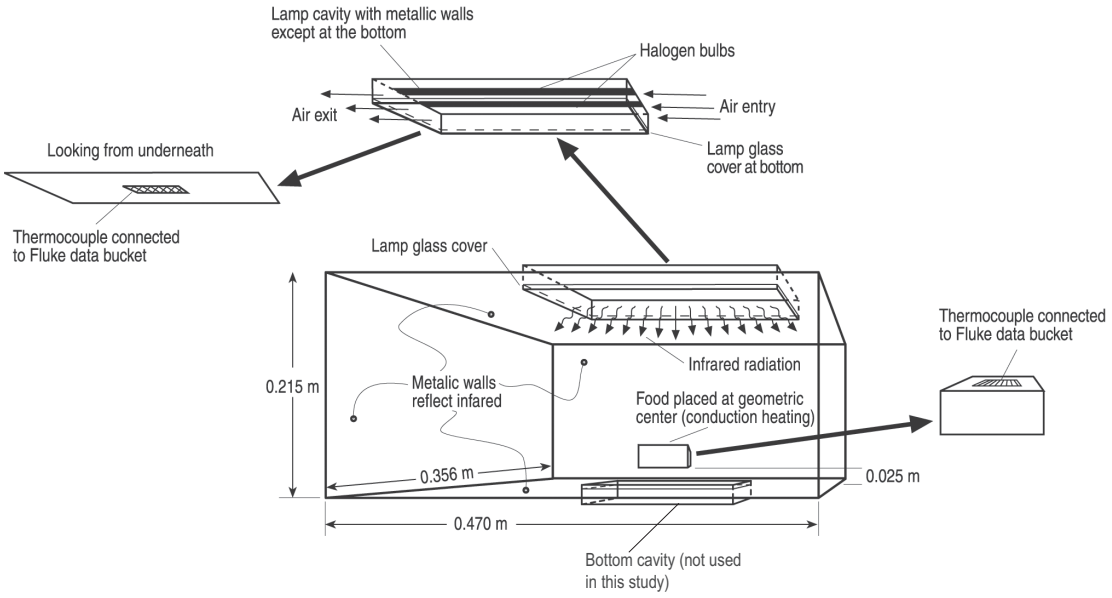

Figure 1.1: Schematic of the radiation dominant problem. The geometry of the oven is rectangular, of size 0.470 m $\times$ 0.356 m $\times$ 0.215 m (volume 3.6 $\times 10^{-2}$ m^3). The food inside the oven is a potato slab of geometry 0.0470 m $\times$ 0.0356 m $\times$ 0.0215 m that has a volume 3.6 $\times 10^{-5}$ m^3. Food is placed at 2.5 cm above the geometric center of the oven's bottom surface and parallel, resting on a quartz glass tray.

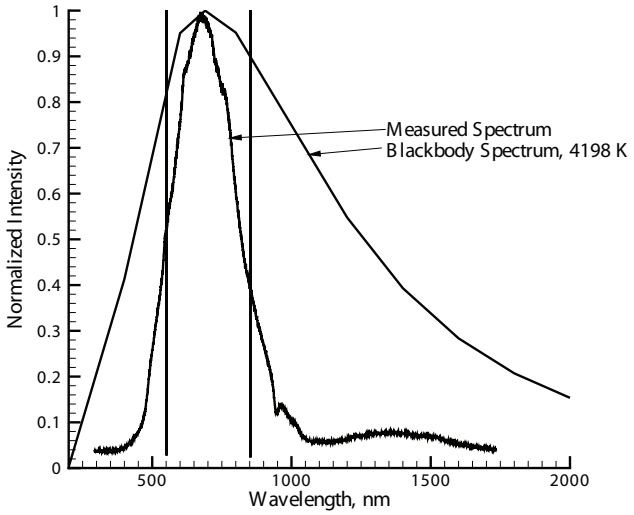

Figure 1.2: Radiation spectrum of the source with blackbody spectrum at 4198 K superimposed on it. Band cuts at 550 nm and 850 nm also shown.

transport equation (RTE), and is coupled with the heat conduction equations for the food and air to solve for temperature.

1.3.1 Assumptions

Some of the major assumptions in developing the mathematical formulation include: 1) All surfaces are diffuse emitters and reflectors, with no directional dependence — the surface roughness of foods and the roughness and coatings on the oven surfaces are likely to support this assumption; 2) Problem is radiation dominant and natural convection effects are minor since the heating is only for a short time interval; 3) Food is a solid conductive body that is opaque to thermal radiation, i.e., all energy is absorbed at the surface. The penetration depth in the food for near infrared radiation has been reported to be small (close to $1.5\ \mathrm{mm}$[21]), which justifies the opaque assumption.

1.3.2 Governing Equation and Boundary Conditions for Radiative Heat Exchange

Governing Equations

Radiation exchange inside the oven involves the heat source, food, oven walls, and glass cover plate on the source. The ambient air is taken as radiatively transparent (i.e., non-participating). The heat source, food, and walls participate only by surface emission and absorption. The glass cover plate absorbs and emits internally, and transmits overall. Within the cover plate, we must solve the radiative transport equation, RTE[22,23], which

is given by

$$\nabla.\,(I(\mathbf{r},\mathbf{s})\mathbf{s}) = -a(I(\mathbf{r},\mathbf{s}) + n^2 I_b(\mathbf{r})) \tag{1.1}$$

where I is the radiation intensity (beam energy per unit time and unit area normal to the beam, and per unit solid angle).

The RTE describes the variation of the radiation intensity, $I(\mathbf{r},\mathbf{s})$, at a location $\mathbf{r}$, in a direction $\mathbf{s}$, and at a specific wavelength λ. The blackbody intensity in the glass is denoted by $I_b(\mathbf{r})$. The two terms of the right side of (Eq. 1.1) account for absorption and emission, respectively, in the glass. The absorption coefficient and index of refraction of the glass are denoted by a and n. We neglect in- and out-scattering inside the glass in Eq. 1.1.

The ambient air is assumed to be radiatively transparent (i.e., non absorbing, emitting, or scattering). Thus, a beam of radiant energy of intensity $I(\mathbf{s})$ leaving a surface is unattenuated as it passes through the air, and is constant (and conserved) until it strikes another surface. Absorption, emission and reflection can occur at the solid surfaces, and, as noted, absorption and emission occur within the glass cover plate. Further, since both $I(\mathbf{r},\mathbf{s})$ and T (in $I_b(\mathbf{r})$) appear in the RTE (Eq. 1.1) for the glass cover plate, the RTE must be solved simultaneously with the appropriate energy equations for all of the materials in the oven.

Boundary Conditions

At the opaque boundaries (oven walls and food surface), the radiative heat balance equation is obtained by combining the radiative surface energy balance and Kirchoff's law, i.e., absorptance equals emittance for zero transmittance. With the diffuse radiation

assumption, the incident radiative heat flux, q_{in}, at a wall is

$$q_{in} = \int_{\mathbf{s}\cdot\mathbf{n}>0} I(\mathbf{r},\mathbf{s})\mathbf{s}\cdot\mathbf{n}d\Omega \tag{1.2}$$

where the integral is over all incident directions above the wall and $d\Omega$ is at differential solid angle. The net radiative flux, q_{out} leaving the surface is given by

$$q_{out} = (1-\epsilon_w)q_{in} + n^2 \int_0^\infty E_{\lambda,w} d\lambda \tag{1.3}$$

where ϵ_w is the surface emittance, n is the refractive index of the medium next to the surface, and $E_{\lambda,w}$ is the emission function for the surface. Note that a directional integral does not appear in Eq. 1.3 due to the diffuse approximation. The boundary radiant intensity for all outgoing directions at the surface is given by

$$I_0 = \frac{q_{out}}{\pi} \tag{1.4}$$

For the semi-transparent boundaries also, i.e., the cavity glass, the reflected and transmitted radiation are assumed to be diffuse. There is no absorption at the semi-transparent boundaries. The interfacial reflectance, r_d, at the smooth, semi-transparent boundaries is assumed to be independent of direction and is estimated with:

$$r_{d,a} = 1 - \frac{(1-r_{d,b})}{n^2} \tag{1.5}$$

$$\begin{aligned} r_{d,b} \quad = \quad & \frac{1}{2} + \frac{(3n+1)(n-1)}{6(n+1)^2} + \frac{n^2(n^2-1)^2}{(n^2+1)^3}\ln\left(\frac{n-1}{n+1}\right) \\ & -\frac{2n^3(n^2+2n-1)}{(n^2+1)(n^4-1)} + \frac{8n^4(n^4+1)}{(n^2+1)(n^4-1)^2}\ln(n) \end{aligned} \tag{1.6}$$

where $n = n_a/n_b > 1$ and a and b denote the two media bounding the semi-transparent surface. Details of reflectance calculation are available elsewhere[23,24].

The radiant flux emitted by the halogen lamps is assumed to emerge as a diffuse heat source emission from two thin strips (representing the lamps, Figure 1.1) at the top surface of the cavity containing the lamps (see also the Section on **Time Varying Boundary Condition for the Infrared Source**).

Non-gray Radiative Exchange

In the present study, to describe the effects of non-gray radiation, we divide the radiation spectrum into four wavelength bands as shown in Figure 1.3: 550-850 nm; 850-1350 nm; 1350-4250 nm; and beyond 4250 nm. We assume constant optical properties in each band. The reason for choosing the four wavelength bands is as follows: the source lamps emit primarily in the range 550-850 nm (Figure 1.2); potato emittance (the food studied) changes at 1350 nm (Figure 1.4); and the absorption coefficient of the glass changes at 4250 nm[20]; thus justifying the band cuts at these wavelengths. The radiation intensity per unit wavelength interval, $I_\lambda(\mathbf{r}, \mathbf{s})$, is solved in each wavelength band:

$$\nabla . (I_\lambda(\mathbf{r}, \mathbf{s})\mathbf{s}) = -a_\lambda(I_\lambda(\mathbf{r}, \mathbf{s}) + n^2 I_{b\lambda}(\mathbf{r})) \tag{1.7}$$

Equation 1.7 is integrated over each wavelength interval, resulting in transport equa-

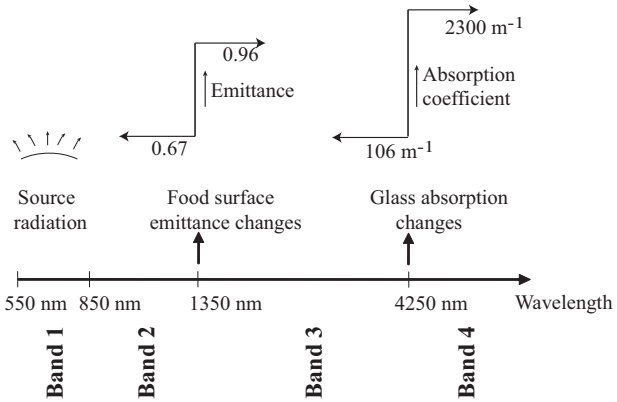

Figure 1.3: Division of the spectrum into gray bands as used in the model, following source, food and cavity glass characteristics.

tions for the quantity $I_\lambda \Delta\lambda$, the radiant energy contained in the wavelength band $\Delta\lambda$. The behavior within each band is assumed to be gray. The blackbody emission in the wavelength band per unit solid angle is written as

$$[F_{(0\to n\lambda_2 T)} - F_{(0\to n\lambda_1 T)}]n^2 \frac{\sigma T^4}{\pi} \tag{1.8}$$

where σ if the Stefan-Boltzmann constant and $F_{(0\rightarrow n\lambda T)}$ is the fraction of radiant energy emitted by a black body in the wavelength interval from 0 to λ at temperature T in a medium of refractive index n and λ_2 and λ_1 are the wavelength boundaries of the band. The total intensity, $I(\mathbf{r},\mathbf{s})$, in each direction $\mathbf{s}$ at position $\mathbf{r}$ is computed using

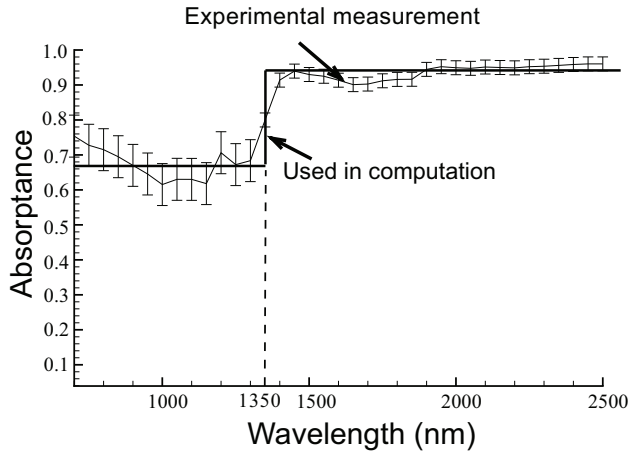

Figure 1.4: Measured spectral absorptance of potatoes in the near and mid-infrared range from[27] and the approximation (solid line) used in this study.

$$I(\mathbf{r},\mathbf{s}) = \sum_k I_{\lambda_k}(\mathbf{r},\mathbf{s})\Delta\lambda_k \tag{1.9}$$

where the summation is over the wavelength bands.

1.3.3 Governing Equations and Boundary Conditions for Heat Conduction

The energy equation (Eq.1.10) is solved for the entire cavity (food, glass and air):

$$\rho c_p \frac{\partial T}{\partial t} + \rho c_p(\mathbf{u}.\nabla T) = k\nabla^2 T + Q \begin{cases} = 0 & food, air \\ = \left(\nabla.\mathbf{q_r} - an^2 I_b(\mathbf{r})\right) & glass \end{cases} \tag{1.10}$$

The density (ρ), specific heat (c_p) and the thermal conductivity (k) are evaluated for food, glass and air, as appropriate. The maximum increase in the food-surface tem-

perature is observed to be approximately 35°C during the heating duration considered (Figure 1.5). The food properties are not expected to change by more than 5% in this temperature range. Therefore, physical properties of the food are assumed to be constant (Table 1.1). The volumetric heat source term, Q, is non-zero only in the glass. The heat source term is equal to the energy absorbed by the glass, $\nabla.\mathbf{q_r}$, minus the energy emitted by the glass, $an^2 I_b(\mathbf{r})$. The radiative heat flux, $\mathbf{q_r}$ is given by:

$$\mathbf{q_r} = \sum_k \left(\int_0^{4\pi} I_{\lambda_k}(\mathbf{r}, \mathbf{s}) \mathbf{s} d\Omega \right) \Delta\lambda_k \tag{1.11}$$

The velocity, $\mathbf{u}$, is zero everywhere except in the lamp cavity. As noted, the ambient air is assumed to be radiatively non-absorbing, i.e., non-participating. The thermal boundary condition on all solid surfaces for the energy equation (Eq. 1.10) is as follows:

$$\underbrace{-k_c \left.\frac{\partial T}{\partial n}\right|_c}_{\substack{\text{conduction from} \\ \text{solid to surface}}} - \underbrace{\left(-k_{\text{air}} \left.\frac{\partial T}{\partial n}\right|_{\text{air}}\right)}_{\substack{\text{conduction from} \\ \text{surface to air}}} = q_{out} + h_c(T_s - T_{\text{air}}) \tag{1.12}$$

where k_c is the thermal conductivity of the solid, k_{air} is the thermal conductivity of the air, n is the outward normal direction to the solid surface, q_{out} is the net radiative flux leaving the solid surface as given by the radiative boundary condition equation (Eq. 1.3). and h_c is a pseudo-convective heat transfer coefficient (more to follow). According to the user's manual for the oven, the lamp cavities are cooled by multiple fans (illustrated in Figure 1.1). It is not possible to measure the air velocity inside the lamp cavities without disturbing the system. Therefore, a sensitivity study of the glass temperature with respect to air velocity in the lamp cavities was carried out; hereafter, the value of velocity (and thus h_c) which gave the best estimate of the glass temperature (as compared to measurements) was used (discussed later in **Results**). This velocity is used in the estimation of the heat transfer coefficient, h_c, over the glass surface inside the lamp cavities, and which accounts for the effect of cooling due to forced convection. The air in the main oven cavity is assumed to be quiescent and, thus, all walls have a

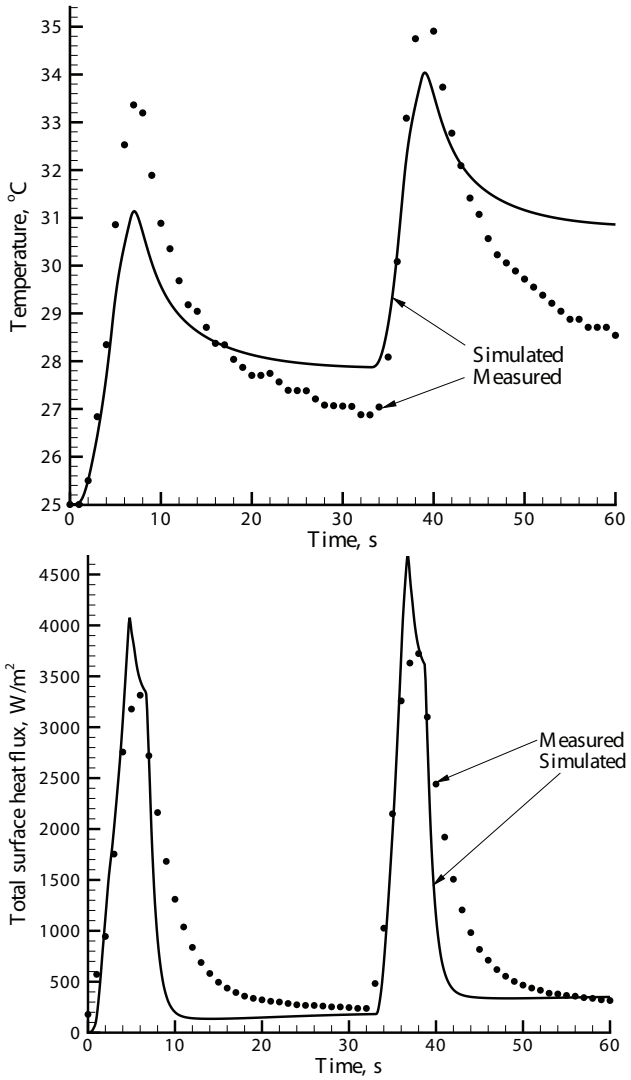

(a) Level I

Figure 1.5: Experimental and computed temperatures and total surface heat fluxes at the center position on the top surface of the food during one minute of heating for three different settings of infrared power level (Levels I, V and X) in the Advantium$^{\mathrm{TM}}$ oven.

Figure 1.5 (continued)

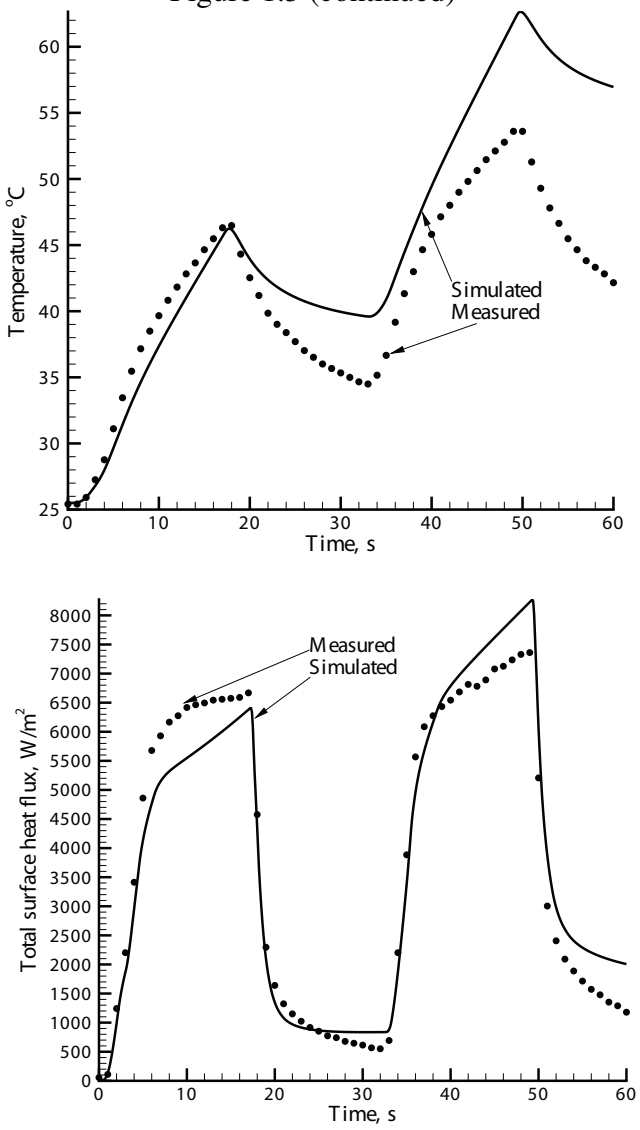

(b) Level V

zero heat transfer coefficient (natural convection is ignored). The two terms on the left side of the heat balance in equation (Eq. 1.12) represent conduction from within the solid to the solid surface, and from the solid surface to the surrounding air, respectively. In order to avoid the complications involved in modeling the oven wall thickness as well as insulation, it is assumed that no heat escapes from the oven cavities. Also, the heat capacity of the walls is assumed to be small. These assumptions are justified considering

Figure 1.5 (continued)

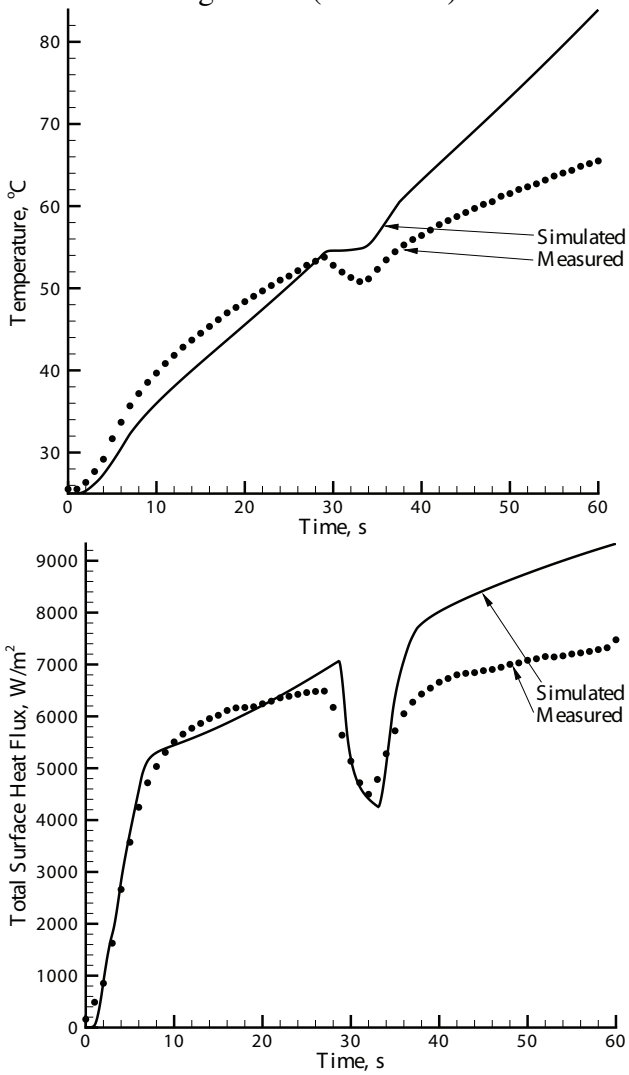

(c) Level X

that the oven walls are made up of thin stainless steel sheets and the cavity is enclosed in a thick insulation material. Since the oven walls are adiabatic, the first term in equation (Eq. 1.12) is set to zero at those walls. For the food surface, this term is calculated using the heat conduction equation (Eq. 1.10) inside the food.

Table 1.1: Input parameters used in simulations of radiative heat transfer in an oven

Parameter	Value	Source
Air density	$1.1614\ \mathrm{kg/m^3}$	Bejan 1993[30]
Air specific heat	$1030\ \mathrm{J/kg \cdot K}$	Bejan 1993[30]
Air thermal conductivity	$0.045\ \mathrm{W/m \cdot K}$	Bejan 1993[30]
Potato density	$1000\ \mathrm{kg/m^3}$	Talburt and Smith 1959[31]
Potato specific heat	$3900\ \mathrm{J/kg \cdot K}$	Talburt and Smith 1959[31]
Potato thermal conductivity	$0.4\ \mathrm{W/m \cdot K}$	Talburt and Smith 1959[31]
Potato emittance (non-gray) ≤ 1350 nm	0.67	Figure 1.4 (Almeida 2004[27])
Potato emittance (non-gray) ≥ 1350 nm	0.96	Figure 1.4 (Almeida 2004[27])
Bulb cavity glass density	$2650\ \mathrm{kg/m^3}$	Wolfe 1965[20]
Bulb cavity glass specific heat	$786\ \mathrm{J/kg \cdot K}$	Wolfe 1965[20]
Bulb cavity glass thermal conductivity	$8.4\ \mathrm{W/m \cdot K}$	Wolfe 1965[20]
Oven surfaces emittance	0.1	Gubareff et al. 1960[29]
Glass absorption coefficient ≤ 4250 nm	$106\ \mathrm{m^{-1}}$	Wolfe 1965[20]
Glass absorption coefficient ≥ 4250 nm	$2300\ \mathrm{m^{-1}}$	Wolfe 1965[20]
Bulb maximum output power	$3\ \mathrm{kW}$	GE Advantium$^{\mathrm{TM}}$ Specifications
Radiation temperature of the bulbs	$4198\ \mathrm{K}$	Measured

1.3.4 Input Parameters

Table 1.1 lists the input parameters used for the simulations. The oven surface emittances are taken as those of stainless steel at $300\ \mathrm{K}$. The potato emittance is set for two different values – 0.67 up to $1350\ \mathrm{nm}$ and 0.96 for wavelengths beyond $1350\ \mathrm{nm}$, for the 4-band non-gray analysis described earlier. The emittance of the heat source is parametrically varied in time to describe the time cycling of the lamps (see discussion in the following paragraph). Quartz glass properties are used for the plate covering the bulb cavity[20]. The glass has absorption coefficients of $106\ \mathrm{m^{-1}}$ and $2300\ \mathrm{m^{-1}}$ for wavelengths below and above $4250\ \mathrm{nm}$, respectively. For the $3.25\ \mathrm{mm}$ glass cover plate thickness, using the Beer-Lambert law, these values translate to absorption values of 29 % and 99 % for wavelengths below and above $4250\ \mathrm{nm}$.

Time-Varying Boundary Condition for the Infrared Source

The halogen lamps that provide infrared energy to the oven cycle on and off, producing a time-varying heat flux. Only the heat flux due to the two halogen bulbs located in the oven ceiling is considered here. The radiation spectrum from the lamps was analysed using a high resolution fiber optic spectrometer, HR4000 (Ocean Optics Inc., Dunedin, FL, USA). Figure 1.2 shows the intensity vs. wavelength obtained from the spectrometer and normalized with respect to the intensity at 690 nm, the wavelength corresponding to the peak. The maximum energy emitted by the lamps per unit time is assumed to be equal to the rated power of the top lamps, i.e., 1.5 kW each. This maximum power is then multiplied by a time function, $f(t)$, with values ranging from 0 to 1, to represent the transient behavior of the lamp. The function, $f(t)$, is found by measuring the radiation intensity at 690 nm versus time, and normalizing as noted in the foregoing. Figure 1.6 shows the $f(t)$ curves obtained in this way for the three power levels (settings on the oven dial) of I, V and X. The time function, $f(t)$, increases as the lamps are turned on and decays as the lamps are turned off. The output energy emitted per unit time, $P(t)$, is related to $f(t)$ by

$$P(t) = 3000 f(t) \tag{1.13}$$

The radiation simulation assumes constant optical properties in each band and cannot handle a spectrum with different emittances at each wavelength. In order to make the model consistent with the actual radiation spectrum of the source lamps, the emitted energy spectrum from the lamps is approximated as follows. The source lamps are replaced by two non-gray strips, at the top wall of the upper lamp cavity, radiating at a fixed temperature, T_s of 4198 K (which matches the peak wavelength of 690 nm), and having a uniform non-zero emittance over the wavelength range 550-850 nm. The energy in this band was set equal to the measured (over all wavelengths) emitted energy. In Figure 1.2, the approximated spectrum (i.e., the band between 550 nm and 850 nm),

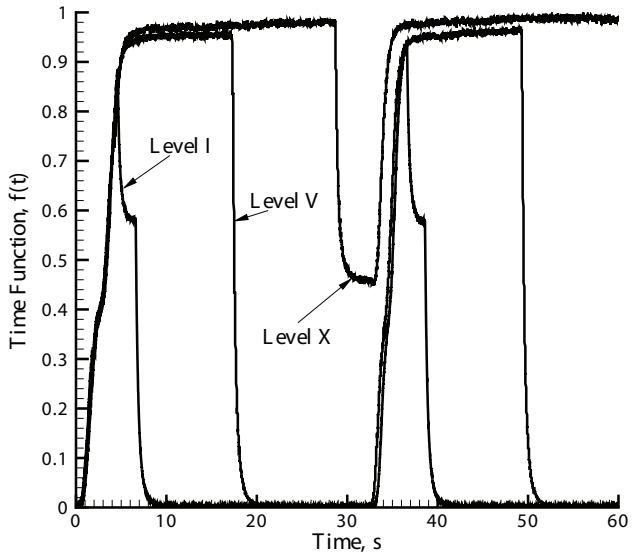

Figure 1.6: Time function, $f(t)$, in Eqn. 1.13 for infrared power level settings I, V and X. The time function represents the radiation intensity at time t as a fraction of the peak intensity.

is shown superimposed over the experimentally-measured spectrum. The emittance of the source, $\epsilon_s(t)$, is then varied with time to represent the cycling of the lamps:

$$\epsilon_s(t) = \frac{P(t)}{\sigma {T_s}^4 A_s F_{(0.85)(4198)-(0.55)(4198)\ \mu\mathrm{mK}}} \tag{1.14}$$

The area of the two strips of the infrared source, A_s, is specified arbitrarily to be 40% of the area of the top wall of the upper cavity. Note that this arbitrary specification of area is done as only the product of emittance and area can be known and not their individual values. The change of area is not expected to significantly change the glass or food fluxes or temperatures, as the total emitted radiation energy and the spectrum remain the same regardless of the chosen area.

Convection Cooling over the Solid Surfaces

The duration of heating in this study is one minute. Natural convection airflows in the main oven cavity are induced with the start of heating and then relax to zero when the

radiant heaters are shut off and the surfaces cool. Due to the high Rayleigh number ($>10^9$) beneath the lamp cavity glass, and because the associated boundary layer would develop in a density-stratified media, the modeling of the natural convection currents inside the main cavity would be a separate study in itself[25]. Although it is possible to estimate the steady-state, fully-developed heat transfer coefficients for a heated rectangular block and the walls inside a cavity[26], it was shown elsewhere[27] that the oven takes several minutes to reach a convective steady-state condition. Thus, for a one minute heating period that includes lamp cycling over even shorter time intervals, a steady-state heat transfer coefficient (the value of $4.5\ \mathrm{W/m^2K}$) would not be appropriate. In this study, for simplification, we have ignored the cooling due to the natural convection of air adjacent to solid surfaces. However, the effect of forced convection cooling in the upper lamp cavity is accounted for by specifying a constant velocity of $12.5\ \mathrm{m/s}$ for the air in the cavity (as discussed under **Governing Equations and Boundary Conditions for Heat Conduction**).

1.3.5 Numerical Solution

The radiative transport equation, RTE (Eq. 1.7), is approximated using the method of Discrete Ordinates (DO)[28] to handle directional effects and is solved numerically, together with the energy equation (Eq. 1.10), using FLUENT$^{\mathrm{TM}}$ 6.3.26, a commercial CFD software package. The RTE has direction as an independent variable, and thus direction is discretized as are the other independent variables, x,y and z. In the present study, each octant of the angular space was divided into 3 (polar) × 3 (azimuthal) control angles of equal extent. Thus, in all 8 × 3 × 3 = 72 directions are solved for each band. Further details of the discretization are available elsewhere[28].

For the energy equation, a hexahedral mesh was used with 381786 cells. A second order upwind scheme was used for the x-y-z spatial discretization, while a first order implicit scheme was used for the time integration. Simulations were performed on an 8 node cluster of Dual Processor 3.6 GHz Xeon EM64T workstations with 4 GB RAM per node. The wall clock time for one second of simulation was about 30 minutes.

1.4 Experimental Measurements

1.4.1 The Oven and the Food System

As shown in Figure 1.1, the GE Advantium$^{\mathrm{TM}}$ oven (Model no. SCA2000BBB 03) is a combination oven with microwave and infrared (halogen) heating capabilities. It has three halogen lamps of 1.5 kW power each, inside two cavities – two lamps in the top cavity and one in the bottom. The top and bottom cavity lamps can be controlled independently. For the purpose of this study, only the top lamps were used so that experiments and simulation could be carefully compared. The oven has microwave heating as an additional heating mode[27], but that mode was not used in the present study.

The dimensions of the main cavity of the oven are 0.470 m $\times$ 0.356 m $\times$ 0.215 m (Figure 1.1), with a volume of 0.036 m^3. All the inside surfaces, besides the lamp covers and the front window, are brushed stainless steel. The power levels of infrared heating are set through a dial on the oven control panel. The dial has 10 settings from I to X which determine the on-off cycle times for the halogen lamp. Larger numbers correspond to longer on-times. Heating duration can be adjusted in intervals of 15 s.

The food sample is a rectangular slab of potato (TOPS SELECT Golds brand), obtained from a local grocery store, and sliced into dimensions 1/10th that of the oven, 0.0470 m $\times$ 0.0356 m $\times$ 0.0215 m. The sides of a potato sample were aligned with the corresponding sides of the oven. The sample was placed 2.54 cm above the geometric center of the bottom surface of the oven. The food sample was stationary during the experiment and was initially at room temperature. A previous study[21] characterized the spectral radiative properties of the potato samples.

1.4.2 Temperature Measurements on Glass Surface below Top Lamp

As illustrated in Figure 1.1, the temperature history of the underside of the glass surface was obtained using a K-type thermocouple (Omega Engineering Inc., Stamford, Connecticut, USA), which has a sensitivity of 41 $\mu\mathrm{V}/^{\circ}\mathrm{C}$, with $\pm 1.5^{\circ}\mathrm{C}$ uncertainty. The sensor was cemented onto the glass using high conductivity Omegatherm paste from the same company and was supported by paper tape. Temperatures were recorded every 1 s for three oven cyclic settings (namely, I, V and X), using the top lamps only.

1.4.3 Temperature and Heat Flux Measurements on the Food Surface

Temperature and incident heat flux on the food surface were recorded using an Omega Thin Film Heat Flux Sensor HFS-3 (Omega Engineering Inc., Stamford, Connecticut, USA). This thermocouple was cemented onto the surface using Omegatherm paste and

paper tape. The heat flux in the differential thermocouple sensor is proportional to the temperature difference across the sensor, which is measured directly. The planar dimensions of the sensor are 35.1 mm $\times$ 28.5 mm, with long lead wire extensions for connections. The upper temperature limit for the sensor is 165°C. The HFS-3 is a precalibrated heat flux sensor, which gives a voltage as output with a sensitivity of 0.95 $\mu\mathrm{V}/(\mathrm{W}/\mathrm{m}^2)$, with $\pm 10\%$ uncertainty. The maximum recommended heat flux for the sensor is 94.6 kW/m^2, much larger than the fluxes encountered in this study. A K-type thermocouple is built into the heat flux sensor to record temperature.

The sensors are interfaced with a FLUKE Data Acquisition Bucket (FLUKE, Washington, USA) which directly measures the voltage with no need of cold-junction compensation. For the three oven infrared settings used in this study, heating was restricted to one minute durations to minimize the effects of evaporation. A one minute duration covers about two lamp cycles. The same data acquisition system was used for the glass cover temperature, the food temperature, and the food heat flux measurements.

1.5 Results and Discussion

Transient radiative exchange analyses were performed for one minute heating cycles of the lamps, as described in **Time-Varying Boundary Condition for the Infrared Source**, to obtain temperature and heat flux values on the food and glass surfaces. Time step convergence and comparisons with experimental temperature and heat flux values will be described. The effects of power level, gray versus non-gray treatments, and various food and wall emittances will be examined.

1.5.1 Time Step Convergence

The significant computational effort involved in the simulation of a 3-D, 4-gray band discrete ordinates radiation model, as discussed in **Numerical Solution**, requires the use of the largest possible time step for which the solution is still independent of time step size. Figure 1.7 shows the temperature at the mid-point of the lower surface of the upper lamp cavity for 15 s of heating time using different time step sizes. The temperature stops changing for time step sizes smaller than about 0.1 s, which is the step size used for all the simulations.

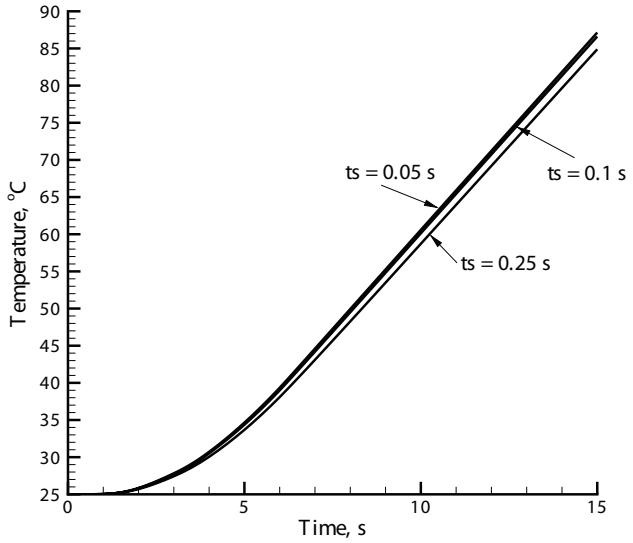

Figure 1.7: Temperature at the center position on the underside of the glass surface covering the top infrared lamps during 15 s of heating for three different time step sizes for infrared power level X

1.5.2 Glass Temperatures

The glass that covers the upper cavity absorbs part of the radiation coming from the lamps and transmits the rest. In order to predict the food temperature and fluxes,

it is essential to accurately account for the glass behavior. Figure 1.8 compares the experimentally-measured and numerically-simulated temperature histories at the geometric center of the bottom surface of the glass for all three power levels. For all three power levels, the glass temperature follows the time function, $f(t)$, as temperature rises initially. The temperature keeps on rising as $f(t)$ becomes flat at its peak value (both lamps switched on at full power) and starts decaying at a very slow rate after the lamps are switched off ($f(t) = 0$). Figure 1.9a shows numerically-calculated glass temperature contours at $t = 4s$ for power level I. We can see that the temperature is the highest in the regions directly below the lamps and is a strong function of the relative distance from the lamp strips. Also, at $t = 12s$, when the lamps are off and the source radiation is subsiding, the glass temperature spatially decreases from the end where the cooling air enters the lamp cavity to the end where the cooling air leaves. The effect of the cooling air in the lamp cavity is further illustrated in Figure 1.10, where the mid-point temperature for power level I is shown for three different assumed air velocities of 7.5 $\mathrm{m/s}$, 12.5 $\mathrm{m/s}$ and 17.5 $\mathrm{m/s}$. For a velocity of 7.5 $\mathrm{m/s}$, the temperature is almost constant after the lamps are switched off. At higher values of velocity, while the peak temperature values are the same, the temperature starts to decrease after the lamps are switched off. Thus, it can be deduced that the cooling air and the relative position from the lamp are the primary factors affecting the glass temperature. These spatial gradients along with the transient nature of the lamp power, $f(t)$, make the comparison of glass temperatures difficult. Nevertheless, the good match demonstrated in Figure 1.10 at the mid-point of the glass plate for all three power levels supports the heat transfer model used for the upper lamp cavity. Note that the objective was to model the temperature history of the glass and not to characterize the flow inside the cavity. Therefore, simulations were run using different velocity values for the upper cavity air to find the best match; the best match was judged to occur for a velocity of 12.5 $\mathrm{m/s}$.

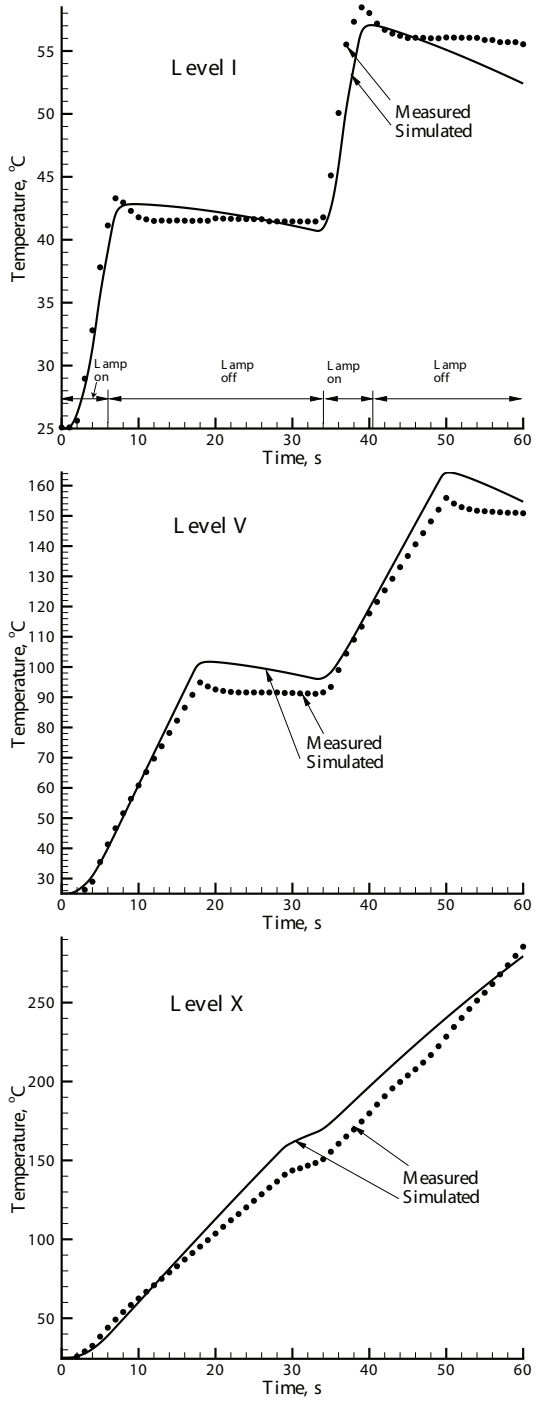

Figure 1.8: Experimental and computed temperatures at the center position on the underside of the glass surface covering the top infrared lamps during one minute of heating for three different settings of infrared power level (Levels I, V and X) in the Advantium $^{\mathrm{TM}}$ oven.

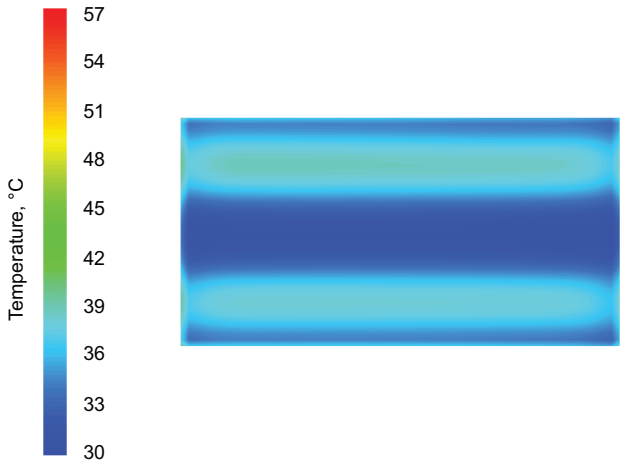

(a) $t = 4$ s

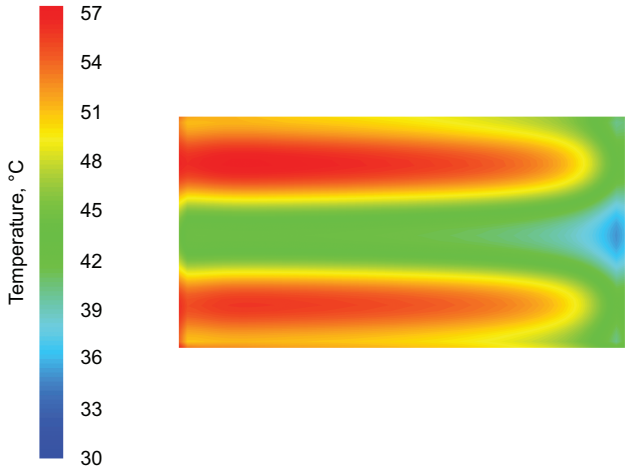

(b) $t = 12$ s

Figure 1.9: Calculated temperature contours on the underside of the glass surface covering the top infrared lamps at 4 s and 12 s for power level I.

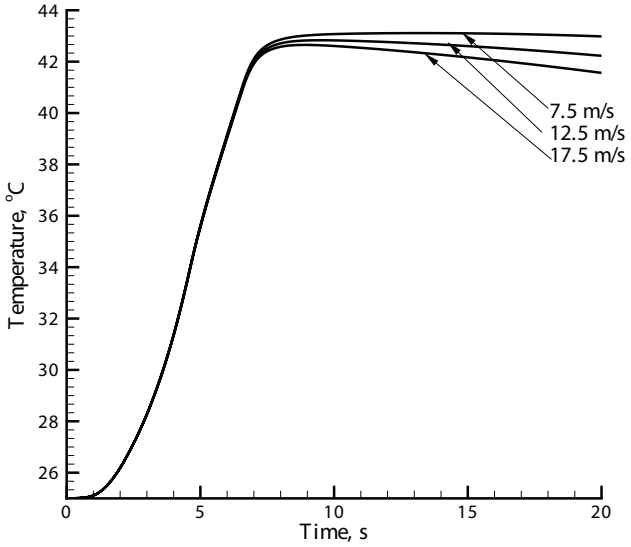

Figure 1.10: Calculated temperatures at the center position on the underside of the glass surface covering the top infrared lamps during 20 sec of heating at power level I with three different values of air velocity in the upper lamp cavity.

1.5.3 Food Fluxes and Temperatures

The primary interests in this study are the temperature and heat flux at the food sample being heated. For validation, Figure 1.5 compares the numerically-computed heat flux and temperature values, averaged over the region covered by the thermocouple sensor on the top of the food, with the experimentally-measured values for three power levels. The fluxes follow the growth and decay transients of the lamp, as expected. Temperature rises with the growth of lamp power and then decays at a slower rate. This decrease in temperature is due to heat loss to the surrounding air as well as heat conduction to the cooler interior regions of the food sample. Figure 1.11 shows temperature contours in the food sample at various cross-sections.

For the three power levels, the food surface temperature reaches peak values of 35°C, 52°C and 65°C, respectively. The model is able to predict the temperature and heat flux cycling reasonably well for the initial 30 seconds and longer. However, during the

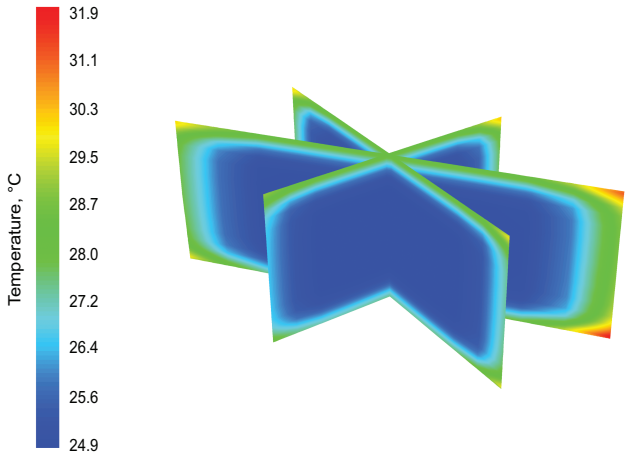

Figure 1.11: Temperature contours at different cross-sections of food at $t = 12$ s for power level I.

times when the lamps are off (from 7 to 34 s and from 41 to 60 s for level I heating; and from 17 to 34 s and from 51 to 60 s for level V heating), the cooling rates are underpredicted. This is most likely due to the neglect of surface evaporation and natural convection in this study (see **Convection Cooling over Solid Surfaces**) which cause the food surfaces to cool faster once the lamps are off. The effect of evaporative cooling becomes prominent at higher temperatures, especially in the level X temperature and heat flux histories (Figure 1.5c), when the heating rate is overpredicted. Even with these limitations, the error in food temperatures and heat fluxes is within 15% for most of the time for all power levels, which is a very good match, considering that the system is a commercial oven and not a laboratory experiment where all the parameters can be controlled.

One of the most interesting features elucidated by the present non-gray radiation analysis is the band-wise distribution of energy absorbed by the food sample. Such information may provide insights as to where design efforts should be spent to improve the efficiency of the process. This information is critical while studying the kinetics of photochemical reactions occurring in the food, which lead to loss of food nutrients and

formation of undesired free radicals[2]. Figure 1.12 shows the power absorbed by the food surface, in the four radiation bands, over time for three power levels. Here, Band 1, i.e., from 550 nm to 850 nm wavelength, is the direct and wall reflected source-lamp radiation band. All the other bands correspond to radiation emitted by other sources, i.e. the oven walls and glass. It can be observed that indirect heating from the walls contributes significantly to the total power absorbed by the food, and constitutes more than 50$\%$ of the flux after the initial few seconds during which the oven walls and the glass are getting heated.

The energy efficiency of the process, i.e., the ratio of the energy absorbed by the food to the total input energy can be an important factor when designing an oven. Considering 3 kW as the input energy, the fraction of energy delivered to the food over its entire surface at the peak of lamp power emission was estimated to be around 0.8$\%$, 1.2$\%$ and 1.5$\%$, respectively, for power levels I, V and X. Such small values are probably due to the small size of the food sample. It would be useful to compare these numbers for different food sizes; however, such a study was beyond the scope of the current project due to the large computational resources required for each simulation. Future work could also consider various combinations of the three possible heating modes: infrared, convection and microwave.

1.5.4 Effect of Food Surface Emittance (Gray vs. Non-gray)

Measured data for the potato surface exhibit non-gray behavior as shown in Figure 1.4, where the emittance is 0.67 for wavelengths < 1350 nm and 0.96 for wavelengths $>$ 4250 nm[27]. These values were used in this study. Typically, however, only wavelength-averaged emittance values are available for foods. The wavelength averaging is defined

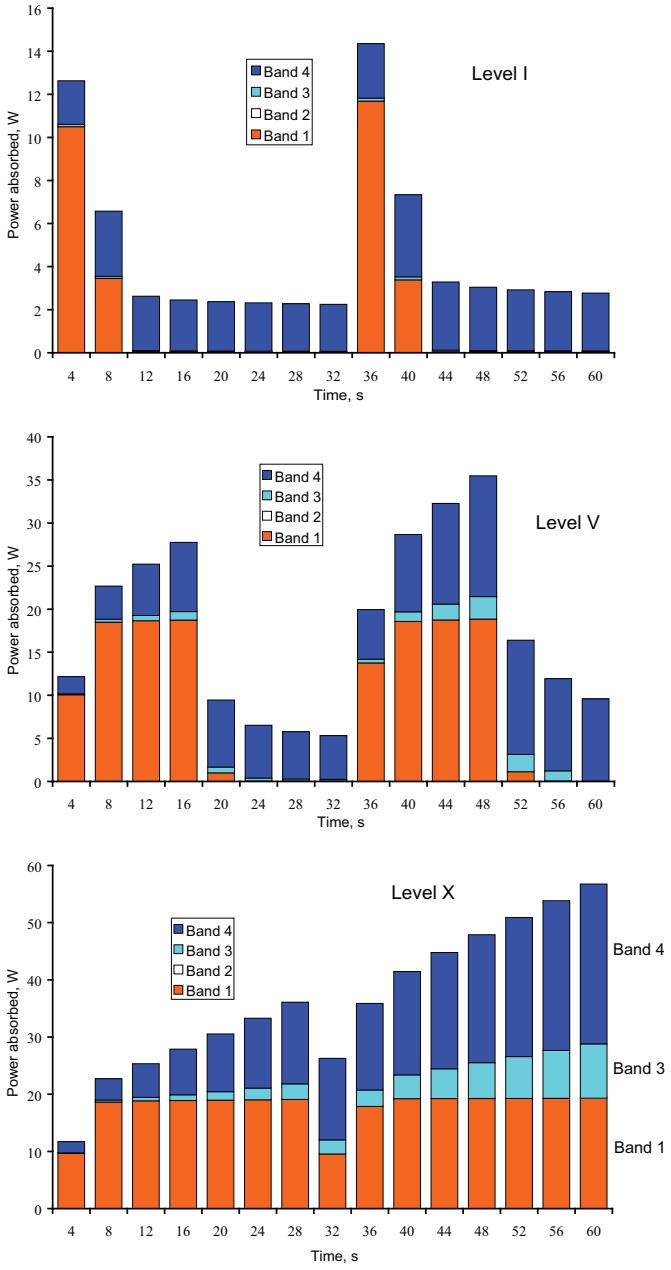

Figure 1.12: Distribution of the total power absorbed by the food in four radiation bands over time for power levels I, V and X. Bands are defined in Figure 1.3. The contribution from Band 2 is negligible for all three power levels at all times.

by:

$$\epsilon_{avg} = \frac{1}{\sigma T^4} \int_0^\infty E_\lambda d\lambda \tag{1.15}$$

Averaging is only accurate when all the radiation sources have identical temperatures. When surfaces at different temperatures are present (e.g., source lamps, glass and oven walls in the current study), the use of such an average may not be appropriate.

We carried out a brief study of gray versus non-gray food emittance. Simulations (for power level X) were carried out for three different food surface emittance combinations: 0.67 for all wavelengths; non-gray surface (0.67 for wavelengths < 1350 nm and 0.96 for wavelengths > 4250 nm); and 0.96 for all wavelengths. Calculated temperature and heat flux profiles at the center of the top surface of the food sample are shown in Figure 1.13. Early in the transients, the flux and temperature profiles for $\epsilon_{food} = 0.67$, which is gray, and the non-gray case nearly coincide. This is because almost all the heat coming to the food is from the source lamp, i.e., with wavelengths < 1350 nm, for which ϵ_{food} in both the cases is 0.67. However, as the oven walls get heated and start contributing significantly to the heat delivered to the food, the profiles with $\epsilon_{food} = 0.67$ start to fall below the non-gray case. This is because the oven walls emit radiation with longer wavelengths, and for which the food emittance should be 0.96 and not 0.67. This effect will be much more pronounced at later times when emission from the oven walls becomes larger and also when the lamps are completely shut off and all the heating is provided by the oven walls. When used for the whole duration of heating, the $\epsilon_{food} = 0.96$ value gives much larger food surface absorbed fluxes and temperatures for obvious reasons.

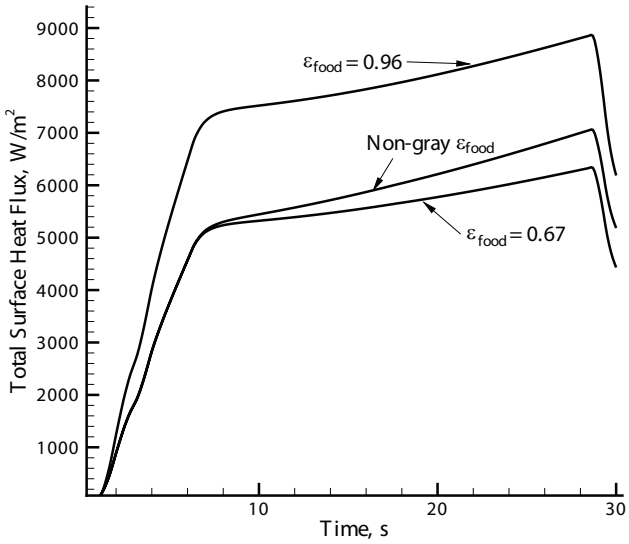

(a) Total surface heat flux

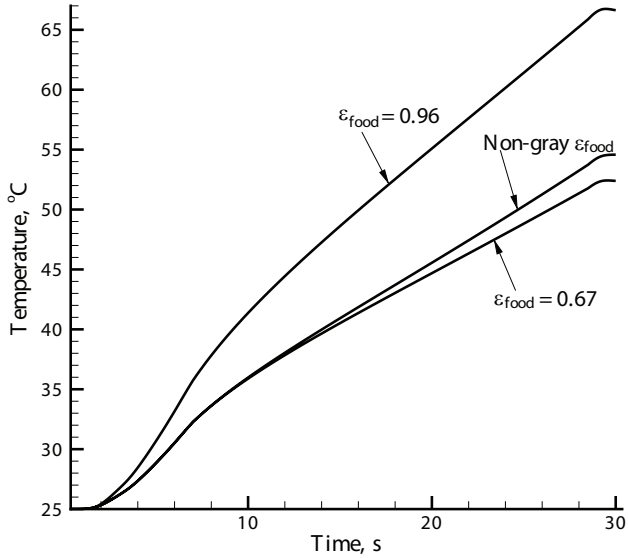

(b) Temperature

Figure 1.13: Experimental and computed temperatures and total surface heat fluxes at the center position on the top surface of the food during 30 seconds of heating for three different food surface emittance values for power level X.

1.5.5 Effect of Wall Emittance

Oven walls reflect the source radiation and after getting heated, emission from the oven walls can be more than 50% of the total heat absorbed by the food sample (see Band 4 in Figure 1.12). Hence, it becomes important to know how the surface properties of an oven can influence food heating. Figure 1.14 compares heat flux and temperature profiles for two different oven wall emittance values, 0.1 and 0.05, for power level X for 30 s of heating. This emittance range brackets the range for clean stainless steel[29]. For the lower wall emittance value, the fluxes and temperatures at the food are higher by around 30% and 15%, respectively, after 8 s of heating because of greater reflection by the walls to the food surface. With time, the difference between the two flux values decreases as direct emission from the walls becomes significant and compensates to a certain extent for the lower reflectance of the $\epsilon_{wall} = 0.1$ surface.

1.6 Conclusion

A 3-D, 4-band, non-gray radiation model was developed which can predict heat transfer inside an oven cavity. The total energy delivered to a food sample was estimated and its distribution among the four wavelength bands was shown to change as heating progressed. The contribution of the oven wall emission was found to be more than 50% after the initial heating-up period. The effect of variation of the food surface emittance with wavelength on the heating process shows that a non-gray treatment is necessary due to the presence of radiation in different wavelength bands. The effect of wall emittance shows that lower emittance (and thus higher reflectance) leads to higher heating rates of the food. In addition to providing fundamental insights into the radiative heating process in an oven, a detailed model can be used to optimize various design parameters

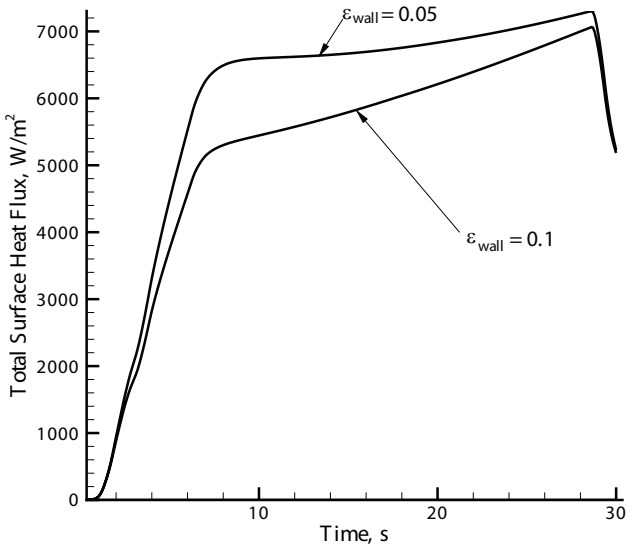

(a) Total surface heat flux

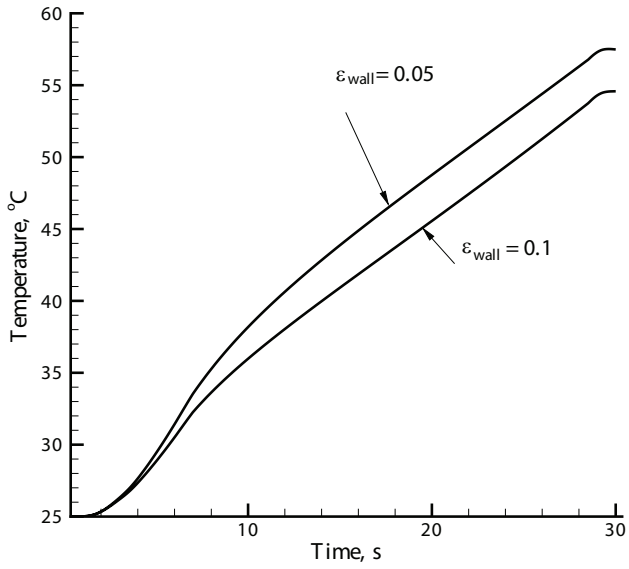

(b) Temperature

Figure 1.14: Experimental and computed temperatures and total surface heat fluxes at the center position on the top surface of the food during 30 seconds of heating for two different oven wall emittance values for power level X.

of an oven such as geometry of the cavity, cycling time, source and food placement and other oven arrangements, thus reducing time and costs associated with trial and error experimentation.

BIBLIOGRAPHY

[1] De Matteis M, inventor; Moulinex SA assignee. Electric Microwave Oven with Improved Energy Distribution. US patent 6 002 120. December 14, 1999.

[2] Uzgiris EE, Ackerman JF, Lillquist RD, inventors; General Electric assignee. Radiant Oven. US patent 6 018 146. January 25, 2000.

[3] Lee K, inventor; LG Electronics Inc. assignee Microwave Oven Having Halogen Lamps. US patent 6 172 347. January 9, 2001.

[4] Cook ER, inventor; Maytag Corporation assignee. Combination high speed infrared and convection conveyor oven and method of using. US patent 6 369 360. April 9, 2002.

[5] Farkas B, Lloyd B, Keener K, inventors; North Carolina State University assignee. Dynamic radiant food preparation methods and systems. US patent 7 307 243. December 11, 2007.

[6] Dagerskog M, Sorenfors P. A comparison between four different methods of frying meat patties. I: Heat transfer, yield and crust formation. *Lebensmittel-Wissenschaft u. Technologie*, 1978;11:306-311.

[7] Shibukawa S, Sugiyama K, Yano T. Effect of heat transfer by radiation and convection on browning of cookies. *Journal of Food Science*, 1989;54(3):621-624,699.

[8] Kathiravan K, Kaur K, Soojin J, Irudayaraj J, Demirci A. Infrared heating in food processing: an overview. *Comprehensive Reviews in Food Science and Food Safety.* 2008;7(1):2-13.

[9] Cenkowski S, Hong JT, Scanlon JG, Arntfield SD. Mathematical modeling of heat and mass transfer during continuous infrared micronization. *Drying Technology*. 2004;22(10):2255-2272.

[10] Wang J, Sheng KC. Modeling of muti-layer far-infrared dryer. *Drying Technology*. 2004;22(4):809-820.

[11] Tanaka F, Morita K, Iwasaki K, Verboven P, Scheerlinck N, Nicolai B. Monte Carlo simulation of far infrared radiation heat transfer: Theoretical approach. *Journal of Food Process Engineering*. 2006;29(4):349-361.

[12] Meeso N, Nathakaranakule A, Madhiyanon T, Soponronnarit, S. Modelling of far-infrared irradiation in paddy drying process. *Journal of Food Engineering*. 2007;78(4):1248-1258.

[13] Tanaka F, Verboven P, Scheerlinck N, Morita K, Iwasaki K, Nicolai B. Investigation of far infrared radiation heating as an alternative technique for surface decontamination of strawberry. *Journal of Food Engineering*. 2007;79(2):445-452.

[14] Sato H, Hatae K, Shimada A. Effect of heating system on the evaporation process of food: Radiation and convection. *Journal of the Japanese Society for Food Science and Technology - Nippon Shokuhin Kagaku Kogaku Kaishi*, 1999;46(8):508-513.

[15] Skjoldebrand C, Andersson C. A comparison of infrared bread baking and conventional baking. *Journal of Microwave Power and Electromagnetic Energy*, 1989;24(2):70-75.

[16] Franca FHR, Ezekoye OA, Howell JR. Inverse boundary design combining radiation and convection heat transfer. *Journal of Heat Transfer*, 2001;123:884-891.

[17] Adams BR, Smith PJ. Three dimensionally discrete ordinates modeling of radiative transfer in a geometrically complex furnace. *Combustion Science and Technology*, 1993;88(5-6):293-308.

[18] Peterson M, Stenstrom S. Modeling of an electric infrared heater at transient con-

ditions - part I: model and validation. *International Journal of Heat and Mass Transfer*, 2000;43:1209-1222.

[19] Ojala KT, Lampinen MJ. Modeling, measurements and efficiencies of infrared dryers for paper drying. In: A.S. Mujumdar, ed. *Handbook of Industrial Drying*, volume 2. New York: Marcel Dekker, Inc., 1995;931-976.

[20] Wolfe WL. *Handbook of military infrared technology*. Washington: Office of Naval Research, Department of the Navy, USGPO, 1965.

[21] Almeida MF, Torrance KE, Datta AK. Measurement of optical properties of foods in near-and mid-infrared radiation. *International Journal of Food Properties*, 2006;9(4):651-664.

[22] Raithby GD, Chui, EH. A finite-volume method for predicting a radiant-heat transfer in enclosures with participating media. *Journal of Heat Transfer*, 1990;112:415-423.

[23] Siegel R, Howell JR. *Thermal Radiation Heat Transfer*. 4th ed. New York: Taylor and Francis, 2001.

[24] Siegel R, Spuckler CM. Effects of refractive-index and diffuse or specular boundaries on a radiating isothermal layer. *Journal of Heat Transfer*, 1994;116:787-790.

[25] Xamán J, Arce J, Álvarez G, Chávez Y. Laminar and turbulent natural convection combined with surface thermal radiation in a square cavity with a glass wall. *International Journal of Thermal Sciences*, 2008;47(12):1630-1638.

[26] Sparrow EM, Abraham JP Heat transfer coefficients and other performance parameters for variously positioned and supported thermal loads in ovens with/without water-filled or empty blockages. *International Journal of Heat and Mass Transfer*, 2002;45:3597-3607.

[27] Almeida MF. *Modeling Infrared and Combination Infrared-Microwave Heating of Foods in an Oven*. [PhD thesis]. Ithaca: Cornell University; 2005.

[28] Murthy JY, Mathur SR Radiative heat transfer in axisymmetric geometries using an unstructured finite-volume method. *Numerical Heat Transfer Part B-Fundamentals*, 1998;33(4):397-416.

[29] Gubareff GG, Janssen JE, Torborg RH *Thermal Radiation Properties Survey – a review of the literature*. Minneapolis - Honeywell Regulator Company, Meneapolis: Honeywell Research Center, 1960.

[30] Bejan A. *Heat Transfer*. New York: John Wiley & Sons, Inc., 1993.

[31] Talburt WF, Smith O. *Potato Processing*. Westport, Connecticut: The Avi Publishing Co, Inc., 1959.

CHAPTER 2

MODELING TRANSPORT IN POROUS MEDIA WITH PHASE CHANGE: APPLICATIONS TO FOOD PROCESSING

This chapter is a joint work with equal contributions from Amit Halder and Ashish Dhall, under Prof. Ashim Datta's guidance.

2.1 Abstract

Background. Fundamental, physics-based modeling of complex food processes is still in the developmental stages. This lack of development can be attributed to complexities in both the material and the transport processes. Society has a critical need for automating food processes (both in industry and at home), while improving quality and making food safe. Product, process and equipment design in food manufacturing requires the more detailed understanding of food processes that is possible only through physics-based modeling. The objectives of this paper are to: 1) develop a general multicomponent and multiphase modeling framework that can be used for different thermal food processes and can be implemented in commercially available software (for wider use); and 2) apply the model to the simulation of deep-fat frying and hamburger cooking processes, and validate the results.

Model details. Treating food material as a porous medium, heat and mass transfer inside such material during its thermal processing is described using equations for mass and energy conservation that include binary diffusion, capillary and convective modes of transport, physicochemical changes in the solid matrix that include phase changes such as melting of fat and water, and evaporation/ condensation of water. Evapora-

tion/condensation is considered to be distributed throughout the domain and is described by a novel non-equilibrium formulation whose parameters have been discussed in detail.

Results. Two complex food processes, deep-fat frying and contact heating of a hamburger patty, representing a large group of common food thermal processes with similar physics, have been implemented using the modeling framework. The predictions are validated with experimental results from the literature. As the food (a porous hygroscopic material) is heated from the surface, a zone of evaporation moves from the surface to the interior. Mass transfer due to the pressure gradient (from evaporation) is significant. As temperature rises, properties of the solid matrix change and the phases of frozen water and fat become transportable, thus affecting the transport processes significantly.

Conclusion. Because the modeling framework is general and formulated in a manner that makes it implementable in commercial software, it can be very useful in computer-aided food manufacturing. Beyond its immediate applicability in food processing, such a comprehensive model can be useful in medicine (for thermal therapies such as laser surgery), soil remediation, nuclear waste treatment and other fields where heat and mass transfer take place in porous media with significant evaporation and other phase changes.

Nomenclature

b	number of components in the solid phase
c	concentration, kg m^{-3}
c_p	specific heat capacity, J $kg^{-1}K^{-1}$
C_g	molar density, kmol m^{-3}
$D_{eff,g}$	effective gas diffusivity, m^2s^{-1}
D	diffusivity, m^2 s^{-1}
$\mathbf{g}$	acceleration due to gravity, kg m^{-3}
h	heat transfer coefficient, W m^{-2} K^{-1}
h_m	mass transfer coefficient of vapor, m s^{-1}
$\dot{I}$	volumetric evaporation rate, kg m^{-3} s^{-1}
k	thermal conductivity, W m^{-2} K^{-1}
k^p	permeability, m^2
K	non-equilibrium evaporation constant, s^{-1}
$K_{i,j}$	non-equilibrium constant for interphase mass transfer from i to j, s^{-1}
L	length scale, m
m	overall mass fraction
M_a, M_v	molecular weight of air and vapor
n	total number of phases
$\mathbf{n}$	total flux, kg m^{-2} s^{-1}
P	gas pressure, Pa
p_v	vapor pressure, Pa
$\mathbf{q}$	heat flux, J m^{-2} s^{-1}
R	universal gas constant, J $kmol^{-1}$ K^{-1}
$\dot{R_{i,j}}$	rate of mass transfer from i to j, kg m^{-3} s^{-1}
S	saturation
t	time, s
T	temperature
u	velocity, m s^{-1}
V	volume, m^3
x	mole fraction

Greek Symbols

ρ	density, kg m^{-3}
λ	latent heat of vaporization, J kg^{-1}
ω_v, ω_a	mass fraction of vapor and air in relation to total gas
ϕ	porosity
μ	dynamic viscosity, Pa s

Subscripts

amb	ambient
a, g, o, s, v, w	air, gas, oil, solid, vapor, water
bw, bf	water, fat in solid phase
cap	capillary
eff	effective
eq	equilibrium
f	final
i	i^{th} liquid phase, initial
in	intrinsic
ini	initial
j	j^{th} component in solid phase
0	at time $t = 0$
r	relative, residual
sat	saturation
$surf$	surface
T	temperature
tot	total

2.2 Introduction

Mathematical modeling has not been able to contribute as much to the development of food processing industries as it has with respect to the mechanical and chemical industries. The primary reason for this is that foods are complex and non-homogenous, and the physics that could explain what happens during processing is still not clearly established. The time and cost involved limit the number of experiments that can be done to achieve this. Looking at recent trends towards the automation of food processes and production of minimally processed healthier foods, it can be said that there is a need to develop accurate mathematical models of these food processes which can be extensively used for equipment design or to ensure food safety. The development of fundamental physics-based models of food processes is not trivial, as it requires physical as well as mathematical insight into the material and the process.

In food systems, an enormous range of thermal processes can be viewed as involving transport of energy, moisture and, in some cases, fat through a hygroscopic porous medium. Examples include extraction, drying, deep fat frying, microwave heating, meat

roasting and rehydration. In the vast majority of food systems, proteins or carbohydrates form a porous skeleton which has water and/or fat physically and chemically bound to it. During heating, water and fat can transport inside the solid matrix or can be released into the pore space and then transported through the porous medium. Other important phenomena that can occur are rapid evaporation due to intensive heating, the melting of ice or fat during the processing of frozen food, and shrinkage due to physicochemical changes in the porous matrix. There is no single model that considers all of these physics together and that can also be implemented in a software application for wide usage.

The existing models of thermal processes can be broadly divided into four groups. The first group consists of totally lumped models for heat and mass transport that do not include any important physics[1–5]. Such models are based entirely on empirical data, are suited for a specified product and processing condition and, therefore, cannot be used for even a slightly different situation. The second group consists of slightly improved models that assume conductive heat transfer for energy and diffusive transport for moisture, solving a transient diffusion equation using experimentally determined effective diffusivity[6–10]. Lumping together all modes of water transport as diffusion cannot be justified under all situations, especially when other phenomena such as pressure-driven flow due to intensive heating or transport due to physicochemical changes in the porous medium become important. Also, the use of effective diffusivity does not yield insights into the prevalent transport mechanisms. These models might provide good matches with experimental results but they cannot be generalized to other conditions.

The third group of models, with a significantly improved formulation compared with those of simple diffusion models, assumes a sharp moving boundary separating the dry and the wet region (e.g., deep-fat frying models[11–13]). This assumption is analogous

to that made in freezing and thawing models of a pure material[14], where a sharp front separates the frozen and unfrozen regions. In contrast to sharp boundary models, distributed evaporation models (the fourth group) assume evaporation occurs over a zone rather than at an interface[15–17]. In a given situation, it is possible that the real evaporation zone is very narrow, closer to the sharp interface, and that a distributed evaporation formulation will, in fact, predict such a narrow evaporation zone.

Evaporation of water in intensive heating food processes, such as deep-fat frying and baking, has usually been implemented using an equilibrium formulation wherein liquid water present in the food is always assumed to be in equilibrium with water vapor present in the pore space[15,16,18]. There's no detailed study of this equilibrium assumption for hygroscopic materials such as food. Only qualitative description of the conditions under which either equilibrium or non-equilibrium assumptions can hold is available[19]. As will be explained later, a non-equilibrium formulation that can also be used to enforce equilibrium is a more general approach and appears to be the obvious alternative. Furthermore, significant effort is required to implement the equations resulting from an equilibrium formulation in the framework of most commercial software, whereas implementation of a non-equilibrium formulation is straight forward.

Overall, accurate models of food processes, which include all the physics, still do not exist. Multiphase porous media models have been used with success in other fields and applications to describe physics that is similar to that involved in food processing. A multiphase porous media approach with conservation equations for relevant components, appropriately including the effect of various phenomena particular to food, has been developed for some food applications[18,20–22]. However, none of these models is general enough to be applied to many different processes. Moreover, these models have been formulated in such a way that they are very difficult to manipulate and implement

in commercial software, and have been solved by user-developed codes. These codes are either publicly unavailable, have limited capabilities or are difficult to use by anyone other than the creator. A general framework applicable to the majority of food processes, which is implementable in commercial software, has not been developed yet. This development is not trivial and requires significant reformulations or in some cases developing a new model altogether. The present study aims to do this.

Some of the physics involved in food processes can be seen in other applications such as geoscience[23], nuclear waste storage and management[24], groundwater contamination[25],[26]), and thermal treatment of tumors or drug delivery in bio-medical engineering[27]. However, food processing applications, involving thermal treatment of heterogeneous materials, are extremely complex. A fundamental physics-based model developed for food processes, which accounts for all the relevant phenomena, can be applied to other fields with simplifications.

The objectives of this study are: (1) to develop a general multiphase model for hygroscopic biological materials that can be used for various thermal processes and can be implemented in commercially available software; (2) to apply the model to simulate deep-fat frying and hamburger cooking processes and validate the results.

The outline of the paper is as follows: A comprehensive mathematical model, which can be used to simulate a large number of thermal processes, is presented first, followed by detailed discussion of a non-equilibrium approach to implementing evaporation/condensation phase change. Two food processes, deep-fat frying of a restructured potato slab and contact heating of a hamburger patty, are modeled using the set of equations developed to show the model's effectiveness in solving different types of thermal food processes. The paper concludes with a discussion of the importance of this comprehensive modeling framework in food processing.

2.3 Mathematical model

A multiphase porous media model is developed that describes heat and mass transfer inside a food material during thermal processing. Mass and energy conservation equations are developed that, depending on the process, may include binary diffusion, capillary and convective modes of transport, the effects of physicochemical changes in the solid matrix on transport, and phase changes such as melting and evaporation-condensation. Evaporation/condensation is assumed to be distributed throughout the domain.

2.3.1 Problem description

The schematic description of a meat matrix as a porous medium is shown in Fig 2.1. The material is assumed to be homogenous. The first and most important step is to identify the distinct phases that are important and significantly affect transport. There can be three types of such phases: solid, liquid and gas. The solid phase in food materials comprises a carbohydrates or proteins matrix with water and, possibly, fat physically and chemically bound to it. So, in all, there can be three components in the solid phase, i.e., the solid matrix, bound water and bound fat. The solid matrix is non-transportable. However, the bound water and fat can transport inside the matrix, even while remaining bound to the solid. In foods, the capacity of the solid matrix to hold water or fat (known as water [or fat] holding capacity in the food science literature) changes with temperature. Usually, as temperature rises, water (or fat) is gradually released from the matrix into the pore space. Thus, water (or fat) undergoes an interphase mass transfer from the solid phase to the pore liquid phase. Therefore, the mass balance of the solid phase is important where the phase change from solid to liquid is significant; otherwise, it can be ignored. In the pores, all immiscible liquids, such as fat and water, can be considered as

separate liquid phases. The third and last type of phase is the gas phase. There cannot be more than one gas phase, as gases are miscible and occupy the total available gas volume available to them. In most food applications, a gas phase is a mixture of air and water vapor.

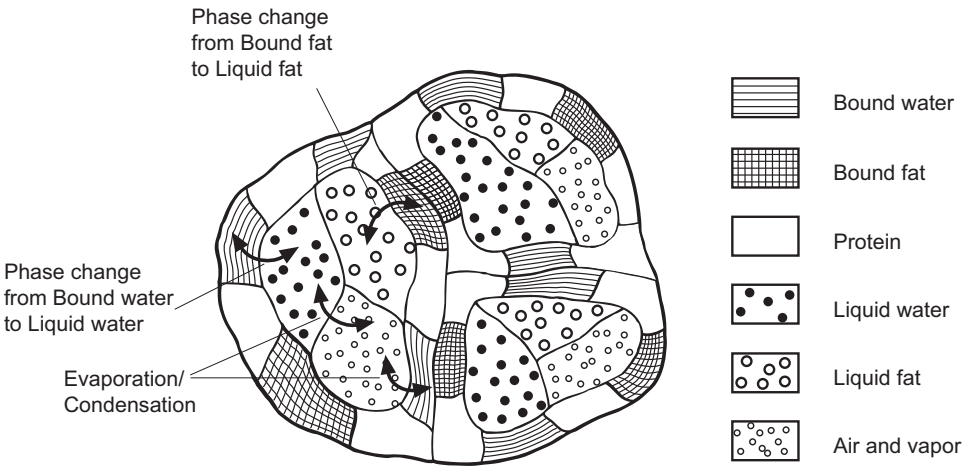

Figure 2.1: Schematic of a porous food material showing mass transfer between various phases

2.3.2 Assumptions

The assumptions made while formulating this multiphase framework are: 1) All the phases (solid, liquids and gas) are in continuum; 2) local thermal equilibrium exists throughout the material between all phases; 3) pressure is shared by all phases, as the effects of capillary pressure have been included as diffusion terms[17,28]; 4) there can be non-equilibrium between water in solid and water-vapor in gas phase, i.e., their concentrations are not given by the moisture isotherms; 5) deformation of the material during processing is not considered.

2.3.3 Governing equations

The mathematical model consists of conservation equations for all the phases and components discussed above. For the sake of generalization, we assume that there are n phases in all. Of these, there is one solid phase, one gas phase and $n-2$ liquid phases. There are b components inside the solid phase and two (vapor and air) inside the gas phase.

Mass balance equations

Porosity, ϕ, is defined as the fraction of the total volume occupied by pores, given by

$$\phi = \frac{V_g + \sum_{i=1}^{n-2} V_i}{V} \tag{2.1}$$

where V_i is the volume occupied by the i^{th} liquid phase in an elemental volume V. If, during a process, the solid matrix loses a bound fluid, such as water, then porosity, ϕ, does not remain constant. As the solid matrix loses water, the porosity increases. In such cases, porosity can be estimated as

$$\phi = 1 - \frac{V_s}{V} = 1 - \sum_{j=1}^{b} \frac{V_j}{V} = 1 - \sum_{j=1}^{b} \frac{c_j}{\rho_j} \tag{2.2}$$

where b is the number of components in the solid phase and c_j and ρ_j are the concentration and density of the j^{th} solid component, respectively. Here, it is assumed that the total volume of the solid can be estimated as the sum of the individual volumes of the solid phase components, with each component retaining its pure state density.

Saturation of a transportable phase is defined as the fraction of pore volume occupied by that particular phase:

$$S_i = \frac{V_i}{\phi V}$$

$$S_g = \frac{V_g}{\phi V} \tag{2.3}$$

where i stands for any liquid phase. The summation of saturation of all transportable phases should lead to unity (Eq. 2.5).

The mass balance equation for a phase solves for saturation of the phase. There are $n-2$ liquid phases and one gas phase. So, $n-2$ mass balance equations (Eq. 2.4) are solved to obtain the saturation (S_i) of each individual liquid phase. The saturation of gas, S_g, is calculated from Eq. 2.5:

$$\frac{\partial}{\partial t}(\phi \rho_i S_i) + \nabla \cdot \mathbf{n_i} = -\dot{R}_{i,j} - \dot{I} \tag{2.4}$$

$$S_g + \sum_{i=1}^{n-2} S_i = 1 \tag{2.5}$$

where $\dot{R}_{i,j}$ denotes interphase mass transfer from the i^{th} liquid phase to the j^{th} solid component. Similarly, $\dot{I}$ denotes the phase change from liquid water to water vapor.

The total flux of the liquid phase, $\mathbf{n_i}$, is due to the liquid pressure, $P - p_{i,cap}$, which is the difference between gas pressure and capillary pressure. This total flux term is given by Darcy's law[28] as:

$$\begin{aligned} \mathbf{n_i} &= -\rho_i \frac{k^p_{in,i} k^p_{r,i}}{\mu_i} \nabla (P - p_{i,cap}) \\ &= -\rho_i \frac{k^p_{in,i} k^p_{r,i}}{\mu_i} \nabla P + \rho_i \frac{k^p_{in,i} k^p_{r,i}}{\mu_i} \left(\frac{\partial p_{i,cap}}{\partial c_i} \nabla c_i + \frac{\partial p_{i,cap}}{\partial T} \nabla T \right) \end{aligned} \tag{2.6}$$

The first term in the right-hand side of the above equation represents flow due to gradients in gas pressure and is significant only in the case of intensive heating of food materials such as microwave heating, deep-fat frying and contact heating at high temperature. The second and third terms can be rewritten in terms of capillary diffusivity, $D_{i,cap}$, and diffusivity due to thermal gradients , $D_{i,T}$, given by:

$$D_{i,cap} = -\rho_i \frac{k^p_{in,i} k^p_{r,i}}{\mu_i} \frac{\partial p_{i,cap}}{\partial c_i} \tag{2.7}$$

$$D_{i,T} = -\rho_i \frac{k_{in,i}^p k_{r,i}^p}{\mu_i} \frac{\partial p_{i,cap}}{\partial T} \tag{2.8}$$

In most of the cases, the gas phase is a mixture of water vapor and air. Spatial variations in the concentration of these components during processing are obtained by solving the respective mass conservation equations in terms of their mass fractions, ω_v and ω_a, with binary diffusion[29]:

$$\frac{\partial(\phi \rho_g S_g \omega_v)}{\partial t} + \nabla \cdot (u_g \rho_g \omega_v) = \nabla \cdot \left(\phi S_g \frac{C_g^2}{\rho_g} M_a M_v D_{eff,g} \nabla x_v \right) + \dot{I} \tag{2.9}$$

$$\omega_v + \omega_a = 1 \tag{2.10}$$

The concentration of components in the solid phase is determined by solving the mass conservation equation for each:

$$\frac{\partial c_j}{\partial t} = \nabla(D_{j,cap} \nabla c_j) + \nabla(D_{j,T} \nabla T) + \dot{R}_{i,j} \tag{2.11}$$

where $R_{i,j}$ is the rate of mass transfer from the liquid phase to the component j in the solid phase, $D_{j,cap}$ is the diffusivity due to concentration gradients and $D_{j,T}$ is the diffusivity due to temperature gradients. Details of $R_{i,j}$ are discussed later in the section on discussion of phase change.

Therefore, $n-2$ Eqs. 2.4, b Eqs. 2.11, along with Eqs. 2.5, 2.9 and 2.10, constitute the set of $n+b+1$ equations from which the concentration variables c_1,c_2,...,c_b,S_1,S_2,...,S_{n-2},S_g, ω_v and ω_a can be found. Temperature and pressure at every point inside the material are determined by invoking gas phase mass conservation and energy conservation equations, as discussed later. Note, however, that there are additional unknowns in these equations for which auxiliary equations will be needed, as discussed later (Eq. 2.37 for the evaporation rate, $\dot{I}$, and Eq. 2.38 for the solid phase change rate, $\dot{R}$).

Momentum balance

The momentum balance equation for a phase solves for the velocity of that phase. In a porous medium with low permeabilities, Darcy flow is valid[28]. Therefore, Darcy's equation for each phase in porous media replaces the standard momentum conservation (Navier-Stokes) equation. However, some software applications do not support Darcy's law (Eq 2.6) directly and instead solve the modified Navier-Stokes equation (Eq. 2.12), which includes the Darcy's term, for momentum balance:

$$\frac{\partial((\phi S_i)\rho_i \mathbf{u_i})}{\partial t} + \nabla.((\phi S_i)^2 \rho_i \mathbf{u_i}\mathbf{u_i}) = -(\nabla P - \rho_i \mathbf{g}) - (\phi S_i)\frac{\mu_i}{k^p_{r,i} k^p_{in,i}}\mathbf{u_i} \tag{2.12}$$

Although Eq. 2.6 is different from Eq. 2.12 due to the additional terms, the inertial terms are shown to be negligible for low-permeability systems[28,30], and Eq. 2.12 reduces to Eq. 2.6 for such systems. Solving Eq. 2.12 for each phase may involve numerous convergence issues as well as large computation times, and should be avoided when addressing low-permeability porous media problems. When there is no option in the software but to solve the Navier-Stokes equation, numerical complications can be reduced by assuming that all the transportable phases share the same pressure and velocity, thereby solving only one equation for the mixture. This is a simplified approach and may lead to erroneous results depending on the problem complexities.

Continuity equation to solve for pressure

The gas pressure, P, is calculated by solving the overall mass balance equation for the gas phase:

$$\frac{\partial}{\partial t}(\phi S_g \rho_g) + \nabla \cdot \mathbf{n_g} = \dot{I} \tag{2.13}$$

where

$$\mathbf{n_g} = -\rho_g \frac{k^p_{r,g} k^p_{in,g}}{\mu_g} \nabla P \tag{2.14}$$

The ideal gas law is used to relate gas phase density and pressure:

$$\rho_g = \frac{PM_g}{RT} \tag{2.15}$$

Pressure, P, is shared by all the phases (the capillary pressure of liquid phases have been included as diffusion). However, Eq. 2.13 cannot be used if saturation of the gas phase goes to zero in any region as pressure cannot be determined in the region— thus leading to the failure of the numerical solution (discussion follows). The gas phase can go to zero under various conditions, such as high condensation rate in a low porosity region or the accumulation of liquids due to favorable pressure gradients. One way to deal with the above problem is to prevent the gas phase from going to zero by forcing the gas phase saturation to a small value such that it does not affect the solution and at the same time does not require any further reformulations. The gas phase can be prevented from going to zero by introducing residual gas saturation or by giving high liquid capillary diffusivity values at low gas saturations[31]. Another method is to drop Eq. 2.13 from the system of equations and solve for pressure using the conservation equation for water. The latter is difficult to implement and used only in specialized porous media codes (e.g., TOUGH2[32]).

Energy equation

Since thermal equilibrium is assumed to exist across all phases (e.g., all phases in a representative elemental volume have the same temperature), the energy balance equation of the mixture (Eq. 2.16) is solved to calculate T:

$$\rho_{eff} c_{p,eff} \frac{\partial T}{\partial t} + (c_p \mathbf{n})_{fluid} \cdot \nabla T = \nabla \cdot (k_{eff} \nabla T) - \lambda \dot{I} \tag{2.16}$$

The properties of the mixture are obtained by averaging those of the pure components, weighted by their mass or volume fractions (volume fraction is also referred to as saturation in this manuscript) as appropriate:

$$\rho_{eff} = \sum_{j=1}^{b} c_j + \phi \left(\sum_{i=1}^{n-2} S_i \rho_i + S_g \rho_g \right) \tag{2.17}$$

$$c_{p,eff} = m_g(\omega_v c_{p,v} + \omega_a c_{p,a}) + \sum_{i=1}^{n-2} m_i c_{p,i} + \sum_{j=1}^{b} m_j c_{p,j} \tag{2.18}$$

$$(c_p \mathbf{n})_{fluid} = \sum_{i=1}^{n-2} \mathbf{n_i} c_{p,i} + \rho_g \mathbf{u_g} (\omega_v c_{p,v} + \omega_a c_{p,a}) \tag{2.19}$$

$$k_{eff} = \left(\sum_{j=1}^{b} \frac{c_j}{\rho_j} k_j \right) + \phi \left(\sum_{i=1}^{n-2} S_i k_i + S_g(\omega_v k_v + \omega_a k_a) \right) \tag{2.20}$$

Note that, in the energy equation, the melting of ice and fat is handled using the apparent specific heat method[33], in which the latent heat of fusion is incorporated by modifying the specific heat in the temperature range of melting.

2.3.4 Boundary conditions

Pressure at the boundary (which is open to the outside environment) in most food processes is the ambient pressure; hence the boundary condition for the continuity equation (Eq. 2.13) can be expressed as:

$$P_{surf} = P_{amb} \tag{2.21}$$

The flux at the boundary for any transportable phase can be due to a combination of phenomenon such as blowing or suction, surface evaporation, and convection outside the surface. By blowing or suction, it is meant that the phases have a normal velocity component at the surface and they either flow out (blowing) or flow into (suction) the porous medium.

If there is an insignificant pressure gradient at the boundary, then vapor can leave the surface by surface convection only. The total vapor flux from a hypothetical surface, with $\phi = 1$ (no solid phase) and only gas phase present, can be written as:

$$n_{v,tot,surf} = h_m(\rho_{g,surf}\omega_{v,surf} - \rho_{v,amb}) \tag{2.22}$$

where h_m is the mass transfer coefficient.

In a multiphase problem, the vapor flux due to surface convection will have contribution from evaporation from liquid water, evaporation from bound water in solid phase, and water-vapor already present at the surface. Also, only a part of the surface is contributing to vapor flux (e.g., non-water phases will not contribute to vapor flux). Therefore, the above expression (Eq. 2.22) is multiplied by the ratio of the contributing surface area to the total surface area to get the total vapor flux. The total vapor flux leaving the surface will have the following expression:

$$n_{v,tot,surf} = h_m \left(\frac{V_w + V_g + V_{bw}}{V} \right) (\rho_{g,surf}\omega_{v,surf} - \rho_{v,amb}) \tag{2.23}$$

Equation 2.23 gives the total vapor flux for the present problem (multiphase problem) assuming that volume fraction is equal to the surface area fraction.

When there is insignificant pressure gradient at the boundary, flux for other liquid phases such as fat or cooking oil, which do not undergo phase change at the boundary, will be zero.

The other extreme can be the case when blowing at the surface dominates over other factors and boundary pressure is specified, in which case flux at the boundary for any i^{th} component will simply be:

$$\begin{aligned} n_{i,surf} &= -\rho_i \frac{k^p_{in,i} k^p_{r,i}}{\mu_i} \nabla (P - p_{i,cap})|_{surf} \\ &= -\rho_i \frac{k^p_{in,i} k^p_{r,i}}{\mu_i} \nabla P|_{surf} - D_{i,cap} \left(\nabla \phi \rho_{l,i} S_{l,i}\right)|_{surf} - D_{i,T} \nabla T|_{surf} \end{aligned} \tag{2.24}$$

For a gas phase component, such as water vapor, the second and third terms in the above equation (2.24) are zero.

However, if neither blowing nor convection at the boundary is dominating, then both phenomena contribute to the mass transfer at the boundary and the total flux of vapor going out is given by:

$$n_{v,surf} = -\rho_v \frac{k^p_{in,g} k^p_{r,g}}{\mu_g} \nabla P|_{surf} + h_m \left(\frac{V_g}{V_{tot}} \right) (\rho_{g,surf} \omega_{v,surf} - \rho_{v,amb}) \quad (2.25)$$

Similarly, for liquid water, if neither blowing nor surface evaporation is dominating, then both contribute to the mass transfer at the boundary and the flux of water going out is given by:

$$n_{w,surf} = -\rho_w \frac{k^p_{in,w} k^p_{r,w}}{\mu_w} \nabla (P - p_{w,cap})|_{surf} + h_m \left(\frac{V_w}{V_{tot}} \right) (\rho_{g,surf} \omega_{v,surf} - \rho_{v,amb}) \quad (2.26)$$

Note that the blowing phenomenon for any water phase becomes significant under conditions of large pressure-driven flow, when surface evaporation is insufficient to take away all the liquid coming out of the boundary[15,34]. Ni et al. (1999)[15] used $S_w = 1$ as the condition at which blowing occurs, whereas Constant et al. (1994)[34] used $P - p_{cw} > P_{atm}$ in the cell adjacent to the boundary.

In simulating the frying process (discussed later)[17] for vapor transport at the boundary, neither blowing nor convective transfer at the surface were dominating throughout the process. No single boundary condition will work for the whole process. During the initial phase of the frying process, blowing is dominant but convection at the surface eventually takes over. So, a single lumped mass transfer coefficient was used to account for both blowing and convection at the surface. In that case, the boundary condition at the surface was gevin by Eqs. 2.25 and 2.26 but the equations resembled Eq. 2.23 with the mass transfer coefficient as a lumped value of blowing and diffusion instead of diffusion only. These factors eventually lead to a changing mass transfer coefficient.

In the case of other liquids such as fat or cooking oil, there is no evaporation and therefore only blowing, and Eq. 2.24 gives the flux. For the energy equation, there is energy going out due to bulk flow, heat lost due to surface evaporation and convective heat transfer with hot air or oil or a heated plate:

$$q_{surf} = h(T_{amb} - T_{surf}) - T \sum_{i=1}^{n-1} (c_{p,i} n_{i,surf}) + \lambda h_m \left(\frac{V_w + V_{bw}}{V_{tot}} \right) (\rho_{g,surf} \omega_{v,surf} - \rho_{v,amb}) \tag{2.27}$$

2.3.5 Initial conditions

Typical initial conditions (I.C.s) are:

$$\text{I.C. for Eq. 2.13 :} \quad P = P_{amb} \tag{2.28}$$

$$\text{I.C. for Eq. 2.16:} \quad T = T_{amb} \tag{2.29}$$

$$\text{I.C. for Eq. 2.4:} \quad S_i = S_{0,i} \tag{2.30}$$

$$\text{I.C. for Eq. 2.9:} \quad \omega_v = \omega_{0,v} \tag{2.31}$$

$$\text{I.C. for Eq. 2.11:} \quad c_j = c_{0,i} \tag{2.32}$$

Initially the food material is at ambient pressure and temperature conditions. Depending on the composition of the food material, the initial phase saturation of the liquids ($S_{0,i}$) is estimated. The water vapor in air is in equilibrium with liquid water initially. Using a moisture sorption isotherm (Eq. 2.34 and 2.35), equilibrium water vapor pressure at ambient temperature is calculated. For example, the mass fraction of vapor in the gas phase, ω_v at 25°C, is calculated as 0.02.

2.3.6 Phase change

The evaporation rate, distributed spatially and over time, is a complex function of food material and process parameters. Phase change can be formulated in two ways, equilibrium and non-equilibrium.

Equilibrium formulation

In the equilibrium formulation of evaporation that is the most common in the literature [15,16], vapor is always assumed to be in equilibrium with the water in the solid matrix:

$$p_v = p_{v,eq} \tag{2.33}$$

where $p_{v,eq}$ is the equilibrium vapor pressure at a particular temperature and moisture content and is given by the moisture isotherm equation:

$$\ln \frac{p_{v,eq}}{p_{sat}(T)} = f(S_w, T) \tag{2.34}$$

where $p_{v,eq}$ is the equilibrium vapor pressure and $p_{sat}(T)$ is the vapor pressure of pure water at temperature T and is given by the Clausius-Clapeyron equation:

$$\ln \frac{p_{sat}(T)}{p_0} = \frac{\Delta \overline{H}_{vap}}{R} \frac{(T - T_0)}{T T_0} \tag{2.35}$$

The relationship $f(S_w, T)$ is generally obtained from experiments and much data exists in the literature. As shown already in Eq. 2.33, in the equilibrium formulation, p_v is always equal to $p_{v,eq}$ and the vapor concentration, ω_v, can be calculated using this relationship. Therefore, the evaporation rate, $\dot{I}$, comes out of the solution as all the terms on the left-hand side of the mass balance equation of the vapor (Eq. 2.9) are known.

Non-equilibrium formulation

In a non-equilibrium formulation, Eq. 2.33 is not used and is replaced by an explicit expression for the evaporation rate, $\dot{I}$, as discussed in this section. To understand this, consider a beaker half filled with liquid water and half with pure nitrogen (with no water vapor). There is a partition between the two halves which prevents any mixing. At time $t = 0$, the partition between liquid water and nitrogen is removed and the system is allowed to come to equilibrium. The whole system comes to equilibrium after time $\triangle t$. This $\triangle t$ depends on the distance that the vapor has to diffuse and the diffusion rate. For this system, during the time $\triangle t$, the average evaporation rate over space and time is given as:

$$\dot{I} = \frac{(\rho_{v,f} - \rho_{v,i})}{\triangle t} = \frac{M_v}{RT}\frac{(p_{v,f} - p_{v,i})}{\triangle t} \tag{2.36}$$

where $\rho_{v,f}$ is the final vapor density after the equilibration time and is equal to the equilibrium vapor density, and $\rho_{v,i}$ is the initial vapor density. The same concept can be applied in the case of evaporation in the pores inside the food. A Representative Elemental Volume, shown in Figure 2.1, may consist of a number of pores and comes to equilibrium after time $\triangle t$ and the evaporation rate is given by Eq. 2.36. Equation 2.36 is identical to the non-equilibrium evaporation rate expression in porous hygroscopic solids used for modeling of phase change[35,36] given by:

$$\dot{I} = K(\rho_{v,eq} - \rho_v)S_g\phi \tag{2.37}$$

where $\rho_v = \rho_g\omega_v$ is the vapor density at a location that comes from solution. Here K is a material and process-dependent parameter signifying the rate constant of evaporation and is the reciprocal of equilibration time $\triangle t$.

Choice of equilibration time. The equilibration time, $\triangle t$, depends on the ratio of the gas phase volume in the pore in which vapor has to diffuse and the surface area available

for evaporation. For a simple cylindrical pore, this ratio scales as the radius of the pore. It has been shown that the time taken for a molecule to make a transition from liquid water to water vapor is 10^{-14} seconds[37]. Using this condition and pure diffusion of vapor from the evaporating surface, the time to equilibrium at one mean free path (1 μm) away from the liquid surface is less than 10^{-6} seconds and for 25 μm away is around 10^{-5} seconds. The time-scale analysis, shown in the Appendix, concludes that all the transport time scales within a pore are greater than the equilibration time scale for food materials with maximum pore size smaller than 25 μm (e.g., potato, meat, etc.). In that case, the non-equilibrium phenomenon is insignificant and an equilibration time that is one order of magnitude below the smallest transport time scale ensures equilibrium. But if pore sizes are on the order of 100 μm (e.g., bread), then the non-equilibrium phenomenon becomes significant and a reasonable value of K should be used. Estimation of precise values of K, by pore scale analysis or otherwise, can be a study in itself. However, high precision in K is not expected to significantly improve the model prediction[38] and, therefore, the value calculated from the pure diffusion approach is reasonable for the model.

Relationship of equilibration time to time step choice. In Halder et al. (2007b) [38], it is also shown that, as the equilibration time is decreased, the dependence of the solution on the equilibration time decreases, such that decreasing the equilibration time from 10^{-3} to 10^{-4} seconds caused negligible change in the solution. This is because, if the temperature and moisture transport time scales are orders of magnitude higher, it is not necessary to use the accurate range of the equilibration time. Using a higher equilibration time than the actual value, but one still smaller than the transport scales, there is negligible change in the solution but the time elapsed to solve the problem is reduced significantly. For accuracy, the time step of the numerical solution should be

smaller than the equilibration and transport time scales.

Coincidentally, an equilibrium formulation is difficult to implement in commercial software. Typically, commercial software application requires the source term (evaporation rate, $\dot{I}$, in the conservation equations) to be explicitly stated in terms of dependent variables in the model. A non-equilibrium formulation, given by Eq. 2.37, allows precisely this, i.e., the explicit expression of the evaporation rate and therefore would be preferred in commercial software application and is therefore used in our model. For infinitely large K, corresponding to instantaneously occurring phase change, Eq. 2.37 reverts back to Eq. 2.33, the equilibrium assumption, making it possible to simulate the equilibrium formulation as well.

Other phase changes

Analogous to the evaporation rate that relates water release from the liquid to the vapor phase, the release of liquids such as fat and liquid water from the solid matrix to the transportable phase, as temperature increases, can also be written in terms of rate expressions, similar to Eq. 2.37, given by:

$$\dot{R}_{i,j} = K_{i,j}(c_{s,j} - c_{s,j,eq}) \tag{2.38}$$

The holding capacity co-relation, $c_{s,j,eq}$, is experimentally determined[39]. It is assumed that the concentrations in the solid phase always remain at equilibrium. Large values of $K_{i,j}$ were selected so that equilibrium is satisfied at each time step, similar to the use of large K to force equilibrium in the non-equilibrium formulation for evaporation discussed above.

2.4 Model implementation and validation

In the following section, the model developed is applied to two food processes, the frying of a restructured potato slab (made from dried potato flakes—see Figure 2.2) and contact heating of a hamburger patty (Figure 2.4), to demonstrate its effectiveness in describing different processes. The model is validated in each case using experimental results.

2.4.1 Deep-fat frying of restructured potato

Deep-fat frying can be defined as a process for cooking foods, by immersing them in an edible oil, at a temperature above the boiling point of water, usually between 150°C and 200°C.

Problem formulation

A schematic of the problem description is shown in Figure 2.2. The restructured potato slab is assumed to be a porous medium. There are four phases: solid, liquid water, oil and gas. The gas phase is a mixture of air and water vapor. Shrinkage during frying and the effects of gravity are ignored. To simulate 1D heat and mass transfer, no flux conditions for mass species and energy are specified at boundaries other than $x = 0$. The problem is considered to be symmetric with $x = L$ as the line of symmetry. The left boundary ($x = 0$) is the frying surface where heat and mass exchange with the environment takes place. In a restructured potato, water in the solid matrix is negligible (as all the water is in the pore space), so interphase mass transfer from solid to liquid is ignored (it cannot be ignored in the case of contact heating of meat as shown later).

This simplifies the overall model, as porosity can be assumed to be constant with time and mass balance of the solid is not required.

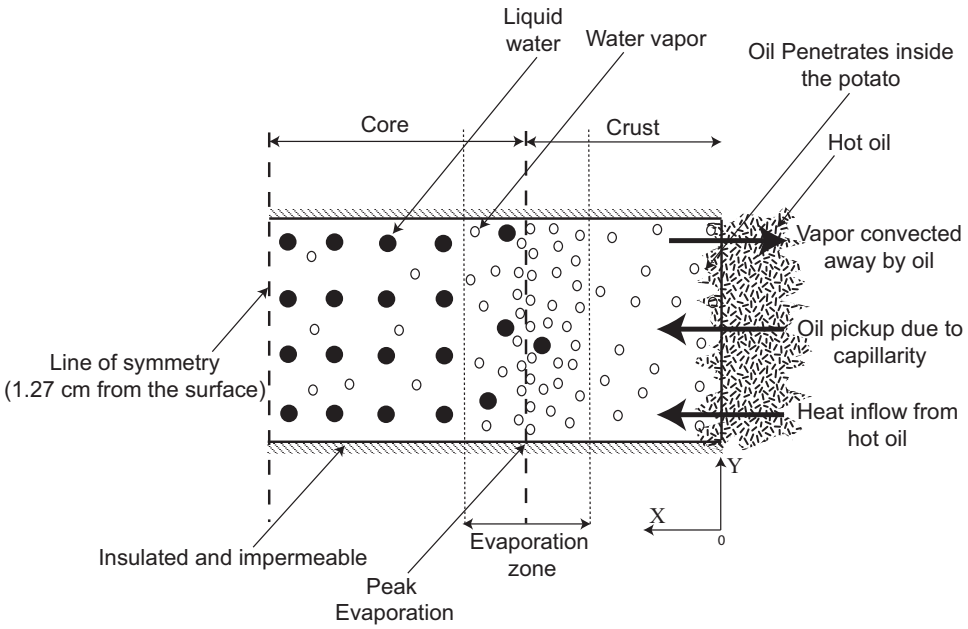

Figure 2.2: Schematic showing computational domain and boundary conditions. Two-dimensional geometry was implemented with the above boundary conditions to simulate an effective one-dimensional problem. For computation, the dimension in the y-direction was chosen to be 0.08 cm.

Mass balance equation

Saturation of liquid water and oil is calculated by solving the mass balance equations of the phases (Eq. 2.4). Saturation of gas is calculated from Eq. 2.5. The gas phase is a mixture of water vapor and air, so the mass balance equation of water vapor is solved using Eq. 2.9 and the mass fraction of air is calculated from Eq. 2.10.

Energy balance equation

Local thermal equilibrium exists between all the phases and, therefore, the energy balance equation for a mixture (Eq. 2.16) is solved to get the temperature, T.

Continuity and Momentum equation

The continuity equation of the gas phase (Eq 2.13) is solved to give the pressure, P. During frying, the gas phase never goes to zero, so solving Eq. 2.13 does not lead to numerical difficulties (discussion in Section 2.3.2). Darcy's law is assumed to be valid and gives the velocities of each phase (liquid water, oil and gas).

Boundary conditions and Initial conditions

Boundary conditions at $x = 0$ are given as:

$$\text{B.C. for Eq. 2.13:} \quad P_{surf} = P_{amb} \tag{2.39}$$

$$\text{B.C. for Eq. 2.16:} \quad q_{surf} = h(T_{amb} - T_{surf}) - (\lambda + c_{p,w}T)n_{w,surf} - c_{p,v}T n_{v,surf} - c_{p,o}T_{amb}n_{o,surf} \tag{2.40}$$

$$\text{B.C. for Eq. 2.4:} \quad n_{w,surf} = h_m S_w(\rho_{g,surf}\omega_{v,surf} - \rho_{v,amb}) \tag{2.41}$$

$$S_{o,surf} = S_{o1} \tag{2.42}$$

$$\text{B.C. for Eq. 2.9:} \quad n_{v,surf} = h_m S_g(\rho_{g,surf}\omega_{v,surf} - \rho_{v,amb}) \tag{2.43}$$

Initial conditions inside the potato before frying are:

$$\text{I.C. for Eq. 2.13:} \quad P = P_{amb} \tag{2.44}$$

$$\text{I.C. for Eq. 2.16:} \quad T = T_{amb} \tag{2.45}$$

$$\text{I.C. for Eq. 2.4:} \quad S_w = 0.3 \tag{2.46}$$

$$S_o = 0 \quad (2.47)$$

$$\text{I.C. for Eq. 2.9:} \quad \omega_v = 0.02 \quad (2.48)$$

Further details and explanations of boundary and initial conditions are given elsewhere [17].

Input parameters and numerical solution

Input parameters and other auxiliary equations used in this frying simulation are given in Table 2.1. A commercially available finite element software, COMSOL Multiphysics (Comsol Inc., Burlington, MA), was used to solve these equations. The computational domain, shown in Figure 2.2, is $0.0127\ \mathrm{m} \times 0.0008\ \mathrm{m}$ and has a mesh consisting of 127×3 quadrilateral elements. Simulating 16 minutes of heating took approximately 6 hours of CPU time for a timestep size of 0.01 seconds on a Pentium 3.4 GHz PC with 2GB RAM.

Table 2.1: Input parameters used in the simulations of deep-fat frying

Parameter	Symbol	Value	Units	Source
Density				
water	ρ_w	998	kg/m^3	
vapor	ρ_v	Ideal gas	kg/m^3	
air	ρ_a	Ideal gas	kg/m^3	
oil	ρ_o	879	kg/m^3	[42]
solid	ρ_s	1528	kg/m^3	[20]
Specific heat capacity				
water	c_{pw}	4178	J/kg K	[43]
vapor	c_{pv}	2062	J/kg K	[43]
air	c_{pa}	1006	J/kg K	[43]
oil	c_{po}	2223	J/kg K	[43]
solid	c_{ps}	1650	J/kg K	[43]
Thermal conductivity				
water	k_w	0.57	W/m K	[43]
vapor	k_v	0.026	W/m K	[43]
air	k_a	0.026	W/m K	[43]
oil (corn)	k_o	0.17	W/m K	[44]
solid	k_s	0.21	W/m K	[43]
Intrinsic permeability				
water	$k^p_{in,w}$	5×10^{-14}	m^2	[15]
air and vapor	$k^p_{in,g}$	10×10^{-14}	m^2	[15]
oil	$k^p_{in,o}$	5×10^{-14}	m^2	[15]
Relative permeability				
water	$k^p_{r,w}$	$((\mathrm{S_w} - 0.08)/0.92)^3$		[45]
air and vapor	$k^p_{r,g}$	$(1 - \mathrm{S_w} - \mathrm{S_f})/0.92$		[45]
oil	$k^p_{r,o}$	$((\mathrm{S_f} - 0.08)/0.92)^3$		[15]
Capillary diffusivity				
water	$D_{w,cap}$	$10^{-8} \exp(-2.8 + 2\mathrm{M})$		[15]
oil	$D_{o,cap}$	$10^{-8} \exp(-2.8 + 2\mathrm{M_o})$		[15]
Viscosity				
water	μ_w	0.988×10^{-3}	Pa s	
air and vapor	μ_g	1.8×10^{-5}	Pa s	
oil	μ_o	$5.05 \times 10^{-6} \exp(\frac{2725}{T})$	Pa s	[42]
Heat transfer coefficient				
Frying	h	graph	W/m^{2}K	[17]
Post-frying cooling	h	20	W/m^{2}K	[46]
Mass transfer coefficient	h_m	graph	m/s	[17]
Latent heat of vaporization	λ	2.26×10^6	J/kg	
Porosity	ϕ	0.928		[20]
Vapor diffusivity in air	$D_{eff,g}$	2.6×10^{-6}	m^2/s	
Oil temperature	T_{oil}	180	°C	
Ambient pressure	P_{amb}	101325	Pa	
Surface oil saturation	S_{o1}	0.11 (frying)		[16]
		0.28 (cooling)		[16]

Results and validation

The simulation results are compared with the experimental data of Farkas et al. (1996b) [20], as shown in Figure 2.3a. The predicted temperatures at a distance of 0.05 cm from the surface are close to experimental values for the first two minutes but there is a considerable difference between them for the next 10 minutes and finally again matching closely for the last 4 minutes of frying. This difference is due to discrepancies in the temperature measurement technique for the depth of 0.05 cm, as discussed in Halder et al. (2007b)[38]. The temperature predictions for locations 0.42 cm and 0.85 cm from the frying surface compare well with the experimental measurements. As shown in Figure 2.3b, the moisture content (dry-basis) of the potato slab dropped from its initial value of 2.50 to 1.56 after 16 minutes of heating. Our model prediction, with improved boundary conditions and evaporation formulation, matches very closely with the experimental results[20], making a better match than in other studies[15,20]. Such close agreement between experimental measurements and model prediction confirms the effectiveness of the model and serves to validate it.

As can be seen in Figures 2.3c and 2.3d, the peak pressure occurs where the evaporation rate is maximum. The evaporation rate is distributed over a narrow zone near the surface, thus validating our assumption that evaporation does not occur at an interface (sharp boundary) but is distributed over a thin zone. In the region where rapid evaporation is taking place, the pressure is always above that of the ambient pressure. Initially, there is condensation in the core region, due to which the pressure falls below ambient pressure. This negative gauge pressure occurs because the gas phase has a negative rate of accumulation in the core – the air present in the core is driven out due to binary diffusion and vapor reaching the core is condensed. As temperature rises and evaporation (and not condensation) starts to occur in the core region, the pressure starts rising and

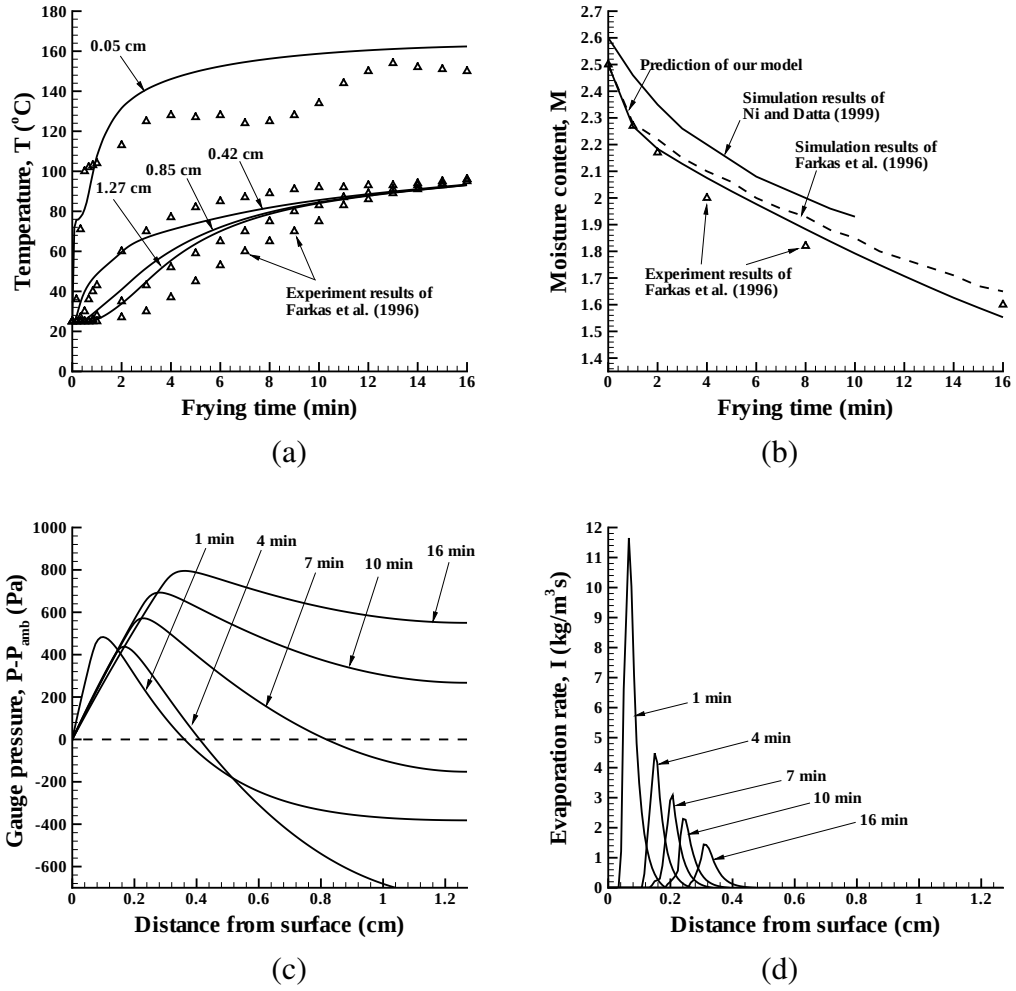

Figure 2.3: Comparison of model predictions for deep-fat frying with experimental data from literature for a)temperature; b) moisture content (dry basis). The spatial pressure and evaporation profiles during different times of frying are shown in (c) and (d), respectively.

finally reaches around 600 Pa after 16 minutes of frying.

2.4.2 Contact heating of a hamburger patty

Meat can be processed and cooked in a variety of ways. For the purpose of this study, double-sided contact heating of hamburger patties[40] is selected, as shown in the

schematic of Figure 2.4. A frozen hamburger patty of cylindrical shape (diameter $10\ \mathrm{cm}$ and height $1\ \mathrm{cm}$), initially stored at $-22^{\circ}\mathrm{C}$, is placed between two hot plates. The gap between the top and bottom heating plates is kept fixed at $1\ \mathrm{cm}$. As temperature rises, water and fat melt, but are still held strongly by the solid matrix. With further rise in temperature, denaturation of muscle proteins occurs, which causes the release of bound water and fat, making both liquids transportable. Mass transfer can also occur between water and vapor in the gas phase due to vaporization and condensation. Gradually, the region near the hot plates loses all the water due to evaporation and a dried crust region develops. The variables of interest for predicting quality and safety aspects of meat cooking are temperature, moisture content, fat content, evaporation rate and their histories.

Problem details

A schematic of the problem description is shown in Figure 2.4. To simulate 1D heat and mass transfer in a cylindrical patty, it is assumed that the exchange of heat and mass with the outside environment takes place through the top and bottom surface of the patty only and the sides are insulated (i.e., radial transport is ignored so gradients are present only in the axial directions). Since the effect of gravity is small, and the top and the bottom plates are at the same temperature, symmetry is assumed at the centerline. The patty is assumed to comprise three transportable fluid phases: liquid water, liquid fat and gas (mixture of air and water vapor), and a solid phase comprising of protein, frozen water and fat.

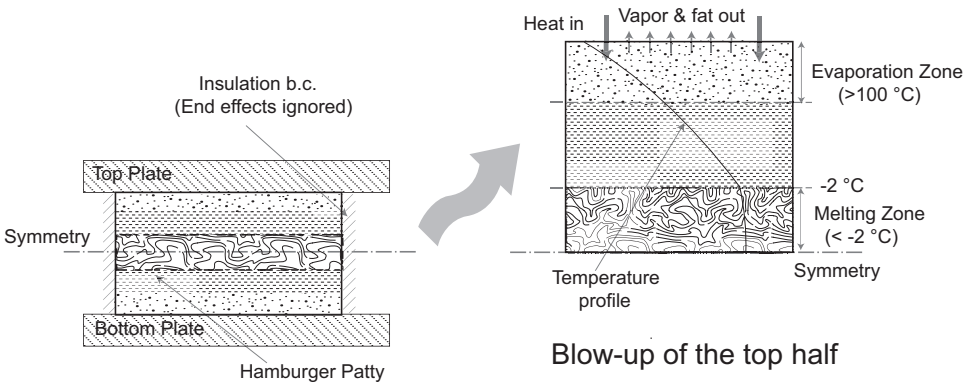

Figure 2.4: Schematic showing computational domain and boundary in the case of contact heating of a hamburger patty.

Mass balance equation

As in frying, the saturations of the water and fat phases are calculated by solving the mass balance equations of the phases (Eq. 2.4). Saturation of gas is calculated from Eq. 2.5. The gas phase is a mixture of water vapor and air, so the mass balance equation of water vapor is solved using Eq. 2.9 and the mass fraction of air is calculated from Eq. 2.10. In meat cooking, where the solid releases water and fat, there are three additional mass balance equations for each component of the solid phase (Eq. 2.11).

Energy balance equation

Thermal equilibrium exists between all the phases and, therefore, the energy balance equation for a mixture (Eq. 2.16) is solved to get the temperature, T.

Continuity and momentum equation

Similar to frying, Eq. 2.13 is solved to obtain pressure, P, and Darcy's law provides the velocities of each phase.

Boundary and initial conditions

In the case of contact heating of meat, the heat transfer coefficient is very high ($> 1000\ \mathrm{W/m^2}$). This leads to high evaporation rates and thus large pressure gradients close to the heated surface. Under such conditions, blowing can be significant. Therefore, the boundary flux for water vapor is given by Eq 2.25. Following Ni et al. (1999)[21], $S_w = 1$ was used as the condition to kick in blowing for liquid water. However, this condition was never satisfied during 150 seconds of heating and liquid water left the patty by surface evaporation only. The time-dependent heat transfer coefficient and plate temperature data are taken from Pan et al. (2000)[40].

Initially frozen at $-22°\mathrm{C}$, the patty is composed of 60% water, 24% fat and 16% protein by weight and all are assumed to be in solid phase. The porosity of frozen patties is taken as 2%[41]. From this data, the initial concentrations for all the components can be calculated. Note that, at the initial temperature, all water and fat are assumed to be in the solid matrix and therefore concentrations of both bulk water and fat are zero. Initially, air is assumed to be saturated with vapor. The equilibrium mass fraction of vapor in the gas phase, ω_v at $-22°\mathrm{C}$, is 0.0015.

Input parameters and numerical solution

Input parameters used in the hamburger patty cooking simulation are given in Table 2.2. A commercially available finite element software, COMSOL Multiphysics (Comsol Inc, Burlington, MA), was used to solve these equations. The computational domain is $0.005\ \mathrm{m}$ in length and has a mesh consisting of 500 elements. Simulation of 150 seconds of heating took approximately 6 hours of CPU time for a timestep size of 0.01 second on a Pentium 3.4 GHz PC with 2GB RAM.

Table 2.2: Input parameters used in the simulations of contact heating of a hamburger patty

Parameter	Symbol	Value	Units	Source
Patty dimensions				
Height		10	mm	[40]
Initial conditions				
Mass fractions				
water	x_{fw}	0.6	–	[40]
fat	x_f	0.24	–	[40]
protein	x_{pr}	0.16	–	[40]
Porosity	ϕ	.02	–	[41]
Temperature	T_{ini}	-22	°C	[40]
Pressure	P_{ini}	101325	Pa	–
Properties				
Water activity	a_w	–	–	[47]
Density				
water	ρ_w	997.2	kg/m^3	[43]
ice	ρ_i	917	kg/m^3	[43]
gas	ρ_v	Ideal gas	kg/m^3	[43]
fat	ρ_f	925.6	kg/m^3	[43]
protein	$\rho_p r$	1330	kg/m^3	[43]
Specific heat capacity				
water	$c_{p,w}$	4178	J/kg K	[43]
ice	$c_{p,i}$	2062	J/kg K	[43]
gas	$c_{p,g}$	1006	J/kg K	[43]
fat	$c_{p,f}$	1984	J/kg K	[43]
protein	$c_{p,pr}$	2008	J/kg K	[43]
Thermal conductivity				
water	k_w	0.57	W/m K	[43]
ice	k_w	2.22	W/m K	[43]
gas	k_g	0.025	W/m K	[43]
fat	k_f	0.18	W/m K	[43]
protein	k_{pr}	0.18	W/m K	[43]
Intrinsic permeability				
water	$k^p_{in,w}$	5×10^{-16}	m^2	[48]
fat	$k^p_{in,f}$	1×10^{-15}	m^2	[48]
gas	$k^p_{in,g}$	5×10^{-16}	m^2	Same as fat
Relative permeability				
water	$k^p_{r,w}$	$((\mathrm{S_w} - 0.08)/0.92)^3$	–	[45]
fat	$k^p_{r,f}$	$((\mathrm{S_f} - 0.08)/0.92)^3$	–	Same as water
gas	$k^p_{r,g}$	$(1 - \mathrm{S_w} - \mathrm{S_f})/0.92$	–	[45]

Table 2.2 (continued)

Parameter	Symbol	Value	Units	Source
Capillary diffusivity				
water	$D_{w,cap}$	$10^{-10}\exp(-2.8+10\mathrm{S_w})$	m^2/s	[47]
fat	$D_{f,cap}$	$10^{-10}\exp(-2.8+10\mathrm{S_f})$	m^2/s	[47]
Viscosity				
water	μ_w	0.988×10^{-3}	Pa s	
gas	μ_g	1.8×10^{-5}	Pa s	
fat	μ_f	0.02	Pa s	[49]
Holding capacities				
water	$c_{bw,eq}$	$c_{bw,ini}\exp(-.0132(\mathrm{T}-303))$	kg/m^3	[39]
fat	$c_{bf,eq}$	$c_{bf,ini}\exp(-.0159(\mathrm{T}-303))$	kg/m^3	[39]
Heat transfer coefficient	h	–	W/m^2K	[40]
Mass transfer coefficient	h_m	0.015	m/s	[15]
Latent heat of vaporization	λ	2.26×10^6	J/kg	
Latent heat of fusion				
water		3.34×10^5	J/kg	
fat		1.5×10^5	J/kg	
Vapor diffusivity in air	$D_{eff,g}$	2.6×10^{-5}	m^2/s	
Grill temperature	T_{surf}	–	°C	[40]
Ambient pressure	P_{amb}	101325	Pa	

Results and validation

Predicted temperature history is compared with the experimental data from[40], as shown in Figure 2.5a. The temperatures at the core of the patty, i.e. the coldest point, follow the experimental results for around 100 seconds. After that the predicted heating rate is slightly lower than the experimentally observed value. The coldest-point temperature is around $70°\mathrm{C}$ after 150 seconds, whereas the measured temperature is $85°\mathrm{C}$. The experimentally observed total weight loss (water and fat) is about 10%, 12%, 16% and 22% (of the initial weight) after 60, 80, 100 and 120 seconds of heating, respectively (Figure 2.5b). The difference between the loss predicted by the simulation and the experimental observed loss is less than 2% (of the initial patty weight) at 60, 80 and 100 seconds and about 5% at 120 seconds.

Once the ice is completely melted, the Biot number for the process is 250 (the heat transfer coefficient is greater than 1000 $\mathrm{W/m^2K}$, patty thickness is 1 cm and thermal conductivity is around 0.4 $\mathrm{W/m^2K}$, which means the heat transfer is internally limited). We compared our thermal conductivity values (estimated by volume averaging) with the values experimentally measured in Pan et al (2001) and found that there is a difference of about 10 %. The averaging correlations for transport property estimation may have an error of +/- 10%[43], which affects the results in the case of internally limited processes, in this case leading to lower heating rate and lower weight losses.

Absolute comparison is difficult to achieve due to limitations in the property estimation correlations. However, the close results validate the more fundamental approach toward the modeling of food cooking. Following this approach, thermal processing of meat products can be simulated by applying the multiphase transport model. This has advanced the existing approach for modeling the meat-cooking process, under which bulk thermal properties of meat (such as enthalpy and thermal conductivity) are mea-

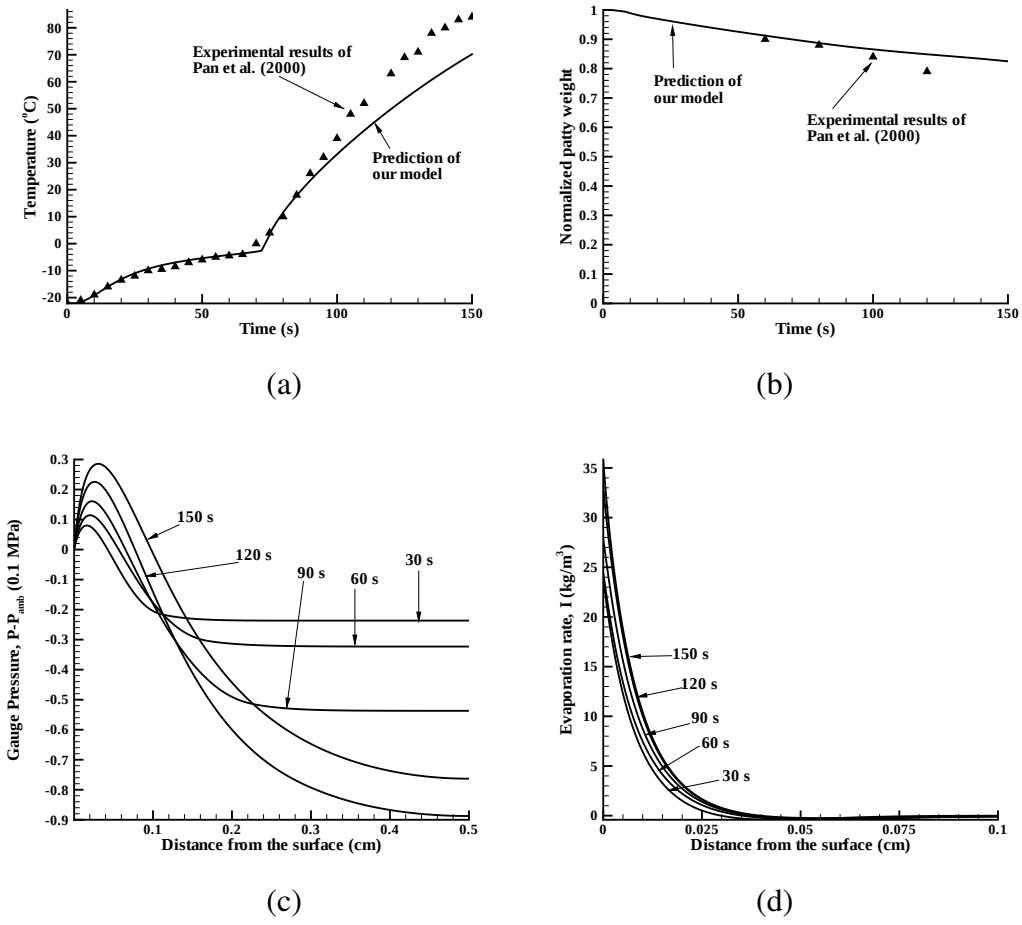

Figure 2.5: (a) Temperature at the center point, (b) average moisture content, (c) spatial pressure and (d) spatial evaporation rate profiles for contact heating of a hamburger patty at different times.

sured as functions of temperature and, then, a simple conduction equation is used to fit the data.

Figures 2.5c and 2.5d show the spatial profiles of the pressure and evaporation rates, respectively, at different times. The evaporation rate and therefore the pressure are maximum near the heated surface. The interior of the patty has negative pressures, due to the diffusion, followed by the condensation, of vapor from the surface to the relatively

cooler interior. Gradually, as the surface dries up, the evaporation and peak pressure zones are expected to move from the surface to the core, as was shown earlier (in Figure 2.3) for deep-fat frying.

2.5 Similarity in fundamental physics

As shown in deep-fat frying and contact heating of hamburger patties (Figures 2.3 and 2.5), the fundamental physics involved in different thermal food processes are similar. As the food (porous hygroscopic material) is heated from the boundary, the temperature inside rises. The rise in temperature causes a phase change, which in turn causes a rise in pressure. The pressure gradient causes the flow of phases toward the boundary where mass transfer takes place. If there is a fluid component absorbed in the solid, then with a rise in temperature and subsequent changes in solid matrix properties it changes into transportable phase. Therefore, a single model is able to solve distinct modes of cooking or processing where the physics is similar and distinct modes of heating are handled by distinct boundary conditions (e.g., frying, baking, etc) or in some cases by source terms (e.g., microwave heating).

2.6 Conclusions

The aim of this paper is to show that transport for many of the thermal processes in food (e.g., frying, baking, meat cooking and microwave heating) can be modeled using the comprehensive framework developed. The developed model includes all the important physics encountered in cooking or food processing (e.g., melting, bound phase, phase change, pressure-driven flow, capillary flow and binary diffusion). Depending on

the food processing situation, this comprehensive model can be simplified by ignoring some physics that are irrelevant for that process and material. For example, in frying of restructured potato, it is assumed that there is no bound water and all the water is available for transport, thus, largely reducing complexities. In meat cooking, all of the physics is necessary and, therefore, it results in the most complex model. The two food processes, the frying of potato and the contact heating of hamburger patty, modeled in this paper demonstrate the effectiveness of the framework in solving different types of thermal processes.

Though meat and potato are completely different in terms of composition, and frying and contact cooking are completely different modes of cooking, transport in the case of frying of potato and meat cooking can be solved by the same model. This is because the developed model is not based on empirical relationships but is a fundamental-based model which can be generalized over a wide range of hygroscopic porous materials and different types of thermal processes. The input parameters required to solve the problem have a physical meaning and are inherent properties of either the process or the food material and can be determined experimentally.

A novel non-equilibrium evaporation formulation is used in the model to describe the evaporation and condensation processes. The non-equilibrium evaporation constant, K, is the reciprocal of the equilibration time and has been investigated in detail in this paper. Further, the same non-equilibrium formulation can be used to implement equilibrium by using a very large value of K. Time-scale analysis shows that the transport scales are much larger than the evaporation time scale for a typical food material. Therefore, a higher value for the equilibration time can be used in a simulation without affecting the solution.

The comprehensive model developed here can also simulate transport in other hygro-

scopic porous materials. Although the immediate applications shown here are to food processes, the model has applications in many different fields, for example, fuel cells, drug delivery through tissues, and nuclear waste treatment. For example, in fuel-cells simulation, there are two different phases (liquid and gas) which experience pressure-driven flow in porous media. There is a chemical reaction in fuel cells between liquid phases to form a gaseous phase, which is analogous to evaporation in frying and meat cooking.

Another unique feature of the modeling framework is that it can be easily implemented in some general purpose CFD software. Most commercial software requires the evaporation rate to be explicitly expressed in terms of dependent variables of the model and the non-equilibrium formulation presented here allows precisely this, unlike the implicit evaporation formulations of the past. Use of the direct Darcy's law over Navier-stokes analog of Darcy flow reduces unnecessary numerical complexities. Because the model is versatile and easily implementable, it can be very useful in product, process and equipment design in the food sector and similar applications in other fields.

Appendix

Transport time-scale analysis:

The minimum length scale (L) of significance for typical food materials is assumed to be 0.1 mm:

$$L \sim 10^{-4}\ [\mathrm{m}] \tag{2.49}$$

The time scale for capillary diffusion (t_{cap}):

$$t_{cap} \sim \frac{L^2}{D_{cap}} = \frac{10^{-8}\ [\mathrm{m}^2]}{10^{-6}\ [\mathrm{m}^2/\mathrm{s}]} = 10^{-2}\ [\mathrm{s}] \tag{2.50}$$

Note that a low value for the length scale and the highest possible value of D_{cap} is used to obtain the minimum relevant diffusion time scale.

The time scale for binary diffusion (t_g):

$$t_g \sim \frac{L^2}{D_{eff,g}} = \frac{10^{-8}\ [\mathrm{m}^2]}{10^{-5}\ [\mathrm{m}^2/\mathrm{s}]} = 10^{-3}\ [\mathrm{s}] \tag{2.51}$$

The time scale for pressure-driven flow (t_p):

$$\begin{aligned} v &\sim \frac{k}{\mu}\frac{\triangle P}{L} = \frac{10^{-15}\ [\mathrm{m}^2]}{10^{-3}\ [\mathrm{Pa\ s}]}\frac{10^{5}\ [\mathrm{Pa}]}{10^{-4}\ [\mathrm{m}]} = 10^{-3}\ [\mathrm{m/s}] \\ t_p &\sim \frac{L}{v} = \frac{10^{-4}\ [\mathrm{m}]}{10^{-3}\ [\mathrm{m/s}]} = 10^{-1}\ [\mathrm{s}] \end{aligned} \tag{2.52}$$

The time scale for heat flow (t_h):

$$t_h \sim \frac{L^2}{\frac{k_{eff}}{\rho_{eff} c p_{eff}}} = \frac{10^{-8}\ [\mathrm{m}^2]}{10^{-7}\ [\mathrm{m}^2/\mathrm{s}]} = 10^{-1}\ [\mathrm{s}] \tag{2.53}$$

Therefore, it can be seen that all the transport time scales are larger than the evaporation equilibrium time scale, which is 10^{-5} seconds for 25 μm-sized pores[37].

BIBLIOGRAPHY

[1] Ateba P, Mittal GS. Modeling the deep-fat frying of beef meatballs. *International Journal of Food Science and Technology*, 1994;29(4):429-440.

[2] Ikediala JN, Correia LR, et al. Finite element modeling of heat transfer in meat patties during single-sided pan-frying, *Journal of Food Science*, 1996;61(4):796-802.

[3] Bengtsson NE, Jakobsson B, et al. Cooking of beef by oven roasting - study of heat and mass-transfer, *Journal of Food Science*, 1976;41(5):1047-1053.

[4] Chau KV, Snyder GV. Mathematical-model for temperature distribution of thermally processed shrimp, *Transactions of the Asae*, 1988;31(2):608-612.

[5] Fowler AJ, Bejan A. The effect of shrinkage on the cooking of meat, *International Journal of Heat and Fluid Flow*, 1991;12(4):375-383.

[6] Dincer I, Yildiz M. Modelling of thermal and moisture diffusions in cylindrically shaped sausages during frying, *Journal of Food Engineering*, 1996;28(1):35-44.

[7] Williams R, Mittal GS. Low-fat fried foods with edible coatings: Modeling and simulation. *Journal of Food Science*, 1999;64(2):317-322.

[8] Shilton N, Mallikarjunan P, et al. Modeling of heat transfer and evaporative mass losses during the cooking of beef patties using far-infrared radiation, *Journal of Food Engineering*, 2002;55(3):217-222.

[9] Wang L, Singh RP. Finite element modeling and sensitivity analysis of double-sided contact-heating of initially frozen hamburger patty, *Transactions of the ASAE*, 2004;47(1):147-157.

[10] Kondjoyan A, Rouaud O, et al. Modelling coupled heat-water transfers during a decontamination treatment of the surface of solid food products by a jet of hot air.

I. Sensitivity analysis of the model and first validations of product surface temperature under constant air temperature conditions, *Journal of Food Engineering*, 2006;76(1):53-62.

[11] Farkas BE, Singh RP, et al. Modeling heat and mass transfer in immersion frying .1. Model development, *Journal of Food Engineering*, 1996;29(2):211-226.

[12] Farid MM, Chen XD. The analysis of heat and mass transfer during frying of food using a moving boundary solution procedure, *Heat and Mass Transfer*, 1998;34(1):69-77.

[13] Bouchon P, Pyle DL. Modelling oil absorption during post-frying cooling - I: Model development, *Food and Bioproducts Processing*, 2005;83(C4):253-260.

[14] Mascarenhas WJ, Akay HU, et al. A computational model for finite element analysis of the freeze-drying process, *Computer Methods in Applied Mechanics and Engineering*, 1997;148(1-2):105-124.

[15] Ni H, Datta AK. Moisture, oil and energy transport during deep-fat frying of food materials, *Food and Bioproducts Processing*, 1999;77(C3):194-204.

[16] Yamsaengsung R, Moreira RG. Modeling the transport phenomena and structural changes during deep fat frying - Part 1: model development, *Journal of Food Engineering*, 2002;53(1):1-10.

[17] Halder A, Dhall A, et al. An improved, easily implementable, porous media based model for deep-fat frying - Part I: Model development and input parameters, *Food and Bioproducts Processing*, 2007;85(C3):209-219.

[18] Zhang J, Datta AK, et al. Transport processes and large deformation during baking of bread, *Aiche Journal*, 2005;51(9):2569-2580.

[19] Zhang J, Datta AK, Rakesh V. Investigation of non-equilibrium in water evaporation, *3rd Inter-American Drying Conference*, Montreal, Canada, 2005.

[20] Farkas BE, Singh RP, et al. Modeling heat and mass transfer in immersion frying .2. Model solution and verification, *Journal of Food Engineering*, 1996;29(2):227-248.

[21] Ni, H., A. K. Datta, et al., 1999, Moisture transport in intensive microwave heating of biomaterials: A multiphase porous media model, *International Journal of Heat and Mass Transfer*, 42(8):1501-1512.

[22] Yamsaengsung R, Moreira RG. Modeling the transport phenomena and structural changes during deep fat frying - Part II: model solution and validation, *Journal of Food Engineering*, 2002;53(1):11-25.

[23] Rutqvist J, Wu YS, et al. A modeling approach for analysis of coupled multiphase fluid flow, heat transfer, and deformation in fractured porous rock, *International Journal of Rock Mechanics and Mining Sciences*, 2002;39(4):429-442.

[24] Buscheck TA, Nitao JJ. Repository-heat-driven hydrothermal flow at Yucca Mountain .1. modeling and analysis, *Nuclear Technology*, 1993;104(3):418-448.

[25] Abriola LM, Pinder GF. A Multiphase approach to the modeling of porous-media contamination by organic-compounds .1. Equation development, *Water Resources Research*, 1985;21(1):11-18.

[26] Arbogast T, Bryant S, et al. Computational methods for multiphase flow and reactive transport problems arising in subsurface contaminant remediation, *Journal of Computational and Applied Mathematics*, 1996;74(1-2):19-32.

[27] Khanafer K, Vafai K. The role of porous media in biomedical engineering as related to magnetic resonance imaging and drug delivery, *Heat and Mass Transfer*, 2006;42(10):939-953.

[28] Datta AK. Porous media approaches to studying simultaneous heat and mass

transfer in food processes. I: Problem formulations, *Journal of Food Engineering*, 2007;80(1):80-95.

[29] Curtiss CF, Bird RB. Multicomponent diffusion, *Industrial and Engineering Chemistry Research*, 2001;40(7):1791-1791.

[30] Vafai K, Tien CL. Boundary and inertia effects on flow and heat-transfer in porous-media, *International Journal of Heat and Mass Transfer*, 1981;24(2):195-203.

[31] Perre P, Moyne C. Processes related to drying .2. Use of the same model to solve transfers both in saturated and unsaturated porous-media, *Drying Technology*, 1991;9(5):1153-1179.

[32] Pruess K. The TOUGH codes - a family of simulation tools for multiphase flow and transport processes in permeable media, *Vadose Zone Journal*, 2004;3:738-746.

[33] Pham QT. Comparison of general-purpose finite-element Methods for the Stefan problem, *Numer Heat Tranf. B-Fundam.*, 1995; 27(4):417-435.

[34] Constant T, Moyne C, Perre P. Drying with internal heat generation: Theoretical aspects and application to microwave heating, *Aiche Journal*, 1996;42(2):359-368.

[35] Le CV, Ly NG, Postle R. Heat and mass-transfer in the condensing flow of steam through an absorbing fibrous medium, *International Journal of Heat and Mass Transfer*, 1995;38(1):81-89.

[36] Scarpa F, Milano G. The role of adsorption and phase change phenomena in the thermophysical characterization of moist porous materials, *International Journal of Thermophysics*, 2002;23(4):1033-1046.

[37] Ward CA, Fang G. Expression for predicting liquid evaporation flux: Statistical rate theory approach, *Physical Review E*, 1999;59(1):429-440.

[38] Halder A, Dhall A, et al. An improved, easily implementable, porous media based model for deep-fat frying - Part II: Results, validation and sensitivity analysis, *Food and Bioproducts Processing*, 2007;85(C3):220-230.

[39] Pan Z, Singh RP. Physical and thermal properties of ground beef during cooking, *Lebensmittel-Wissenschaft Und-Technologie-Food Science and Technology*, 2001;34(7):437-444.

[40] Pan Z, Singh RP, et al. Predictive modeling of contact-heating process for cooking a hamburger patty. *Journal of Food Engineering*, 2000;46(1):9-19.

[41] Boukouvalas CJ, Krokida MK, et al. Density and porosity: Literature data compilation for foodstuffs. *International Journal of Food Properties*, 2006;9(4):715-746.

[42] Tseng YC, Moreira R, Sun X. Total frying-use time effects on soybean-oil deterioration and on tortilla chip quality, *International Journal of Food Science and Technology*, 1996;31:287-294.

[43] Choi Y, Okos MR. Thermal properties of liquid foods – review, in *Physical and Chemical Properties of Food*, Okos, M. R. (editor), American Society of Agricultural Engineers, St Joseph, MI, USA 1986:35-77.

[44] Lewis MJ. Physical properties of foods and food processing systems. Deerfield Beach, FL: VCH 1987.

[45] Bear J. Dynamics of fluids in porous media, American Elsevier Publishing company, Inc., New York 1972.

[46] Hanreich G, Nicolics J. Measuring the natural convective heat transfer coefficient

at the surface of electronic components, *IEEE Instrumentation and Measurement Technology Conference*, 2001:1045-1050.

[47] Hallstrom B. Mass transport of water in foods a consideration of the engineering aspects, *Journal of Food Engineering*, 1990;12(1):45-52.

[48] Oroszvari BK, Rocha CS, et al. Permeability and mass transfer as a function of the cooking temperature during the frying of beefburgers. *Journal of Food Engineering*, 2006;74(1):1-12.

[49] Goodrum JW, Geller DP, et al. Rheological characterization of yellow grease and poultry fat. *Journal of the American Oil Chemists Society*, 2002;79(10):961-964.

CHAPTER 3

MULTIPHASE AND MULTICOMPONENT TRANSPORT WITH PHASE CHANGE DURING MEAT COOKING

The complete authorship of this work should be read as Ashish Dhall, Amit Halder and Ashim K. Datta.

3.1 Abstract

A multiphase model based on unsaturated flow in a hygroscopic porous medium, which accounts for the important physical phenomena that take place during thermal treatment of meat, is developed. Frozen meat is considered as a porous solid comprising of water, fat and protein with gas trapped in its pores. As it is heated, water and fat melt, and, are gradually released from the solid protein matrix to the pore space. With further rise in temperature, liquid water evaporates. Since four fluid components (liquid water phase, liquid fat phase, water vapor and air) are present in the pore space, a mass balance equation is written for each component. Local thermal equilibrium assumption leads to one energy balance equation for the whole system. The model is validated for double-sided contact heating of hamburger patties by comparing temperature and moisture profiles with experimental studies. Dominant modes of transport are identified.

Nomenclature

c	concentration, kg m^{-3}
c_p	specific heat capacity, J $kg^{-1}K^{-1}$
C_g	molar density, kmol m^{-3}
$D_{eff,g}$	effective gas diffusivity, m^2s^{-1}
D_i	diffusivity of a component, i, m^2 s^{-1}
$D_{i,T}$	diffusivity due to temperature gradient of a component, i, kg m^{-1} s^{-1} K^{-1}
h	heat transfer coefficient, W m^{-2} K^{-1}
h_m	mass transfer coefficient of vapor, m s^{-1}
$\dot{I_w}, \dot{I_{sw}}$	evaporation rate from pore space water and solid matrix water, $\mathrm{kg\ m^{-3}s^{-1}}$
k_eff	effective thermal conductivity of the multiphase system, W $\mathrm{m^{-2}}$ K^{-1}
$k^p_{in,i}$	intrinsic permeability of component, i, m^2
$k^p_{r,i}$	relative permeability of component, i,
K	non-equilibrium evaporation constant, s^{-1}
K_1	constant for mass transfer from solid matrix water to pore space, s^{-1}
K_2	nconstant for mass transfer from solid matrix fat to pore space, s^{-1}
$\dot{m_{sw}}$	rate of mass transfer from solid matrix water to pore space, kg m^{-3} s^{-1}
$\dot{m_{sf}}$	rate of mass transfer from solid matrix fat to pore space, kg m^{-3} s^{-1}
M_a, M_v	molecular weight of air and vapor
$\overrightarrow{n_i}$	total flux of component, i, kg m^{-2} s^{-1}
$p_{i,cap}$	capillary pressure of a fluid phase, i Pa
P	gas pressure, Pa
q	heat flux, J m^{-2} s^{-1}
r	radial coordinate, m
R	universal gas constant, J $kmol^{-1}$ K^{-1}
S_i	saturation of a fluid phase, i
t	time, s
T	temperature, K
$\triangle V$	differential volume, m^3
x_v, x_a	mole fraction of vapor and air in relation to total gas
y_i	volume fraction of a solid matrix component, i
z	axial coordinate, m
Greek Symbols	
ρ	density, kg m^{-3}
$\rho_{v,sat}$	saturation vapor density, kg m^{-3}
λ	latent heat of vaporization, J kg^{-1}
ω_v, ω_a	mass fraction of vapor and air in relation to total gas
ϕ	porosity
μ	dynamic viscosity, Pa s
Subscripts	
amb	ambient
a, g, f, s, v, w	air, gas, fat, solid, vapor, water
pr, sw, sf	protein, water, fat in solid matrix
eff	effective
eq	equilibrium
i	i^{th} component
0	at time $t = 0$
$surf$	surface

3.2 Introduction

Foodborne diseases cause 76 million illnesses in the United States each year[1]. Since many of these diseases result from insufficient destruction of pathogens, safety of cooked meat is one of the primary concerns among food scientists and technologists. Safety of a food material includes protection from microbial, chemical and physical hazards or contamination that may occur at any stage of food production and handling. As far as meat cooking is concerned, time-temperature history determines microbial destruction and, thus, is the primary indicator of safety. The cooking recommendations for safe consumption of meat are given in terms of temperature and holding times of the slowest heating points[2,3] to guard against lethal microbial activity.

In addition to safety, the eating quality of the meat product, characterized by nutrient composition, flavor, color and texture (tenderness), is of importance to the consumer. As meat is cooked, its toughness lasts till 50°C, after which the meat product starts becoming tender and, thus, tasteful[4]. Elasticity of meat is adversely affected above 65°C leading to a tougher, more brittle meat at higher temperatures. Thus, quality and safety put opposing demands on the temperature range, and the most tasty and microbially safe meat requires cooking within a narrow temperature range. Apart from temperature, water and fat content are other important parameters determining meat quality. Moisture content and distribution inside the meat protein fibers and extracellular spaces determine its juiciness and flavor. Computer modeling of a meat cooking process can go a long way in establishing a better understanding of the transport processes that take place inside, which is vital for quality prediction and improvement. However, underlying physics is complex due to highly heterogeneous nature of the material.

3.2.1 Previous Studies

Heat and mass transport studies during cooking of meat have been reported at various levels of complexity. The simplest of the models consider only heat transfer, treating meat as a non-porous solid[5–7] and solve heat conduction equation. Such models can give a very good match for the specified product and processing conditions, as the thermal properties (thermal conductivity, heat transfer coefficient etc.) are often used as the fitting parameters for the experimental data obtained. However, such models cannot be easily extended to other products and conditions. Some models consider moisture loss from the meat as a lumped system without any internal resistances to transport[8,9]. Most of the studies, however, include heat transfer and diffusive transport for moisture, solving a transient diffusion equation for the latter using experimentally determined effective diffusivity of moisture[10–12]. Pressure driven flow is ignored in all the studies. Lumping of all modes of water transport as diffusion cannot be justified for all situations, as pressure driven flow may become important under intensive heating. For instance, pressure driven drip loss was identified as the main mechanism behind water loss during frying of beefburger patties[13]. Since the use of effective diffusivity does not give insights into the transport mechanisms in action, the source of pressure gradients (evaporation, capillarity, protein matrix shrinkage etc.) is not known.

A meat cooking process often involves heating the meat from frozen state. Thus, water and fat first melt and are then released from the solid matrix for transport. Melting, in case of biological materials, occurs over a range of temperatures and is usually accounted for by apparent specific heat or enthalpy gradient formulations[14,15]. Water holding capacity (WHC) of meat fibers was considered in the modeling efforts of Pan et al (2000)[8], as an experimentally-determined exponential-function of temperature[16]. It was assumed that the fibers start losing water only after temperature reaches a certain

minimum value. Fat melting and its holding capacity were also treated analogous to that of water while fat transport, as in case of water, was ignored.

Evaporation in a porous medium can be handled by various ways: at the boundary, by assuming a moving interface at which phase change occurs[17], and by distributing evaporation over the domain based on local vapor pressure[18]. Pros and cons of these formulations have been discussed[19], and the distributed evaporation has been the preferred choice, as this is the most general way and can predict boundary evaporation or a moving interface. However, none of the meat cooking models considered distributed internal evaporation based on local vapor pressure as this involves additional complexity of solving for separate conservation equations for the gas phase (water vapor and air).

3.2.2 Objectives

This objectives of this work are to 1) formulate a generalized transport model based on unsaturated fluid flow in a hygroscopic porous medium which accounts for the important physical phenomena (heat, moisture and fat transfer with phase changes) that take place while intensive heating (cooking) of meat, 2) validate the model for double-sided contact heating of hamburger patties by comparing temperature and moisture profiles with experimental studies[13,20,21] available in literature, and 3) identify the dominant modes of heat and mass transport in operation.

3.3 Theory

In this section, a porous media based multiphase and multicomponent model that describes heat and mass transfer during heating of a typical meat (whole meat or processed

meat products such as sausages and hamburgers) is developed. Major assumptions, governing equations, along with auxiliary conditions are described in detail. Mathematical treatment of various phase change phenomena occurring is also discussed.

3.3.1 Qualitative Description of the Problem

A number of simplifying assumptions are needed to arrive at a mathematical description of the meat cooking problem. The pore space in a meat product is assumed to comprise of three transportable fluid phases – water, fat and a multicomponent gas (comprising of air and water vapor) with the solid matrix itself comprising of three components – protein, water and fat (Figure 3.1). Here, the solid matrix represents the intracellular region as described in physiological description of meat[4]. The pore space, thus, means the extracellular region and, henceworth, the two terms will be used interchangeably. In uncooked meat, almost all water and fat are present in the solid matrix (water inside the myofibrils and fat, in bundles, near the connective tissue). A small amount of water (5%[22]) is always bound to protein layers, is unfrozen at all temperatures, and has zero vapor pressure. Note that the use of oft-repeated terms such as 'bound water', 'free water', 'bound fat', and 'free fat' is avoided in this study because of ambiguity in their definitions in literature.

Local thermal equilibrium is assumed, i.e., all the phases have the same temperature at a given location. As temperature rises due to cooking, water and fat melt, but are still held strongly by the solid matrix. With further rise in temperature, muscle proteins denaturate and release water that can participate in transport outside the solid matrix. Similarly, liquid fat is also released from the matrix. Since fat content is usually much less than water, it can be present as a dispersed phase and will only get transported if

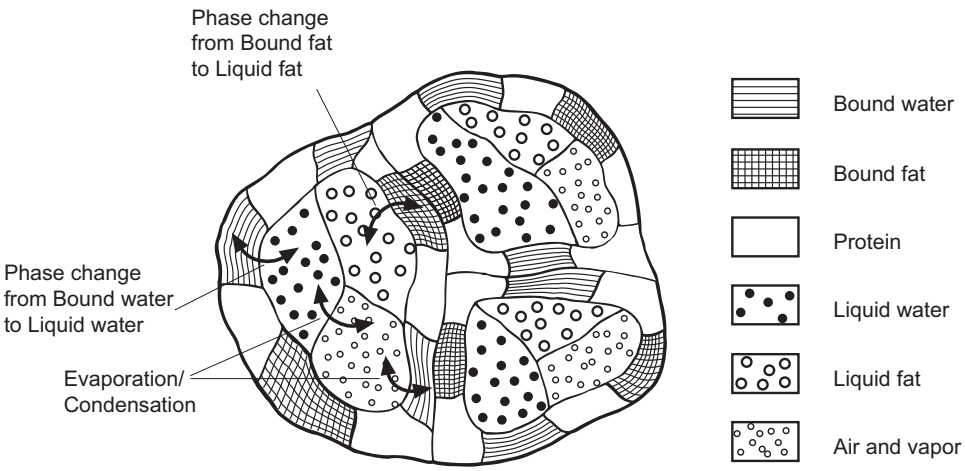

Figure 3.1: Schematic of a porous meat product showing mass transfer between various phases

enough fat channels are formed after melting[36]. Interphase mass transfer also occurs between liquid water (in the matrix and extracellular space) and vapor in gas phase due to vaporization and condensation. Here, it is assumed that non-equilibrium can potentially exist between liquid water and water vapor i.e., vapor concentrations are not directly given by moisture isotherms. Note that the effect of shrinkage of the solid matrix (such as squeezing out of the fluids), is not explicitly included in the model.

3.3.2 Mathematical Model

Porosity at any point, $\phi(r, z)$, is defined as the fraction of total volume occupied by the fluid phases, given by

$$\phi(r, z) = \frac{\sum_{i=w,f,g} \triangle V_i}{\triangle V} \tag{3.1}$$

where $\triangle V_i$ is the volume occupied by the i^{th} phase in an elemental volume $\triangle V$ and w, f and g stand for liquid water, liquid fat and gas phases, respectively. All the symbols used in this manuscript are defined in the nomenclature section. Saturation of a fluid phase is defined as the fraction of total fluid volume occupied by a particular phase

$$S_i = \frac{\triangle V_i}{\phi \triangle V} \tag{3.2}$$

where i stands for water, fat or gas. Similarly, volume fractions for the solid matrix components (water, fat, protein) can be defined as

$$y_i = \frac{\triangle V_i}{(1-\phi)\triangle V} \tag{3.3}$$

As the solid matrix loses water and fat, the porosity increases. In such cases, porosity can be estimated as the ratio of solid matrix volume to total volume subtracted from one

$$\phi = 1 - \frac{\triangle V_s}{\triangle V} = 1 - \left(\frac{\triangle V_{pr}}{\triangle V} + \frac{\triangle V_{sw}}{\triangle V} + \frac{\triangle V_{sf}}{\triangle V} \right) = 1 - \left(\frac{c_{sw}}{\rho_w} + \frac{c_{sf}}{\rho_f} + \frac{c_{pr}}{\rho_{pr}} \right) \tag{3.4}$$

where c_i and ρ_i stand for volumetric concentration and pure state density for the i^{th} component. Symbols pr, sw and sf stand for components of the solid matrix – protein, water and fat, respectively. It is assumed that the total volume of solid can be estimated as sum of the individual volumes of solid matrix components with each component retaining its pure state density.

Conservation Equations

Mass conservation equations are written for all the independent concentrations that exist in the system. These are the two liquid phases in the extracellular space (water and fat), two components of the extracellular gas phase (water vapor and air) and three components of the solid matrix (water, fat and protein).

$$\text{Liquid water phase:} \quad \frac{\partial}{\partial t}(c_w) + \nabla . \vec{n}_w \quad = \quad -\dot{I}_w + \dot{m}_w \tag{3.5}$$

$$\text{Liquid fat phase:} \quad \frac{\partial}{\partial t}(c_f) + \nabla.\vec{n}_f = \dot{m}_f \tag{3.6}$$

$$\text{Water vapor in gas phase:} \quad \frac{\partial}{\partial t}(\omega_v c_g) + \nabla.\vec{n}_v = \dot{I}_w + \dot{I}_{sw} \tag{3.7}$$

$$\text{Air in gas phase:} \quad \frac{\partial}{\partial t}(\omega_a c_g) + \nabla.\vec{n}_a = 0 \tag{3.8}$$

$$\text{Water in solid matrix:} \quad \frac{\partial}{\partial t}(c_{sw}) + \nabla.\vec{n}_{sw} = \dot{I}_{sw} - \dot{m}_w \tag{3.9}$$

$$\text{Fat in solid matrix:} \quad \frac{\partial}{\partial t}(c_{sf}) + \nabla.\vec{n}_{sf} = -\dot{m}_f \tag{3.10}$$

$$\text{Protein in solid matrix:} \quad \frac{\partial}{\partial t}(c_{pr}) = 0 \tag{3.11}$$

Each of the above equations solves for volumetric concentration of a component, c_i, which is related to its saturation or volume fraction as $c_i = \rho_i \phi S_i$ (for fluid phases) and $c_i = \rho_i(1-\phi)y_i$ (for the solid matrix components). In the water vapor and air conservation equations (Eqs. 3.7 and 3.8), ω_v and ω_a stand for mass fractions of vapor and air, respectively, in the gas phase. Therefore, volumetric concentrations of vapor and air, c_v and c_a, are written as $\omega_v c_g$ and $\omega_a c_g$, respectively. $\dot{I}_w$ and $\dot{I}_{sw}$ are the source terms due to evaporation from liquid water phase and from water in solid matrix respectively, while $\dot{m}_w$ and $\dot{m}_f$ represent sources due to release of water and fat, respectively, from solid phase (Discussed under Phase Change later).

Water vapor and air conservation equations, can be added to give the gas phase mass conservation equation

$$\frac{\partial}{\partial t}(c_g) + \nabla.\vec{n}_g = \dot{I}_w + \dot{I}_{sw} \tag{3.12}$$

Thus, only two equations out of 3.7, 3.8 and 3.12 are independent and can be used to solve for gas phase concentrations. It is assumed that gas phase obeys the ideal gas law, so pressure is a function of gas concentration, c_g. For heat transfer, local thermal equilibrium is assumed. Hence, one energy balance equation can be written for the entire multi-phase system

$$\sum \left(c_i c_{p,i}\right) \frac{\partial T}{\partial t} + \sum \left(\vec{n}_i c_{p,i}\right).\nabla T = \nabla.(k_{eff} \nabla T) - \lambda \left(\dot{I}_w + \dot{I}_{sw}\right) \tag{3.13}$$

Equations 3.5, 3.6, 3.7, 3.9, 3.10, 3.11, 3.12 and 3.13 along with auxillary conditions discussed later are numerically solved to calculate c_w, c_f, ω_v, c_{sw}, c_{sf}, c_{pr}, P and T.

Fluxes

The liquid phase (water and fat) fluxes are due to gradients of liquid pressure, $P - p_{i,cap}$, which can be written as the difference between the gas pressure and the capillary pressure. This flux is given by Darcy's law[19] as

$$\begin{aligned} \vec{n}_i &= -\rho_i \frac{k^p_{in,i} k^p_{r,i}}{\mu_i} \nabla (P - p_{i,cap}) \\ &= -\rho_i \frac{k^p_{in,i} k^p_{r,i}}{\mu_i} \nabla P + \rho_i \frac{k^p_{in,i} k^p_{r,i}}{\mu_i} \left(\frac{\partial p_{i,cap}}{\partial c_i} \nabla c_i + \frac{\partial p_{i,cap}}{\partial T} \nabla T \right) \end{aligned} \tag{3.14}$$

The first term in the right hand side of Eq. 3.14 (second line) represents flow due to gradients in gas pressure. The second and third terms are due to gradients in capillary pressure. The capillary pressure, $p_{i,cap}$, is positive for a wetting fluid, which means that the fluid is attracted by the solid matrix. However, the absolute value of capillary pressure in biological materials is difficult to estimate. Moreover, we are interested in the flux due to capillary pressure gradients and not the value of the capillary pressure itself. Since capillary pressure is a function of temperature and fluid concentration, the flux term due to capillary pressure gradients can be written in terms of temperature and concentration gradients. The coefficients of these two terms can be defined as diffusivity due to concentration gradients, D_i, and diffusivity due to thermal gradients, $D_{i,T}$:

$$D_i = -\rho_i \frac{k^p_{in,i} k^p_{r,i}}{\mu_i} \frac{\partial p_{i,cap}}{\partial c_i} \tag{3.15}$$

$$D_{i,T} = -\rho_i \frac{k^p_{in,i} k^p_{r,i}}{\mu_i} \frac{\partial p_{i,cap}}{\partial T} \tag{3.16}$$

Similar to flux terms for the liquid phases in the extracellular space, water and fat present in the solid matrix can also transport due to concentration and temperature gradients (Eq.

3.17). However, unlike pore spaces, gas is not expected to be present in the solid matrix and, therefore, gas pressure driven flow is ignored in the solid matrix. Flux terms for the components of the solid matrix can now be written as:

$$\vec{n}_i = -\nabla(D_i \nabla c_i) - \nabla(D_{i,T} \nabla T) \tag{3.17}$$

Experimentally, it has been observed that water and fat holding capacities of the protein matrix are strong functions of temperature due to temperature-dependent denaturation of proteins[16]. Therefore, the flux terms due to temperature gradients are expected to play a significant role during meat cooking. Note that van der Sman (2007)[23] arrived at the same flux terms for water starting from arguments of the Flory-Rehner theory.

Flux values of the gas phase components (vapor and air) comprise of Darcy's flow (convection) and binary diffusion:

$$\vec{n}_v = -\rho_v \frac{k^p_{in,g} k^p_{r,g}}{\mu_g} \nabla P - \frac{C_g^2}{\rho_g} M_a M_v D_{eff,g} \nabla x_v \tag{3.18}$$

$$\vec{n}_a = -\rho_a \frac{k^p_{in,g} k^p_{r,g}}{\mu_g} \nabla P - \frac{C_g^2}{\rho_g} M_a M_v D_{eff,g} \nabla x_a \tag{3.19}$$

The total gas flux, $\vec{n}_g$ is defined as the sum of vapor and air fluxes:

$$\vec{n}_g = \vec{n}_v + \vec{n}_a = -\rho_g \frac{k^p_{in,g} k^p_{r,g}}{\mu_g} \nabla P \tag{3.20}$$

Phase change

Meat cooking involves three important phase changes — melting of ice and fat, release of water and fat from the solid matrix to transportable phase, and evaporation of water. Melting of ice and fat is handled using the apparent specific heat method[15] that captures phase change over a temperature range. The other two phase changes are handled by adding source terms to the respective equations. Non-equilibrium formulation of evaporation is implemented[25,26], where total evaporation rate is proportional to the difference

between actual vapor density, ρ_v and saturation vapor density, $\rho_{v,sat}$. Therefore, the total evaporation rate (in $\mathrm{kg/m^3s}$) is given by

$$\dot{I_w} + \dot{I_{sw}} = K(\rho_{v,sat} - \rho_v) \tag{3.21}$$

Note that the rate can be increased or decreased by changing the value of the proportionality constant, K with larger values of K leading to conditions closer to equilibrium. The individual values of evaporation from pore space water, $\dot{I_w}$ and from solid matrix water, $\dot{I_{sw}}$ are determined by distributing the total evaporation rate between the two, according to their concentrations. The maximum pore size in meat is less than 100 $\mu\mathrm{m}$, as reported by mercury porosimetry study for ground meat (beef[27]), which is expected to have larger pore size than raw meat. For this small pore sizes, water vapor is expected to be in equilibrium with liquid water. Therefore, high value of K can be selected[28,29] so that equilibrium is satisfied at each time step.

Analogous to evaporation rate, the rates of release of water and fat, from the solid matrix to the pore space, are given by

$$\dot{m}_w = K_1(c_{sw} - c_{sw,eq}) \tag{3.22}$$

$$\dot{m}_f = K_2(c_{sf} - c_{sf,eq}) \tag{3.23}$$

where K_1 and K_2 are proportionality constants, and $c_{sw,eq}$ and $c_{sw,eq}$ are the temperature dependent equilibrium concentrations of water and fat[16]. Large values of K_1 and K_2 can be selected so that equilibrium is satisfied at each time step, similar to the use of large K in the evaporation formulation above.

3.4 Contact Heating of Hamburger Patties

Meat can be cooked in a variety of ways. For the purpose of this study, contact heating of ground beef (hamburger) patties was selected, although the model developed can be applied to other situations with appropriate boundary and initial conditions. During this process, a cylindrically-shaped frozen patty is cooked by heating it between two hot plates at equal temperature, as illustrated in Figure 3.2. The variables of interest for predicting quality and safety aspects of hamburger cooking are spatial profiles and temporal histories temperature, moisture content, fat content and evaporation rate.

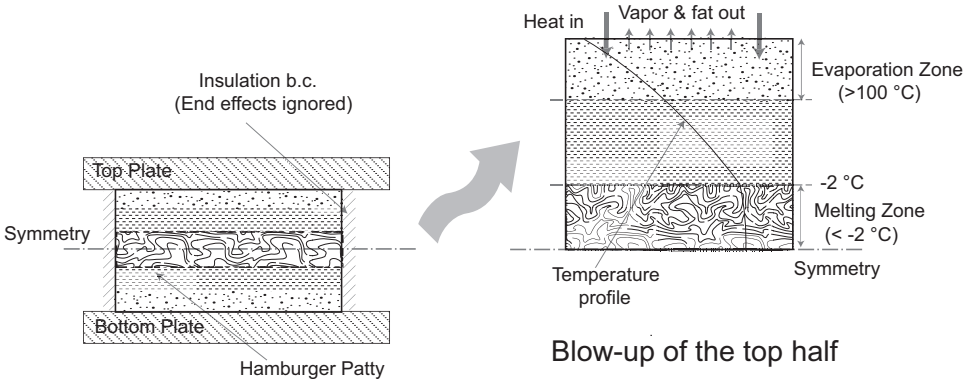

Figure 3.2: Schematic showing computational domain and boundary in case of contact heating of hamburger patty.

3.4.1 Geometry

The patty is cylindrical in shape with height 10 mm and radius 50 mm (Figure 3.2). The effect of gravity is expected to be small as compared to pressure gradients and is ignored. Since the temperatures at the top and bottom plates are identical, there is a symmetry line at the center. Therefore, only top half of the patty is simulated. For simplification, the end effects near the circumference of the patty are considered small and 1-dimensional

problem is solved in the axial direction. The large diameter-to-height ratio (10 : 1) of the patty supports this assumption. However, fluxes in the radial direction may be significant in the regions close to the circumference. Hence, the predictions from this model are applicable far from the circumference.

3.4.2 Initial and Boundary Conditions

Experimental work done by Tornberg and coworkers is chosen to validate the model [13,20,21]. Initially frozen at $-20°\mathrm{C}$, the composition of the patty in terms of weight percentages of water, fat and protein is known. At this temperature, all water and fat are considered to be in the solid matrix and, therefore, concentrations of both liquid water and fat phases in the pore space are zero. The initial gas porosity of the patty is also known (2% [30]). Gas phase in the pore space is saturated with vapor, which gives mass fraction of vapor in gas phase, ω_v to be 0.0015 at $-20°\mathrm{C}$. From this data, the initial conditions for all the governing equations can be calculated.

$$\text{I.C. for Eq. 3.5:} \quad c_w = 0 \tag{3.24}$$

$$\text{I.C. for Eq. 3.6:} \quad c_f = 0 \tag{3.25}$$

$$\text{I.C. for Eq. 3.7:} \quad \omega_v = 0.0015 \tag{3.26}$$

$$\text{I.C. for Eq. 3.9:} \quad c_{bw} = c_{bw,0} \tag{3.27}$$

$$\text{I.C. for Eq. 3.10:} \quad c_{bf} = c_{bf,0} \tag{3.28}$$

$$\text{I.C. for Eq. 3.12:} \quad P = P_{amb} \tag{3.29}$$

$$\text{I.C. for Eq. 3.13:} \quad T = -20°\mathrm{C} \tag{3.30}$$

Since the problem is 1-dimensional, two boundary conditions are required – at either ends of the geometry. Also, the patty is symmetric about the center. Therefore, no flux boundary condition is applied at the end representing the patty center, for all equations.

The boundary conditions at the other end (which is exposed to the hot plate) are

$$\text{B.C. for Eq. 3.5:} \quad n_w|_{surf} = \vec{n}_w.\mathbf{n}_{\text{surf}} \tag{3.31}$$

$$\text{B.C. for Eq. 3.6:} \quad n_f|_{surf} = \vec{n}_f.\mathbf{n}_{\text{surf}} \tag{3.32}$$

$$\text{B.C. for Eq. 3.7:} \quad n_v|_{surf} = w_v\rho_g\vec{u}_g.\mathbf{n}_{\text{surf}} - h_m(\phi S_g(\rho_v - \rho_{v,amb})) \tag{3.33}$$

$$\text{B.C. for Eq. 3.9:} \quad n_{bw}|_{surf} = \vec{n}_{bw}.\mathbf{n}_{\text{surf}} \tag{3.34}$$

$$\text{B.C. for Eq. 3.10:} \quad n_{bf}|_{surf} = \vec{n}_{bf}.\mathbf{n}_{\text{surf}} \tag{3.35}$$

$$\text{B.C. for Eq. 3.12:} \quad P|_{surf} = P_{amb} \tag{3.36}$$

$$\text{B.C. for Eq. 3.13:} \quad q|_{surf} = h(T_{amb} - T_{surf}) - \sum \left(\vec{n}_i c_{p,i} T\right).\mathbf{n}_{\text{surf}} \tag{3.37}$$

During meat cooking, convective heat transfer occurs between the plates and the meat surface (Eq. 3.37). The surface heat transfer coefficient varies during the process, and has been estimated experimentally for heating of hamburger patties of same height, similar composition and temperature settings, by Pan et al. (2000)[8]. In case of convective heat transfer, other important term that need to be included in the energy boundary condition is the energy lost due to expulsion of other fluids from the surface.

As proteins denaturate, liquid water and liquid fat (both from the pore space and the solid matrix) are pushed out of the patty. The boundary fluxes of liquid water and fat, thus, do not depend on external factors and are known as drip losses (Eqs. 3.31, 3.32, 3.34, 3.35). The vapor exits the patty surface due to bulk flow of the gas phase and also convective mass transfer at the surface (Eq. 3.33). Total pressure at the surface is atmospheric and remains constant throughout the process (Eq. 3.36). The assumption here is that a thin film of gas exists at atmospheric pressure in the space between plate and the patty surfaces.

3.4.3 Input parameters

Input parameters used in this study are listed in Table 3.1. The physical and thermal properties of hamburger patties — density, specific heat and thermal conductivity, are estimated from their compositions using the correlations proposed by Choi and Okos (1986)[31]. The intrinsic permeability of beef (raw as well as ground) is found[32,33] to be around 1×10^{-17} m^2. Intrinsic permeability, however, changes during the cooking process due to change in porosity. Taking 1×10^{-17} m^2 as the initial value, Kozeny-Carman permeability-porosity relationship is used to predict intrinsic permeability of the beef patty as a function of porosity

$$k_{in}^{p} \propto \frac{\phi^3}{1-\phi^2} \tag{3.38}$$

The same intrinsic permeability value was used for all the three fluid phases in pore space – water, fat and gas. The relative permeabilities of gas and liquid water are taken from literature[34]:

$$k_{r,g}^{p} = \begin{cases} 1.1S_g - 0.1 & S_g < 0.1/1.1 \\ 0 & S_g > 0.1/1.1 \end{cases} \tag{3.39}$$

$$k_{r,w}^{p} = \begin{cases} \left(\frac{S_w - 0.08}{1-0.08}\right)^3 & S_w > 0.08 \\ 0 & S_w < 0.08 \end{cases} \tag{3.40}$$

Due to lack of fat permeability data, the relative permeability relation for water is also used for fat phase

$$k_{r,f}^{p} = \begin{cases} \left(\frac{S_f - 0.08}{1-0.08}\right)^3 & S_f > 0.08 \\ 0 & S_f < 0.08 \end{cases} \tag{3.41}$$

Diffusivities of liquid water phase and fat phase due to concentration gradients and temperature gradients (as functions of temperature and moisture) are very difficult to

Table 3.1: Input parameters used in the simulations of contact heating of hamburger patty

Parameter	Symbol	Value	Units	Source
Patty dimensions				
Height		10	mm	Oroszvari et al. (2005)[20]
Initial conditions				
Composition		Patty 1 in Table 3.2		Oroszvari et al. (2005)[20]
Porosity	ϕ	.02	–	Boukouvalas et al (2006)[30]
Temperature	T_{ini}	-20	°C	Oroszvari et al. (2005)[20]
Pressure	P_{ini}	101325	Pa	–
Properties				
Water activity	a_w	–	–	Hallstrom (1990)[35]
Density				
water	ρ_w	997.2	kg/m^3	Choi and Okos (1986)[31]
ice	ρ_i	917	kg/m^3	Choi and Okos (1986)[31]
gas	ρ_v	Ideal gas	kg/m^3	Choi and Okos (1986)[31]
fat	ρ_f	925.6	kg/m^3	Choi and Okos (1986)[31]
protein	$\rho_p r$	1330	kg/m^3	Choi and Okos (1986)[31]
Specific heat capacity				
water	$c_{p,w}$	4178	J/kg K	Choi and Okos (1986)[31]
ice	$c_{p,i}$	2062	J/kg K	Choi and Okos (1986)[31]
gas	$c_{p,g}$	1006	J/kg K	Choi and Okos (1986)[31]
fat	$c_{p,f}$	1984	J/kg K	Choi and Okos (1986)[31]
protein	$c_{p,pr}$	2008	J/kg K	Choi and Okos (1986)[31]
Thermal conductivity				
water	k_w	0.57	W/m K	Choi and Okos (1986)[31]
ice	k_w	2.22	W/m K	Choi and Okos (1986)[31]
gas	k_g	0.025	W/m K	Choi and Okos (1986)[31]
fat	k_f	0.18	W/m K	Choi and Okos (1986)[31]
protein	k_{pr}	0.18	W/m K	Choi and Okos (1986)[31]
Intrinsic permeability				
water	$k^p_{in,w}$	1×10^{-17}	m^2	Datta (2006)[33]
fat	$k^p_{in,f}$	1×10^{-17}	m^2	Same as water
gas	$k^p_{in,g}$	1×10^{-17}	m^2	Same as water
Relative permeability				
water	$k^p_{r,w}$	$((\mathrm{S_w} - 0.08)/0.92)^3$	–	Bear (1972)[34]
fat	$k^p_{r,f}$	$((\mathrm{S_f} - 0.08)/0.92)^3$	–	Same as water
gas	$k^p_{r,g}$	$(1 - \mathrm{S_w} - \mathrm{S_f})/0.92$	–	Bear (1972)[34]

estimate. Almost all diffusivity values for meat and other biomaterials are reported at low temperatures and cannot be used for the cooking process. The diffusivity values reported in literature that are closest to our application are that of liquid water during beef roasting[23]. The same value is used in this study for both water and fat. The water activity, and the water and fat holding capacities of ground meat were taken from Hallstrom (1990)[35] and Pan et al (2000)[8]. All other input parameters and their sources are

Input parameters used in the simulations of contact heating of hamburger patty – contd.

Parameter	Symbol	Value	Units	Source
Capillary diffusivity				
water	$D_{w,cap}$	10^{-7}	m^2/s	vandersman (2007)[23]
fat	$D_{f,cap}$	10^{-7}	m^2/s	same as water
Viscosity				
water	μ_w	0.988×10^{-3}	Pa s	
gas	μ_g	1.8×10^{-5}	Pa s	
fat	μ_f	0.02	Pa s	Goodrum (2002)[39]
Holding capacities				
water	$c_{bw,eq}$	$c_{bw,0}\exp(-.0132(T-303))$	kg/m^3	Pan and Singh (2001)[16]
fat	$c_{bf,eq}$	$c_{bf,0}\exp(-.0159(T-303))$	kg/m^3	Pan and Singh (2001)[16]
Heat transfer coefficient	h	–	W/m^2K	Pan et al. (2000)[8]
Mass transfer coefficient	h_m	0.015	m/s	Ni et al. (1999)[18]
Latent heat of vaporization	λ	2.26×10^6	J/kg	
Latent heat of fusion				
water		3.34×10^5	J/kg	
fat		1.5×10^5	J/kg	
Vapor diffusivity in air	$D_{eff,g}$	$2.6 \times 10^{-5} \left(S_g\phi\right)^{3-\phi}/\phi$	m^2/s	Moldrup et al (2005)[40]
Grill temperature	T_{surf}	–	°C	Pan et al. (2000)[8]
Ambient pressure	P_{amb}	101325	Pa	

given in Table 3.1. Note that patty number 1 (which was used in all other simulations) in Table 3.2 represents the patty made from brisket fat, whose composition is taken from Oroszvari et al (2005)[20].

3.4.4 Numerical solution

Equations 3.5, 3.6, 3.7, 3.12, 3.9, 3.10, 3.11 and 3.13 are numerically solved to calculate c_w, c_f, ω_v, P, c_{sw}, c_{sf}, c_{pr} and T respectively, with boundary conditions (Equations 3.31 - 3.37) and initial conditions (Equations 3.24 - 3.30). Auxiliary conditions, such as 3.21, are used to compute the remaining variables. A commercially available finite element software, COMSOL Multiphysics 3.5a (Comsol Inc., Burlington, MA), was used to solve these equations. The computational domain has a thickness of 0.01 m, and is divided into 500 elements. Linear shape functions were used to discretize all the equations. Simulating 150 seconds of heating took approximately 4 hours, for variable

time stepping with a maximum timestep size of 0.01 second specified in the software, on a Pentium-4 3.4 GHz PC with 2GB RAM.

3.5 Results and Discussion

Profiles of temperature, moisture, pressure, fluxes and evaporation rate are discussed in this section. For validation, predicted spatial temperature profiles at two locations are compared with the experimental values from literature. Overall moisture and fat losses and their dependence on patty composition is also compared with the experiments.

3.5.1 Spatial and Temporal Distribution of Temperature

Predicted temperature histories at 5 axial locations are plotted in Figure 3.3a. Point temperature measurements from literature at the center of the patty ($5\ \mathrm{mm}$ from the patty surface) and at a point $2\ \mathrm{mm}$ from the patty surface are also shown[20]. The predicted center temperatures (i.e., at the coldest point) match very well, with the times to reach $0°\mathrm{C}$ (completion of thawing at that location), $36°\mathrm{C}$ and $72°\mathrm{C}$ predicted within an error of less than 5 seconds. At $2\ \mathrm{mm}$ beneath the surface, whereas time to reach $0°\mathrm{C}$ is accurately predicted, not so for two other times (time to reach $60°\mathrm{C}$ and time when the center temperature reaches $72°\mathrm{C}$, the cold point temperature at which the patty is considered safe to eat[2,3]). This difference is attributed to huge temperature gradients in the vicinity of the $2\ \mathrm{mm}$ point. For most of the heating duration, the temperature at points $1\ \mathrm{mm}$ above and below this location differ by more than $40°\mathrm{C}$. Given the finite size of the thermocouple and very high precision required in its placement (due to huge gradients), exact match with point temperature measurements near the surface is impractical. The

most appropriate inference that can be drawn from such a comparison is that the measurements at 2 mm beneath the surface lie within the predicted temperature histories of locations 1 mm and 3 mm beneath the surface.

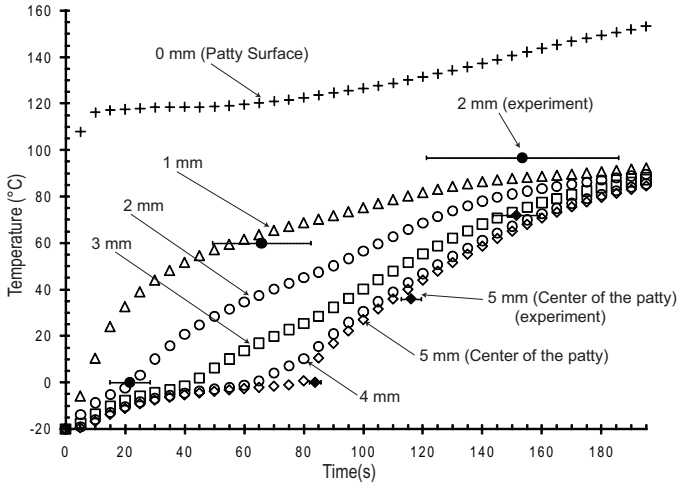

(a)

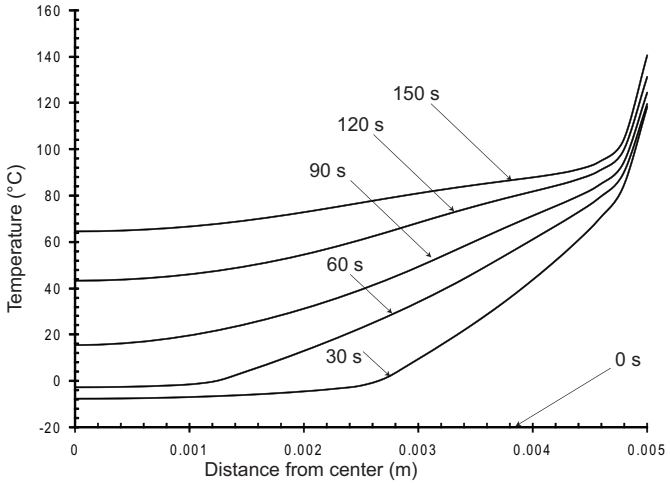

(b)

Figure 3.3: (a) Predicted time-temperature history at different axial locations in the patty. Experimentally observed temperature measurements[20] are also shown as filled symbols with experimental error. Data labels indicate distance from the patty surface. (b) Spatial profiles of temperature at different heating times. Steep gradients can be seen near the dry surface region and nearly flat profiles in the wet core region.

The spatial profiles of temperature are plotted in Figure 3.3b. The temperature pro-

files are almost flat in the frozen region as all the heat is taken up by the melting ice. Once melting is over at a point, the temperature rises rapidly. The slope of spatial profile changes again close to 100°C, when all the water is evaporated and all the incoming heat is available for increasing the temperature.

3.5.2 Water and Fat Loss Histories

Figure 3.4a shows overall water loss as a function of average temperature of the patty for four different patty compositions. The compositions are listed in Table 3.2, and are selected so as to cover the range of fat compositions present in different hamburger types. It can be seen that water losses are independent of the composition and have a linear relationship with temperature rise. Approximately 40% of initial water is lost when the average temperature of the patty reaches 80°C (a 100°C rise from an initial temperature of -20°C). This prediction is also in agreement with experiments[21], which reported water loss at a rate of $0.4\%^{\circ}\mathrm{C}^{-1}$ till an average temperature of 80°C. Fat loss

Table 3.2: Composition of the four patties used in the simulations

Patty number	Weight of water (%)	Weight of fat (%)
1	57.9	25.9
2	67.9	5.9
3	62.9	15.9
4	52.9	35.9

as a function of average temperature is plotted in Figure 3.4b. Unlike water loss, the fat loss is not independent of the initial fat composition and increases with increasing initial fat content–starting from 30% (for 5.9% initial weight percentage of fat) to greater than 40% (for 35.9% initial fat), respectively. Oroszvari et al. (2006)[13] also observed dependence of fat losses to fat composition; the range of losses predicted by them, however, was much greater–from 15% (for 6.7% initial fat percentage) to 55% (for 39% initial

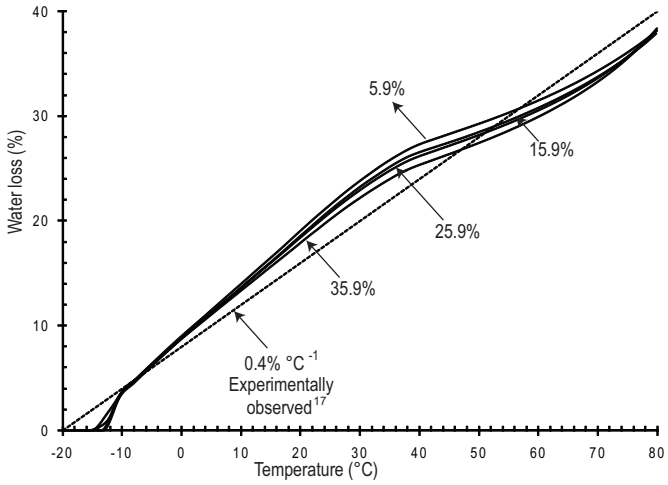

(a)

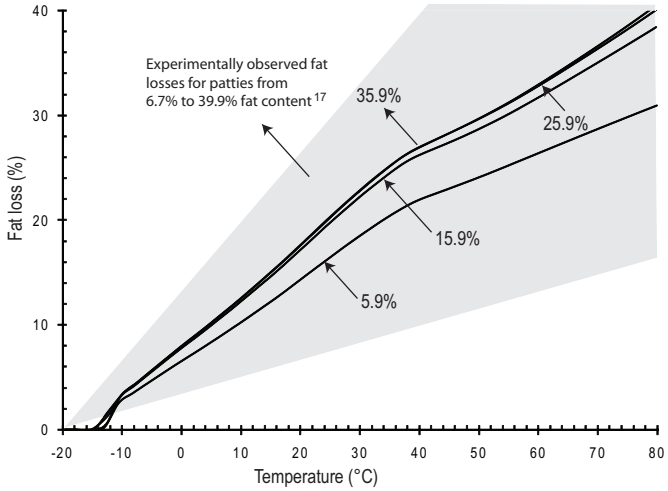

(b)

Figure 3.4: Experimental and predicted (a) water loss and (b) fat loss as functions of average temperature of the patty. Data labels indicate initial fat content (as percentage of initial patty weight). It can be seen that water losses are independent of fat content, while the fat losses are not.

fat percentage). Since the transport properties of fat are considered the same as that of water due to lack of data, this dependence probably indicates that the transport properties (diffusivity and permeability) are much stronger functions of composition than the corresponding properties of water. In meat literature also, it has been observed[36] that fat may exist as a dispersed phase, and formation of fat channels (which is a function of total fat content) dictates its transport and loss from the matrix. The focus of this study being model development, which is already quite complex, improved measurement/estimation of transport properties could not be pursued any further and can be considered for future studies.

Figure 3.5 shows histories of three types of weight losses from the patty – water coming out of the patty in liquid form (water drip loss), all fat coming out of the patty (fat drip loss) and water loss in vapor form (evaporation loss). Starting after about 5 seconds of heating, drip loss of water rises fast and most of it happens in the first minute. Fat loss, 100% of which is drip, also follows a similar history. The difference between total water and fat losses, of course, is absence of evaporation loss in fat. It can be seen that most of water loss (more than 80% of the total water loss till 90 s and 70% till 150 s) occurs due to drip, with water loss due to evaporation playing a minor role. This agrees with the speculation of Oroszvari et al. (2006)[13] that the contribution from drip can be as high as 80%. Although absolute match with the experiments is difficult due to inherent variabilities and complexities present in the material and the process, the predictions of temperature, water and fat losses (as functions of temperature and composition), and overall drip and evaporation losses validate the more fundamental approach toward modeling of the meat cooking process. Following this approach, meat products under different heating situations can be simulated. This is an advancement from the existing approach, under which bulk thermal properties (such as enthalpy, thermal conductivity and effective diffusivity) are measured as functions of temperature, and, then,

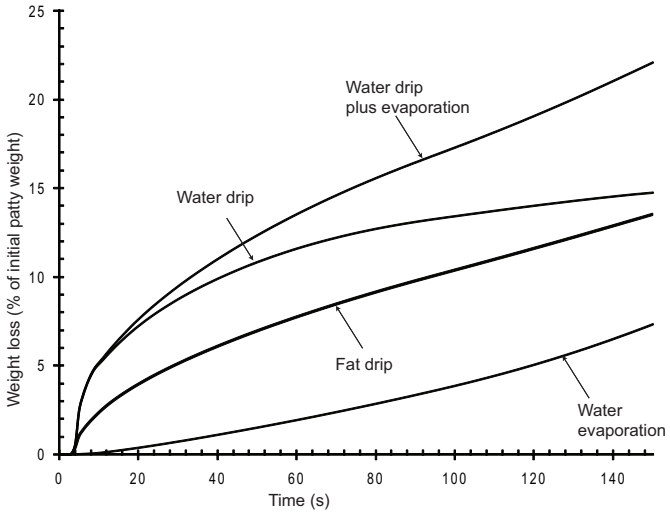

Figure 3.5: Variation of predicted water drip, water evaporation and fat drip loss (as percentages of initial patty weight) with heating time. Water drip dominates initially, with evaporation picking up in the late half of heating time. Fat is lost only due to drip.

conduction/diffusion equations are used to fit the data.

3.5.3 Spatial and Temporal Distribution of Moisture and Fat

Spatial distribution of moisture content (normalized by its initial value, Table 3.2) at different times of heating is plotted in Figure 3.6a. The outer surface of the patty dries up within 30 seconds of heating and an almost linear profile is formed from the dried surface to an inner location where moisture is still at its initial value. The near-linear pseudo-steady state like moisture profile is due to very high diffusivity (10^{-7} m^2/s), while its flat nature in the inner core is because there is no transport at temperatures lower than the melting point. Moisture level starts to increase in the core region after 60 seconds. This phenomenon of increased moisture content has also been observed experimentally[37]. Two different mechanisms contribute to this rise of moisture – 1) Rapid evaporation causes pressure to rise near the heated surface with the unheated

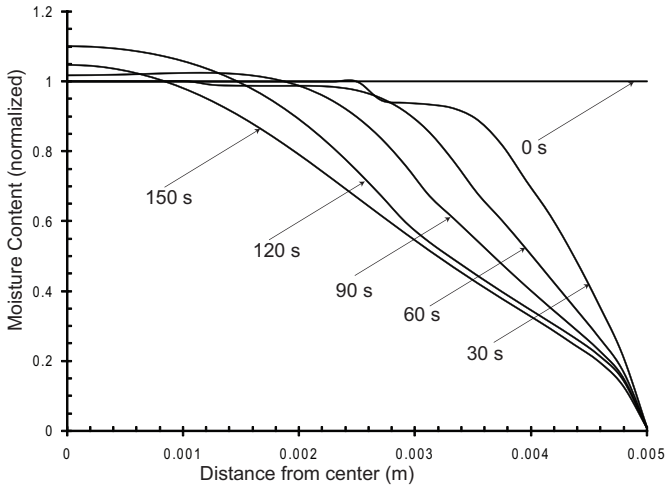

(a)

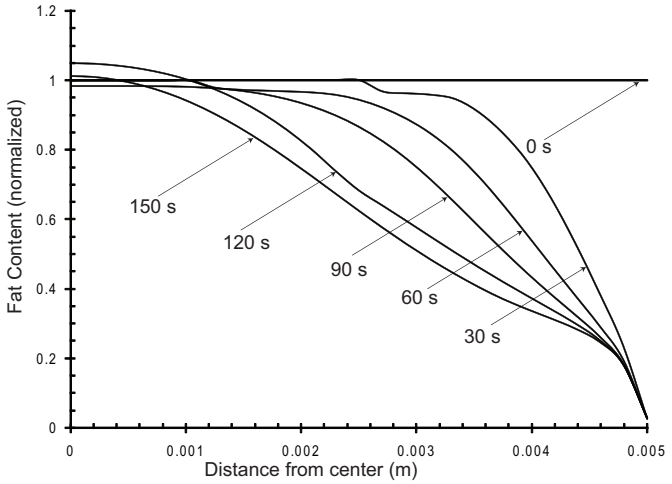

(b)

Figure 3.6: Spatial profiles of (a) water content and (b) fat content (normalized by their initial content) at different heating times. For both water and fat, some accumulation can be seen in the core region.

inner core still at atmospheric pressure. This favorable pressure gradient toward the core can lead to transport in both liquid and vapor forms. Vapor going toward the core condenses due to decrease in temperature, which leads to further lowering of pressure in the inner region and suction of fluids inside. 2) Positive temperature gradient exists from the patty surface to the cooler inner core, which can also cause liquid moisture transport towards the core when diffusivity due to thermal gradients (defined Eq. 3.16)

is finite. The relative contribution of the two phenomena are elucidated in Figure 3.7, which is now discussed.

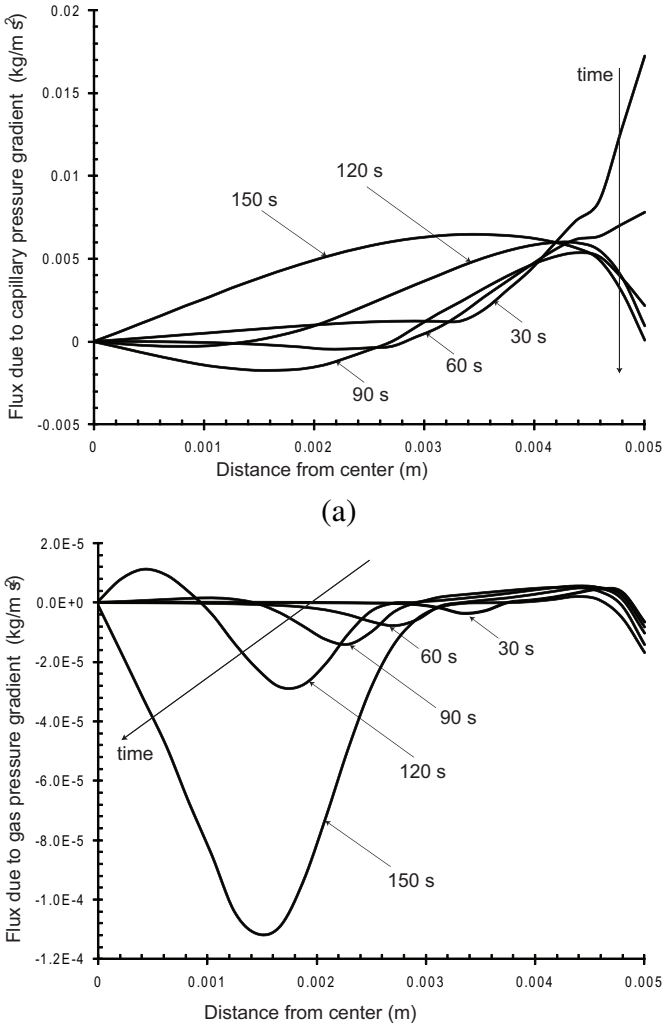

Figure 3.7: Spatial profiles of water fluxes (direction away from center) due to (a) capillary pressure gradients and (b) gas pressure gradients at different heating times. Near the surface, capillary pressure fluxes dominate and, thus, are responsible for most of drip loss. Both the fluxes contribute to accumulation in the core region.

Moisture fluxes due to capillary pressure gradient and due to gas pressure gradient are plotted in Figure 3.7. It can be seen that net moisture flux due to capillary pressure gradient at the surface is highest during initial few seconds, and, drops down very

rapidly. This was also seen previously in Figure 3.5, where the water drip loss rate was highest initially. In the core region, the capillary pressure flux becomes negative after 30 seconds and stays that way till 90 seconds. After 90 seconds of heating, the flux becomes positive again in the inner core and drives moisture out. On the other hand, fluxes due to gas pressure gradients (Figure 3.7b) are negative for most of the time in core region, with the peak negative flux point (which can be called a point of accumulation) moving toward the core (from the surface) with time. Near the surface, fluxes due to gas pressure gradients are very small (by at least two orders of magnitude) as compared to fluxes due to capillary pressure gradients. These gas pressure gradient fluxes become more significant in the inner core region, where their contribution to negative flux (toward the core) can exceed 50% to the total negative flux.

Note that, since the hamburger patty is treated as a rigid porous material, the effect of shrinkage on pressure rise is not included; and only evaporation/condensation and temperature increase contribute to changes in pressure (and, thus, development of pressure gradients). A good match obtained with the experiments even after ignoring shrinkage does not necessarily mean that the contribution due to shrinkage is small. This is because the moisture diffusivity value taken from literature was estimated[23] for a slow heating (so that pressure generation due to evaporation is small and can be neglected) process of meat, in which contributions of shrinkage and capillary pressure gradients are clubbed. Therefore, future work should include modeling meat as a deformable porous material with a better experimental estimation of moisture diffusivity, which is required for a more in-depth analysis and separation of contributions of shrinkage and capillary pressure toward moisture fluxes.

Spatial distribution of fat is very similar to that of water (Figure 3.6). This is because pressure (gas and capillary) driven transport of the two phases in the patty are very sim-

ilar (provided the fat content is high enough to form sufficient channels of transport, an implicit assumption in the continuum porous media model). Evaporation/condensation phenomena, which plays a relatively minor role, is the only difference between the two fluids. The contribution of vapor transport to moisture profiles is only visible in the core region, where water accumulation is greater than fat accumulation due to vapor movement in the core and, subsequent condensation.

3.5.4 Spatial and Temporal Distribution of Pressure and Evaporation Rate

Spatial distributions of pressure in gas phase (gauge pressure, i.e., absolute pressure minus atmospheric pressure) and rate of evaporation (in $\mathrm{kg/m^3s}$) at different times of heating are plotted in Figure 3.8. The peak pressure occurs close to the surface, at a location almost coinciding with the peak of evaporation rate. Gas pressure is less than atmospheric in the inner core region due to the combined effect of vapor condensation and removal of air due to binary diffusion. Such negative pressures are also predicted during drying of clay[38]. Condensation can also be seen just beneath the patty surface before the point of peak evaporation. This is because the completely dried-up surface has zero equilibrium vapor pressure and, thus, the vapor coming from inside can condense. However, this condensation does not cause any moisture accumulation near the surface, as the region of condensation is too small ($< 0.1\mathrm{mm}$) and any condensate is lost due to drip.

The magnitude of peak negative gauge pressure (in the core) is orders of magnitude higher than the peak of positive gauge pressure (near the surface). This is due to lower porosity (which means lower permeability as per the Kozeny-Carman relationship) in

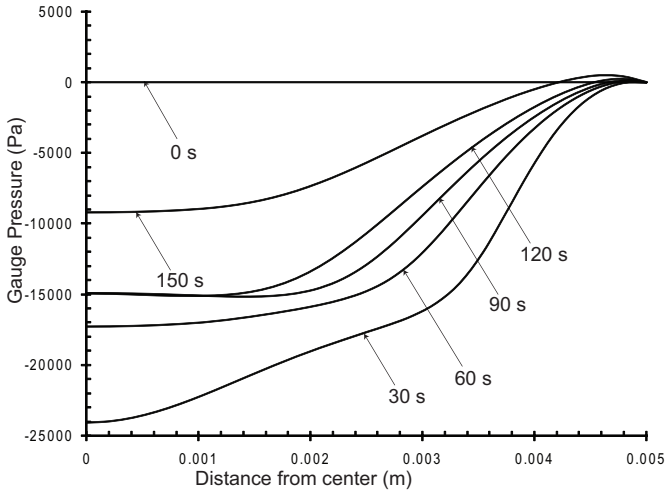

(a)

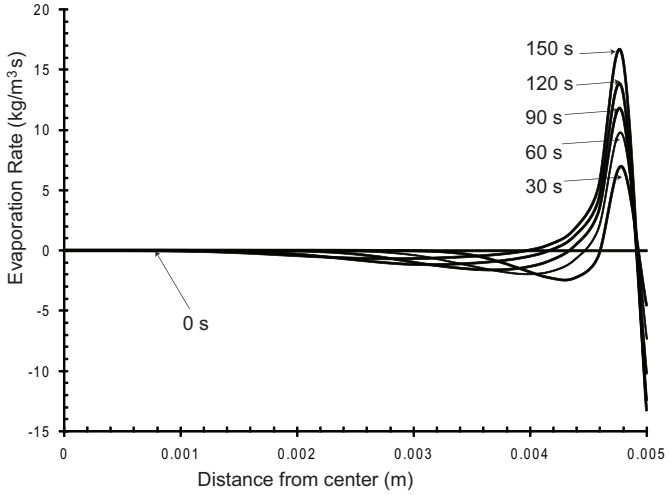

(b)

Figure 3.8: Spatial profiles of (a) gas pressure and (b) evaporation rate at different heating times. Position of peak evaporation rate is very near the surface and almost coincides with the location of peak pressure. Gauge pressure is negative in the core due to condensation of vapor and removal of air due to binary diffusion.

the core region. Note that the lower gas pressure in the core region does not represent the net pressure of all the fluids (that acts on the solid matrix). The net fluid pressure acting on the solid surface, usually defined as the average of pressures of different fluid phases present weighted by their volume fractions, can be very different from the gas pressure. Since the pore space in the core is mostly filled up with water and fat, the contribution due to gas pressure is expected to be less. In this study, estimation of water and fat pressures is not feasible as fluxes due to capillary pressure gradients are converted into diffusive fluxes due to unavailability of capillary pressure-saturation and capillary pressure-temperature curves.

To summarize, spatial profiles of temperature show early development of a thin crust region ($T > 100°\mathrm{C}$), and gradual heating of the patty interior due to high internal resistance to heat transfer. Most of the water loss and all fat loss from the patty happen as drip. Moisture losses due to evaporation are about 30% of the total water loss, and pick up in later half of heating duration as the temperature rises. The contribution of pressure generation due to evaporation/condensation toward moisture flux is relatively small. And separation of the effects of pressure gradients due to shrinkage and capillarity on moisture fluxes requires modeling meat as a deformable porous media.

3.6 Conclusion

A multiphase multicomponent hygroscopic porous media based model, which is a significant advancement from the existing approaches, has been developed for intensive heating of meat. Spatial profiles and temporal histories of different variables of interest such as temperature, water and fat concentrations are discussed in detail, and the modeling approach is validated against existing experimental data. The model can be used to

elucidate the relative contribution of various modes of transport and phase change such as capillary pressure, gas pressure and evaporation, which is not possible through experiments or other simpler models. The fundamental basis of the model that does away with empirical parameters, makes its extension to other thermal processes of meat and to thermal processing of other biological materials easier and, thus, it can be an important tool in making safety, quality and product design related predictions.

BIBLIOGRAPHY

[1] [cited Oct 22, 2009] http://www.cdc.gov/foodsafety/

[2] Food Code. U.S. Public Health Service, Food and Drug Administration – 1999 Washington, D.C.

[3] USDA urges consumers to use food thermometer when cooking ground beef patties. FSIS News Release. Food Safety and Inspection Service. U.S. Department of Agriculture – 1998 Washington, D.C.

[4] Tornberg E. Effects of heat on meat proteins - implications on structure and quality of meat products. *Meat Science*. 2005;70(3):493-508,Sp. Iss. SI.

[5] Bengtsson NE, Jakobsson B, Dagerskog M.Cooking of Beef by Oven Roasting - Study of Heat and Mass-Transfer. *Journal of Food Science*.1976;41(5):1047-1053.

[6] Chau KV, Snyder GV. Mathematical-Model for Temperature Distribution of Thermally Processed Shrimp, *Transactions of the ASAE*. 1988;31(2):608-612.

[7] Fowler AJ, Bejan A. The Effect of Shrinkage on the Cooking of Meat. *International Journal of Heat and Fluid Flow*. 1991;12(4):375-383.

[8] Pan Z, Singh RP, Rumsey, TR. Predictive modeling of contact-heating process for cooking a hamburger patty. *Journal of Food Engineering*. 2000;46(1):9-19.

[9] Sebastian P, Bruneau D, Collignan A, Rivier M. Drying and smoking of meat: Heat and mass transfer modeling and experimental analysis. *Journal of Food Engineering*. 2005;70(2):227-243.

[10] Shilton N, Mallikarjunan P, Sheridan, P. Modeling of heat transfer and evaporative mass losses during the cooking of beef patties using far-infrared radiation. *Journal of Food Engineering*. 2002;55(3):217-222.

[11] Wang L, Singh RP. Finite element modeling and sensitivity analysis of double-sided contact-heating of initially frozen hamburger patty. *Transactions of the ASAE*. 2004;47(1):147-157.

[12] Kondjoyan A, Rouaud O, McCann MS, Havet M, Foster A, Swain M, Daudin JD. Modelling coupled heat-water transfers during a decontamination treatment of the surface of solid food products by a jet of hot air. I. Sensitivity analysis of the model and first validations of product surface temperature under constant air temperature conditions. *Journal of Food Engineering*. 2006;76(1):53-62.

[13] Oroszvari BK, Bayod E, Sjoholm I, Tornberg E. The mechanisms controlling heat and mass transfer on frying of beefburgers. III. Mass transfer evolution during frying. *Journal of Food Engineering*. 2006;76(2):169-178.

[14] Cleland AC, Earle RL. Assessment of freezing time prediction methods. *Journal of Food Science*. 1984:49(4):1034-1042.

[15] Pham QT. Comparison of General-Purpose Finite-Element Methods for the Stefan Problem. *Numer Heat Tranf. B-Fundam.* 1995;27(4):417-435.

[16] Pan Z, Singh RP. Physical and thermal properties of ground beef during cooking. *Lebensmittel-Wissenschaft Und-Technologie-Food Science and Technology*. 2001;34(7):437-444.

[17] Farkas BE, Singh RP, Rumsey TR. Modeling heat and mass transfer in immersion frying. Part 1. Model development. *Journal of Food Engineering*. 1996;29(2):211-226.

[18] Ni H, Datta AK. Moisture, oil and energy transport during deep-fat frying of food materials, *Food and Bioproducts Processing*. 1999;77(C3):194-204.

[19] Datta AK. Porous media approaches to studying simultaneous heat and mass

transfer in food processes. I: Problem formulations. *Journal of Food Engineering*. 2007;80(1):80-95.

[20] Oroszvari BK, Sjoholm I, Tornberg E. The mechanisms controlling heat and mass transfer on frying of beetburgers. I. The influence of the composition and comminution of meat raw material. *Journal of Food Engineering.* 2005;67(4):499-506.

[21] Oroszvari BK, Bayod E, Sjoholm I, Tornberg E. The mechanisms controlling heat and mass transfer on frying of beefburgers. Part 2: The influence of the pan temperature and patty diameter. *Journal of Food Engineering*. 2005;71(1):18-27.

[22] Miles CA, van Beek G, Veerkamp CH. Calculation of Thermophysical Properties of Foods. In: *Physical Properties of Foods*. New York:Applied Science Publishers, 1983:269-312.

[23] van der Sman RGM. Soft condensed matter perspective on moisture transport in cooking meat. *AIChE Journal*. 2007;53(11):2986-2995.

[24] van der Sman RGM. Moisture transport during cooking of meat: An analysis based on Flory-Rehner theory. *Meat Science*. 2007;76(4):730-738.

[25] Halder A, Dhall A, Datta AK. An improved, easily implementable, porous media based model for deep-fat frying - Part I: Model development and input parameters. *Food and Bioproducts Processing.* 2007;85(C3):209-219.

[26] Halder A, Dhall A, Datta AK. An improved, easily implementable, porous media based model for deep-fat frying - Part II: Results, validation and sensitivity analysis. *Food and Bioproducts Processing.* 2007;85(C3):220-230.

[27] Kassama LS, Ngadi MO, Raghavan GSV. Structural and instrumental textural properties of meat patties containing soy protein. *International Journal of Food Properties*. 2003;6(3):519-529.

[28] Bixler NE. NORIA – A finite element computer program for analyzing water, vapor, air, and energy transport in porous media. Technical Report: Sandia National Laboratories. 1985.

[29] Scarpa F, Milano G. The role of adsorption and phase change phenomena in the thermophysical characterization of moist porous materials. *International Journal of Thermophysics*. 2002;23(4):1033-1046.

[30] Boukouvalas CJ, Krokida MK, Maroulis ZB, Marinos-Kouris D. Density and porosity: Literature data compilation for foodstuffs. *International Journal of Food Properties*. 2006;9(4):715-746.

[31] Choi Y, Okos MR. Thermal properties of liquid foods – review. In: *Okos MR (editor). Physical and Chemical Properties of Food* Saint Joseph, Michigan: American Society of Agricultural Engineers, 1986:35-77.

[32] Oroszvari BK, Rocha CS, Sjoholm I, Tornberg E. Permeability and mass transfer as a function of the cooking temperature during the frying of beefburgers. *Journal of Food Engineering*. 2006;74(1):1-12.

[33] Datta AK. Hydraulic permeability of food tissues. International *Journal of Food Properties.* 2006;9(4):767-780.

[34] Bear J. Dynamics of fluids in porous media. New York: American Elsevier Publishing company, Inc., 1972.

[35] Hallstrom B. Mass Transport of Water in Foods a Consideration of the Engineering Aspects. *Journal of Food Engineering*. 1990;12(1):45-52.

[36] Andersson A, Andersson K, Tornberg E. A comparison of fat-holding between beefburgers and emulsion sausages. *J. Sci. Food Agric.*. 2000;80(5):555-560.

[37] Thorvaldsson K, Skjoldebrand C. Water transport in meat during reheating. *Journal of Food Engineering*. 1996;29(1):13-21.

[38] Chemkhi S, Jomaa W, Zagrouba F. Application of a coupled thermo-hydro-mechanical model to simulate the drying of nonsaturated porous media. *Drying Technology*. 2009;27(7):842-850.

[39] Goodrum JW, Geller DP, Adams TT. Rheological characterization of yellow grease and poultry fat. *Journal of the American Oil Chemists Society*, 2002;79(10):961-964.

[40] Moldrup P, Olesen T, Yoshikawa S, Komatsu T, Rolston DE. Predictive-descriptive models for gas and solute diffusion coefficients in variably saturated porous media coupled to pore-size distribution: I. Gas dlifusivity in repacked soil. *Soil Sci*. 2005;170(11):843-853.

CHAPTER 4

MODELING OF MULTIPHASE TRANSPORT DURING DRYING OF HONEYCOMB CERAMIC SUBSTRATES

This research was funded by Corporate Research, Corning Incorporated. The complete authorship of this work should be read as Ashish Dhall, Gary Squier, Muluwork Geremew, William A. Wood, Jacob George and Ashim K. Datta.

4.1 Abstract

Multiphase transport model during drying of Corning substrates in a conventional (hot air) drier is developed. The model is validated against experiments done for drying of cylindrical substrates, by comparing histories and axial profiles of moisture loss and point temperature histories at various locations. Drying experiments are performed at two different values of drier temperature settings of 103°C and 137°C, at relative humidity value of 5%. Sensitivity analysis reveals a process that is controlled by external heat and internal water vapor transport.

Nomenclature

A	Area, m^2
c_i	Concentration of species i, $\mathrm{kg/m^3}$
$c_{p,i}$	Specific heat of species i, $\mathrm{J/kgK}$
$CPSI$	Cells per square inch
dw	Cell wall thickness in inches
$\bar{\bar{D}}$	Diffusivity tensor, $\mathrm{m^2/s}$
h	Heat transfer coefficient, $\mathrm{W/m^2K}$
h_m	Mass transfer coefficient, $\mathrm{m/s}$
$\dot{I}$	Evaporation rate, $\mathrm{kg/m^3s}$
k	Thermal conductivity, $\mathrm{W/mK}$
$k_{g,cha}$	Permeability of air in the channels, m^2
K', K''	Evaporation rate constants, $1/\mathrm{s}$
L	Characteristic length scale, m
LOD	Loss on drying
n_i	Mass flux of species i, $\mathrm{kg/m^2s}$
OFA	Open frontal area fraction
P	Pressure, Pa
q	Heat flux, $\mathrm{W/m^2}$
S_i	Saturation (volume fraction in the pores) of species i
T	Temperature, K
$\vec{u}_i$	Velocity vector for species i, $\mathrm{m/s}$
w_i	Mass fraction of species i (air or vapor) in gas phase

Greek Letters

ρ_i	Density of species i, $\mathrm{kg/m^3}$
λ	Heat of vaporization, $\mathrm{J/kg}$
ϕ	Porosity
μ	Viscosity, $\mathrm{Pa\,s}$

Subscripts

0	At time, $t = 0$
air	Air
amb	Ambient
bin	Binary diffusion
cha	Channels
eff	Effective property for the honeycomb
g	Gas
sat	Saturation (as in saturation vapor pressure)
$solid$	Solid
$surf$	Surface
v	Vapor
w	Water

4.2 Introduction

Honeycomb ceramic substrates are widely used in the industry, especially as particulate filters and catalyst supports for emission control, both for stationary applications (such as power plants, refineries, chemical processing plants) and mobile applications (diesel and gasoline cars and trucks)[1]. Honeycombs are also used as adsorbers, membrane-coated gas filters and finned monolithic reactors. The manufacturing process of the honeycombs involves drying of freshly-extruded wet substrates to complete dryness before further processing and sintering[2]. Although drying (using hot air or microwaves) is a classic process and mathematical modeling of the drying process is widely studied [3,4], the kinetics becomes complex in this case due to the channeled geometry of the substrates. The presence of channels requires careful consideration of the relevant transport mechanisms and anisotropic transport properties.

4.2.1 Objective

The objective of the present study is to use mathematical modeling to elucidate relevant factors affecting drying of the substrates, so that the process can be optimized under energy and quality constraints. Specifically, this paper discusses 1) development of a multiphase model for drying of a channeled ceramic substrate, treating it as an effective porous continuum; 2) validation of the model by comparing the model predictions with experimentally observed temperature profiles and drying rates for hot air drying at two values of ambient temperature; and 3) sensitivity analyses with the model for the input parameters to elucidate the contributions from transport mechanisms in effect.

4.3 Model Development

In this section, the heat and mass transport model is described in detail– starting with physical description of the honeycomb substrates and the drying process, scale analysis, the key assumptions, the governing equations and the boundary conditions. Input parameters and model implementation are described at the end.

4.3.1 Physical Description

Figure 4.1 shows the physical geometry of the honeycomb structure of the substrate, whose drying is studied. The substrate is cylindrical in shape with open channels along its axis. The honeycomb structure is characterized by the thickness of the channel walls (usually expressed in mil, one-thousandth of an inch $= 0.0254$ mm) and cell density (expressed in number of channels per square inch, CPSI)[5]. Usual ranges for the wall thickness and cell density are $2 - 10.5$ mil and $200 - 1200$ CPSI, respectively[5]. The ceramic material of the honeycomb can be considered as a porous solid matrix, with liquid water and gas (air and water vapor) occupying its pores. As the honeycomb is exposed to hot-air or microwaves, its temperature rises leading to evaporation and transport of liquid water and vapor through the walls and the channels of the honeycomb. The drying rate is expected to be dependent on the rate of heat supplied, rate of moisture transport through the walls and the channels, and the rate at which vapor is carried away from the honeycomb by ambient air.

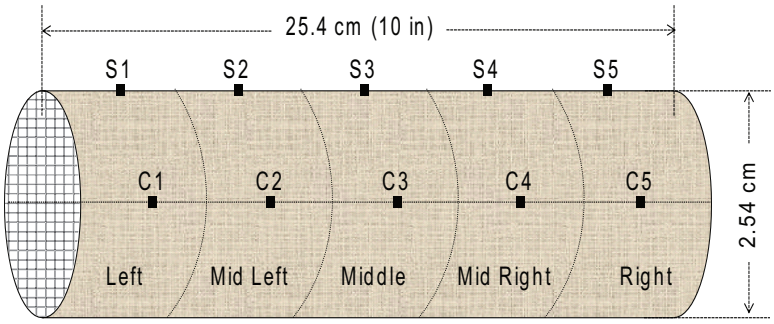

Figure 4.1: A schematic of the honeycomb substrate showing the channels. The 10 thermocouple locations (C1-C5 on the central axis and S1-S5 on the surface) and the 5 pieces cut for measurement of axial moisture profile are also shown.

4.3.2 Assumptions

The key assumptions while developing the drying model are: i) The honeycomb structure is treated as an effective continuum. There are no explicit channels present in the model geometry and a representative elementary volume (REV) assumption of porous media is invoked to homogenize the concentrations over the walls and the channels. A more detailed analysis is possible by considering heat and mass transfer at multiple scales[6–10]. However, a comprehensive single-scale analysis is necessary before moving to multiscale modeling, as the latter requires significant development time and huge computational resources (potentially) to resolve thousands of channels for large honeycombs encountered in industry. ii) Internal evaporation in a wet porous material can lead to pressure rise leading to pressure-driven flow of liquid water[11,15]. During intensive heating conditions such as high ambient temperature or presence of microwaves, water can be expelled from the porous material in liquid form, contributing significantly to the drying rate. However, in honeycomb substrates, it is observed that open channels do not allow significant pressure rise in the walls, thus impeding pressure-driven expulsion from the walls. In this study, it is assumed that the pressure in the walls is close to atmospheric such that pressure-driven expulsion of liquid water from the walls of the

honeycomb is negligible. However, as described later, pressure driven vapor flow in the channels is possible. iii) At all times, at a given location in the honeycomb, which is homogenized for the purpose of modeling, temperature is shared by all the phases; iv) The contribution of liquid and gaseous moisture transport to energy transport is considered small and is ignored in this study, i.e convective terms are ignored in the energy equation; v) Liquid water and water vapor may not be at equilibrium with each other (more discussion later) vi) Deformation of the honeycomb during drying is small and can be ignored; and vii) The gas phase obeys ideal gas law.

4.3.3 Governing Equations

The honeycomb substrate is considered as a porous medium with two transportable phases - liquid water and gas. The gas phase comprises two components– air and water vapor. As the temperature in the substrate rises, the water present in the walls of the substrate evaporates. Liquid water in the walls of the substrate transports due to capillarity, which is modeled as capillary diffusion[13]. The gas phase components, present in the channels as well as the walls, transport due to diffusion as well as convection.

Energy Transport

Local thermal equilibrium exists between all the phases. Therefore, a single energy equation is solved to get temperature, T:

$$\left(\rho_{eff} c_{p,eff}\right) \frac{\partial T}{\partial t} = \nabla . \left(\bar{\bar{k}}_{eff} \nabla T\right) - \lambda \dot{I} \tag{4.1}$$

where ρ_{eff}, $c_{p,eff}$ and $\bar{\bar{k}}_{eff}$ are the effective density, specific heat and thermal conductivity of the substrate, respectively and $\dot{I}$ is the evaporation rate per unit volume. The

effective density and effective specific heat can be estimated by appropriately averaging the properties of individual phases:

$$\rho_{eff} = c_w + c_{solid} \tag{4.2}$$

$$c_{p,eff} = x_w c_{p,w} + x_{solid} c_{p,solid} \tag{4.3}$$

However, estimation of thermal conductivity is more complicated. In the axial direction, there are two parallel pathways for heat conduction– through the walls and the channels. Therefore, effective thermal conductivity in the axial direction can be estimated as:

$$k_{eff}\big|_{axial} = k_a OFA + k_{wall}\,(1 - OFA) \tag{4.4}$$

where k_{wall} is the thermal conductivity of the wall (taken as volumetric average of the thermal conductivities of the individual phases) and k_a is the thermal conductivity of the channels (i.e. gas phase). Open Frontal Area, OFA, is the fraction of the transverse cross-section area open to the channels:

$$OFA = \frac{A_{cha}}{A_{wall} + A_{cha}} \tag{4.5}$$

In the radial direction also, heat transfer can be considered to occur through two parallel pathways: one straight though the walls and another in which walls and channels are in series:

$$k_{eff}\big|_{radial} = k_{wall}\left(1 - \sqrt{OFA}\right) + \frac{\sqrt{OFA}}{\left(1 - \sqrt{OFA}\right)/k_{wall} + \sqrt{OFA}/k_a} \tag{4.6}$$

Liquid Water Transport

Since the pressure-driven flow has been ignored in the walls, the equation of transport for liquid water in the walls of the substrate can be written with the capillary diffusion term and the evaporation term:

$$\frac{\partial c_w}{\partial t} = \nabla.\left(\bar{\bar{D}}_{eff} \nabla c_w\right) - \dot{I} \tag{4.7}$$

where $\bar{\bar{D}}_{eff}$ is the capillary diffusivity. The capillary diffusivity values in the radial and the axial directions are estimated in the same way as the thermal conductivity (Equations 4.4 and 4.6). The only difference is, since there is no liquid water in the channels, the contribution from the second pathway in the radial direction (walls and channels in series, second term in Eq. 4.6) is zero.

Water Vapor Transport

The transport of water vapor in the walls of the substrate as well as the channels is governed by the following equation:

$$\frac{\partial}{\partial t}\left(c_g w_v\right) + \nabla.\left(w_v \rho_g \bar{u}_g\right) = \nabla.\left(\rho_g \bar{\bar{D}}_{bin} \nabla w_v\right) + \dot{I} \tag{4.8}$$

where $\bar{\bar{D}}_{bin}$ is the binary diffusivity. Binary diffusivity values in the radial and the axial directions are estimated in the same way as the corresponding thermal conductivity (Equations 4.4 and 4.6) and the capillary diffusivity values. The second term on LHS of equation 4.8 is the convection term due to gas phase velocity in the channels. Even in the absence of any forced air, gas velocity in the channels can be finite because of pressure generated due to evaporation. These pressure gradients are small and do not cause any liquid water expulsion from the walls, but can still contribute to significant vapor transport in the channels because the permeability of the channels is very high (10^{-7} m^2, Table 4.1) as compared to that of the walls (10^{-17} m^2, measured at Porous Media Inc, Ithaca, NY).

Gas Transport

If the contribution of gas (vapor + air) transport due to pressure gradients is significant in the channels, the gas pressure needs to be solved for. Mass conservation equation for

the gas phase can be used to calculate pressure:

$$\frac{\partial}{\partial t}\left(c_g\right) + \nabla.\left(\rho_g \bar{u}_g\right) = \dot{I} \tag{4.9}$$

Darcy's law is applied to estimate velocity of the gas phase, $\vec{u}_g$:

$$\vec{u}_g = -\frac{k_{g,cha}}{\mu_g}\nabla P \tag{4.10}$$

where $k_{g,cha}$ is the gas permeability in the channels. Here the assumption is that the Reynolds number for gaseous flow in the channels should be small enough for Darcy's law to hold.

Equations 4.1, 4.7, 4.8 and 4.9 constitute the drying model and are solved simultaneously to get the four dependent variables - temperature, T, liquid water concentration, c_w, water vapor mass fraction, w_v and pressure, P. All other quantities can be determined from these 4 variables.

Evaporation Rate

Accurate determination of evaporation rate inside a porous medium is a challenging task [14]. Empirical information is usually required to get a good estimate of rate of evaporation. As discussed earlier, open channels of the honeycomb keep the pressure in the honeycomb close to atmospheric, which means that the wet honeycomb cannot achieve a temperature beyond the boiling point of water at atmospheric pressure, i.e. 100°C. Thus, any extra heat supplied to wet honeycomb, which can raise its temperature beyond 100°C, should always go towards evaporation of liquid water. Therefore, evaporation rate, $\dot{I}$ can simply be written as:

$$\dot{I} = K' \frac{\rho_{eff} c_{p,eff}\left(T - 373\right)}{h_{vap}} \quad for \;\; T > 100°\mathrm{C} \tag{4.11}$$

In Equation 4.11, the proportionality constant, K' is chosen high enough such that temperature stays at 100°C till there is finite moisture. Note that this assumption of temperature staying at 100°C may break down at very high heating rates, if the vapor transport is slow (causing pressure to build up). Further, significant regions of the honeycomb stay at a temperature lower than 100°C during drying, and still contribute to evaporation. The rate of evaporation in these regions can be written as:

$$\dot{I} = K''(\rho_{v,sat} - \rho_v) \quad for \;\; T < 100°\mathrm{C} \tag{4.12}$$

For small pores, the time scale of reaching local equilibrium between liquid water and vapor (i.e., $\rho_{v,sat} = \rho_v$) is smaller than the time scales of transport[14]. A large value of K'' (relative to the time scale of vapor transport) will force this in Equation 4.12. However, in honeycombs, large channels mean that the transport time scales are smaller and, locally, non-equilibrium may exist between liquid water and vapor ($\rho_{v,sat} \neq \rho_v$). In such cases, the only way to determine the constant of proportionality, K'', is to fit the model predictions to experimentally observed data, which is followed in this study.

4.3.4 Boundary Conditions

For the energy equation, forced convection heat transfer boundary condition is applied at the outer surfaces of the honeycomb. Since evaporation is also present at these surfaces, heat taken by the evaporating water is subtracted from the heat flux supplied by the hot air. Therefore, the net heat flux at the surface becomes:

$$q|_{surf} = h(T_{amb} - T|_{surf}) - h_{vap}\, n_w|_{surf} \tag{4.13}$$

The total water vapor flux that is carried away by the ambient air is made up of a "blowing" part and a diffusive part:

$$n_{v,total}|_{surf} = w_v c_g \vec{u}_g.\vec{n}_{surf} + h_m \phi \left(\rho_{v,sat}|_{surf} - \rho_v|_{amb} \right) \tag{4.14}$$

The diffusive part (second term) in Equation 4.14 has contributions from two phenomena– liquid water evaporating at the outer surface of the honeycomb and the diffusive vapor flux from the honeycomb. Therefore, this term is divided in the ratio of volume fractions of water and gas phases at the honeycomb surface:

$$n_w|_{surf} = h_m \phi S_w \left(\rho_{v,sat}|_{surf} - \rho_v|_{amb} \right) \tag{4.15}$$

$$n_v|_{surf} = w_v c_g \vec{u}_g . \vec{n}_{surf} + h_m \phi S_g \left(\rho_{v,sat}|_{surf} - \rho_v|_{amb} \right) \tag{4.16}$$

In case of internal-resistance limited transport, the resistance due to mass transfer coefficient is expected to be small, and fixed concentrations of vapor and liquid water can be imposed on the boundary, such that $\rho_{v,sat}|_{surf} = \rho_v|_{amb}$ is satisfied. The boundary condition for the gas phase equation comes by imposing atmospheric pressure at the surface:

$$P|_{surf} = P|_{amb} \tag{4.17}$$

To summarize, equations 4.13, 4.15, 4.16 and 4.17 are used as boundary conditions for equations 4.1, 4.7, 4.8 and 4.9, respectively.

4.3.5 Input Parameters

Table 4.1 lists the input parameters and their respective sources used in the study. Cylindrical honeycombs (50.8 mm (2 inch) diameter and 254 mm (10 inches) height) with 0.33 mm (13 mil) wall thickness and 300 square-shaped cells per square inch (CPSI) are used. The physical properties of the solid phase (density, thermal conductivity and specific heat), diffusivity of liquid moisture in the solid and the porosity of the walls (excluding the channels) are listed in Table 4.1. The capillary diffusivity of liquid water is of the order of 10^{-10} m^2/s, which is too small to play any role in the drying kinetics (more later). The dependence of binary diffusivity (between air and water vapor) on the

Table 4.1: Input parameters used in simulations

Parameter	Value
Wall thickness	13 mil (0.33 mm)
CPSI	300
Initial moisture content	0.154 (dry basis)
Porosity of the walls	0.346
Liquid water density	998 $\mathrm{kg/m^3}$
Solid phase density	3000 $\mathrm{kg/m^3}$
Gas phase density	Ideal gas
Specific heat of water	4184 $\mathrm{J/kgK}$
Specific heat of solid	900 $\mathrm{J/kgK}$
Thermal conductivity of water	0.57 $\mathrm{W/mK}$
Thermal conductivity of solid	5.5 $\mathrm{W/mK}$
Thermal conductivity of gas phase	0.026 $\mathrm{W/mK}$
Diffusivity of liquid water	10^{-10} $\mathrm{m^2/s}$
Binary diffusivity in the walls[16]	$2.6 \times 10^{-6} \frac{(S_g \phi)}{\phi}^{3-\phi}$ $\mathrm{m^2/s}$
Viscosity of air	10^{-3} $\mathrm{Pa\,s}$
Evaporation rate constant	0.15 $\mathrm{s^{-1}}$
Absolute permeability in the channels[12]	10^{-7} $\mathrm{m^2}$
Latent heat of vaporization	2.26×10^6 $\mathrm{J/kg}$
Heat transfer coefficient	20 $\mathrm{W/m^2K}$

porosity and gas volume fraction in the honeycomb walls, has been taken from literature data for repacked soil[16]. All other parameters are taken from literature.

4.3.6 Numerical Solution

The model described above is implemented using a commercial Finite Element package, COMSOL Multiphysics 3.5a to simulate convective drying in a hot-air dryer. A 2D axisymmetric geometry is used, which means that the surface of the substrate is exposed to uniform temperature and relative humidity. COMSOL has built-in transient convection-diffusion equation with non-zero source terms. Specifically, conduction-convection equation, convection-diffusion equation, Stefan-Maxwell diffusion equation

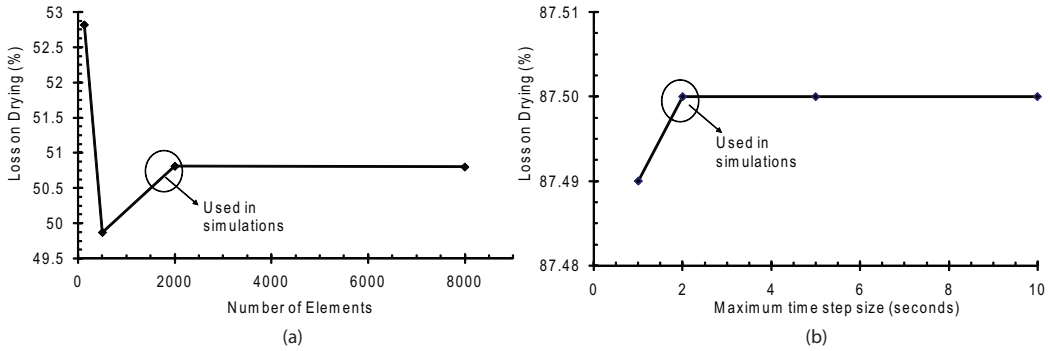

Figure 4.2: a) Mesh size convergence (Percentage of Moisture Lost for ambient air temperature of 137°C after 1 hr on y-axis), b) Time-step size convergence (Percentage of Moisture Lost for ambient air temperature of 137°C after 1.5 hr on y-axis). Number of elements and the time-step size used in the simulations are indicated.

(Chemical Engineering module of COMSOL) and Darcy's law (Chemical Engineering module of COMSOL) are used to solve for temperature, liquid water concentration, vapor mass fraction and pressure fields, respectively. Mapped quad mesh elements with quadratic shape functions are used with equal mesh size in both directions. UMFPACK Direct solver is selected as it is very robust for highly coupled systems and has reasonable memory requirements for 2D geometries. Plots for mesh and time step size convergence, and the mesh and time step sizes used are shown in Figure 4.2.

4.4 Experimental Measurements

For experimental validation, the honeycombs (placed horizontally) are dried in a hot-air dryer at two different ambient temperature values (103°C and 137°C). The relative humidity for both the temperature values is kept fixed at 5%. The weight of the substrate is measured using a weighing scale after different drying times. Since the initial mass of the sample and the initial moisture content are known (and assuming that all the weight loss is due to moisture), moisture content at any time can be estimated from

the weight of the substrate. Axial profiles of moisture are determined by cutting the substrates axially into 5 equal pieces (Figure 4.1) and, then, measuring the moisture content individually in all the pieces. Temperature histories are recorded at 10 different locations (5 each on the central axis and the surface, Figure 4.1) in the honeycomb using FISO Fiber Optic temperature probes (Quebec, QC CANADA). The probe locations are also the mid-points on the central axis and the surface of the 5 pieces cut for moisture measurement.

4.5 Results and Discussion

In this section, moisture loss and temperature histories at various locations and axial profiles of moisture loss at different times are compared with experimentally observed values for the two ambient temperature values discussed above. Moisture loss is expressed as loss on drying, LOD, which is defined as amount of water lost as a fraction of initial water content:

$$LOD = 1 - c_w/c_{w,0} \tag{4.18}$$

In equation 4.18, c_w is the moisture concentration solved for in equation 4.7 and $c_{w,0}$ is the initial moisture concentration (at time, $t = 0$). After histories, contours of temperature and moisture loss at different drying times are discussed. This is followed by sensitivity analysis of the drying process kinetics to various parameters.

4.5.1 Moisture Loss Histories and Axial Profiles

Figure 4.3 shows a comparison between predicted and experimentally observed overall moisture loss for the honeycomb sample (expressed as percentage of initial moisture

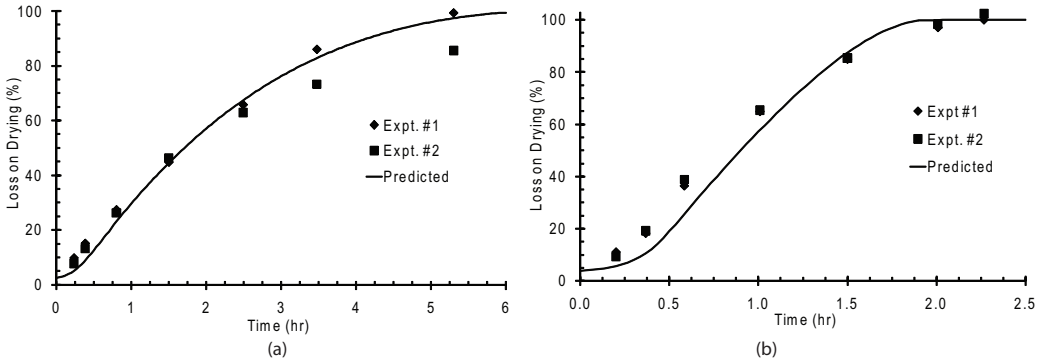

Figure 4.3: Predicted and observed histories of overall moisture loss of the substrate for the two values of ambient temperature– (a) 103°C and (b) 137°C. The solid lines represent predictions (showing the S-shaped moisture loss history) and the points represent observed values

content) for the two values of ambient temperature (103°C and 137°C). It can be seen that the substrate dries out in about six hours at 103°C and in two and half hours at 137°C. At both temperatures, the moisture loss history follows an S-shaped curve—there is an initial heating-up period during which drying is slow, followed by rapid drying and, again, lowering of drying rate as the material dries up. Predicted overall moisture loss matches the experimentally observed values very well, with the maximum difference between predicted and observed overall moisture loss being less than 10%. Figure 4.4 shows axial profiles of predicted and experimentally observed moisture loss at seven different drying times. The two outer pieces of the cylindrical substrate dry out faster, while the drying rate for the three center pieces is almost identical. This means that the end effects (in the axial direction) are small for at least 60% of the substrate volume. Again, as with the overall moisture loss histories, model predictions for the axial moisture loss profiles match well with the experimentally observed values.

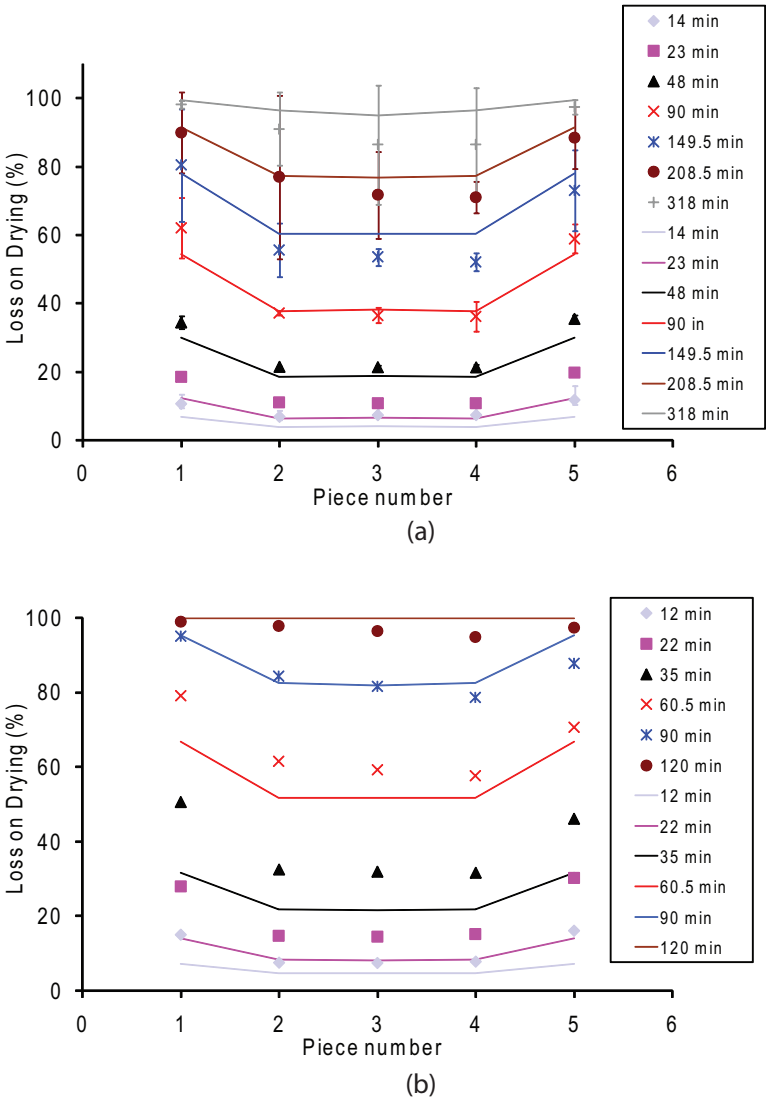

Figure 4.4: Predicted and observed axial profiles of moisture loss at different times for the two values of ambient temperature– (a) 103°C and (b) 137°C, showing the end effects in the two outer pieces and uniform profiles in the 3 center ones. The solid lines represent predictions and the points represent observed values

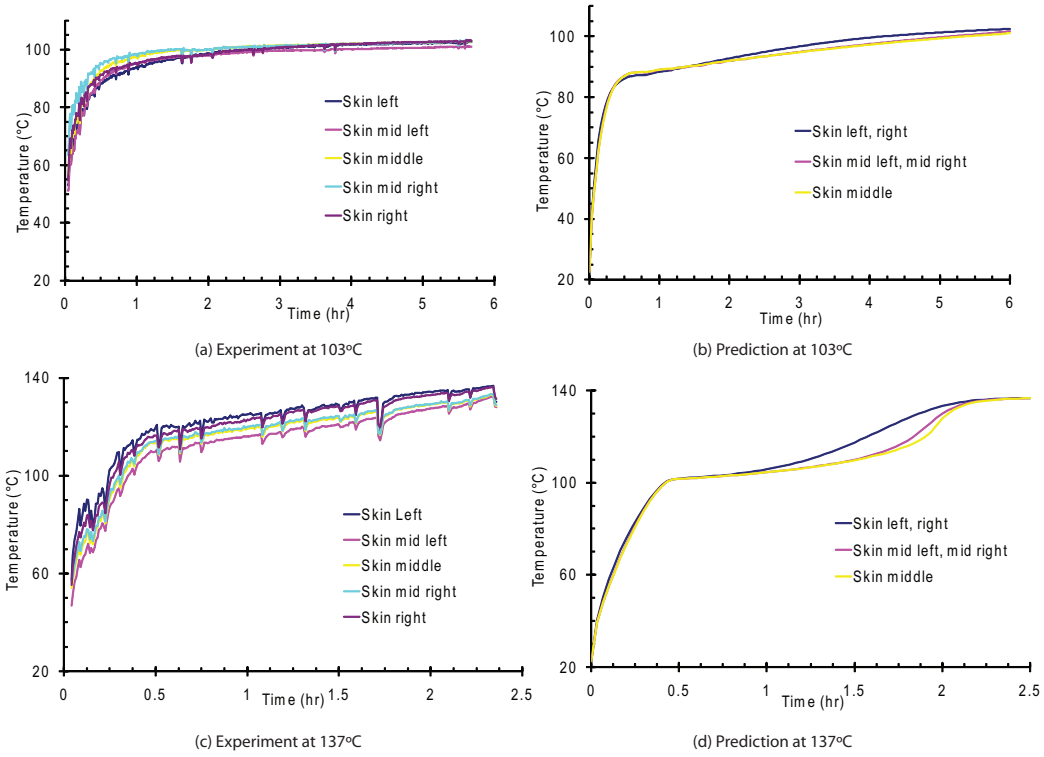

Figure 4.5: Predicted (right) and observed (left) temperature histories showing relative uniformity in temperature at different axial locations on the surface.

4.5.2 Point Temperature Histories

Predicted and observed temperature histories at 5 equidistant locations at the surface and at the central axis (core) of the substrate are plotted in Figures 4.5 and 4.6 respectively. For both values of ambient temperatures, surface temperatures rise fast (nearly linear) for about 30 minutes, followed by a slow rise and gradual approach to the ambient temperature. For a given ambient temperature, the maximum difference in temperature readings between the 5 axial locations is about 10°C – indicating a uniformity in surface temperatures in the axial direction. Core temperatures rise at a slower rate as compared to skin temperatures. For the 103°C ambient temperature, the middle three locations stay at around 95°C, while temperature at the outer two locations increases steadily throughout the heating duration. As the outer locations dry faster, the temperature pro-

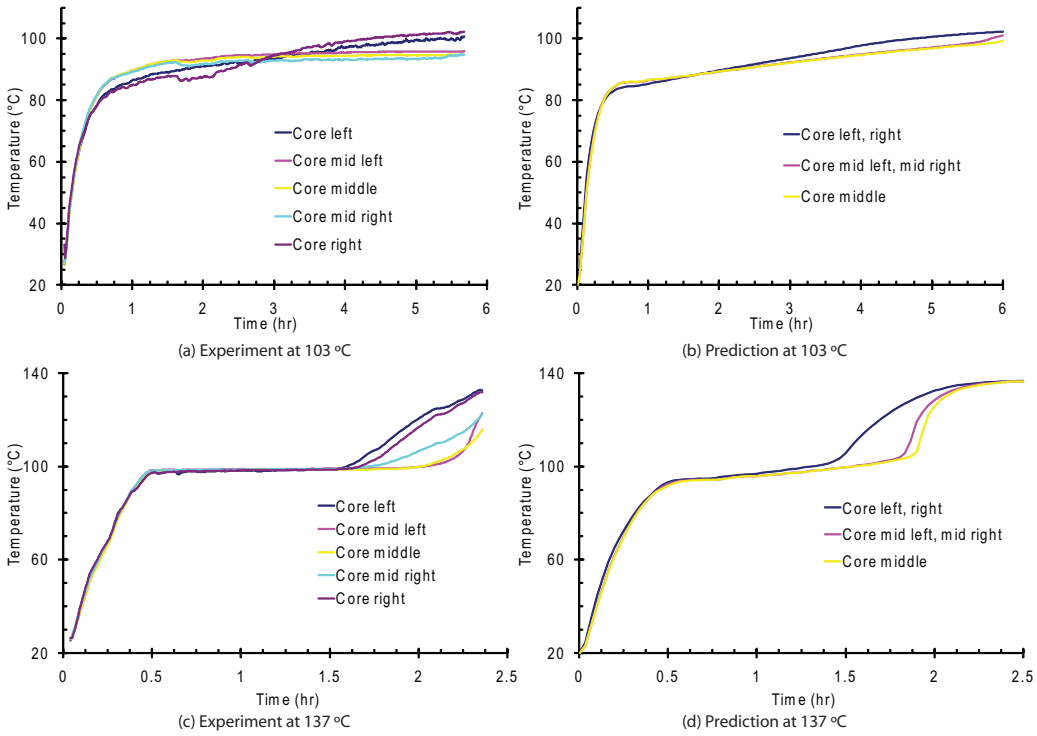

Figure 4.6: Predicted and observed temperature histories showing relative uniformity in temperature at different axial locations on the central axis. Comparing Figures 4.5 and 4.6, it can be seen that temperature difference is more in the radial direction as compared to the axial direction.

files at these locations reach the oven temperature earlier than the middle locations. For the 137°C ambient temperature, core temperatures at any location stay constant at 100°C till that location dries out completely. The outer locations (left, right) dry out after approximately 1.5 hr of heating, while the middle locations dry out after about 2 hours. Again, as the outer locations dry faster, the temperature profiles at these locations reach the oven temperature earlier than the middle locations. All these observed trends of temperature profiles are captured by the model. However, there is one significant difference — the temperature at which the profiles start to bend and approach the ambient temperature. The predicted ones bend at a temperature around 5-10 °C lower than the observed ones for 103°C and at least 10°C for 137°C ambient temperature. This difference could be because of the evaporation rate formulation. As mentioned before, since it is not pos-

sible to independently determine volumetric evaporation rates (and the evaporation rate constant has to be fitted to match the observed overall drying rates), some discrepancy in local evaporation rates (and thus temperature profiles) is unavoidable. Experimental error can be another reason for this discrepancy. Errors can arise because in the honeycomb, the temperature probes are in contact with air also, which can be at a slightly different temperature than the honeycomb walls. Other reasons for lower temperature prediction near the skin can be pressure generation (and related temperature rise) in the substrate walls which is not accounted for in the model. Detailed experimentation (with precise estimation of moisture history near the surface) and modeling (which includes pressure generation inside the walls), required to resolve this anomaly are beyond the scope of this study.

4.5.3 Temperature and Moisture Contours

Temperature and moisture loss contours for the dryer temperature of $103°\mathrm{C}$ are plotted in Figure 4.7. As expected temperature near the outer surfaces is close to the ambient temperature, while the inner regions are cooler. However, overall, the temperature in the honeycomb is fairly uniform, with maximum temperature difference between any two locations being less than $10°\mathrm{C}$. Moisture gradients, on the other hand, are much larger than the temperature gradients. This indicates that the energy transport is probably externally limited, while internal resistance controls mass transport. Contours for dryer temperature of $137°\mathrm{C}$ (omitted to avoid repetition) show similar behavior. Relative contributions of various transport mechanisms will be further explored in the next section.

To summarize, the proposed model is able to predict the overall trends as well as

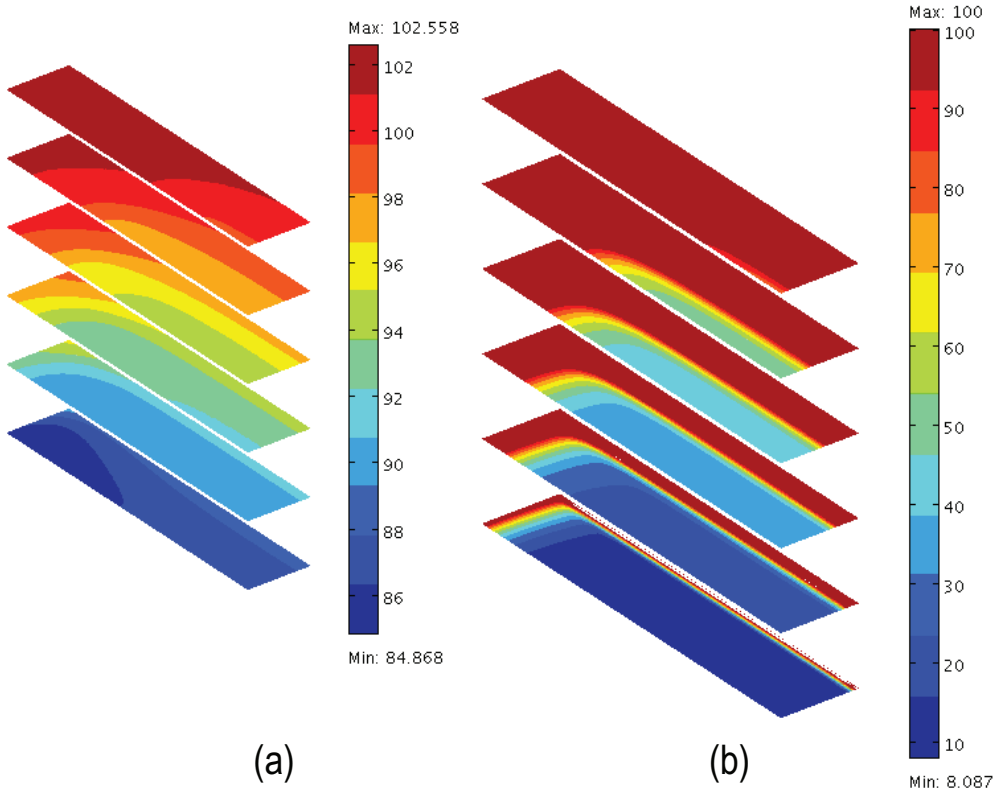

Figure 4.7: Predictions of (a) temperature, (°C) and (b) moisture loss (LOD, %) contours at 1 hour intervals for ambient temperature of 103°C, showing higher moisture loss gradients than temperature gradients in both radial and axial directions

axial distributions of moisture loss at the two ambient temperatures considered. The temperature histories are also predicted with reasonable accuracy–these serve to validate the model. The next section explores the sensitivity of model predictions to various important parameters in order to identify the rate determining ones.

4.6 Sensitivity Analysis

The effect of various model parameters on predicted temperature and moisture is discussed here. In particular, effect of heat transfer coefficient, thermal conductivity, liquid water diffusivity, binary diffusivity of vapor, and the evaporative rate constant are de-

scribed.

4.6.1 Energy Transport

The forced convection heat transfer coefficient over the cylindrical honeycomb substrate is estimated to be about 20 $\mathrm{W/m^2K}$ (for hot-air drying at a low air velocity of about $0.01\mathrm{m/s}$). The effective thermal conductivity of the substrate is around 2 $\mathrm{W/mK}$ and the characteristic length scale (volume to surface area ratio for the cylindrically shaped substrate) is of the order of 1 cm. This gives a heat transfer Biot number of about 0.1. Such a low value of the Biot number means that most of the resistance comes from the heat transfer coefficient and energy transfer should be relatively insensitive to the thermal conductivity of the substrate. Figure 4.8 and Figure 4.9 show the sensitivity of the histories of overall moisture loss and temperature at the mid-point of the core (cold-point of the substrate) to heat transfer coefficient and thermal conductivity, respectively. From Figure 4.8a, it can be seen that a 20% change in heat transfer coefficient results in a significant change in the drying time. The cold-point temperature also follows the same trend (Figure 4.8b). However, changes in thermal conductivity of the solid result in little change in the drying time or cold-point temperature (Figure 4.9), confirming that the drying process is externally controlled. Therefore, changing ambient air velocity (and thus the heat transfer coefficient) can be more effective in changing drying profiles than, say, altering the material composition (and thus the thermal conductivity).

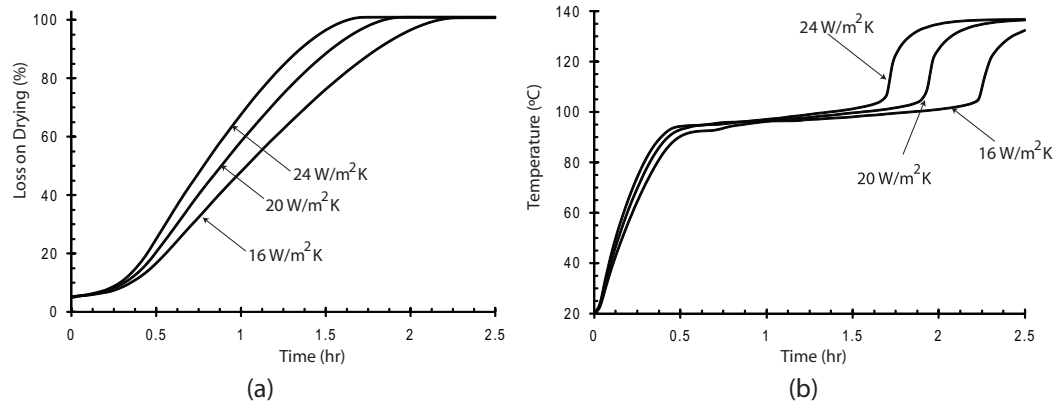

Figure 4.8: Effect of heat transfer coefficient on a) overall moisture loss and b) cold-point temperatures for ambient temperature of $137°\mathrm{C}$

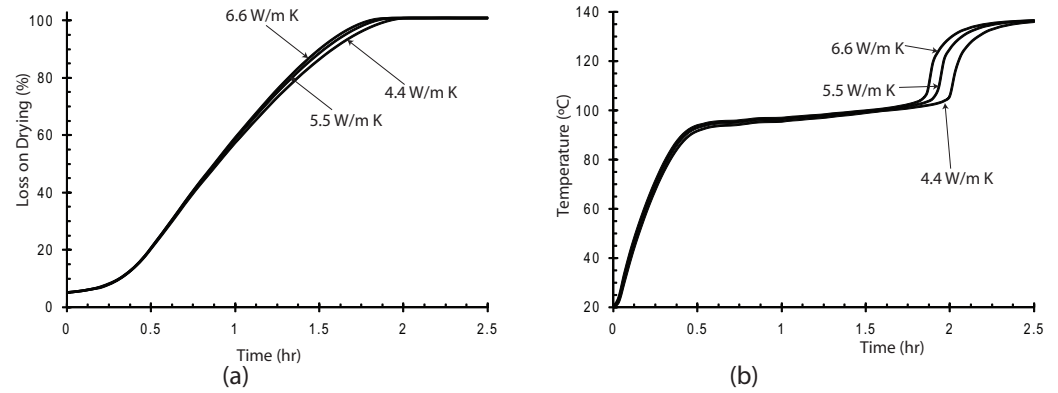

Figure 4.9: Effect of solid thermal conductivity on a) overall moisture loss and b) cold-point temperatures for ambient temperature of $137°\mathrm{C}$. From figures 4.8 and 4.9, it can be seen that heat transfer is externally-controlled

4.6.2 Liquid Water Transport

The diffusivity of the liquid water in the solid substrate without any channels is measured to be of the order of $10^{-10}\ \mathrm{m}^2/\mathrm{s}$. The mass transfer coefficient at honeycomb surfaces ($\sim 0.02\ \mathrm{m/s}$) can be estimated by Lewis number analogy from convective heat transfer coefficient. From this data, mass transfer Biot number is estimated to be $>> 1$, which means that the drying rate should be more sensitive to changes in internal resistance (diffusivity) than external resistance (mass transfer coefficient). However, the time scale in which such a low diffusivity value can contribute significantly is of the order of

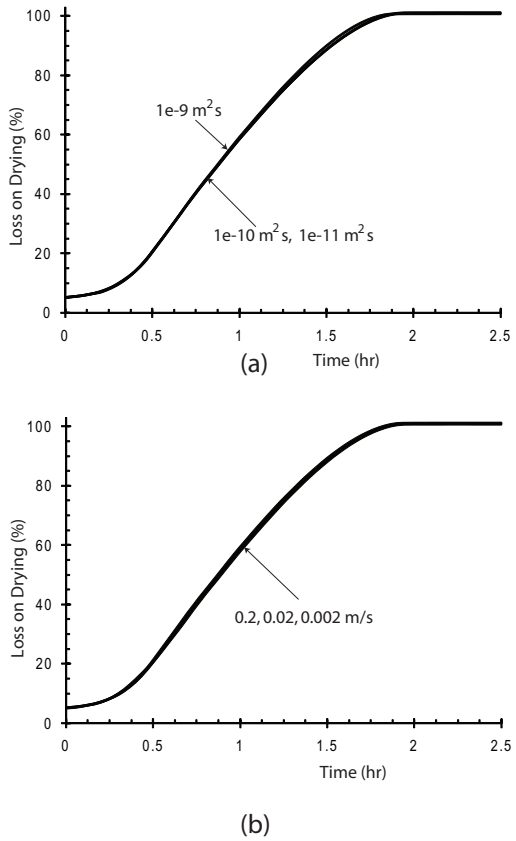

Figure 4.10: (a) Effect of liquid diffusivity and (b) mass transfer coefficient on overall moisture loss for ambient temperature of 137°C, illustrating the almost negligible contribution of liquid moisture transfer on drying rate

$L^2/4D$, which is $\sim 10^6$ s, much larger than time scale of the drying process. Thus, the effect of both mass transfer coefficient and diffusivity on the temperature and moisture profiles is expected to be negligible, which is seen in the computation shown in Figure 4.10.

4.6.3 Water Vapor Transport

For water vapor transport in the open channels, the binary diffusivity is of the order of 10^{-5} m^2/s. The mass transfer coefficient (discussed above) is ~ 0.02 m/s. This leads to a mass transfer Biot number for vapor transport greater than 10. This implies that,

like liquid water transport, internal resistance to vapor transport (due to binary diffusion) dominates over external resistance (mass transfer coefficient). However, unlike liquid transport due to capillary diffusion alone, convective as well as diffusive vapor transport are present in the channels. Therefore, sensitivities of both binary diffusivity and velocity of air in the channels are studied. Effective binary diffusivity of vapor in the honeycomb depends on binary diffusivity in air (channels) and binary diffusivity in the porous solid walls (See Section 4.3.3). Since diffusivity of vapor in air is known and is always fixed, only binary diffusivity in the walls is varied for sensitivity analysis. For convection, a hypothetical forced air velocity of $0.1\ \mathrm{m/s}$ is introduced as opposed to that calculated from pressure gradients in the channel.

Figure 4.11 shows the effect of varying binary diffusivity on the overall moisture loss and cold-point temperature. For the lower two values of binary diffusivities, the drying rates and temperature histories are nearly identical. The overall drying time for these lower diffusivity values is approximately 5% more than that for the highest value. Also, for the highest binary diffusivity, the cold-point temperature stabilizes at a lower value. This is because a decrease in resistance to vapor transfer increases evaporation rate, reducing temperatures. However, the effect of binary diffusivity in the walls on drying rate is small overall, as the binary diffusion in the channels dominates (and the binary diffusivity in the channels is constant). Figure 4.12 shows the sensitivity of the histories of overall moisture loss and temperature cold-point to air velocity in the channels. It can be seen that an air velocity of $0.1\ \mathrm{m/s}$ increases the drying rate very significantly. Also, since the drying rate has increased, especially in the inner regions, the cold-point temperature also starts to rise early. Therefore, introduction of hot dry air in the channels can be an effective method of reducing drying times as well as temperature differences at the core and the skin.

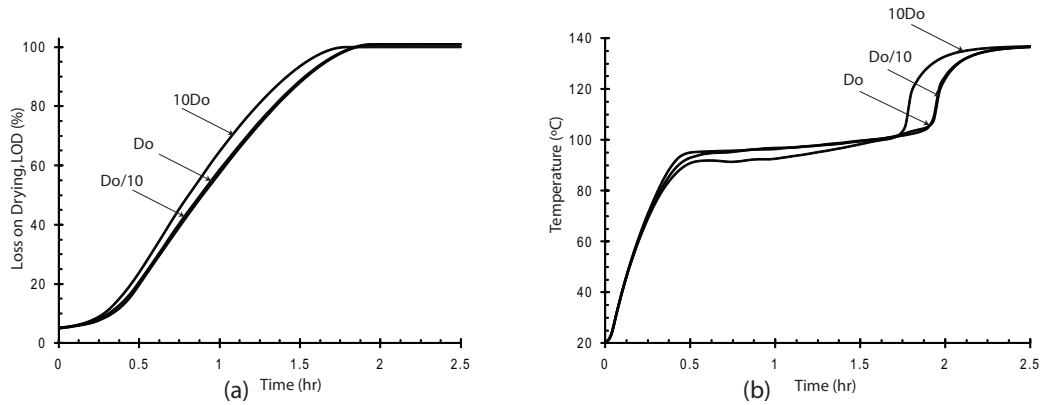

Figure 4.11: Effect of binary diffusivity on a) overall moisture loss and b) cold-point temperatures, for ambient temperature of 137°C. Three diffusivity values are chosen– $10D_0$, D_0 (from Table 4.1) and $D_0/10$

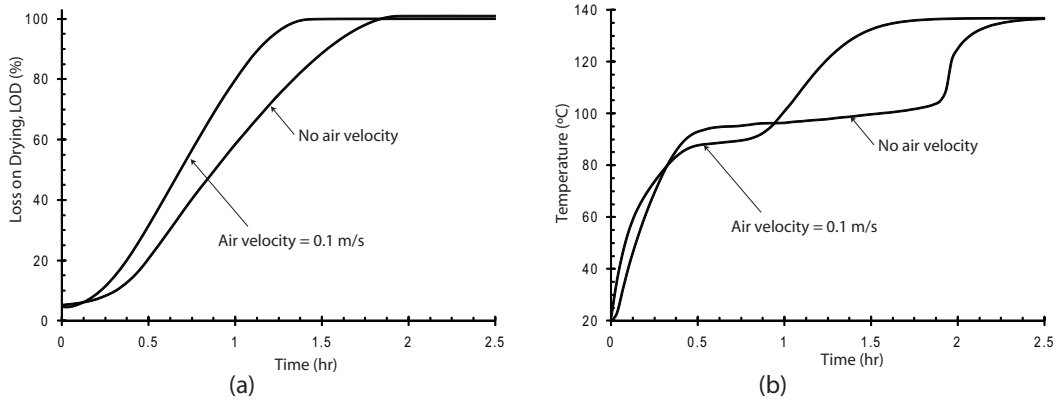

Figure 4.12: Effect of forced air velocity in the channels on a) overall moisture loss and b) cold-point temperatures for ambient temperature of 137°C, indicating decrease in drying rate on introduction of dry air in the channels

4.6.4 Evaporation Rate Constant

As discussed earlier, determination of volumetric rate of evaporation is a difficult task and only an approximate value of the evaporation rate constant, K'', can be determined by matching the overall drying rate. Therefore, it is critical to study the impact of evaporation rate constant on drying profiles. Figure 4.13 shows the sensitivity of the histories of overall moisture loss of the log and temperature at the mid-point of the core (cold-point of the substrate) to evaporation rate constant. This is because the higher rate

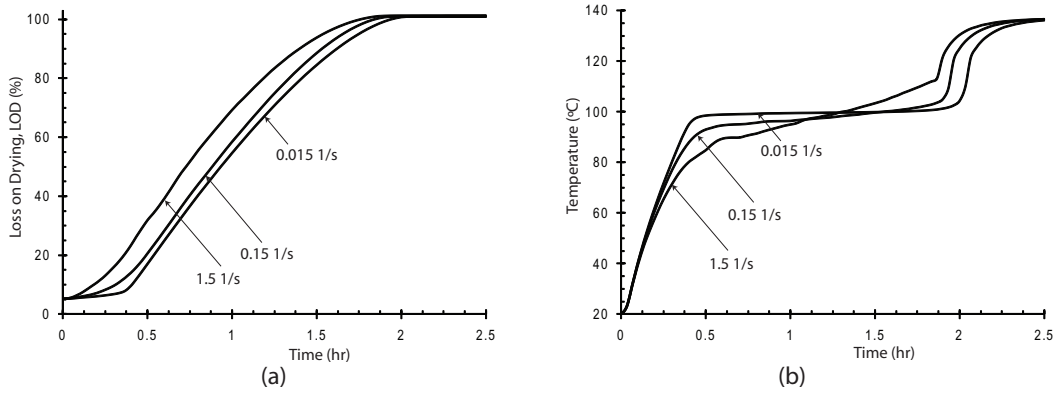

Figure 4.13: Effect of evaporation rate constant, K'' on a) overall moisture loss and b) cold-point temperatures for ambient temperature of 137°C

constant makes the vapor pressure closer to the equilibrium, thus increasing the rate of evaporation. Change in rate constant changes the drying rates significantly – the greater the rate constant, the faster the drying. The temperature profiles are also affected by the rate constant (Figure 4.13b) – with higher rate constant leading to lower temperatures in the beginning. Also, since the drying is completed faster, the temperature starts to rise earlier at the end. To summarize the results of the sensitivity analysis, the factors that play a significant role in convective drying of the honeycomb substrate are energy and vapor transport. The resistance for energy transport lies externally (heat transfer coefficient), while for vapor transport it is internal (convection and binary diffusion), with convection playing the dominant role if forced air is introduced. Finally, uncertainty lies in the evaporation rate constant and its value needs to be empirically determined for accurate prediction.

4.7 Conclusion

A multiphase porous media based model for drying of honeycomb substrates has been developed. The model has been validated for high temperature convective air drying at

temperatures 103°C and 137°C by comparing the predicted axial loss on drying profiles and histories, and temperature histories at various locations with the corresponding experimentally observed values. The study shows that the channels of a honeycomb structure provide a path of little resistance to vapor transport, which leads to multiple effects: i) the time-scale of vapor transport becomes much smaller than the time scale of liquid moisture transport, making the latter phenomena insignificant; ii) local equilibrium between liquid water and water vapor breaks down; and iii) the effect of heat transfer on drying rates becomes more pronounced. At ambient temperature of 137°C, time to complete dryness is less than 50% of the corresponding time at ambient temperature of 103°C. This happens because all the heat above 100°C goes in evaporation and not in raising temperature (or pressure). A sensitivity study on the energy and mass transfer parameters indicates that, for this honeycomb substrate, the drying rate can still be enhanced by i) introducing forced air in the channels (i.e., further increasing vapor removal rate) and ii) increasing the heat transfer coefficient (as the resistance to heat transfer is external due to high thermal conductivity of the substrate material).

BIBLIOGRAPHY

[1] Bardhan P. Ceramic honeycomb filters and catalysts. *Current Opinion in Solid State and Materials Science*. 1997;2(5):577-583.

[2] Wight J. Honeycombs. In: Scheffler M, Colombo P, eds. Cellular ceramics: structure, manufacturing, properties and applications. Weinheim: Wiley-VCH; 2005.

[3] Tsotsas E, Mujumdar AS, eds. Modern Drying Technology: Computational tools at different scales. Weinhein: Wiley-VCH; 2007.

[4] Turner I, Mujumdar AS. Mathematical modeling and numerical techniques in drying technology. New York: Marcel Dekker, Inc. ; 1997.

[5] Williams JL. Monolith structures, materials, properties and uses. *Catalysis Today.* 2001;69(1-4):3-9.

[6] Perre P, Turner IW. A dual-scale model for describing drier and porous medium interactions. *AIChE Journal.* 2006;52(9):3109-3117.

[7] Perre P, Remond R. A dual-scale computational model of kiln wood drying including single board and stack level simulation. *Drying Technology.* 2006;24(9):1069-1074.

[8] Perre P, Remond R, Aleon D. Energy saving in industrial wood drying addressed by a multiscale computational model: Board, stack, and kiln. *Drying Technology.* 2007;25(1-3):75-84.

[9] Perre P. Multiscale aspects of heat and mass transfer during drying. *Transport in Porous Media.* Jan 2007;66(1-2):59-76.

[10] Remond R, Perre P. Drying strategies capable of reducing the stress level of a stack of boards as defined by a comprehensive dual scale model. *Maderas-Ciencia Y Tecnologia.* 2008;10(1):3-18.

[11] Constant T, Moyne C, Perre P. Drying with internal heat generation: Theoretical aspects and application to microwave heating. *AIChE Journal.* 1996;42(2):359-368.

[12] Datta AK. Biological and bioenvironmental heat and mass transfer. New York: Marcel Dekker, Inc. ; 2002.

[13] Datta AK. Porous media approaches to studying simultaneous heat and mass transfer in food processes. I: Problem formulations. *Journal of Food Engineering.* 2007;80(1):80-95.

[14] Halder A, Dhall A, Datta AK. Modeling Transport in Porous Media with Phase Change: Applications to Food Processing. *ASME Journal of Heat Transfer* (in press).

[15] Ni H, Datta AK, Torrance KE. Moisture transport in intensive microwave heating of biomaterials: a multiphase porous media model. *International Journal of Heat and Mass Transfer.* 1999;42(8):1501-1512.

[16] Moldrup P, Olesen T, Yoshikawa S, Komatsu T, Rolston DE. Predictive-descriptive models for gas and solute diffusion coefficients in variably saturated porous media coupled to pore-size distribution: I. Gas diffusivity in repacked soil. *Soil Sci*. 2005;170(11):843-853.

CHAPTER 5

TRANSPORT IN DEFORMABLE FOOD MATERIALS: A POROMECHANICS APPROACH

5.1 Abstract

A comprehensive poromechanics-based modeling framework that can be used to model transport and deformation in food materials under a variety of processing conditions and states (rubbery or glassy) has been developed. Simplifications to the model equations have been developed, based on driving forces for deformation (moisture change and gas pressure development) and on the state of food material for transport. The framework is applied to two completely different food processes (contact heating of hamburger patties and drying of potatoes). The modeling framework is implemented using Total Lagrangian mesh for solid momentum balance and Eulerian mesh for transport equations, and validated using experimental data. Transport in liquid phase dominates for both the processes, with hamburger patty shrinking with moisture loss for all moisture contents, while shrinkage in potato stops below a critical moisture content.

Nomenclature

a_w	water activity
c_i	concentration of species i, kg m^{-3}
c_p	specific heat capacity, J kg^{-1}K^{-1}
c	molar density, kmol m^{-3}
C	constant of proportionality in Equation 5.59
D	diameter, m
D_{bin}	effective gas diffusivity, m^{2}s^{-1}
D_b	effective diffusivity due to gradients of b, m^2 s^{-1}
$D_{a,b}$	diffusivity of a due to gradients of b, m^2 s^{-1}
$\mathbf{E}$	Green-Lagrange strain tensor
$\mathbf{F}$	deformation tensor
$\vec{g}$	acceleration due to gravity, kg m^{-3}
h	heat transfer coefficient, W m^{-2} K^{-1}
h_m	mass transfer coefficient of vapor, m s^{-1}
$\dot{I}$	volumetric evaporation rate, kg m^{-3} s^{-1}
$\mathbf{I}$	Identity tensor
J	Jacobian
k_{eff}	effective thermal conductivity, W m^{-2} K^{-1}
k_i	permeability of phase i, m^2
K	bulk modulus, Pa
K_1	defined by equation 5.40
M	moisture content (dry basis)
M_a, M_v	molecular weight of air and vapor
$\vec{N}$	normal vector

$\vec{n_{i,j}}$	mass flux of species i w.r.t. j, kg m^{-2} s^{-1}
p_i	pressure of phase or species i, Pa
$\vec{q}$	heat flux, J m^{-2} s^{-1}
R	universal gas constant, J kmol^{-1} K^{-1}
REV	Representative Elementary Volume
$\mathbf{S}''$	Piola-Kirchoff stress tensor, Pa
S_i	saturation of phase i
t	time, s
T	temperature
$v_{i,j}$	velocity of species i w.r.t. j, m s^{-1}
v_w	molar volume of water, m^3 mol^{-1}
V	volume, m^3
V^*	critical volume at which shrinkage stops, m^3
W	strain energy density, Pa
x_i	mole fraction of species i

Greek Symbols

ϵ	strain tensor, volume fraction
ρ	density, kg m^{-3}
λ	latent heat of vaporization, J kg^{-1}
μ	shear modulus, Pa
μ_i	dynamic viscosity of a phase, i, Pa s
ν	Poisson's ratio
$\boldsymbol{\sigma}$	stress tensor, Pa
$\boldsymbol{\sigma}'$	effective stress tensor, Pa
$\boldsymbol{\sigma}''$	effective stress tensor due to mechanical load only, Pa
ϕ	porosity
Ψ_w	water potential, Pa
ω_v, ω_a	mass fraction of vapor and air in relation to total gas

Subscripts

amb	ambient
a, g, s, v, w	air, gas, solid, vapor, water
c	capillary
eff	effective
el	elastic
eq	equilibrium
f	fluid
G	ground (stationary observer)
i	i^{th} phase
m	mechanical
M	moisture
0	at time $t = 0$
$surf$	surface
$surfd$	drip at the surface
$surfe$	evaporation at the surface
T	temperature

Superscripts

$\bar{\phi}$	Volumetric average of ϕ over an REV

5.2 Introduction

Factors affecting food safety (presence of pathogens, toxins) and food quality (porosity, pore size distribution, texture, color) are functions of the state (temperature, moisture, composition) of the food material and its processing history. Fundamentals-based understanding of physics of food processing can help a long way in predicting the state and the history of a food material and, thus, its safety and quality. The underlying physics of many food processes, such as drying, rehydration (soaking), frying, baking, grilling, puffing, cooking etc., is essentially energy and moisture transport in a deforming porous medium[1]. Although, transport in deformable porous media has been extensively studied for non-food applications (such as geomaterials (soils, rocks, concrete, ceramics), biomaterials (plant and animal tissues), gels, polymers, etc., still the combination of specific characteristics (softness, hygroscopicity and phase transitions) and processing conditions of food materials, result in unique complexities in study of transport and deformation in food materials.

The general mathematical framework of deformation in saturated and unsaturated porous media (also known as poromechanics) was developed by Biot . The theory was later extended to include multiphase transport using theory of mixtures by various studies. An alternate approach is volume-averaging, i.e. begin with conservation equations at the microscale and, then, use averaging or macroscopization to obtain relationships at the macroscale[2]. In both the approaches, the constitutive relationships can be written either empirically or by invoking second law of thermodynamics through entropy inequality (nonequilibrium thermodynamics). Lewis and Schrefler (2002)[3] provide a detailed review of the similarities and dissimilarities, and the pros and cons of these poromechanics theories. Although applied extensively to non-food materials, there are no examples of a comprehensive poromechanics-based approach in food science litera-

ture.

Majority of the existing transport models in food science literature are either curve fits of lumped empirical data[4–8] or, in a slightly improved version, assume purely conductive heat transfer for energy and purely diffusive transport for moisture[9–13], solving a transient conduction (or diffusion) equation using experimentally determined effective conductivity (or diffusivity). One notable exception to lumped analysis is the application of Stefan's moving boundary approach to track liquid-vapor interface during internal vaporization[14–16]. In this type of modeling, the liquid-vapor interface, where all the vaporization occurs, separates completely saturated and completely dry region of a food material. Some examples of detailed description of transport mechanisms based on a porous media approach are— inclusion of vaporization generated pressure-driven flow during intensive heating processes by Datta and coworkers[17,18]; nonequilibrium thermodynamics based Hybrid Mixture Theory approach towards Case-II diffusion by Singh [19] and Achanta[20]; and, more recently, application of Flory-Rehner theory to predict swelling-pressure driven moisture transport in meat by van der Sman (2007)[21].

Fundamentals-based description of deformation in food materials is even less frequent than the detailed description of transport itself. Two different approaches are generally followed; either the experimental shrinkage data is empirically fitted as a function of moisture content, or the additivity of volumes of different components is used to predict deformation from moisture loss data[22,23]. Modeling of transport in deformable food materials as a solid mechanics problem and solving the linear momentum balance for the solid matrix is rare in food, although this approach is frequently used to study drying of some other materials such as wood and ceramics. Notable exceptions are study of bread baking[24] and microwave puffing of potatoes[25]. For detailed review of drying models including shrinkage effects including pioneering works by Perre[26], Kowalski

[27]and others, the reader is referred to the review by Katekawa and Silva (2006)[23].

With this background, the current study is an attempt to develop a poromechanics-based modeling framework for the coupled physics of transport and large deformation in food materials. The macroscale governing equations are based on extended Biot's theory of poromechanics[3]. Phenomenological constitutive laws are used in both transport and deformation equations.

5.3 Mathematical Model

A mathematical model is developed that describes deformation and transport (energy and moisture) inside a food material during thermal processing. First, the physics of deformation of the solid matrix is described and, then, special cases, depending on the driving mechanism causing deformation, are discussed. Later, transport modeling in a deforming food material and special cases are described.

5.3.1 Assumptions

1) Food is treated as a multiphase porous material, in which all the phases are in continuum 2) Local thermal equilibrium is assumed, i.e. temperature is shared by all the phases. Also, pressure in the liquid water phase is given as the gas pressure minus the capillary pressure (or the water potential). 3) The solid skeleton is an incompressible hyperelastic material. Solid volume remains constant during any process.

5.3.2 Deformation of the Solid Matrix: Model Development for a General Case

Macroscopic total stress tensor, $\bar{\boldsymbol{\sigma}}$, at any given location in a food material can be defined as volumetric average of total stress tensor, $\boldsymbol{\sigma}$, in the representative elementary volume (REV) around the location[3]:

$$\bar{\boldsymbol{\sigma}} = \frac{1}{V}\int_V \boldsymbol{\sigma}\, dV \tag{5.1}$$

Now, total volume of an REV can be written as a sum of volumes of the solid and the fluids present in the pores:

$$V = V_s + \sum_i V_i \tag{5.2}$$

Therefore, the total stress tensor can also be written as sum of averages in the individual phase volumes:

$$\begin{aligned}
\bar{\boldsymbol{\sigma}} &= \frac{1}{V}\left(\int_{V_s} \boldsymbol{\sigma}\, dV + \sum_i \left(\int_{V_i} \boldsymbol{\sigma}\, dV\right)\right) \\
&= \frac{V_s}{V}\left(\frac{1}{V_s}\int_{V_s} \boldsymbol{\sigma}\, dV\right) + \sum_i \frac{V_i}{V}\left(\frac{1}{V_i}\int_{V_i} \boldsymbol{\sigma}\, dV\right) \\
&= \epsilon_s \bar{\boldsymbol{\sigma}}_s + \sum_i (\epsilon_i \bar{\boldsymbol{\sigma}}_i)
\end{aligned} \tag{5.3}$$

where ϵ_i and $\bar{\boldsymbol{\sigma}}_i$ are, respectively, the volume fraction and the volume-averaged stress of a phase, i. Given that shear stress is negligible in fluids, stress in a fluid, $\bar{\boldsymbol{\sigma}}_{\boldsymbol{i}}$ can be approximated as

$$\bar{\boldsymbol{\sigma}}_i = -p_i \mathbf{I} \tag{5.4}$$

Substituting fluid stresses from Equation 5.4 in Equation 5.3, we obtain

$$\begin{aligned}
\bar{\boldsymbol{\sigma}} &= \epsilon_s \bar{\boldsymbol{\sigma}}_s - \sum_i (\epsilon_i p_i)\, \mathbf{I} \\
&= (1-\phi)\, \bar{\boldsymbol{\sigma}}_s - \phi \sum_i (S_i p_i)\, \mathbf{I} \\
&= (1-\phi)\left(\bar{\boldsymbol{\sigma}}_s + \sum_i (S_i p_i)\, \mathbf{I}\right) - \sum_i (S_i p_i)\, \mathbf{I}
\end{aligned} \tag{5.5}$$

Defining the first term in Equation 5.5 as the effective stress on the solid skeleton, $\bar{\boldsymbol{\sigma}}'$, and the second term as pore pressure, $p_f \left(= S_g p_g + S_w p_w\right)$, the well-known effective stress principle of Terzaghi is recovered:

$$\bar{\boldsymbol{\sigma}} = \bar{\boldsymbol{\sigma}}' - p_f \mathbf{I} \tag{5.6}$$

Now, by invoking the quasi-steady state assumption for deformation (acceleration term equal to zero), the solid momentum balance leads to divergence-free field of overall stress, which implies divergence of effective stress is equal to gradient of pore pressure:

$$\nabla.\bar{\boldsymbol{\sigma}} = 0 \;\Rightarrow\; \nabla.\bar{\boldsymbol{\sigma}}' \;=\; \nabla p_f \tag{5.7}$$

In case of two-phase flow, when the pores are occupied by liquid water and gas (comprising of air and water vapor), the pore pressure, p_f, can also be written as, $p_g - S_w p_c$. Inserting this relationship in the solid momentum balance, we obtain:

$$\nabla.\bar{\boldsymbol{\sigma}}' = \nabla p_g - \nabla\left(S_w p_c\right) \tag{5.8}$$

where the first term on the RHS is the gas pressure gradient, and the second term is a function of the temperature and moisture content of the food material. Gas pressure gradients are finite either for processes involving intensive internal vaporization such as microwave heating[28] or processes involving gas generation reactions such as carbon dioxide in bread baking[24]. For most other processes, such as drying and rehydration (soaking), gas is at atmospheric pressure and, thus, the solid momentum balance reduces to

$$\nabla.\bar{\boldsymbol{\sigma}}' = \nabla p_w = -\nabla\left(S_w p_c\right) \tag{5.9}$$

In equation 5.9, capillary pressure, p_c has a physical meaning only when capillary suction is the only attractive force between the solid surface and the liquid water. In the presence of other attractive forces like monolayer surface adsorption, multilayer absorption etc., water potential, Ψ_w, is a more appropriate term. Kelvin's law is usually

applied to relate water potential, Ψ_w (expressed in units of pressure) to water activity, a_w

$$\Psi_w = \frac{RT}{v_w} ln(a_w) \tag{5.10}$$

After replacing p_c by $-\Psi_w$, equation 5.9 can be used for liquid water in the presence of multiple attractive forces. On the other hand, some high moisture food materials (with water activity, $a_w \approx 1$), which undergo a change in their capacity to hold water with temperature rise, require a different approach for estimation of pressure in liquid water. van der Sman (2007)[21] applied Flory-Rehner theory to estimate swelling pressure (equal to pore pressure in the absence of gas phase) for such materials (more in Section 5.4.1).

5.3.3 Deformation of the Solid Matrix: Special Cases

Usual factors that lead to deformation in food materials are moisture change (examples include drying and rehydration) and internal pressure generation (puffing and bread baking). Between the two, deformation due to moisture change is a complex phenomena and is highly dependent on the state of the food material. The physics of deformation due to gas transport is relatively easy as the effect of gas pressure can be easily expressed as a source term in the solid momentum balance (more later).

Processes with Moisture Change as the Driving Mechanism

Most wet food materials are initially in a soft rubbery state. For such materials, it is usually observed that total volume change at equilibrium is equal to volume of moisture lost or gained[20]. In other words, as long as the material is in rubbery state and drying rate is not too high to cause surface cracks, the solid matrix remains saturated and the gas phase does not enter the pores. In such a case, the pore pressure is simply the pressure

of liquid water, and Equation 5.7 can be written as:

$$\nabla.\bar{\boldsymbol{\sigma}}' = \nabla p_w \tag{5.11}$$

In a series of papers, moisture transport has been investigated in detail by Scherer[29,30] for soft and deforming polymer gels, which behave in a similar fashion. Scherer argued that for a uniform pore size medium with inert liquids in its pores, effective stress at equilibrium (or during a slow drying process) is equal to pore pressure:

$$\bar{\boldsymbol{\sigma}}' = p_w \tag{5.12}$$

As a soft material dries out, two important phenomena happen, the pores shrink and the bulk modulus of the material increases (turning a soft, rubbery food into a rigid, glassy state). For uniform moisture distribution, the volume change is equal to the volume of water lost. The material will stop shrinking when the liquid-vapor meniscus moves inside the matrix and, with the increased bulk modulus, the solid stresses can balance the compressive capillary pressure, p_c^*. Until that point, the solid skeleton is too soft to allow the meniscus to move inside and create compressive pressure. Assuming the solid skeleton to be elastic, the normal effective stress (shear stress will be zero at equilibrium as there are no pressure gradient or external shear load) can be related to volume change:

$$d\bar{\boldsymbol{\sigma}}' = K dV/V \tag{5.13}$$

Inserting the stress-strain relation from Equation 5.13 into differential form of Equation 5.12 and integrating from initial stress-free volume, V_0 to final volume at which shrinkage stops, V^*, we obtain:

$$\int_{V_0}^{V^*} \frac{K}{V} dV = -p_c^* \tag{5.14}$$

For a simple material with uniform pore size and a known bulk modulus-moisture content relationship (hardening of the material with moisture loss), an explicit value for

critical volume, V^* can be established from Equation 5.14. However, due to highly heterogeneous and hygroscopic nature of food material, we can only say that since K and p_c are functions of moisture content, M and temperature, T, critical volume, V^*, will also be a function of temperature and moisture at equilibrium.

$$V^* = V^*(M, T) \tag{5.15}$$

Also, for a general food material with range of pore sizes, the capillaries will empty at different values of shrinkage. Thus, in food materials, we may observe a gradual decrease (rather than a sharp change which is expected for uniform pore size material) in the slope of volume vs. moisture content plot to zero, as shown in Figure 5.1 (dotted line instead of the solid line). Fortunately, volume vs. moisture content data is available for many food materials. This allows us to treat volume change due to moisture loss as a free strain analogous to thermal expansion.

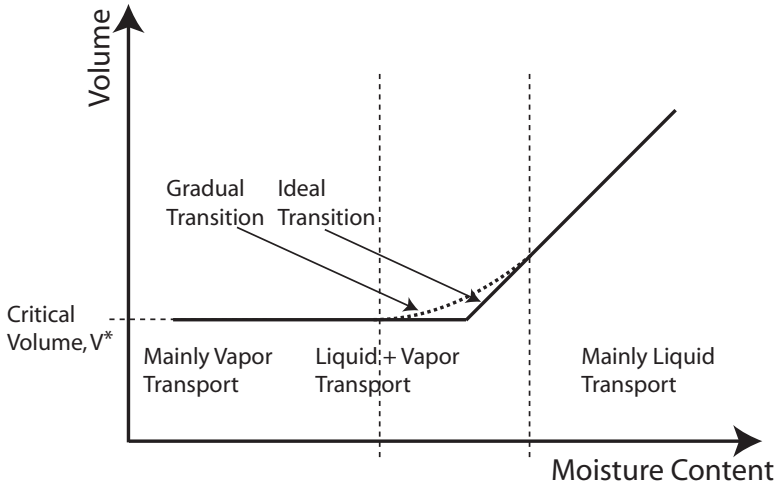

Figure 5.1: Volume change versus moisture content curve for a typical food material

Small Deformation

For small deformation, volume changes due to temperature and moisture change, i.e., the moisture and thermal strains ($\boldsymbol{\varepsilon}_M$ and $\boldsymbol{\varepsilon}_T$, respectively) are subtracted from the total

strain to get the mechanical strain, $\boldsymbol{\varepsilon}_m$:

$$\boldsymbol{\varepsilon}_m = \boldsymbol{\varepsilon} - \boldsymbol{\varepsilon}_M - \boldsymbol{\varepsilon}_T \tag{5.16}$$

Now, with the effect of liquid (moisture) pressure accounted for as a free strain, the mechanical strain, $\boldsymbol{\varepsilon}_m$ can be related to the stress due to mechanical load only, $\bar{\boldsymbol{\sigma}}''$, i.e the effective stress, $\bar{\boldsymbol{\sigma}}'$ minus the pressure of water, p_w:

$$\left(\bar{\boldsymbol{\sigma}}' - p_w\right) = \bar{\boldsymbol{\sigma}}'' = \mathbf{D}.\boldsymbol{\varepsilon}_m \tag{5.17}$$

The solid momentum balance, Equation 5.11 can also be written in terms of $\bar{\boldsymbol{\sigma}}''$

$$\nabla.\bar{\boldsymbol{\sigma}}'' = 0 \tag{5.18}$$

Depending on the time scales of the process and deformation, the food material can be treated as elastic or viscoelastic and the corresponding stress-strain relationship can be used along with the solid momentum equation.

Large Deformation

For large deformation analysis, a multiplicative split[31] in deformation gradient tensor, $\mathbf{F}$, can be used to separate volume changes due to moisture and temperature changes from volume change due to mechanical effects. As shown in Figure 5.2, the material is first assumed to under go stress-free deformations due to moisture and temperature changes and, then, mechanical stresses act on this stress-free deformed material. The deformation tensor, $\mathbf{F}$, can be split as:

$$\mathbf{F} = \mathbf{F}_\mathrm{T}\mathbf{F}_\mathrm{M}\mathbf{F}_\mathrm{el} \tag{5.19}$$

The dilatation (volume-changing) stress is related to elastic jacobian, $J_{el} = det(\mathbf{F}_\mathrm{el})$, which is obtained as the ratio of total volume change and volume change due to moisture and temperature effects (details in Section 5.4.1). Thermal jacobian, $J_T = det(\mathbf{F}_\mathrm{T})$ is often small for food materials and is usually ignored. Moisture jacobian, $\mathbf{F}_\mathrm{M}$ can easily be obtained from volume change vs. moisture content relationship (Figure 5.1).

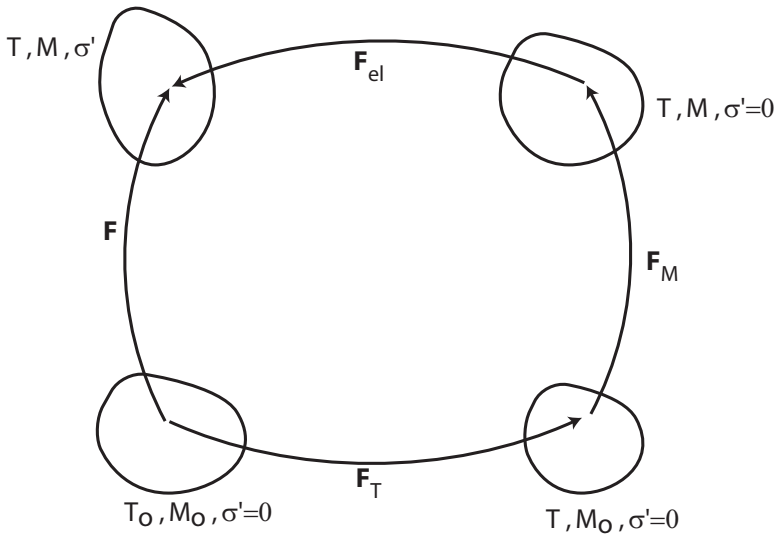

Figure 5.2: Steps indicating multiplicative split in the deformation tensor, separating moisture, temperature and mechanical effects

Processes with Gas Pressure as the Driving Mechanism

For some processes such as microwave heating or bread-baking, large internal pressure generation (due to water vapor in microwave heating and carbon dioxide in baking) can cause swelling/puffing of the material. In such cases, the gas pressure gradient term of Equation 5.8 (first term on RHS) may dominate. Swelling due to gas pressure in such cases can be much larger than shrinkage due to moisture loss, and, therefore, stresses and strains due to the latter can be ignored. In the absence of thermal strains, the total strain is approximately equal to the mechanical strain:

$$\boldsymbol{\varepsilon}_m \approx \boldsymbol{\varepsilon} \tag{5.20}$$

Also, as the stress due to moisture transport is neglected, the solid momentum balance 5.8 becomes

$$\nabla.\bar{\boldsymbol{\sigma}}' = \nabla p_g \tag{5.21}$$

with effective stress, $\bar{\boldsymbol{\sigma}}'$ related to strain, $\boldsymbol{\varepsilon}$.

Of course, if deformation due to both phenomena (moisture change and gas pressure) need to be accounted for, the governing equation and the constitutive law will take the form:

$$\nabla.\bar{\boldsymbol{\sigma}}'' = \nabla p_g, \bar{\boldsymbol{\sigma}}'' = \mathbf{D}.\boldsymbol{\varepsilon}_m \tag{5.22}$$

5.3.4 Heat and Moisture Transport: Model Development for a General Case

Transport modeling for food processes using the multiphase porous media approach has been reviewed elsewhere[1]. In this section, only equations relevant to deformable materials are summarized and the reader should refer to Datta (2007)[1] for details for rigid materials.

Governing Equations

The governing equations for non-isothermal transport of two-phases (liquid water and gas) in an unsaturated porous medium comprise of energy conservation and mass conservation of gas phase, water vapor and liquid water phase, respectively :

$$\left(\rho_{eff} c_{p,eff}\right) \frac{\partial T}{\partial t} + \sum \left(\vec{n}_{i,G}.\nabla \left(c_{p,i} T\right)\right) = \nabla.\left(k_{eff} \nabla T\right) - \lambda \dot{I} \tag{5.23}$$

$$\frac{\partial c_g}{\partial t} + \nabla.\left(\vec{n}_{g,G}\right) = \dot{I} \tag{5.24}$$

$$\frac{\partial \left(c_g \omega_v\right)}{\partial t} + \nabla.\left(\vec{n}_{v,G}\right) = \dot{I} \tag{5.25}$$

$$\frac{\partial c_w}{\partial t} + \nabla.\left(\vec{n}_{w,G}\right) = -\dot{I} \tag{5.26}$$

The energy equation is used to solve for temperature and the mass conservation equations for their respective concentrations. The gas concentration, c_g, is related to pressure by invoking the ideal gas law. Note that not all four equations are needed for all processes (Figure 5.3). Just as the energy equation is needed only for non-isothermal processes; the gas phase equation is solved only in case of significant internal pressure generation, when pressure driven flow and/or deformation due to gas pressure gradients becomes important. Also, the vapor equation is rarely required as vapor can be assumed to be at equilibrium with the liquid moisture (more later). In a deforming medium, since

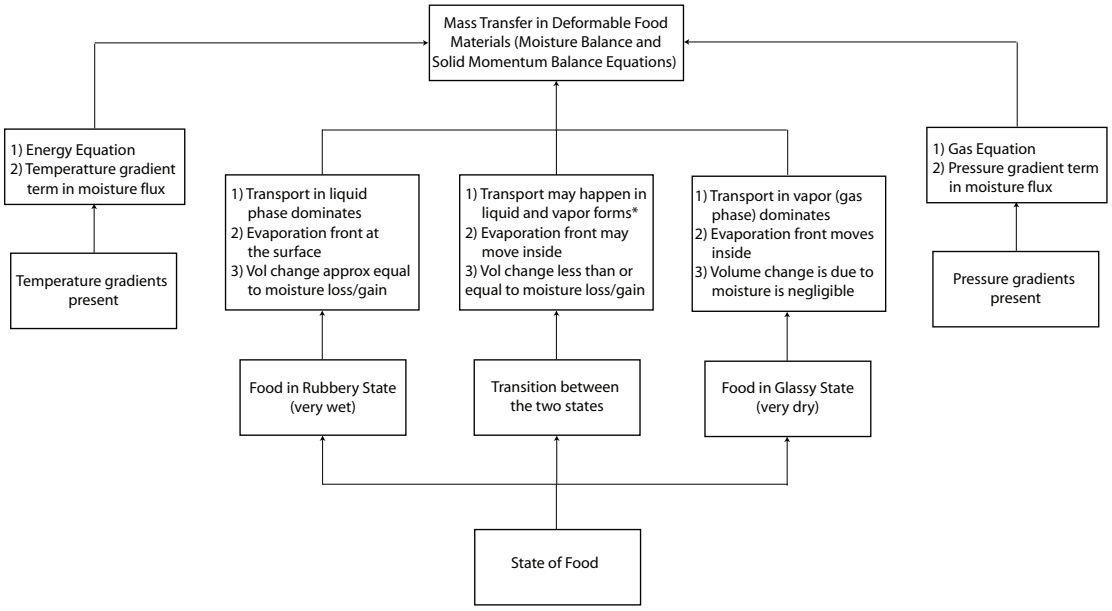

Figure 5.3: A framework for modeling of transport and deformation in food materials based on the state of the material and its processing conditions

the solid has a finite velocity, $\vec{v}_{s,G}$, the mass flux of a species, i with respect to stationary observer, $\vec{n}_{i,G}$ (used in Equations 5.23-5.26) can be written as sum of flux w.r.t. solid and flux due to movement of solid:

$$\vec{n}_{i,G} = \vec{n}_{i,s} + c_i \vec{v}_{s,G} \tag{5.27}$$

Mass Fluxes

Mass fluxes in an unsaturated porous medium can be attributed to two primary mechanisms– convection (for both gases and liquids) and binary diffusion (between vapor and air). Reynolds number is very low (usually less than 1) for transport in food materials and, therefore, Darcy's law is applied to determine convective fluxes. For binary diffusion between vapor and air in the gas phase, Fick's law is used:

$$\vec{n}_{g,s} = -\rho_g \frac{k_g}{\mu_g} \left(\nabla p_g - \rho_g \vec{g} \right) \tag{5.28}$$

$$\vec{n}_{v,s} = -\rho_v \frac{k_g}{\mu_g} \left(\nabla p_g - \rho_g \vec{g} \right) - \left(\frac{c^2}{\rho_g} \right) M_v M_a D_{bin} \nabla x_v \tag{5.29}$$

$$\begin{aligned} \vec{n}_{w,s} &= -\rho_w \frac{k_w}{\mu_w} \left(\nabla p_w - \rho_w \vec{g} \right) \\ &= -\rho_w \frac{k_w}{\mu_w} \left(\nabla \left(p_g - p_c(M,T) \right) - \rho_w \vec{g} \right) \\ &= -\rho_w \frac{k_w}{\mu_w} \left(\nabla \left(p_g - \frac{\partial p_c}{\partial M} \nabla M - \frac{\partial p_c}{\partial T} \nabla T \right) - \rho_w \vec{g} \right) \end{aligned} \tag{5.30}$$

Dry basis moisture content, M, is defined as

$$M = \frac{c_w}{c_s} = \frac{c_w}{(1-\phi)\,\rho_s} \tag{5.31}$$

Taking density of solid, ρ_s as constant, moisture content, M can be expressed as $M = M(c_w, \phi)$ (where $c_w = \rho_w \epsilon_w$) and equation 5.30 can be re-written as

$$\begin{aligned} \vec{n}_{w,s} &= -\rho_w \frac{k_w}{\mu_w} \left(\nabla \left(p_g - \frac{\partial p_c}{\partial M} \frac{\partial M}{\partial c_w} \nabla c_w - \frac{\partial p_c}{\partial M} \frac{\partial M}{\partial \phi} \nabla \phi - \frac{\partial p_c}{\partial T} \nabla T \right) - \rho_w \vec{g} \right) \\ &= -\rho_w \frac{k_w}{\mu_w} \left(\nabla p_g - \rho_w \vec{g} \right) - D_{w,c_w} \nabla c_w - D_{w,\phi} \nabla \phi - D_{w,T} \nabla T \end{aligned} \tag{5.32}$$

where diffusivity due to moisture gradient, D_{w,c_w}, diffusivity due to porosity gradient, $D_{w,\phi}$ and diffusivity due to temperature gradient, $D_{w,T}$ are defined as:

$$\begin{aligned} D_{w,c_w} &= -\rho_w \frac{k_w}{\mu_w} \frac{\partial p_c}{\partial M} \frac{\partial M}{\partial c_w} \\ D_{w,\phi} &= -\rho_w \frac{k_w}{\mu_w} \frac{\partial p_c}{\partial M} \frac{\partial M}{\partial \phi} \end{aligned}$$

$$D_{w,T} = -\rho_w \frac{k_w}{\mu_w} \frac{\partial p_c}{\partial T} \tag{5.33}$$

Equations 5.23-5.26, alongwith fluxes from equations 5.28, 5.29 and 5.32, solid velocity, $\vec{v}_{s,G}$ from solid momentum balance and an explicit expression for evaporation rate, $\dot{I}$ complete the model development. Estimation of evaporation rate, however, is not always easy[32] and an accurate determination of $\dot{I}$ is possible only in some special situations, e.g. when local equilibrium between liquid water and vapor can be assumed. Details of estimation of $\dot{I}$ are mentioned elsewhere[32].

Addition of Liquid Water and Vapor Equations

If water vapor can be assumed to be in equilibrium with liquid water (i.e. time-scale required to achieve equilibrium is smaller than other relevant time scales for the process), vapor pressure becomes a function of moisture and temperature (through Clausius-Clapeyron equation and moisture sorption isotherms) and its conservation equation need not be solved. In such cases, vapor flux (ignoring gravity) can be written as

$$\begin{aligned}
\vec{n}_{v,s} &= -\rho_v \frac{k_g}{\mu_g} \nabla p_g - \left(\frac{c^2}{\rho_g}\right) M_v M_a D_{bin} \nabla \left(p_v \left(M\left(c_w, \phi\right), T\right) / p_g\right) \\
&= -\left(\rho_v \frac{k_g}{\mu_g} + \left(\frac{c^2}{\rho_g}\right) M_v M_a D_{bin} \frac{p_v}{{p_g}^2}\right) \nabla p_g - D_{v,c_w} \nabla c_w \\
&\quad -D_{v,\phi} \nabla \phi - D_{v,T} \nabla T
\end{aligned} \tag{5.34}$$

where vapor diffusivity due to moisture gradient, D_{v,c_w}, vapor diffusivity due to porosity gradient, $D_{v,\phi}$, and diffusivity due to temperature gradient, $D_{v,T}$, are defined as:

$$\begin{aligned}
D_{v,c_w} &= -\left(\frac{c^2}{\rho_g}\right) M_v M_a \frac{D_{bin}}{p_g} \frac{\partial p_v}{\partial M} \frac{\partial M}{\partial c_w} \\
D_{v,\phi} &= -\left(\frac{c^2}{\rho_g}\right) M_v M_a \frac{D_{bin}}{p_g} \frac{\partial p_v}{\partial M} \frac{\partial M}{\partial \phi} \\
D_{v,T} &= -\left(\frac{c^2}{\rho_g}\right) M_v M_a \frac{D_{bin}}{p_g} \frac{\partial p_v}{\partial T}
\end{aligned} \tag{5.35}$$

Now, adding liquid water and water vapor conservation equations to eliminate evaporation rate, $\dot{I}$ and inserting flux relationships, we obtain the equation for overall moisture balance

$$\frac{\partial}{\partial t}(c_w) + \nabla.\left(c_w \vec{v}_{s,G}\right) = \nabla.\left(K_1 \nabla p_g + D_{c_w} \nabla c_w + D_\phi \nabla \phi + D_T \nabla T\right) \tag{5.36}$$

where

$$K_1 = -\rho_w \frac{k_w}{\mu_w} - \rho_v \frac{k_g}{\mu_g} - \left(\frac{c^2}{\rho_g}\right) M_v M_a D_{bin} \frac{p_v}{{p_g}^2} \tag{5.37}$$

$$D_{c_w} = D_{w,c_w} + D_{v,c_w} \tag{5.38}$$

$$D_\phi = D_{w,\phi} + D_{v,\phi} \tag{5.39}$$

$$D_T = D_{w,T} + D_{v,T} \tag{5.40}$$

are the effective permeability and the effective diffusivities due to moisture concentration gradient, porosity gradient and temperature gradient, respectively. In equation 5.36, it is assumed that water vapor can contribute to transport terms but not to accumulation term (this is because density of vapor is 3 orders of magnitude smaller than density of liquid water.)

For a majority of food processes, moisture fluxes due to temperature, porosity and pressure gradients is considered small as compared to that for moisture gradients (sometimes, without justification). The conditions under which these assumptions can be justified are

- Gas pressure is atmospheric ($\nabla p_g = 0$),
- The material is either saturated ($\phi \approx c_w/\rho_w$ and the porosity gradient term can be merged with moisture gradient term) or the material is rigid ($\nabla \phi = 0$), and,
- Water activity (in turn, capillary pressure, p_c) is independent of temperature gradient ($D_T = 0$)

In such cases, the overall moisture balance reduces to the well-known equation:

$$\frac{\partial c_w}{\partial t} + \nabla.\left(c_w \vec{v}_{s,G}\right) = \nabla.\left(D_{c_w} \nabla c_w\right) \tag{5.41}$$

After ignoring the flux due to solid velocity (again, usually done without justification), equation 5.41 is extensively used in the food literature to model drying-like processes. Its great advantage lies in the fact that rate of evaporation, $\dot{I}$ is not required. Also, effective diffusivity, D_{c_w} can be easily estimated by fitting experimentally observed drying curves. However, the rate of evaporation may be required to solve equation 5.23 and equation 5.24 (if pressure gradients are significant).

5.3.5 Heat and Moisture Transport: Special Cases

As discussed in case of deformation, transport models can also be simplified. Energy and gas phase equations are only required when temperature and pressure gradients, respectively, are significant. In the following sections, simplifications based on the state of a food material, as illustrated in Figure 5.3, are discussed. Two extreme states of a food material are 1) wet, rubbery state (above glass-transition temperature); and 2) almost-dry, glassy state (below glass-transition temperature). In the intermediate region, near glass transition, Moisture transport may exhibit non-Fickian behavior (Case-II diffusion). Traditional form of Darcy's law (which assumes that the flux is proportional to pressure gradients) breaks down for such regions and needs to be modified. Various approaches have been explored (especially in the polymer science literature) to account for non-Fickian or Case II diffusion. The most fundamental of these approaches is developed by Cushman and coworkers[19,20] to derive modified constitutive equations such as Darcy's law, Fick's law, and solid stress-strain relationship based on nonequilibrium thermodynamics. The approach Cushman and coworkers followed, known as Hybrid

Mixture Theory, is described in detail elsewhere[33], and not discussed further in this manuscript. We now discuss simplifications in governing equations of transport based on the state (rubbery or glassy) of a food material.

5.3.5.1 Wet-Rubbery State: Liquid Moisture Transport as the Dominating Mechanism

In the rubbery state, free shrinkage/swelling compensates for moisture loss/gain – which means, at equilibrium, change in volume of a food material is equal to the volume of water lost/gained (Section 5.3.3). During rehydration/dehydration of such materials, the evaporation front stays at the surface of the material and there is no vapor generation or transport within the food. So, the evaporation rate, $\dot{I}$ is equal to 0, permeability in equation 5.36 is just liquid permeability, and the effective diffusivities reduce to just those of liquid moisture. Therefore, the model reduces to equation 5.36 for moisture and equation 5.42 for temperature, with solid velocity, $\vec{n}_{v,G}$, from the solid momentum balance.

$$\left(\rho_{eff} c_{p,eff}\right) \frac{\partial T}{\partial t} + \left(\vec{n}_{w,G}.\nabla \left(c_{p,w} T\right)\right) = \nabla.\left(k_{eff} \nabla T\right) \tag{5.42}$$

For soft materials, shear modulus is very small as compared to the bulk modulus, which means shear stresses (for an unconstrained material) that restrict free swelling/shrinkage are also small, and volume change at every point in the material can be approximated by the free volume change, even under large moisture gradients. Thus, if the only deformation information required is volume change at every point and estimation of stresses and shear strains is not important, solid momentum balance can be skipped. Divergence in solid velocity can be estimated from the solid mass balance (assuming constant and uniform solid density):

$$\frac{\partial \left(\rho_s \epsilon_s\right)}{\partial t} + \nabla.\left(\rho_s \epsilon_s v_{s,G}\right) \quad = \quad 0 \tag{5.43}$$

$$\frac{D^s \epsilon_s}{Dt} + \epsilon_s \nabla . v_{s,G} = 0 \tag{5.44}$$

$$\nabla . v_{s,G} = -\frac{1}{\epsilon_s}\frac{D^s \epsilon_s}{Dt} = \frac{1}{1-\epsilon_w}\frac{D^s \epsilon_w}{Dt} \tag{5.45}$$

where $\frac{D^s}{Dt}$ stands for material derivative in the reference frame of the solid. Divergence of solid velocity, $v_{s,G}$ from equation 5.45 can now be inserted in liquid water equation (which is then solved in the reference frame of the solid for constant and uniform density of water):

$$\frac{D^s \epsilon_w}{Dt} + \epsilon_w \nabla . v_{s,G} + \nabla . (\epsilon_w v_{w,s}) = 0 \tag{5.46}$$

5.3.5.2 Almost-dry, Glassy State: Vapor Transport as the Dominating Mechanism

Food at very low moisture content exists in a rigid-glassy state. As discussed earlier in deformation analysis, there is no deformation below a certain moisture content. The material can be assumed to be rigid and deformation analysis is not required. Also, the food material can be highly unsaturated at low moisture contents, which means the permeability of liquid water, k_w can become very low, while the binary diffusivity of vapor and air, D_{bin} can be very high. In such conditions, the transport can be dominated by vapor transport terms, i.e. $D_{w,c_w} << D_{v,c_w}$, $D_{w,T} << D_{v,T}$ and transport in liquid phase can be ignored. From equation 5.26, ignoring transport terms we get:

$$\dot{I} = -\frac{\partial c_w}{\partial t} \tag{5.47}$$

Under such conditions, the model (for processes in which transport due to temperature and pressure gradients is small) reduces to equation 5.41 for moisture and equation 5.48 for temperature:

$$\left(\rho_{eff} c_{p,eff}\right)\frac{\partial T}{\partial t} = \nabla . \left(k_{eff} \nabla T\right) + \lambda \frac{\partial c_w}{\partial t} \tag{5.48}$$

This assumption of neglecting liquid transport terms is, however, justified only when the material is very dry and may happen only for a small range of moisture content such as

during rehydration of dry cereals due to high humidity levels.

5.4 Model Implementation and Validation

In the following section, the modeling framework developed is applied to two food processes – drying of a potato slab and single-sided contact heating of a hamburger patty (Figure 5.4) to predict deformation, mass and energy transport kinetics. Hamburger patty cooking is an example of single phase (liquid water only) transport in a rubbery solid matrix, while potato drying involves development of air porosity and two-phase transport. In each case, the model predictions are validated using experimental results.

5.4.1 Contact Heating of a Hamburger Patty

Meat can be processed and cooked in a variety of ways. For the purpose of this study, single-sided contact heating of hamburger patties (Figure 5.4) bought from a local grocery store (USDA Nutrition Database entry no. 23557[34], 95% lean and 5% fat) is selected. A refrigerated hamburger patty of cylindrical shape (diameter 10 cm and height 1.8 cm), initially stored at 5°C, is heated on a commercial griddle (George Foreman Model No. GR0215G) at a fixed plate temperature of 140°C. As temperature rises, water at the surface of the patty evaporates. Since ground meat is in a rubbery state, the patty shrinks with loss of moisture, and, at equilibrium (in the absence of gradients of any temperature and moisture fields) the shrinkage should be equal to the volume of water lost (Figure 5.1). With further rise in temperature, denaturation of muscle proteins occurs, which leads to decrease in water holding capacity of the meat. Since the surface of meat in contact with the griddle gets heated up quickly, the water holding capacity

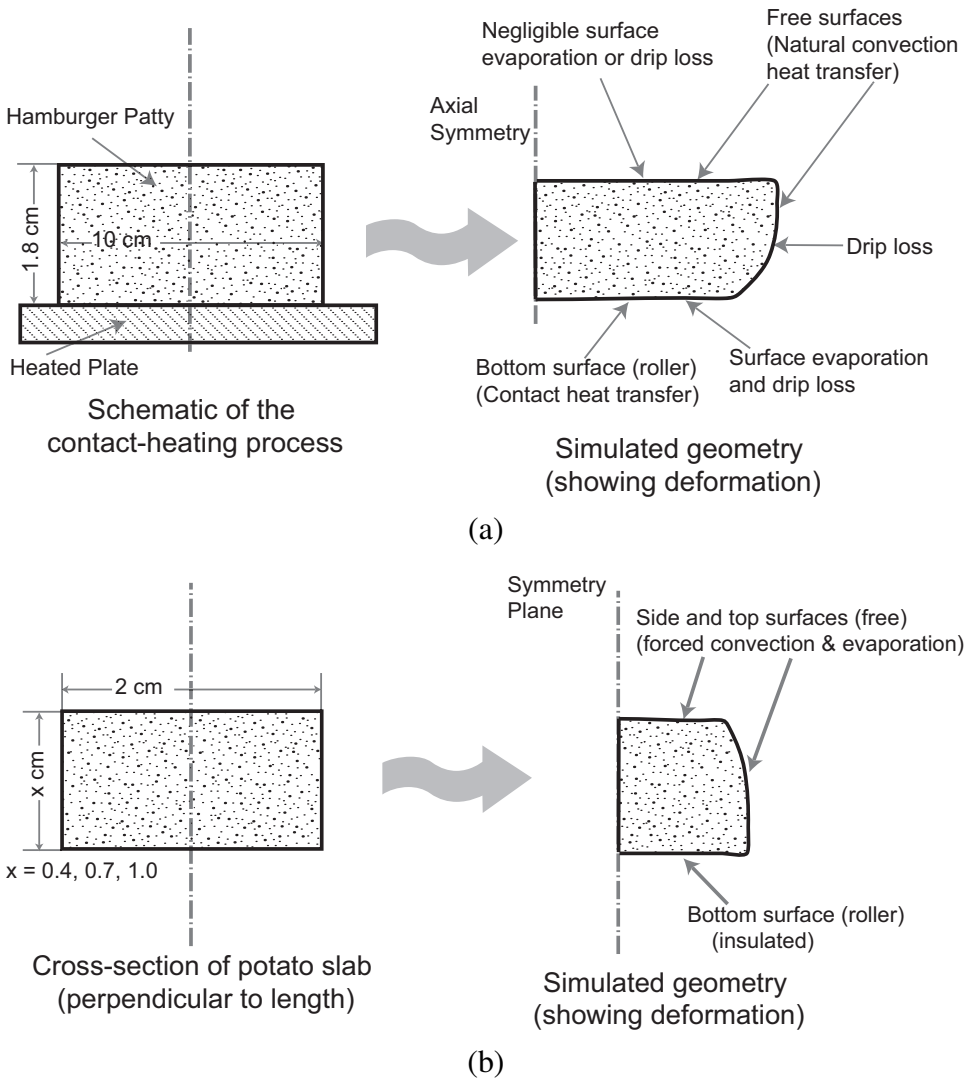

Figure 5.4: Schematic of the two processes simulated– a) single-sided contact heating of hamburger patties, and b) drying of potato slabs, showing the modeled geometry and boundary conditions. Input parameters are listed in Tables 5.1 and 5.2

near the surface may drop faster as compared to the drop in moisture concentration due to evaporation. This leads to dripping of water from the patty. The variables of interest for predicting quality and safety aspects of meat cooking are temperature, moisture content, shrinkage, evaporation rate and their histories.

Problem Details

The patty is simulated as a 2D axisymmetric geometry, as the exchange of heat and mass with the outside environment does not have angular dependence and only a cross-section of the cylindrical patty needs to be simulated. The effect of gravity on mass transfer is ignored as the effect of pressure gradients is much larger on moisture velocity. Since the patty is in a soft and rubbery state, evaporation stays on the surface during the entire cooking process. Even if a rigid glassy region develops at the heated surface, it is assumed to be small and its effect can be neglected. Therefore, according to the modeling framework outlined in Figure 5.3, the rubbery state of food can be selected. Also, as the temperature gradients are significant, the energy equation needs to be solved along with the moisture transport and solid momentum balance equations. Since there is no internal gas pressure generation, vapor and gas equations are not required.

Solid Momentum Balance

A patty can shrink by 30% or more of its initial volume during contact heating process, which necessitates the use of large deformation analysis for solid deformation. Since the evaporation front stays at the surface and there is no internal gas pressure generation, first term in Equation 5.8 can be ignored, and, thus, Equation 5.18 can be used as the solid momentum balance in this case. For large deformation, Lagrangian measures of stress and strain are used, and equation 5.18 is written in Lagrangian coordinates

$$\nabla_X . \left(\mathbf{S}'' . \mathbf{F}_{\text{el}}{}^{\text{T}} \right) = 0 \tag{5.49}$$

where $\mathbf{S}''$ is the second Piola-Kirchhoff (PK2) stress tensor, $\mathbf{F}_{\text{el}}$ is the elastic deformation gradient tensor. PK2 stress, $\mathbf{S}''$ is related to Cauchy stress, $\boldsymbol{\sigma}''$ by the following

relationship

$$\mathbf{S}'' = J.\mathbf{F}_{\mathrm{el}}{}^{-1}.\boldsymbol{\sigma}''.\mathbf{F}_{\mathrm{el}}{}^{-\mathrm{T}} \tag{5.50}$$

PK2 stress is energy conjugate to the Green-Lagrange elastic strain tensor, $\mathbf{E}_{\mathrm{el}}$

$$\mathbf{E}_{\mathrm{el}} = \frac{1}{2}\left(\mathbf{F}_{\mathrm{el}}{}^{\mathrm{T}}\mathbf{F}_{\mathrm{el}} - \mathbf{I}\right) \tag{5.51}$$

and, thus, $\mathbf{S}''$ and, $\mathbf{E}_{\mathrm{el}}$ are related as follows:

$$\mathbf{S}'' = \frac{\partial W_{el}}{\partial \mathbf{E}_{\mathrm{el}}} \tag{5.52}$$

Now, we need a constitutive equation for the elastic strain energy density, W_{el}. Rubbery state means the stress relaxation time scales are expected to be small (as compared to the time scale of the cooking process which is in minutes, Deborah number ~ 0) and the solid skeleton can be can be treated as a hyperelastic material. Also, the fibers in ground meat are randomly oriented. Therefore, although meat fibers are anisotropic with different properties along and across the fibers, the averaged mechanical properties are isotropic. A modified Neo-Hookean constitutive model is chosen which accounts for the volume change due to moisture loss also:

$$W_{el} = \frac{K}{2}\left(J_{el} - 1\right)^2 - \frac{\mu}{2}\left(\bar{I}_1 - 3\right) \tag{5.53}$$

where K and μ are the Bulk Modulus and the Shear Modulus, respectively. J_{el} is the elastic Jacobian as defined earlier, and $\bar{I}$ is the first invariant of the right-Cauchy Green tensor, $\bar{\mathbf{C}}\left(= \bar{\mathbf{F}_{\mathrm{el}}}^{\mathrm{T}}\bar{\mathbf{F}_{\mathrm{el}}}\right)$ for deviatoric part of elastic deformation gradient, i.e., $\bar{\mathbf{F}_{\mathrm{el}}}$. Deviatoric part of elastic deformation gradient is related to elastic deformation gradient, $\mathbf{F}_{\mathrm{el}}$, and its dilatation part, $J_{el}^{1/3}$, as

$$\mathbf{F}_{\mathrm{el}} = J_{el}^{1/3}\bar{\mathbf{F}_{\mathrm{el}}} \tag{5.54}$$

Now, to estimate elastic Jacobian, J_{el}, we need to calculate Jacobian due to moisture change, J_M (Equation 5.19). This is easy, as under stress-free conditions, patty

shrinks/swells by the amount of moisture lost/gained. Let V be the REV volume at moisture volume fraction, ϵ_w. Then, change in volume of REV can be equated to change in volume of moisture in REV:

$$V - V_0 = \epsilon_w V - \epsilon_{w,0} V_0 \tag{5.55}$$

$$J_M = \frac{V}{V_0} = \frac{1 - \epsilon_{w,0}}{1 - \epsilon_w} \tag{5.56}$$

Similarly, porosity at any time t, $\phi(t)$ can be determined using incompressibility of the solid skeleton, equating the initial volume of solid in an REV to solid volume at time, t:

$$(1 - \phi(t))\, V(t) = (1 - \phi_0)\, V_0 \tag{5.57}$$

$$\phi(t) = 1 - \frac{1 - \phi_0}{V(t)/V_0} = 1 - \frac{1 - \phi_0}{J(t)} \tag{5.58}$$

Note that while Jacobian due to moisture change, J_M is a state function (depending on the moisture content), porosity, $\phi(t)$ is a process variable, depending on the actual Jacobian, $J(t)$.

Moisture and Energy Transport Equations

Moisture flux in case of meat needs to be treated differently than the discussion in section 5.3. Water activity of meat at room temperature is $\sim$ 1, which gives capillary pressure, p_c or water potential, Ψ_w close to 0 (using Kelvin's law[35]). Thus, equation 5.30 cannot be used to calculate moisture flux. Also, with increase in temperature, meat proteins denaturate leading to a drop in water holding capacity[36]. As time scales of temperature rise in the patty during intensive cooking such as contact-heating being are smaller than time scales of moisture transport, moisture concentration in much of the patty is more than its water holding capacity at equilibrium.

Liquid water pressure (called swelling pressure) in meat has been estimated by using the Flory-Rehner theory[21]. Taking the swelling pressure to be 0 at equilibrium moisture

volume fraction, and linearizing the Flory-Rehner expression near equilibrium, it can be shown that the swelling pressure is proportional to the difference between the actual and equilibrium moisture concentrations:

$$p_w = C\left(c_w - c_{w,eq}(T)\right) \tag{5.59}$$

where $c_{w,eq}$ is the equilibrium moisture concentration at a given temperature and the constant of proportionality, C, though constant here, can be temperature dependent. Inserting this expression of liquid pressure, p_w in Darcy's law (line 1 in equation 5.30), we get (ignoring gravity):

$$\vec{n}_{w,s} = -\left(D_{w,c_w}\nabla c_w + D_{w,T}\nabla T\right) \tag{5.60}$$

where, the new definitions of diffusivities due to moisture gradient and temperature gradient are:

$$\begin{aligned} D_{w,c_w} &= \rho_w \frac{k_w}{\mu_w} C \\ D_{w,T} &= \rho_w \frac{k_w}{\mu_w} C \frac{\partial c_{w,eq}}{\partial T} \end{aligned} \tag{5.61}$$

Thus, the moisture transport equation reduces to Equation 5.62 with new definitions of diffusivity (Equations 5.61):

$$\frac{\partial c_w}{\partial t} + \nabla.\left(c_w \vec{v}_{s,G}\right) = \nabla.\left(D_{w,c_w}\nabla c_w + D_{w,T}\nabla T\right) \tag{5.62}$$

The energy balance equation remains the same as discussed for rubbery materials in section 5.3 (Eq. 5.42).

Boundary and Initial Conditions

Solid Momentum Balance

Normal displacement of the axisymmetric boundary and the bottom surface (lying on

the griddle) is set to zero. The other two boundaries are unconstrained and free to move (Figure 5.4).

Liquid Water Equation

The boundary condition for liquid water equation consists of two flux terms: evaporation and drip. The evaporation flux, $n_{w,s,surfe}$ is simply given by mass transfer coefficient multiplied by the vapor density difference between the surface and the boundary:

$$n_{w,s,surfe} = h_m \left(\rho_{v,surf} - \rho_{v,amb}\right) \tag{5.63}$$

Water is lost from the matrix in liquid form (as drip) only when surface moisture concentration, $c_{w,surf}$ is more than the water holding capacity, $c_{w,eq}$. The drip loss, $n_{w,s,surfd}$ under such conditions is equal to the total moisture flux reaching the surface subtracted by that taken by surface evaporation, $n_{w,s,surfe}$:

$$n_{w,s,surfd} = \vec{n}_{w,s}.\vec{N}_{surf} - h_m \left(\rho_{v,surf} - \rho_{v,amb}\right) \tag{5.64}$$

Therefore, the total moisture flux at the surface w.r.t stationary observer is equal to the sum of drip loss, evaporation loss and flux due to movement of the surface itself:

$$n_{w,G,surf} = n_{w,s,surfe} + n_{w,s,surfd} + c_w \vec{v}_{s,G} \tag{5.65}$$

Energy Equation

For energy equation, forced convection heat transfer boundary condition (5.1) is applied to get the heat flux at the surface, q_{surf}

$$q_{surf} \;=\; h(T_{amb} - T_{surf}) - \lambda n_{w,s,surf} - \sum \left(\vec{n}_{i,G} c_{p,i} T\right).\vec{N}_{surf} \tag{5.66}$$

In equation 5.66, The first term on the RHS is the convective heat transfer coefficient multiplied by the temperature difference, the second term is the latent heat taken up by surface evaporation and the third term is energy carried by convection terms normal to the boundary.

Initial Conditions

Initially refrigerated at 5°C, the composition of the patty is taken from USDA Nutrient Database[34] and is listed in Table 5.1. Since the weight percentages of the proximates add up to 100.74, the weight percentages were normalized. The volume fraction of air in the patties is considered small and, thus, ignored. From this data, the initial concentrations of water and solid (protein, fat and ash) can be calculated.

Input Parameters and Numerical Solution

Input parameters used in the hamburger patty cooking simulation are given in Table 5.1.[1] A commercially available finite element software, COMSOL Multiphysics 3.5a (Comsol Inc, Burlington, MA), was used to solve the equations. The solid momentum balance is solved in the Total Lagrangian reference frame (i.e. frame moving with the solid) for the axisymmetric geometry equation in the Structural Mechanics Module, while convection-conduction and convection-diffusion equations (in the main COMSOL Multiphysics module) were used for energy and moisture transport, respectively. Deformed mesh equations (again, in the main COMSOL Multiphysics module) were used to track the material deformation in the Eulerian reference frame, and move the mesh accordingly. The transport equations were solved in the Eulerian reference frame (i.e. frame of the stationary observer) on the deformed mesh. The computational domain was rectangular, 5 cm $\times$ 1.8 cm and had an unstructured quadrilateral mesh consisting of 3864 elements. Linear shape functions were used. The simulation of 900 seconds of heating took approximately 4 hours of CPU time for an adaptive timestepping scheme (maximum timestep size of 0.05 second) on a 3.00 GHz dual-core Intel Xeon workstation with 16GB RAM. Mesh and timestep convergence were ensured by checking that any dependent variable (temperature, moisture content or displacement) did not change

[1] Details of measured and other input parameters are available in Chapter 6

Table 5.1: Input parameters used in the simulations of single-sided contact heating of hamburger patties. Number under source column refer to bibliographic order.

Parameter	Value	Units	Source
2D axisymmetric patty dimensions			
Height	1.8	cm	Measured
Diameter	10	cm	Measured
Patty composition	Actual (used)	Weight	[34]
Water	73.28 (72.74)	%	
Protein	21.41 (21.25)	%	
Fat	5.00 (4.96)	%	
Ash	1.05 (1.04)	%	
Initial conditions			
Air Volume Fraction	0	–	
Temperature	5	°C	Measured
Processing Conditions			
Ambient Temperature	60	°C	Measured
Plate Temperature	120	°C	Measured
Heat Transfer Coefficient	400	W/m^2K	Measured
Mass Transfer Coefficient	0.01	m/s	[17]
Properties			
Water Holding Capacity	Figure 6.2	–	Measured
Density			[41]
water	997.2	kg/m^3	
fat	925.6	kg/m^3	
protein	1330	kg/m^3	
Specific heat capacity			[41]
water	4178	J/kg K	
fat	1984	J/kg K	
protein	2008	J/kg K	
Thermal conductivity			[41]
water	0.57	W/m K	
fat	0.18	W/m K	
protein	0.18	W/m K	
Diffusivity	10^{-7}	m^2/s	[21]
Bulk Modulus	$\frac{K_w}{\epsilon_w}$	Pa	[37]
Poisson's Ratio	0.49	–	Rubbery state

by more than 1% of the total change (at any time at all four vertices of the geometry) by reducing the timestep-size or mesh-size by half.

Results and Validation

Spatial and Temporal Distribution of Moisture Content

Figure 5.5 shows a comparison between predicted and experimentally observed[2] total moisture loss history of the patty for 15 minutes of heating time. Total moisture loss is almost linear with time, with the patty losing about 17% (26 g for a 155 g patty) of the initial moisture content in 15 minutes. The predicted moisture loss history follows the observed history closely, and the difference between the two at any time is 0.01% or less. The cumulative evaporation and drip losses are also plotted in figure 5.5. Evaporation loss with time is slightly concave upwards (rate of loss always increases throughout the heating duration). On the other hand, cumulative drip loss curve with time is S-shaped and stabilizes (rate of drip loss goes to 0) at around 5 minutes as moisture concentration at the patty surface falls below equilibrium concentration. Evaporation loss and its rate exceed the drip loss and the drip loss rate, at any time during heating. Contours of moisture content (dry basis) after every 3 minutes of heating (starting at 3 minutes) are plotted in figure 5.6. It can be seen that the moisture gradients dominate in the axial direction and end effects are restricted to a small region near the lateral surface of the patty. Also, even at the end of heating, the minimum moisture content (near the griddle plate) is still high (0.891), which means the surface has not dried up. On the other hand, moisture content close to the exposed top surface (away from the griddle) rises to 2.731 (from an initial value of 2.6) during the process.

Spatial and Temporal Distribution of Temperature

Figure 5.7 shows a comparison between predicted and experimentally observed temper-

[2]Details of experimental measurements are available in Chapter 6

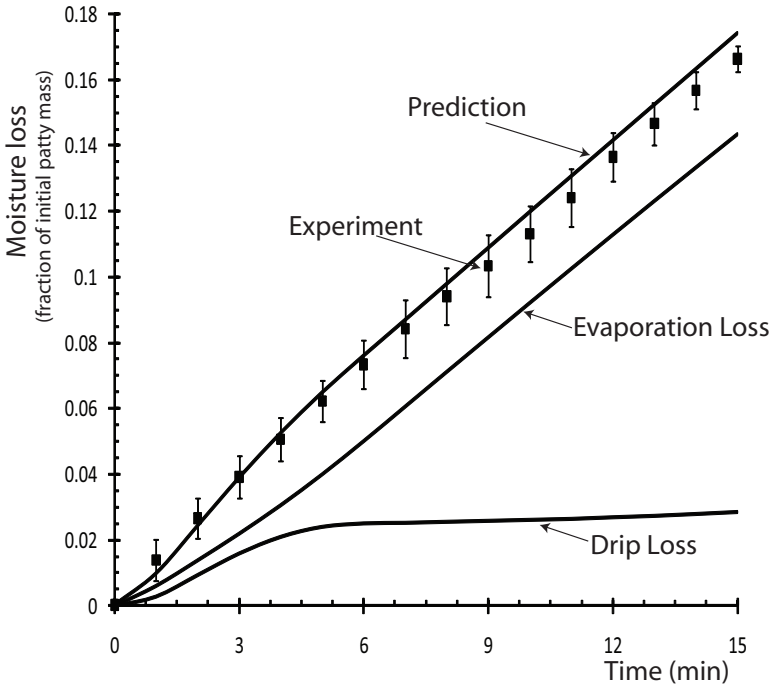

Figure 5.5: Cumulative total moisture loss (predicted and experimentally observed), evaporation moisture loss (predicted) and drip loss (predicted) for single-sided contact heating of hamburger patties. It can be seen that drip losses level-off after 5 minutes and evaporation losses dominate for the rest of the heating duration

ature history at two locations on the central axis of the patty: 1) at the mid-point between the heated and exposed surfaces,and 2) on the exposed top surface. With the initial lead time of about 50 sec, temperature at the midpoint follows the concave downwards curve reaching a value of 56°C after 15 minutes. The predicted curve follows the observed one closely, with the difference between the two at any time being 1°C or less. Temperature history at the surface is more interesting. While the observed history is similar to that of the midpoint, having an initial lead time followed by a concave downwards curve; the predicted history shows a quick initial heating period which is absent in the observed history. The discrepancy between the predicted and observed histories for the first 300 seconds of heating can be attributed to changing ambient conditions of temperature and relative humidity at the exposed surface during the cooking process. At the top surface,

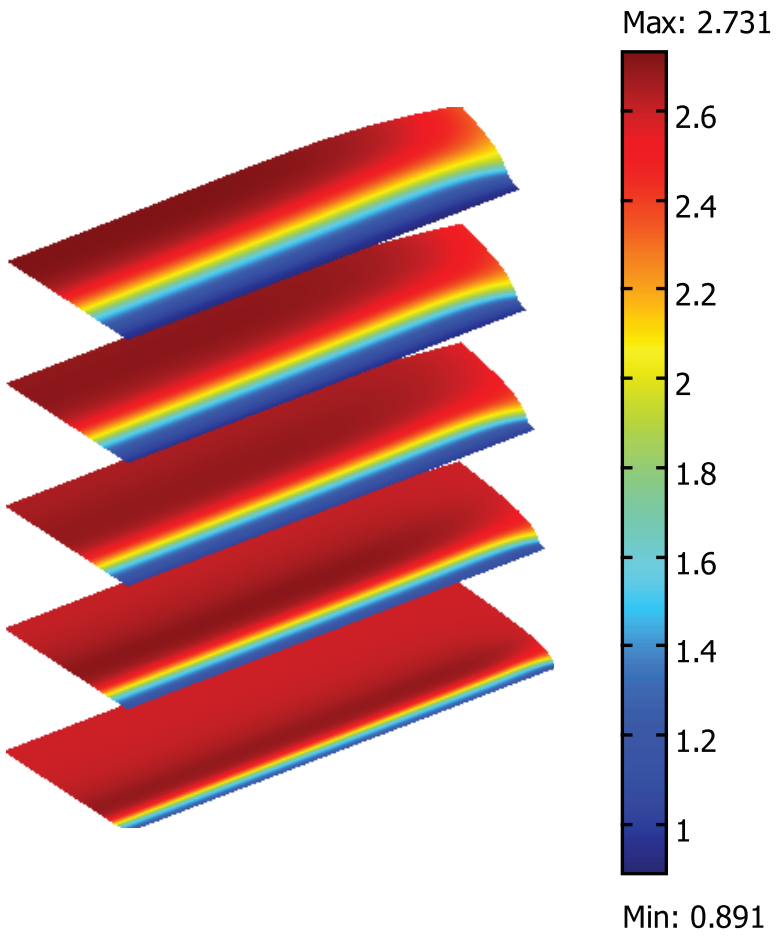

Figure 5.6: Contours of moisture content (dry basis) after 3, 6, 9, 12 and 15 minutes of single-sided contact heating of hamburger patties, showing low moisture at the heated surface and some accumulation in the center. Moisture gradients are primarily in the axial direction.

a fixed ambient air temperature of 60°C (Table 5.1) and negligible moisture loss, as compared to moisture loss from the bottom surface, were used; which may not be valid at all times and an error in prediction is seen when the effect of boundary conditions dominates. Similar to moisture content, temperature contours (Figure 5.8) show small end effects. The heated surface reaches around 90°C early in the heating process and stabilizes. Temperature at the exposed surface rises slowly and reaches about 50°C after 15 minutes.

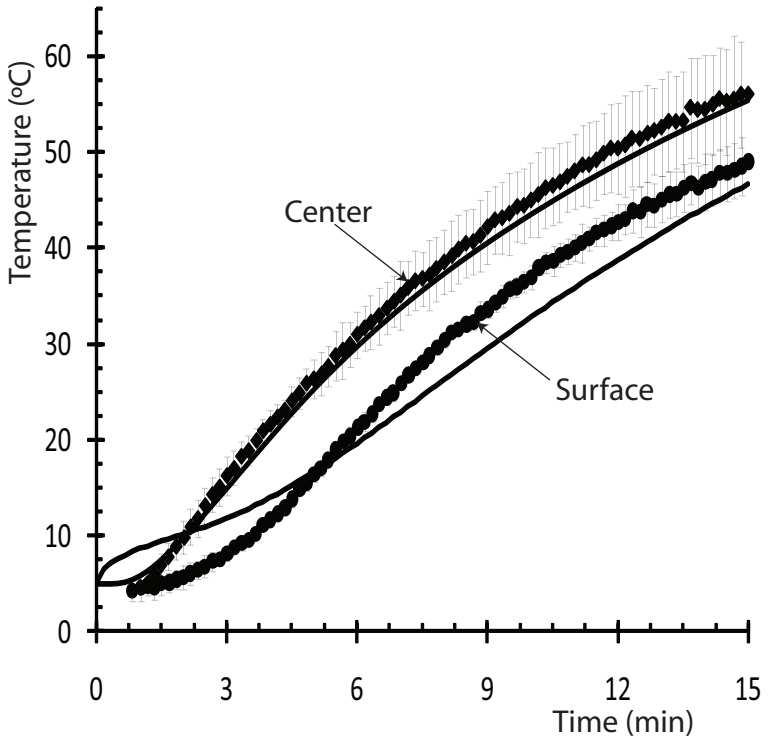

Figure 5.7: Temperature histories (prediction and experimental observation) at the mid-point and the surface on the central axis for single-sided contact heating of hamburger patties. Solid lines are predictions.

Spatial and Temporal Distribution of Deformation Field

Figure 5.9 compares the histories of experimentally observed diameter with the predicted diameter (averaged for diameter at different heights). The patty diameter reduces to about 91% of the original value in 15 minutes, which is as predicted by the simulations. For reference, the diameter, $D(t)$ assuming uniform shrinkage throughout the patty and computed from the equation:

$$\frac{D(t)}{D_0} = 1 - \left(\frac{V(t)}{V_0}\right)^{1/3} \tag{5.67}$$

is also plotted. At any time, the diameter assuming uniform shrinkage is much larger than the predicted or observed diameters, indicating the non-uniformity in patty shrinkage. Also, this means that such a simplified relationship as equation 5.67 cannot be used to predict diameter with solid deformation equations not solved. Predicted thickness

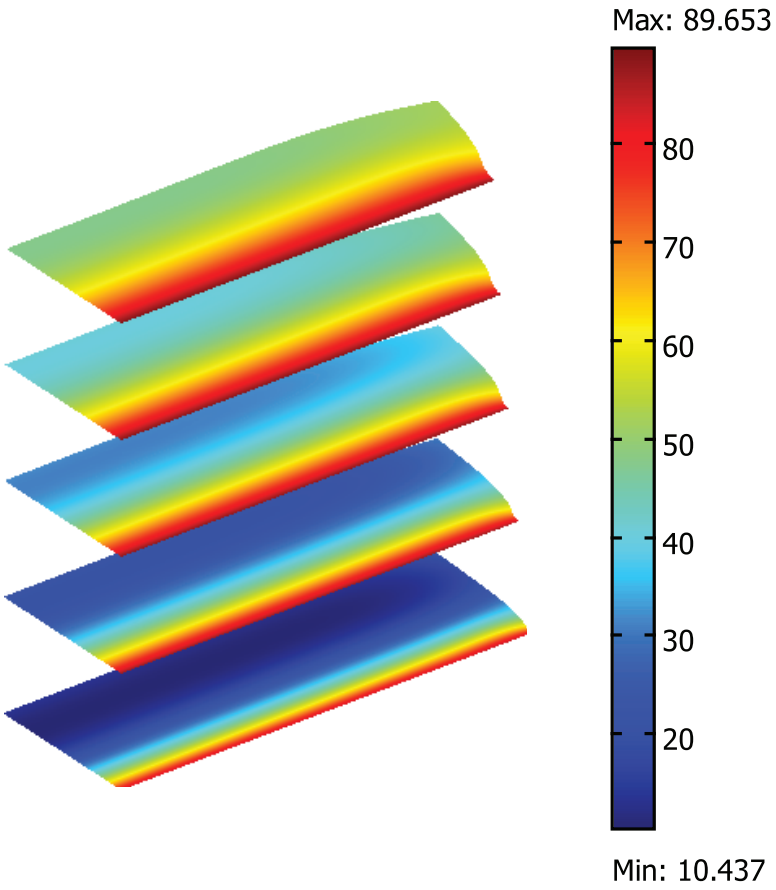

Figure 5.8: Temperature contours (in °C) after 3, 6, 9, 12 and 15 minutes of single-sided contact heating of hamburger patties showing constant heated surface temperature and gradients primarily in the axial direction.

(normalized) and thickness assuming uniform shrinkage are plotted in Figure 5.10. The final value of thickness is approximately 95% of the initial value, which means the patty shrinks by less than 1 mm in thickness in 15 minutes.

Predicted values of thickness were not compared to its observed values because of high variability in patty thickness (it varied by more than 2 mm at different locations on a single patty) and also due to variability in shear effects that cause rise of the bottom surface of the patty near the center. In this simulation, the bottom surface was considered fixed in the z-direction. However, this could not be achieved in all the experiments at all times. Some patties rose by 1-2 mm in the middle, while some others stuck to the

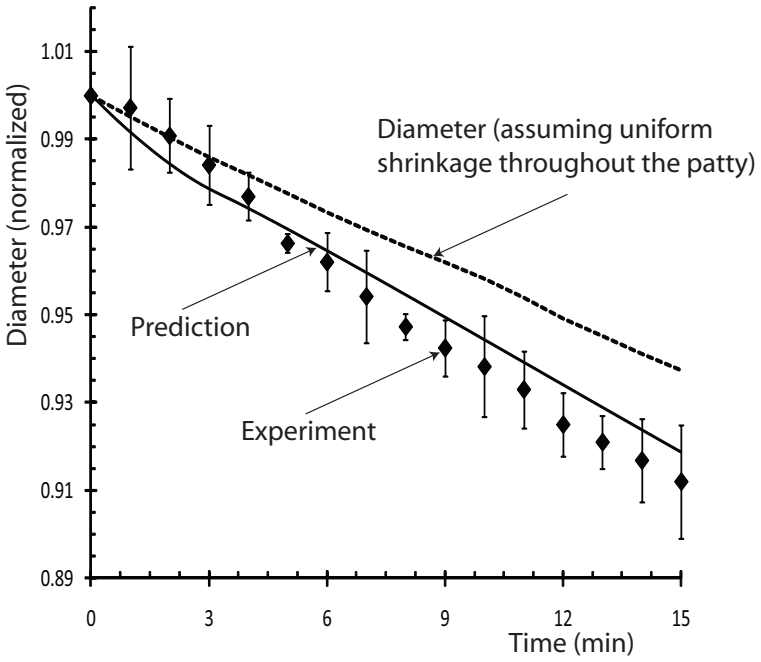

Figure 5.9: Diameter change histories (prediction and experimental observation) for single-sided contact heating of hamburger patties. Also, diameter calculated assuming uniform shrinkage throughout the patty is plotted showing assumption of uniform shrinkage will lead to erroneous results.

griddle plate. Therefore, uncertainty (more than 2 mm) in height was more than the total expected change in height ($\sim$ 1 mm) and, thus, it was meaningless to compare the observed and predicted thickness values.

Figure 5.11, which plots the contours of elastic Jacobian, J_{el} $(= J/J_M)$, at different times, helps us arrive at a very good (albeit, more involved) method to predict shrinkage. Figure 5.11 shows that the ratio of actual Jacobian, J to the Jacobian due to moisture change J_M lies in the narrow range of 0.98% to 1.01%. The region near the heated surface is under tension, while the other cooler regions are under compression. The narrow range of elastic Jacobian, J_{el}, is due to the high bulk modulus to shear modulus ratio (Poisson ratio, $\nu \approx 0.5$). For such cases, if estimation of stresses is not important, solid momentum balance can be avoided and Jacobian, J can be assumed to be

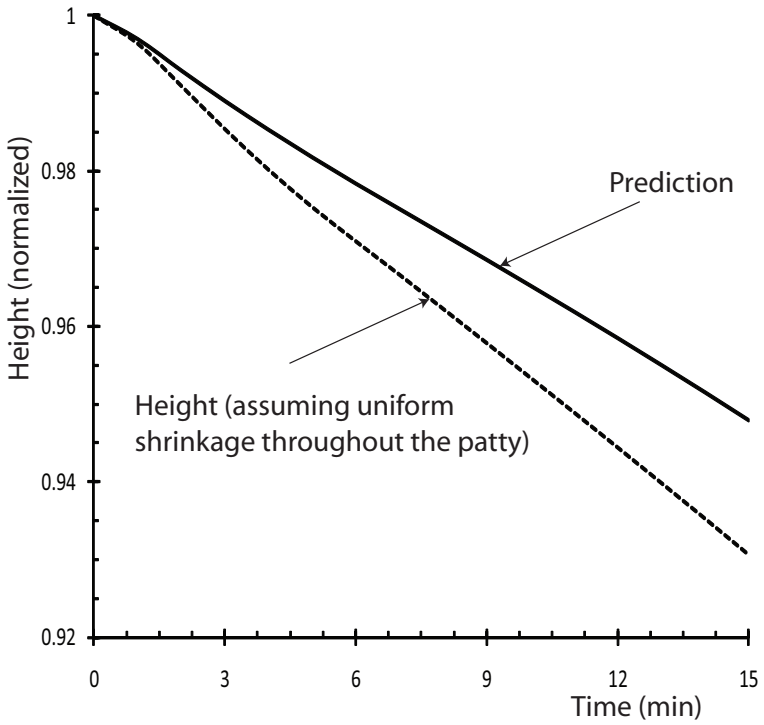

Figure 5.10: Height change history for single-sided contact heating of hamburger patties. Note that height change was too small to be compared with experiments. Also, height calculated assuming uniform shrinkage throughout the patty is plotted showing assumption of uniform shrinkage will lead to erroneous results.

equal to the moisture change Jacobian, J_M. In the absence of significant shear strains, the dilatational strains and, thus, deformation field can be estimated from Jacobian, J only. Displacements due to this deformation field can now be calculated and used in the deformed mesh equations to get new geometry.

5.4.2 Convective Drying of a Potato Slab

Drying of potato slabs, as described by Wang and Brennan (1992)[38,39], is numerically implemented as a second example. The potatoes slabs (Desiree variety) are 45 mm long and 20 mm wide, with thickness varying from 4 to 10 mm. The drying experiments

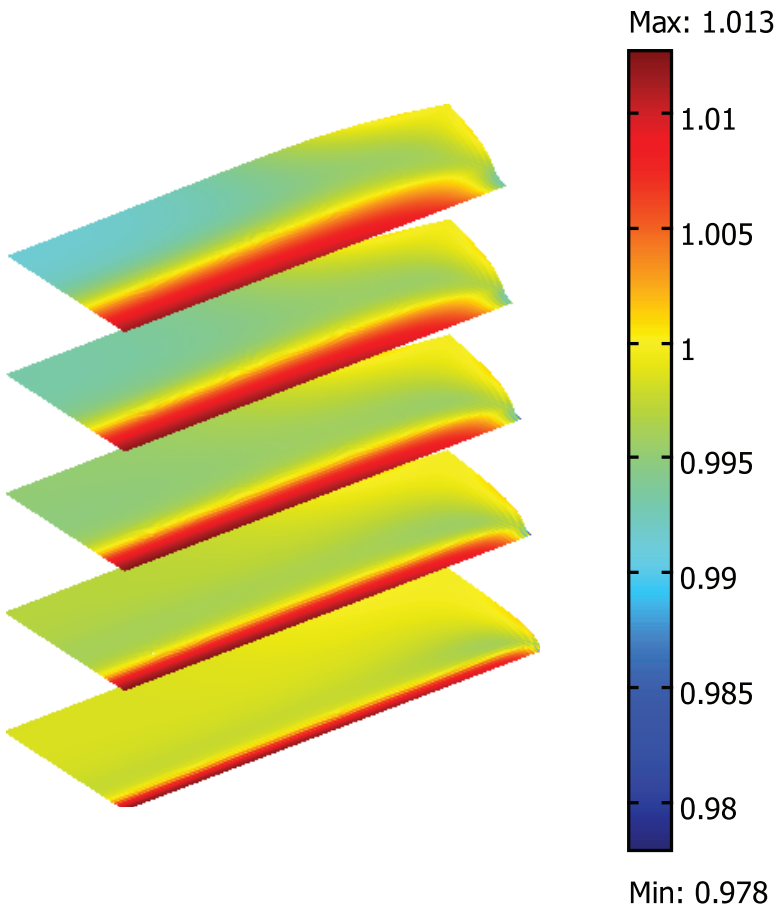

Figure 5.11: Elastic Jacobian, J_{el} (ratio of actual volume to free volume) contours after 3, 6, 9, 12 and 15 minutes of single-sided contact heating of hamburger patties. It can be seen that the surface is stretched and the heated interior is compressed by a maximum of 2% from free volume.

were carried out at air temperatures between 40°C and 70°C, at a constant absolute humidity of 16 g (vapor)/kg (dry air). Initially, the potato slab is in a rubbery state and shrinks with loss of moisture. However, unlike meat, it becomes rigid towards the end of drying and stops shrinking with moisture loss, allowing the evaporation front to move in. As before, the variables of interest are temperature, moisture content, shrinkage, evaporation rate and their histories.

Problem Formulation and Modeling Details

To reduce computational complexities, a 2D cross-section of the potatoes (perpendicular to length) is modeled and the end-effects are ignored (Figure 5.4). Only half of the width is simulated as all the physics is symmetric about the center. Initially, the potato is in a soft and rubbery state, and gradually becomes rigid allowing moisture to move at moisture content, $M = 0.3$. According to the modeling framework outlined in Figure 5.3, the transition state of food can be selected. Since the glass transition occurs at a very low moisture content and there is no evidence of Case-II diffusion (as discussed in Section 5.3.5) in potatoes, the traditional constitutive relationship for moisture flux holds. In this case, the energy balance (Equation 5.23) is solved along with the moisture balance, (Equation 5.41) and solid momentum balance (Equation 5.49). Assuming equilibrium between liquid water and water vapor, evaporation rate, $\dot{I}$, is estimated using Equation 5.25. Also, since the volume change with moisture stops at $M = 0.3$, Jacobian due to moisture change, J_M is modified as

$$J_M = \frac{1-\epsilon_{w,0}}{1-\epsilon_w} \quad M > 0.3 \tag{5.68}$$

$$= J_M|_{M=0.3} \quad M <= 0.3 \tag{5.69}$$

For boundary condition of the solid momentum equation, the bottom and the left edges are treated as a roller and a symmetry, respectively. The other two edges are free. The bottom and the left edges are insulated for energy and moisture transport equations, while surface evaporation and convective heat and mass transport takes place at the other two edges. Thus, equations 5.65 and 5.66 (with no drip loss) are used as boundary conditions for moisture and energy transport. As with the hamburger patties, initial moisture content and temperature of the potato slabs are known. Other input parameters used in the simulation are listed in Table 5.2. The solution strategy remains the same, with the simulation of 1000 minutes of drying taking approximately 30 minutes of CPU

time for a maximum timestep size of 60 second (784 linear quadrilateral elements) on a 3.00 GHz dual-core Intel Xeon workstation with 16GB RAM.

Results and Validation

Figures 5.12 and 5.13 compare model predictions with the experimental observations– a) temperature history at the top surface for drying a 7 mm thick slab at an drying temperature of 55°C, moisture content histories for slabs of thickness 10 mm, 7 mm and 4 mm at drying temperature of 55°C, and normalized volume as a function of moisture content for a 10 mm thick slab at drying temperatures of 70°C and 40°C. The surface temperature rises from 32.5°C to 50°C in 200 minutes and stabilizes, reaching about 54°C after 800 minutes of drying. The predicted temperature history closely follows the observed one. The predicted moisture content histories for 3 different values of slab thickness also follow the observed history very well, with 4 mm, 7 mm and 10 mm thick slabs drying in 400 minutes, 800 minutes and 1000 minutes, respectively. The shrinkage of the potato slabs at the two drying temperature values (70°C and 40°C) is a little less than the volume of moisture lost till moisture content of 0.3, with volume at 70°C equal to or more than that at 40°C. The simulations capture the trends very well, apart from the small difference in the observed volumes at the two drying temperatures, which the predictions could not capture. As the experimental error values are not available, it is difficult to conclusively say if the small difference in volumes at the two temperatures is a real effect. Nevertheless, the accurate predictions of moisture loss, temperature and shrinkage histories for the drying process serve to validate the modeling approach followed.

Table 5.2: Input parameters used in the simulations of drying of potato slabs. Number under source column refer to bibliographic order.

Parameter	Value	Units	Source
2D Slab dimensions			
Height	$4, 7, 10$	mm	[38,39]
Half width	10	mm	[38,39]
Initial conditions			
Moisture vol. frac.			
	0.865 ($T_{amb} = 55°\mathrm{C}$)	–	[39]
	0.838 ($T_{amb} = 40, 70°\mathrm{C}$)	–	[38]
Air vol. frac.	0	–	
Temperature	32.5	°C	[39]
drying Conditions			
Temperature	$40,\ 55,\ 70$	°C	[38,39]
Absolute humidity	0.16	g/kg	[39]
Heat transfer Coeff.	40	W/m^{2}K	Laminar flow
Mass Transfer Coeff.	0.01	m/s	Lewis analogy
Properties			
Water activity	–	–	[40]
Density			[41]
water	998	kg/m^3	
air	Ideal gas	kg/m^3	
solid	1592	kg/m^3	
Specific heat capacity			[41]
water	4178	J/kg K	
solid	1650	J/kg K	
Thermal conductivity			[41]
water	0.57	W/m K	
air	0.026	W/m K	
solid	0.21	W/m K	
Moisture Diffusivity	$4.49 \times 10^{-5}\exp(\frac{-2172}{\mathrm{T}})$	m^2/s	[39]
Binary diffusivity	$2.6 \times 10^{-6}\epsilon_g$	m^2/s	[18]
Bulk Modulus			
	10^9 $M > 0.3$	Pa	Saturated
	10^6 $M < 0.3$	Pa	Unsaturated
Poisson's Ratio			
	0.49 $M > 0.3$	–	Rubbery
	0.3 $M < 0.3$	–	Glassy

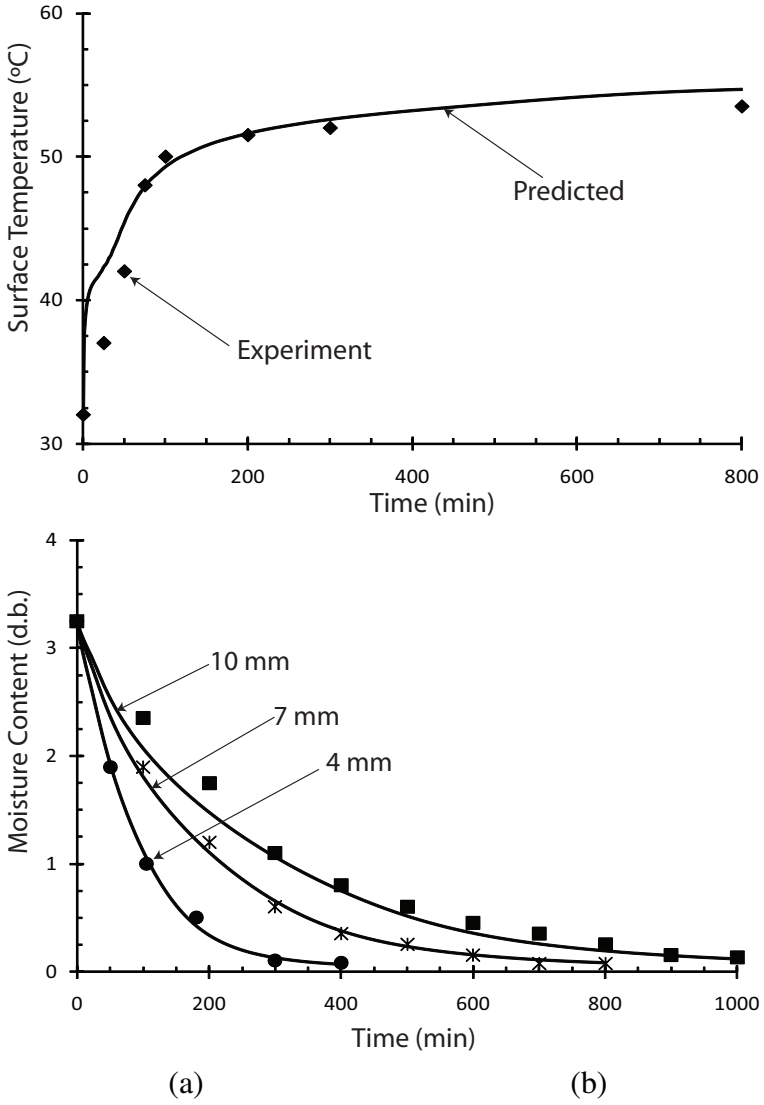

Figure 5.12: (a) Surface temperature and (b) moisture content histories for drying of potato slabs. Solid lines are model predictions and points are experimental data from the work of Wang and Brennan (1992)[39]. Drying temperature is 55°C and other input parameters are provided in Table 5.2.

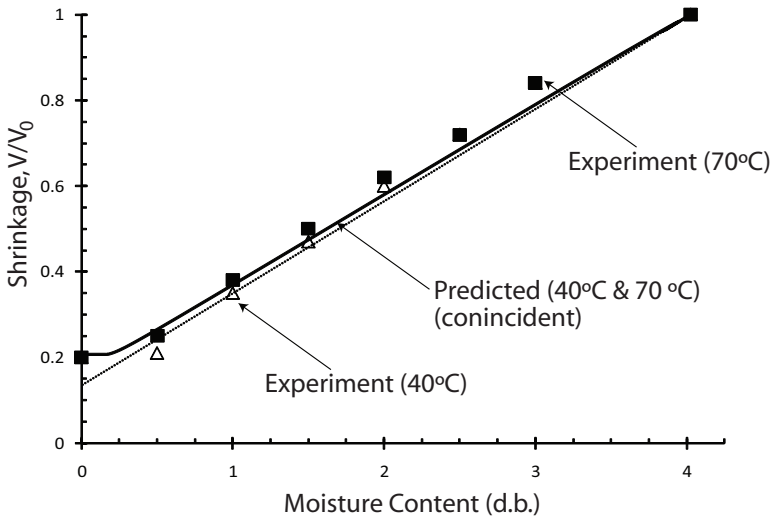

Figure 5.13: Volume change versus moisture content (drying temperatures 40 and 70°C, 10 mm thickness). Solid lines are model predictions and points are experimental data from the work of Wang and Brennan (1995)[38]. Dotted line is for shrinkage equal to moisture loss.

5.4.3 Importance of Solid Mechanics Analysis

Since the volume change is almost equal to moisture change for the two food materials studied (above a critical moisture content for potato), the advantage of solving the solid momentum equation does not lie in predicting volume change due to moisture content. The real value of solid mechanics analysis lies in predicting small deviations from free shrinkage, which lead to stresses and can be important indicators of food quality. As an example, Figure 5.14 plots the maximum value of elastic Jacobian, J_{el} as a function of normalized moisture content for hamburger cooking and potato drying (10 mm thick slab at 70°C). The large value of $max(J_{el})$ in case of potato is because of the greater shear modulus for potato which leads to deviations from free shrinkage. For hamburger patties, Poisson's ratio, ν, stays close to 0.5, and, thus, much smaller deviations from free shrinkage are observed. As potato slab is under a much larger expansive strains (near the surface as it dries up) as compared to meat, its surface is more prone to

cracking. Thus, $max(J_{el})$ can be used as a criteria to predict and, avoid drying situations most prone to cracking. Apart from cracking, other important quality parameters, such as porosity development, case hardening (surface drying leading to large increase in shear modulus and reduced shrinkage), etc., can also be predicted from deformation analysis.

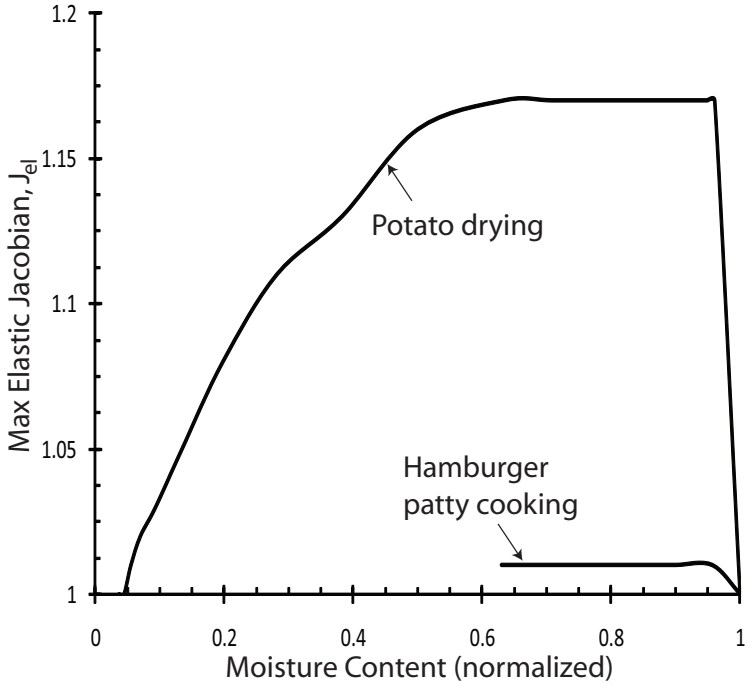

Figure 5.14: Maximum value of elastic Jacobian, J_{el} (ratio of actual volume to free volume) versus moisture content (normalized w.r.t initial moisture content) for the two processes simulated, showing larger expansive strains for potato drying as compared to hamburber patty cooking.

5.5 Conclusions

A poromechanics-based approach to mathematically model the coupled physics of transport and deformation during processing of food materials is developed. Following this

comprehensive approach, food materials existing in a range of states (glassy to rubbery) and being processed under a variety of conditions, can be simulated to predict important food quality and safety parameters (spatial and temporal histories of temperature, moisture and deformation). For deformation, primary driving forces are identified and their effect to the solid momentum balance is discussed in detail. The driving forces being– 1) gas pressure, which causes the food material to swell (gas pressure gradient can be directly treated as a source term for the solid momentum balance), and, 2) moisture change, which can be treated analogous to thermal expansion/contraction to get the free volume change. For transport, temperature, moisture, vapor concentration and gas pressure are the primary variables of interest. As gas does not enter the pores during processing of wet-rubbery materials, gas phase equation is not required for such materials. Even if gas is present, significant pressure generation occurs only for intensive heating processes such as microwave cooking and processes with internal generation such as bread baking. Also, solution of vapor equation is not required unless local equilibrium between vapor and liquid moisture breaks down. Assuming equilibrium vapor concentration, liquid water and water vapor flux can be added to get the total moisture flux relationship, which with further simplifications takes the form of Fick's law. Two different food processes are simulated as implementations of the modeling framework developed– 1) single-sided cooking of hamburger patties, for which shrinkage is equal to moisture loss throughout the process and 2) convective drying of potato slabs, for which shrinkage stops under a critical moisture content. For both the cases, transport of moisture in liquid form dominates. The difference lies in greater strains experienced by the potato due to greater shear modulus at low moisture contents. Accurate predictions of the experimental observations for two completely different processes, show the versatility of the modeling framework. Being comprehensive and fundamentals-based, the framework can be widely applicable in food product, process and equipment design,

accounting for both food quality and safety as design parameters.

BIBLIOGRAPHY

[1] Datta AK. Porous media approaches to studying simultaneous heat and mass transfer in food processes. I: Problem formulations. *Journal of Food Engineering*. 2007;80(1):80-95.

[2] Whitaker S. Simultaneous heat, mass and momentum transfer in porous media: A theory of drying. *Advances in Heat Transfer.* 1977;13:114-203.

[3] Lewis RW, Shrefler BA. The Finite Element Method in the Static and Dynamic Deformation and Consolidation of Porous Media. 2nd ed. New York: John Wiley and Sons, Ltd. 1999.

[4] Ateba P, Mittal GS. Modeling the deep-fat frying of beef meatballs. *International Journal of Food Science and Technology*, 1994;29(4):429-440.

[5] Ikediala JN, Correia LR, et al. Finite element modeling of heat transfer in meat patties during single-sided pan-frying, *Journal of Food Science*, 1996;61(4):796-802.

[6] Bengtsson NE, Jakobsson B, et al. Cooking of beef by oven roasting - study of heat and mass-transfer, *Journal of Food Science*, 1976;41(5):1047-1053.

[7] Chau KV, Snyder GV. Mathematical-model for temperature distribution of thermally processed shrimp, *Transactions of the Asae*, 1988;31(2):608-612.

[8] Fowler AJ, Bejan A. The effect of shrinkage on the cooking of meat, *International Journal of Heat and Fluid Flow*, 1991;12(4):375-383.

[9] Dincer I, Yildiz M. Modelling of thermal and moisture diffusions in cylindrically shaped sausages during frying, *Journal of Food Engineering*, 1996;28(1):35-44.

[10] Williams R, Mittal GS. Low-fat fried foods with edible coatings: Modeling and simulation. *Journal of Food Science*, 1999;64(2):317-322.

[11] Shilton N, Mallikarjunan P, et al. Modeling of heat transfer and evaporative mass losses during the cooking of beef patties using far-infrared radiation, *Journal of Food Engineering*, 2002;55(3):217-222.

[12] Wang L, Singh RP. Finite element modeling and sensitivity analysis of double-sided contact-heating of initially frozen hamburger patty, *Transactions of the ASAE*, 2004;47(1):147-157.

[13] Kondjoyan A, Rouaud O, et al. Modelling coupled heat-water transfers during a decontamination treatment of the surface of solid food products by a jet of hot air. I. Sensitivity analysis of the model and first validations of product surface temperature under constant air temperature conditions, *Journal of Food Engineering*, 2006;76(1):53-62.

[14] Farkas BE, Singh RP, et al. Modeling heat and mass transfer in immersion frying .1. Model development, *Journal of Food Engineering*, 1996;29(2):211-226.

[15] Farid MM, Chen XD. The analysis of heat and mass transfer during frying of food using a moving boundary solution procedure, *Heat and Mass Transfer*, 1998;34(1):69-77.

[16] Bouchon P, Pyle DL. Modelling oil absorption during post-frying cooling - I: Model development, *Food and Bioproducts Processing*, 2005;83(C4):253-260.

[17] Ni H, Datta AK. Moisture, oil and energy transport during deep-fat frying of food materials, *Food and Bioproducts Processing*. 1999;77(C3):194-204.

[18] Halder A, Dhall A, Datta AK. An improved, easily implementable, porous media based model for deep-fat frying - Part I: Model development and input parameters. *Food and Bioproducts Processing.* 2007;85(C3):209-219.

[19] Singh PP. Effect of viscoelastic relaxation on fluid and species transport in

biopolymeric materials [Ph.D.]. United States – Indiana, Purdue University; 2002.

[20] Achanta S. Moisture transport in shrinking gels during drying [Ph.D.]. United States – Indiana, Purdue University; 1995.

[21] van der Sman RGM. Soft condensed matter perspective on moisture transport in cooking meat. *AIChE Journal*. 2007;53(11):2986-2995.

[22] Mayor L, Sereno AM. Modelling shrinkage during convective drying of food materials: a review. *Journal of Food Engineering.* 2004;61(3):373-386.

[23] Katekawa ME, Silva MA. A review of drying models including shrinkage effects. Drying Technology. 2006;24(1):5-20.

[24] Zhang J, Datta AK, Mukherjee S. Transport processes and large deformation during baking of bread. *AIChE Journal*. 2005;51(9):2569-2580.

[25] Rakesh V. Transport in rigid and deformable hygroscopic porous media during electromagnetic and combination heating [Ph.D.]. United States – New York, Cornell University; 2010.

[26] Perre P, May BK. A numerical drying model that accounts for the coupling between transfers and solid mechanics. Case of highly deformable products. Drying Technology. 2001;19(8):1629-1643.

[27] Kowalski SJ. Toward a thermodynamics and mechanics of drying processes. *Chemical Engineering Science*. 2000;55(7):1289-1304.

[28] Ni H, Datta AK, et al. Moisture transport in intensive microwave heating of biomaterials: A multiphase porous media model, *International Journal of Heat and Mass Transfer*. 1999;42(8):1501-1512.

[29] Scherer GW. Drying Gels .8. Revision And Review. *Journal of Non-Crystalline Solids.* 1989;109(2-3):171-182.

[30] Smith DM, Scherer GW, Anderson JM. Shrinkage During Drying Of Silica-Gel. *Journal of Non-Crystalline Solids.* 1995;188(3):191-206.

[31] Vujosevic L, Lubarda VA. Finite-strain thermoelasticity based on multiplicative decomposition of deformation gradient. *Theoretical and Applied Mechanics*. 2002;28-29:379-399.

[32] Halder A*, Dhall A*, Datta AK. Modeling Transport in Porous Media with Phase Change: Applications to Food Processing. *Journal of Heat Transfer.* 2010 (Accepted). * Equal Contribution

[33] Cushman JH. The physics of fluids in hierarchical porous media: angstroms to miles. Norwell, MA: Kluwer Academic Publishers 1997.

[34] USDA Nutrition Database http://www.nal.usda.gov/fnic/foodcomp/search/. Accessed July 31, 2010.

[35] Lu N, Likos WJ. Unsaturated Soil Mechanics. John Wiley and Sons 2004.

[36] Tornberg E. Effects of heat on meat proteins - implications on structure and quality of meat products. *Meat Science*. 2005;70(3):493-508,Sp. Iss. SI.

[37] Hashin Z. Large Isotropic Elastic Deformation of Composties and Porous Media. *International Journal of Solids and Structures*. 1985;21(7):711-720.

[38] Wang N, Brennan JG. Changes In Structure, Density And Porosity Of Potato During Dehydration. *Journal of Food Engineering.* 1995;24(1):61-76.

[39] Wang N, Brennan JG. Effect of water binding on the drying behaviour of potato. In: Majumdar AS, ed. *Drying '92 Part B.* New York: Elsevier, Amsterdam; 1992:1350-1359.

[40] Ratti C, Crapiste GH, Rotstein E. A New Water Sorption Equilibrium Expression for Solid Foods Based on Thermodynamic Considerations. *Journal of Food Science*. 1989;54(3):738-&

[41] Choi Y, Okos MR. Thermal properties of liquid foods – review. In: *Okos MR (editor). Physical and Chemical Properties of Food* Saint Joseph, Michigan: American Society of Agricultural Engineers, 1986:35-77.

CHAPTER 6

TRANSPORT AND DEFORMATION DURING SINGLE-SIDED CONTACT-HEATING OF HAMBURGER PATTIES

6.1 Abstract

A heat and mass transport model is developed based on saturated flow in a deformable porous medium, which accounts for the important physical phenomena that take place during single-sided contact-heating of lean hamburger patties. The patty is treated as a porous medium comprising of liquid water in the pore space of a solid matrix. As the patty is heated from refrigeration temperature, proteins denaturate and water holding capacity of the patty drops, resulting in moisture transport in the pore space. Loss of moisture results in shrinkage. Moisture transport and shrinkage of the patty are modeled using mass conservation and solid momentum balance equations, respectively. The model is experimentally validated by comparing temperature, moisture and diameter change histories. Uncertainty in the model predictions is quantified by performing a sensitivity analysis on heat transfer coefficient, mass transfer coefficient, moisture diffusivity and time-scale of protein denaturation. Heat transfer coefficient affects moisture concentration and temperature near heated surface. Mass transfer coefficient changes the nature of moisture loss– drip or evaporation. Moisture diffusivity affects spatial moisture profiles, and time-scale of protein denaturation affects drip losses by changing the equilibrium moisture concentration at the surface.

Nomenclature

a_w	water activity
c_i	concentration of species i, kg m^{-3}
c_p	specific heat capacity, J kg^{-1}K^{-1}
C	Constant of proportionality in Equation 6.12
D	Diameter, m
$\mathbf{E}$	Green-Lagrange strain tensor
$\mathbf{F}$	deformation tensor
h	heat transfer coefficient, W m^{-2} K^{-1}
h_m	mass transfer coefficient of vapor, m s^{-1}
J	Jacobian
k_{eff}	effective thermal conductivity, W m^{-2} K^{-1}
k_i	permeability of phase i, m^2
K	bulk modulus, Pa
M	moisture content (dry basis)
$\vec{N}$	normal vector
$\vec{n_{i,j}}$	mass flux of species i w.r.t. j, kg m^{-2} s^{-1}
p_i	pressure of phase or species i, Pa
$\vec{q}$	heat flux, J m^{-2} s^{-1}
REV	Representative Elementary Volume
$\mathbf{S}''$	Piola-Kirchoff stress tensor, Pa
t	time, s
T	temperature
$v_{i,j}$	velocity of species i w.r.t. j, m s^{-1}
V	volume, m^3
W	strain energy density, Pa

Greek Symbols

ϵ	volume fraction of species i
ρ	density, kg m^{-3}
λ	latent heat of vaporization, J kg^{-1}
μ	shear modulus, Pa
μ_i	dynamic viscosity of a phase, i, Pa s
ν	Poisson's ratio
$\boldsymbol{\sigma}''$	effective stress tensor due to mechanical load only, Pa
ϕ	porosity

Subscripts

amb	ambient
s, w	solid, water
eff	effective
el	elastic
eq	equilibrium
f	fluid
G	Ground (stationary observer)
i	i^{th} phase
M	moisture
0	at time $t = 0$
$surf$	surface
$surfd$	drip at the surface
$surfe$	evaporation at the surface
T	temperature

6.2 Introduction

Computer modeling of a meat cooking process can go a long way in establishing a better understanding of the transport processes that take place inside, which is vital for quality and safety prediction and improvement. However, underlying physics is complex due to highly heterogeneous nature of the material. Over the years, heat and mass transport studies during cooking of meat have been reported at various levels of complexity[1–8]. Recently, van der Sman (2007)[9] applied Flory Rehner theory to estimate liquid pressure in meat, while its proteins undergo deformation. Details of these studies are discussed in Chapter 3. However, none of the models till date consider deformation and transport in meat from poromechanics point of view.

This objectives of this work are to 1) apply the already developed poromechanics-based transport model that accounts for the important physical phenomena (heat transfer, moisture transport and deformation) to simulate single-sided contact-heating of lean hamburger patties, 2) validate the model by comparing temperature, moisture and patty diameter change histories with experimental results and 3) perform sensitivity analysis to identify the dominant modes of heat and mass transport in operation.

6.3 Mathematical Model

6.3.1 Problem Definition

Single-sided contact heating of hamburger patties is studied. A refrigerated hamburger patty of cylindrical shape is heated on a commercial griddle (George Foreman Model No. GR0215G) at a fixed plate temperature. As temperature rises, water at the surface

of the patty evaporates. Since ground meat is in a rubbery state, the patty shrinks with loss of moisture, and, at equilibrium (in the absence of gradients of temperature and moisture fields) the shrinkage should be equal to the volume of water lost. With further rise in temperature, denaturation of muscle proteins occurs, which leads to decrease in water holding capacity of the meat. Since the surface of meat in contact with the plate gets heated up quickly, the water holding capacity near the surface may drop faster as compared to the drop in moisture concentration due to evaporation. This leads to dripping of water from the patty. The variables of interest for predicting quality and safety aspects of meat cooking are temperature, moisture content, shrinkage, evaporation rate and their histories.

6.3.2 Modeling Assumptions

1) A poromechanics-based approach of energy and mass transport in deformable porous materials (developed elsewhere[10]) is used to model the process. 2) The patty is simulated as a 2D axisymmetric geometry, as the exchange of heat and mass with the outside environment does not have angular dependence and only a cross-section of the cylindrical patty needs to be simulated (Figure 6.1). 3) The effect of gravity on mass transfer is ignored as the effect of pressure gradients is much larger on moisture velocity. 4) Since the patty is in a soft and rubbery state, evaporation stays on the surface during the entire cooking process and the patty remains saturated. Even if a rigid glassy region develops at the heated surface, it is assumed to be small and its effect can be neglected.

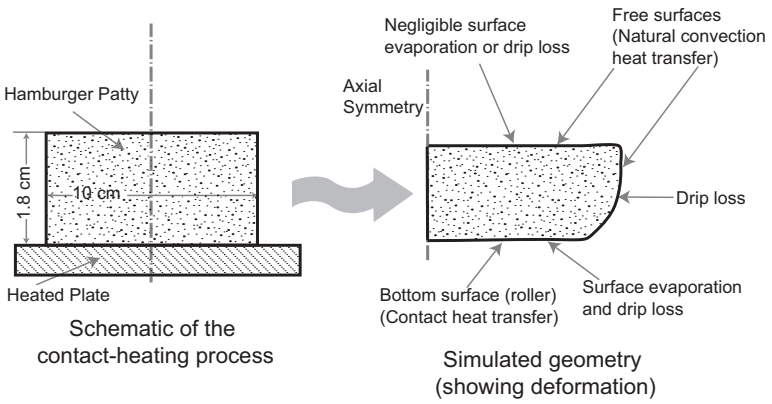

Figure 6.1: Schematic of the single-sided contact-heating of hamburger patties.

6.3.3 Solid Momentum Balance

Deformation in meat products like hamburger patties occurs due to moisture loss. Detailed derivation of the solid momentum balance for food materials is given in Dhall and Datta (2010)[10]. The final solid momentum balance and the constitutive model are described here. Since the patty can shrink by 30% or more of its initial volume, large deformation analysis is required.

Multiplicative Split

The treatment is analogous to that of finite-strain thermoelasticity in which the thermal and mechanical effects are separated by a multiplicative split in the deformation gradient tensor[11]. Similarly, in this case, a multiplicative split of moisture effects and elastic effects on deformation is performed:

$$\mathbf{F} = \mathbf{F}_{\mathrm{M}}\mathbf{F}_{\mathrm{el}} \tag{6.1}$$

where $\mathbf{F}$, $\mathbf{F}_{\mathrm{M}}$ and $\mathbf{F}_{\mathrm{el}}$ are, respectively, overall deformation gradient tensor, deformation gradient tensor due to moisture effects and deformation gradient tensor due to elastic effects. Now, the strain energy density, W_{el} is a function of $\mathbf{F}_{\mathrm{el}}$ (more later).

Governing Equation

For large deformation, Lagrangian measures of stress and strain are used, and solid momentum balance (for elastic stresses and strains) is written in Lagrangian coordinates

$$\nabla_X . \left(\mathbf{S}'' . \mathbf{F}_{\mathrm{el}}{}^{\mathrm{T}} \right) = 0 \tag{6.2}$$

where $\mathbf{S}''$ is the second Piola-Kirchhoff (PK2) stress tensor, $\mathbf{F}_{\mathrm{el}}$ is the elastic deformation gradient tensor. The evaporation front stays at the surface and, therefore, there is no body force term on the Right Hand Side due to gas pressure generation. PK2 stress, $\mathbf{S}''$ and, Green-Lagrange tensor for elastic strains, $\mathbf{E}_{\mathrm{el}}$ are related as follows:

$$\mathbf{S}'' = \frac{\partial W_{el}}{\partial \mathbf{E}_{\mathrm{el}}} \tag{6.3}$$

Constitutive Law

We need a constitutive equation for the elastic strain energy density, W_{el}. Rubbery state means the stress relaxation time scales are expected to be small (as compared to the time scale of the cooking process which is in minutes, Deborah number ~ 0) and the solid skeleton can be can be treated as a hyperelastic material. Also, the fibers in ground meat are randomly oriented. Therefore, although meat fibers are anisotropic with different properties along and across the fibers, the averaged mechanical properties are isotropic. A modified Neo-Hookean constitutive model is chosen which accounts for the volume change due to moisture loss also:

$$W_{el} = \frac{K}{2} \left(J_{el} - 1 \right)^2 - \frac{\mu}{2} \left(\bar{I}_1 - 3 \right) \tag{6.4}$$

where K and μ are the Bulk Modulus and the Shear Modulus, respectively. J_{el} is the elastic Jacobian, and $\bar{I}$ is the first invariant of the right-Cauchy Green tensor, $\bar{\mathbf{C}} \left(= \bar{\mathbf{F}_{\mathrm{el}}}^{\mathrm{T}} \bar{\mathbf{F}_{\mathrm{el}}} \right)$ for deviatoric part of elastic deformation tensor, i.e., $\bar{\mathbf{F}_{\mathrm{el}}}$. Deviatoric part

of deformation gradient, $\bar{\mathbf{F}}_{\mathrm{el}}$, is related to deformation gradient, $\mathbf{F}_{\mathrm{el}}$, and its dilatation part, $J_{el}^{1/3}$, as

$$\mathbf{F}_{\mathrm{el}} = J_{el}^{1/3}\bar{\mathbf{F}}_{\mathrm{el}} \tag{6.5}$$

To estimate elastic deformation gradient tensor, $\mathbf{F}_{\mathrm{el}}$, we need to calculate deformation gradient tensor due to moisture change, $\mathbf{F}_{\mathrm{M}} = J_M\mathbf{I}$.

Jacobian due to Moisture Change, J_M

Calculation of J_M is easy, as under stress-free conditions, patty shrinks/swells by the amount of moisture lost/gained. Let V be the REV volume at moisture volume fraction, ϵ_w. Then, change in volume of REV can be equated to change in volume of moisture in REV:

$$V - V_0 = \epsilon_w V - \epsilon_{w,0} V_0 \tag{6.6}$$

$$J_M = \frac{V}{V_0} = \frac{1-\epsilon_{w,0}}{1-\epsilon_w} \tag{6.7}$$

Similarly, porosity at any time t, $\phi(t)$ can be determined using incompressibility of the solid skeleton, equating the initial volume of solid in an REV to solid volume at time, t:

$$(1-\phi(t))\,V(t) = (1-\phi_0)\,V_0 \tag{6.8}$$

$$\phi(t) = 1 - \frac{1-\phi_0}{V(t)/V_0} = 1 - \frac{1-\phi_0}{J(t)} \tag{6.9}$$

Note that while Jacobian due to moisture change, J_M is a state function (depending on the moisture content), porosity, $\phi(t)$ is a process variable, depending on the actual Jacobian, $J(t)$.

6.3.4 Moisture and Energy Transport Equations

The governing equations for non-isothermal transport in unsaturated porous materials comprise of energy conservation and mass conservation of liquid water:

$$\left(\rho_{eff} c_{p,eff}\right) \frac{\partial T}{\partial t} + \sum \left(\vec{n}_{i,G} . \nabla \left(c_{p,i} T\right)\right) = \nabla . \left(k_{eff} \nabla T\right) \tag{6.10}$$

$$\frac{\partial c_w}{\partial t} + \nabla . \left(c_w \vec{v}_{s,G} - \rho_w \frac{k_w}{\mu_w} \nabla p_w \right) = 0 \tag{6.11}$$

Liquid water pressure (called swelling pressure) during cooking of meat products has been estimated[9] by using the Flory-Rehner theory. Taking the swelling pressure to be 0 at equilibrium moisture volume fraction, and linearizing the Flory-Rehner expression near equilibrium, it can be shown that the swelling pressure is proportional to difference between the actual and equilibrium moisture concentrations:

$$p_w = C \left(c_w - c_{w,eq}(T)\right) \tag{6.12}$$

where $c_{w,eq}$ is the equilibrium moisture concentration at a given temperature and the constant of proportionality, C, though constant here, can be temperature dependent. Inserting this expression of liquid pressure, p_w in Equation 6.11, we get:

$$\frac{\partial c_w}{\partial t} + \nabla . \left(c_w \vec{v}_{s,G}\right) = \nabla . \left(D_{w,c_w} \left(\nabla c_w + \nabla c_{w,eq}\right)\right) \tag{6.13}$$

where, the definition of diffusivity is:

$$D_{w,c_w} = \rho_w \frac{k_w}{\mu_w} C \tag{6.14}$$

Equations 6.2, 6.13 and 6.10 for deformation, moisture and temperature fields, respectively form the mathematical model for the process.

6.3.5 Boundary and Initial Conditions

Solid Momentum Balance

Normal displacement of the axisymmetric boundary and the bottom surface (lying on the plate) is set to zero. The other two boundaries are unconstrained and free to move (Figure 6.1).

Liquid Water Equation

The boundary condition for liquid water equation consists of two flux terms: evaporation and drip. The evaporation flux, $n_{w,s,surfe}$, is simply given by mass transfer coefficient multiplied by the vapor density difference between the surface and the boundary:

$$n_{w,s,surfe} = h_m \left(\rho_{v,surf} - \rho_{v,amb}\right) \tag{6.15}$$

Water is lost from the matrix in liquid form (as drip) only when surface moisture concentration, $c_{w,surf}$, is more than the water holding capacity, $c_{w,eq}$. The drip loss, $n_{w,s,surfd}$, under such conditions is equal to the total moisture flux reaching the surface subtracted by that taken by surface evaporation, $n_{w,s,surfe}$:

$$n_{w,s,surfd} = \vec{n}_{w,s}.\vec{N}_{surf} - h_m \left(\rho_{v,surf} - \rho_{v,amb}\right) \tag{6.16}$$

Therefore, the total moisture flux at the surface w.r.t stationary observer is equal to the sum of drip loss, evaporation loss and flux due to movement of the surface itself:

$$n_{w,G,surf} = n_{w,s,surfe} + n_{w,s,surfd} + c_w \vec{v}_{s,G} \tag{6.17}$$

The bottom surface of the patty loses water both due to evaporation and drip. Water coming out of the top surface as drip stays on the patty surface. Also, evaporation losses from the lateral and top surfaces are much smaller than the losses from the bottom surface and can be neglected.

Energy Equation

For energy equation, forced convection heat transfer boundary condition is applied to get the heat flux at the surface, q_{surf}

$$q_{surf} = h(T_{amb} - T_{surf}) - \lambda n_{w,s,surf} - \sum \left(\vec{n}_{i,G} c_{p,i} T\right) . \vec{N}_{surf} \qquad (6.18)$$

In equation 6.18, The first term on the RHS is the convective heat transfer coefficient multiplied by the temperature difference, the second term is the latent heat taken up by surface evaporation and the third term is the energy carried by convection terms normal to the boundary. The ambient temperatures and heat transfer coefficients for the bottom surface and the exposed surfaces (top and lateral) are listed in Table 6.1.

Initial Conditions

Initially refrigerated at 5°C, the composition of the patty is known (more later). The volume fraction of air in the patties is considered small and, thus, ignored. From this data, the initial concentrations of water and solid (protein, fat and ash) can be calculated.

6.3.6 Implementation

A commercially available finite element software, COMSOL Multiphysics 3.5a (Comsol Inc, Burlington, MA), was used to solve the equations. The solid momentum balance is solved in the Total Lagrangian reference frame (i.e. frame moving with the solid) for axisymmetric geometry equation in the Structural Mechanics Module, while convection-conduction and convection-diffusion equations (in the main COMSOL Multiphysics module) were used for energy and moisture transport, respectively. Deformed

mesh equations (again, in the main COMSOL Multiphysics module) were used to track the material deformation in the Eulerian reference frame, and move the mesh accordingly. The transport equations were solved in the Eulerian reference frame (i.e. frame of the stationary observer) on the deformed mesh. The computational domain was rectangular, 5 cm $\times$ 1.8 cm and had an unstructured quadrilateral mesh consisting of 3864 elements. Linear shape functions were used. The simulation of 900 seconds of heating took approximately 4 hours of CPU time for an adaptive timestepping scheme (maximum timestep size of 0.05 second) on a 3.00 GHz dual-core Intel Xeon workstation with 16GB RAM. Mesh and timestep convergence were ensured by checking that any dependent variable (temperature, moisture content or displacement) did not change by more than 1% of the total change (at any time at all four vertices of the geometry) by reducing the timestep-size or mesh-size by half.

6.3.7 Input Parameters

Input parameters used in the simulation are given in Table 6.1. A lean patty (5% fat by weight) is chosen so that fat transport can be neglected. The composition of the patty is taken from USDA Nutrient Database (Entry no. 23557[12]). Since the weight percentages of the proximates add up to 100.74, the weight percentages were normalized. Prior to use, the patties were refrigerated at 5°C. The ambient air temperature near the patty (60°C) and the water holding capacity as a function of temperature (Figure 6.2) were measured. A number of studies have attempted to estimate the contact heat transfer coefficient between the patty and the hot plate, both for single-sided and double-sided heating[16–19]. A high degree of variability exists in the heat transfer coefficient due to a number of factors: location on the underside of the patty, patty composition and size, surface roughness (of both the patty and the heating plate), plate temperature, pressure

Table 6.1: Input parameters used in the simulations of single-sided contact heating of hamburger patties. Number under source column refer to bibliographic order.

Parameter	Value	Units	Source
2D axisymmetric patty dimensions			
Height	1.8	cm	Measured
Diameter	10	cm	Measured
Patty composition	Actual (used)	Weight	[12]
Water	73.28 (72.74)	%	
Protein	21.41 (21.25)	%	
Fat	5.00 (4.96)	%	
Ash	1.05 (1.04)	%	
Initial conditions			
Air Volume Fraction	0	–	
Temperature	5	°C	Measured
Processing Conditions			
Ambient Temperature	60	°C	Measured
Plate Temperature	120	°C	Measured
Heat Transfer Coefficient	400	W/m^2K	Measured
Mass Transfer Coefficient	0.01	m/s	[13]
Properties			
Water Holding Capacity	Figure 6.2	–	Measured
Density			[14]
water	997.2	kg/m^3	
fat	925.6	kg/m^3	
protein	1330	kg/m^3	
Specific heat capacity			[14]
water	4178	J/kg K	
fat	1984	J/kg K	
protein	2008	J/kg K	
Thermal conductivity			[14]
water	0.57	W/m K	
fat	0.18	W/m K	
protein	0.18	W/m K	
Diffusivity	10^{-7}	m^2/s	[9]
Bulk Modulus	$\frac{K_w}{\epsilon_w}$	Pa	[15]
Poisson's Ratio	0.49	–	Rubbery state

applied on the patty and stage in heat treatment. For single-sided heating, the heat transfer coefficient is reported to be about 300 W/m^{2}K[19] for 11.3 mm thick patties. For thicker patties (18 mm) used in this study, the heat transfer coefficient is expected to be higher. The upper limit can be estimated from the value for double-sided cooking (without any extra pressure), which is about 500 W/m^{2}K[19]. Therefore, a value of 400 W/m^{2}K was selected, with sensitivity analysis performed for 300, 400 and 500 W/m^{2}K (more later). For experimental measurements performed in this study (described below), the temperature of the heating plate was set at 140°C. However, as reported in literature, the plate temperature can drop by 30 to 40°C as the patty is kept on the plate and, then, starts to rise. The plate temperature may not reach the set-point temperature even at the end of the cooking process. Also, like heat transfer coefficient, significant variability exists in plate temperature histories at various locations on the underside of the patty. In this study, 120°C was selected as a guesstimate of spatial and temporal average of the plate temperature profiles. Note that due to high variability and uncertainty in both the heat transfer coefficient and the plate temperature, an appropriate way to select the boundary conditions is to make a reasonable estimate and, then, analyze the sensitivity of the predictions due to the input parameters. The density, specific heat and thermal conductivity of the patty are estimated from the composition using the correlations proposed by Choi and Okos (1986)[14]. van der Sman (2007)[9] provides a detailed discussion on moisture diffusivity (as defined in Equation 6.14) in meat during protein denaturation. An estimate of 10^{-7} m^2/s was made based on minimization of L_2 norm between predictions (moisture and temperature profiles) and experimental observations and, also, confirmed by an order of magnitude estimate of swelling pressure, p_w, liquid moisture permeability, k_w, and the constant of proportionality in Equation 6.12, C. The same value is used in this study. Since the patties are considered to be saturated and in a soft, rubbery state throughout the heating duration, the estimation of Bulk Modulus and

Poisson's ratio was easy. By definition of soft materials, the Poisson's ratio is expected to be about 0.5. A value of 0.49 was used to help convergence. For saturated porous materials with incompressible solid skeleton, the bulk modulus (for small elastic strains) is given by[15]

$$K = \frac{1}{\epsilon_f}\left(K_f + \frac{4G_s}{3}\left(1-\epsilon_f\right)\right) \tag{6.19}$$

Since the bulk modulus of water, K_w (2.2×10^9 Pa) is much greater than the shear modulus of the solid matrix, G_s ($< 10^6$ Pa), it justifies a Poisson ratio close to 0.5, and equation 6.19 reduces to

$$K = \frac{K_w}{\epsilon_w} \tag{6.20}$$

6.4 Experimental Measurements

For validation of the predictions from the model, experimental measurements during single-sided contact heating of the hamburger patties (Figure 6.1) bought from a local grocery store are performed. A refrigerated hamburger patty of cylindrical shape (diameter 10 cm and height 1.8 cm), initially stored at 5°C, is heated on a commercial griddle (George Foreman Model No. GR0215G) at a fixed plate temperature. Three different measurements were taken for validation:

6.4.1 Moisture Loss

The weight of the patty was measured (using a electronic balance with 0.1 g least count) after every minute to estimate moisture loss. For every measurement, a different patty was used so that a patty once removed from the plate for weight measurement is not put back. Also, each measurement was repeated thrice. Knowing the initial water content in

the patty and assuming that all the mass lost is water, moisture content at any time can be estimated.

6.4.2 Diameter Change

The diameter of the patty was measured by Image Analysis. After every minute of heating, a picture of the patty was taken by a Sony (Model DSC-T700) digital camera and change in diameter was then estimated from the images. The initial patty diameter of 10 cm was covered in about 1000 pixels, which means a resolution of 0.01 cm/pixel (much smaller than the observed variability in diameter). The measurements were repeated thrice, each at a height of 0.9 cm from the plate (mid-point of the central axis).

6.4.3 Point Temperature History

A K-type thermocouple probe (Omega Engineering Inc., Stamford, Connecticut, USA) was used to obtain temperature histories at two locations on the central axis of the patty: the top (exposed) surface, and the midpoint (between the exposed and the heated surfaces). Temperature was recorded at 1 sec intervals.

6.4.4 Water Holding Capacity

Small pieces of the patties ($\sim$2 mm in thickness and rectangular cross-section of approximately 2 cm $\times$ 2 cm) were heated in a waterbath (Fisher Scientific, Isotemp 210) at fixed temperatures for 20 minutes to ensure equilibrium. The waterbath temperatures were controlled at 30, 40, 50, 60, 70, 80, 90°C. Figure 6.2 plots the equilibrium mois-

ture content as a function of temperature showing that the water holding capacity drops significantly above 50°C and stops dropping beyond 80°C. Note that the water holding capacity experiments were performed by heating the pieces with and without plastic bags and no significant difference was seen between the two observations.

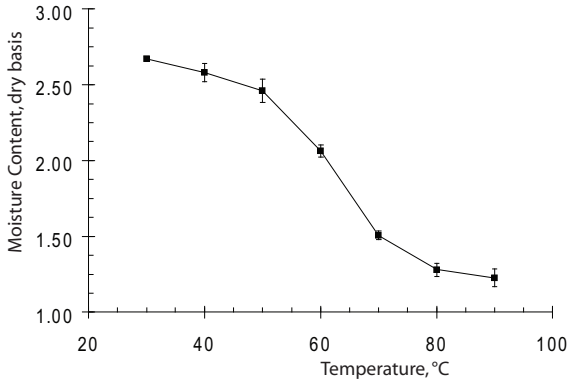

Figure 6.2: Water holding capacity (WHC) in terms of moisture content (dry basis) as a function of temperature showing a large drop in WHC near 60°C.

6.5 Results and Discussion

In this section, distributions of temperature, moisture and deformation are discussed. For validation, predicted moisture loss, change in diameter and point temperature histories at two locations are compared with the experimental values from literature.

6.5.1 Spatial and Temporal Distribution of Moisture Content

Figure 6.3 shows a comparison between predicted and experimentally observed total moisture loss history of the patty for 15 minutes of heating time. Total moisture loss

is almost linear with time, with the patty losing about 17% (26 g for a 155 g patty) of the initial moisture content in 15 minutes. The predicted moisture loss history follows the observed history closely, and the difference between the two at any time is 0.01% or less. The evaporation and drip losses are also plotted in figure 6.3. Evaporation loss with time is slightly concave upwards (rate of loss always increases throughout the heating duration). On the other hand, cumulative drip loss curve with time is S-shaped and stabilizes (rate of drip loss goes to 0) at around 5 minutes as moisture concentration at the patty surface falls below equilibrium concentration. Evaporation loss and its rate exceed the drip loss and the drip loss rate, at any time during heating. Contours of moisture content (dry basis) after every 3 minutes of heating (starting at 3 minutes) are plotted in figure 6.4. It can be seen that the moisture gradients dominate in the axial direction and the end effects are restricted to a small region near the lateral surface of the patty. Also, even at the end of heating, the minimum moisture content (near the griddle plate) is still high (0.891), which means the surface has not dried up. On the other hand, moisture content close to the exposed top surface (away from the plate) rises to 2.731 (from an initial value of 2.6) during the process.

6.5.2 Spatial and Temporal Distribution of Temperature

Figure 6.5 shows a comparison between predicted and experimentally observed temperature history at two locations on the central axis of the patty: 1) at the mid-point between the heated and exposed surfaces, and 2) on the exposed top surface. With the initial lead time of about 50 sec, temperature at the midpoint follows the concave downwards curve reaching a value of 56°C after 15 minutes. The predicted curve follows the observed one closely, with the difference between the two at any time being 1°C or less. Temperature

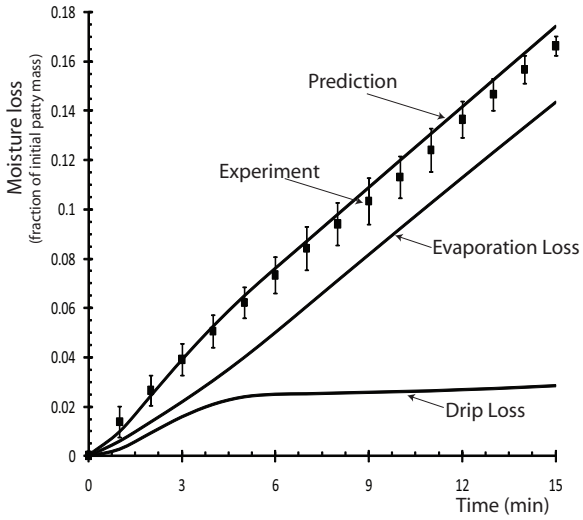

Figure 6.3: Cumulative total moisture loss (predicted and experimentally observed), evaporation and drip loss histories. It can be seen that drip losses level-off after 5 minutes and evaporation losses dominate for the rest of the heating duration

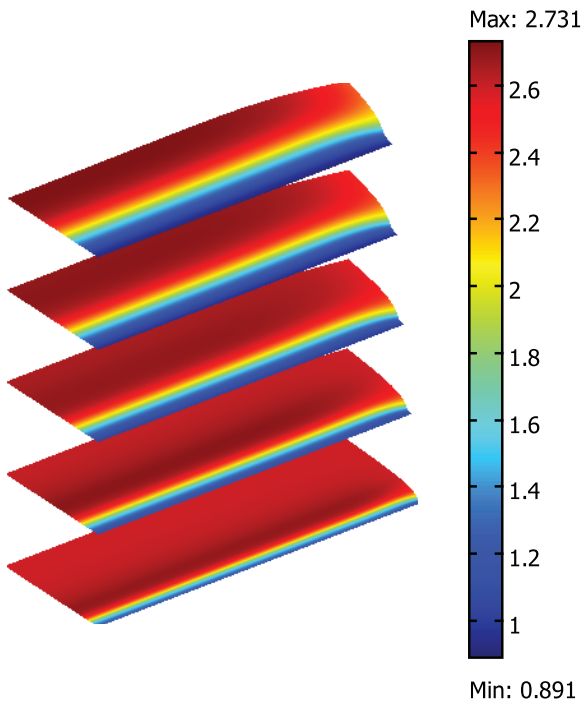

Figure 6.4: Contours of moisture content (dry basis) after 3, 6, 9, 12 and 15 minutes of heating, showing low moisture at the heated surface and some accumulation in the center. Moisture gradients are primarily in the axial direction.

history at the surface is more interesting. While the observed history is similar to that of the midpoint, having an initial lead time followed by a concave downwards curve; the predicted history shows a quick initial heating period which is absent in the observed history. The discrepancy between the predicted and observed histories for the first 300 seconds of heating can be attributed to changing ambient conditions of temperature and relative humidity at the exposed surface during the cooking process. At the top surface, a fixed ambient air temperature of 60°C and negligible moisture loss (as compared to moisture loss from the bottom surface) were used (Table 6.1), which may not be valid at all times and an error in prediction is seen when the effect of boundary conditions dominates. Similar to moisture content, temperature contours (Figure 6.6) show small end effects. The heated surface reaches around 90°C early in the heating process and stabilizes. Temperature at the exposed surface rises slowly and reaches about 50°C after 15 minutes.

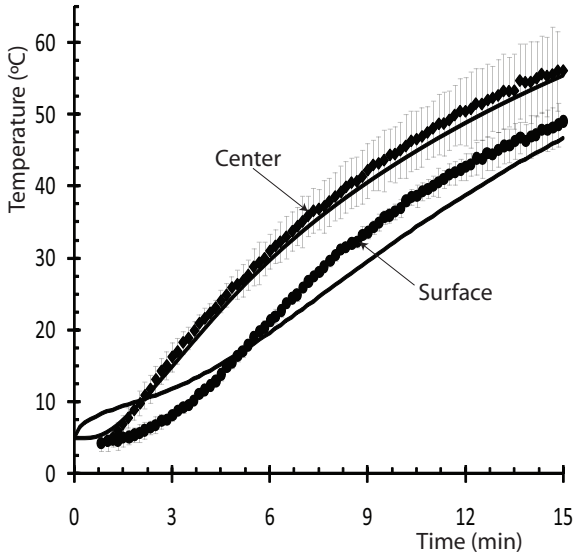

Figure 6.5: Temperature histories (prediction and experimental observation) at the midpoint and the surface on the central axis. Solid lines are predictions.

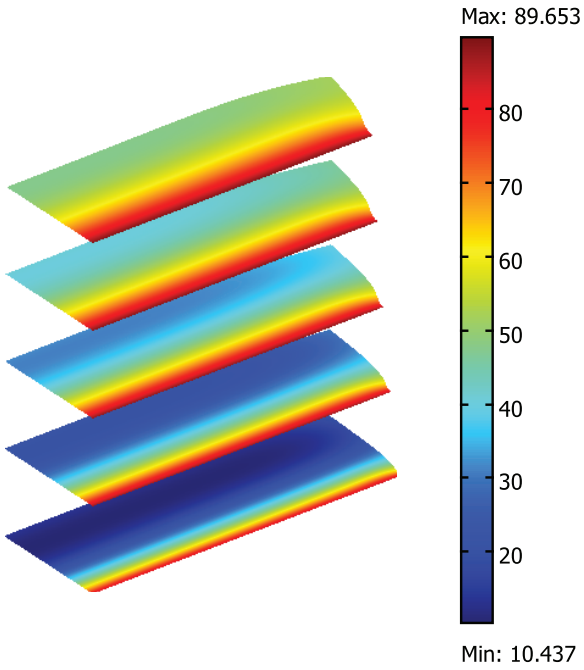

Figure 6.6: Temperature contours (in °C) after 3, 6, 9, 12 and 15 minutes of heating, showing constant heated surface temperature and gradients primarily in the axial direction.

6.5.3 Spatial and Temporal Distribution of Deformation Field

Figure 6.7 compares the histories of experimentally observed diameter with the predicted diameter (averaged for diameter at different heights). The patty diameter reduces to about 91% of the original value in 15 minutes, which is as predicted by the simulations. For reference, the diameter, $D(t)$ assuming uniform shrinkage throughout the patty and computed from the equation:

$$\frac{D(t)}{D_0} = 1 - \left(\frac{V(t)}{V_0}\right)^{1/3} \tag{6.21}$$

is also plotted. At any time, the diameter assuming uniform shrinkage is much larger than the predicted or observed diameter, indicating the non-uniformity in patty shrinkage. Also, this means that such a simplified relationship as equation 6.21 cannot be used to predict diameter when solid deformation equations are not solved. Predicted

thickness (normalized) and thickness assuming uniform shrinkage are plotted in Figure 6.8. The final value of thickness is approximately 95% of the initial value, which means the patty shrinks by less than 1 mm in thickness in 15 minutes. Predicted values of

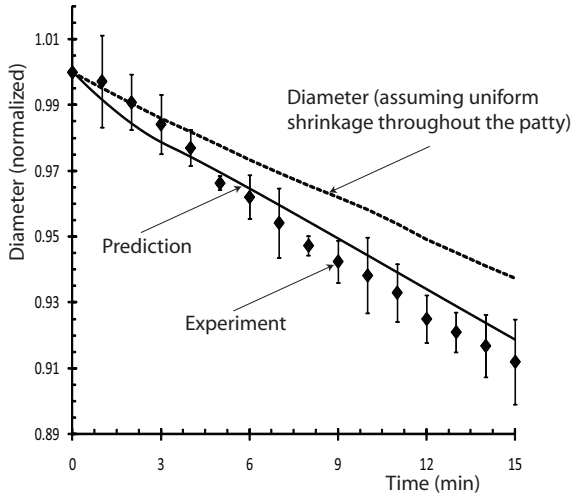

Figure 6.7: Diameter change histories (prediction and experimental observation). Also, diameter calculated assuming uniform shrinkage throughout the patty is plotted showing assumption of uniform shrinkage will lead to erroneous results.

thickness were not compared to its observed values because of high variability in patty thickness (it varied by more than 2 mm at different locations on a single patty) and also due to variability in shear effects that cause rise of the bottom surface of the patty near the center. In this simulation, bottom surface was considered fixed in the z-direction. However, this could not be achieved in all the experiments at all times. Some patties rose by 1-2 mm in the middle, while some others stuck to the griddle plate. Therefore, uncertainty (more than 2 mm) in height was more than the total expected change in height ($\sim$ 1 mm) and, thus, it was meaningless to compare the observed and predicted thickness values.

Figure 6.9, which plots the contours of elastic Jacobian, J_{el} ($= J/J_M$), at different times, helps us arrive at a very good (albeit, more involved) method to predict shrinkage.

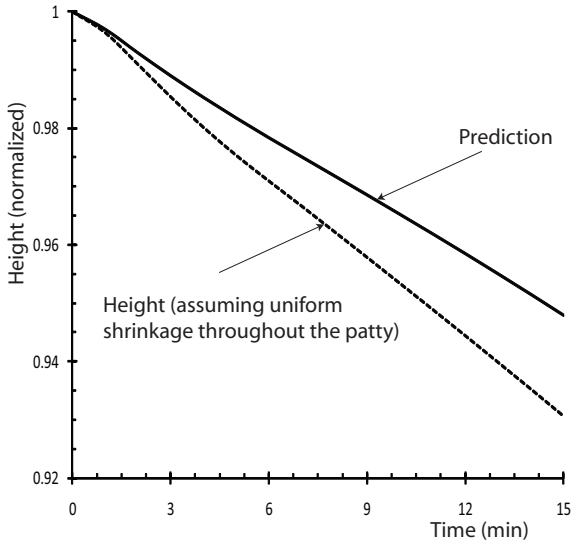

Figure 6.8: Height change history. Note that height change was too small to be compared with experiments. Also, height calculated assuming uniform shrinkage throughout the patty is plotted showing assumption of uniform shrinkage will lead to erroneous results.

Figure 6.9 shows that the ratio of actual Jacobian, J, to the Jacobian due to moisture change, J_M, lies in the narrow range of 0.98% to 1.01%. The region near the heated surface is under tension, while the other cooler regions are under compression. The narrow range of elastic Jacobian, J_{el}, is due to the high bulk modulus to shear modulus ratio (Poisson ratio, $\nu \approx 0.5$). For such cases, if estimation of stresses is not important, solid momentum balance can be avoided and Jacobian, J can be assumed to be equal to moisture change Jacobian, J_M. In the absence of significant shear strains, the dilatational strains and, thus, deformation field can be estimated from Jacobian, J only. Displacements due to this deformation field can now be calculated and used in the deformed mesh equations to get new geometry.

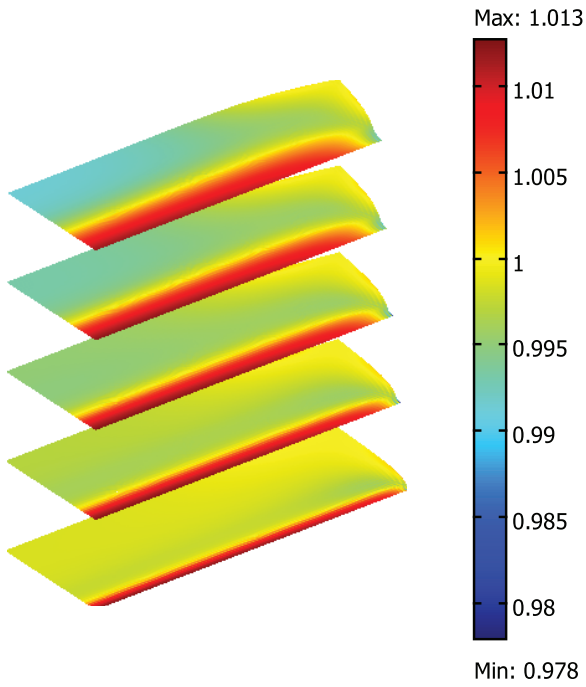

Figure 6.9: Elastic Jacobian, J_{el} (ratio of actual volume to free volume) contours after 3, 6, 9, 12 and 15 minutes of heating. It can be seen that the surface is stretched and the heated interior is compressed by a maximum of 2% from free volume.

6.6 Sensitivity Analysis

Large variability in properties of food materials and their processing conditions necessitates a detailed sensitivity analysis of the input parameters. In this study, the input parameters chosen for sensitivity analysis are– heat transfer coefficient, mass transfer coefficient, moisture diffusivity and time taken by water holding capacity to reach the equilibrium value at a given temperature.

6.6.1 Heat Transfer Coefficient

As discussed earlier, there exists a high degree of uncertainty in the input heat flux from the plate. Therefore, the process was simulated with a $\pm 25\%$ variation in heat

transfer coefficient. Moisture contours on the deformed geometry for the three values used (300, 400, 500 W/m^{2}K) after 15 minutes of heating are plotted in Figure 6.10a. The moisture contours and the deformation are almost identical, with the contours for h = 300 W/m^{2}K (or 500 W/m^{2}K) showing small decrease (or increase, respectively) in moisture loss near the heated surface. Variation of total moisture loss and drip loss with h after 15 minutes of heating is plotted in Figure 6.10b. Both total moisture loss and drip loss rise by about 10% with 25% rise in heat transfer coefficient, indicating significant uncertainty due to this parameter. Similar to moisture content, small increase in surface temperatures was also observed with increase in h (not shown). Like most thermal food processes, as heat transfer is controlled by internal resistance in this case also, little effect of change in h was visible far from the heated surface.

6.6.2 Mass Transfer Coefficient

For food processes, uncertainty in convective mass transfer coefficient, h_m, is usually much more than the heat transfer coefficient as the measurement of the former is not easy. The values used in a number of studies of intensive heating of food materials are all of the order of 0.01 m/s, the same value is used in this study. Given the high uncertainty, the process was also simulated with h_m values of 0.02 m/s (twice the original value) and 0.005 m/s (one-half of the original value). Moisture contours on the deformed geometry, and moisture losses (total and drip) for the three values used (0.005, 0.01, 0.02 m/s) after 15 minutes of heating, plotted in Figure 6.11, show interesting trends. Although the total moisture loss for the two smaller values (0.005, 0.01 m/s) differs by only about 10%, the nature of moisture loss changes (most of the loss being drip for 0.005 m/s and evaporation for 0.01 m/s). This is because low evaporation loss for h_m = 0.005 m/s, leads to higher surface concentration (Figure 6.11b), which, in turn, causes more drop

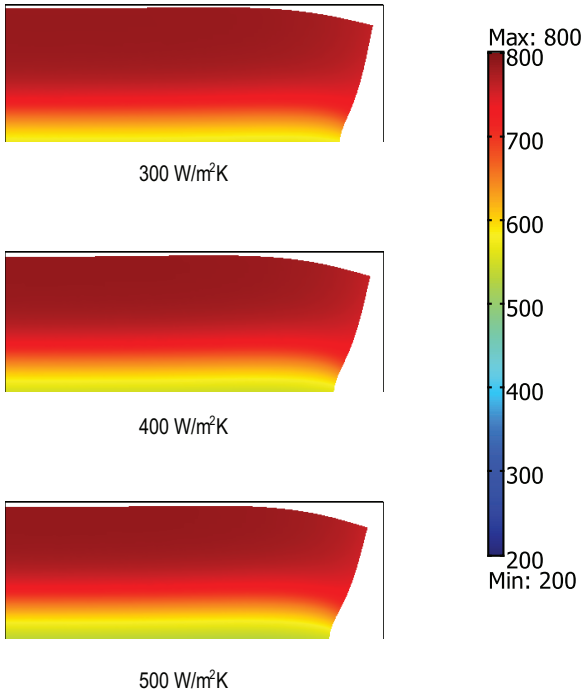

(a)

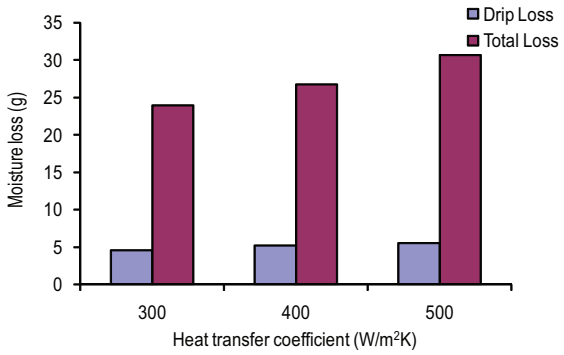

(b)

Figure 6.10: a) Contours of moisture concentration (kg/m^3) and (b) total moisture loss and drip loss, after 15 minutes of heating for heat transfer coefficient, h = 300, 400, 500 W/m^{2}K. Moisture concentration near the heated surface decreases with increase in heat transfer coefficient due to higher evaporation loss.

loss, offsetting the effect of low h_m. At $h_m = 0.02$ m/s, surface moisture concentration is much less due to large increase in evaporation rate, and, thus, there is little drip loss. Moreover, the total moisture loss increases by 25%, indicating that external resistance plays a significant role, although an h_m of 0.02 m/s seems to be on the higher end of a reasonable estimate. The presence of liquid water on the plate surface (observed during experiments) also indicates some drip loss. Thus, although there is uncertainty in the nature of moisture loss due to uncertainty in mass transfer coefficient, the prediction of total moisture loss is fairly accurate.

6.6.3 Diffusivity

Effective moisture diffusivity data is available for a variety of food materials at different moisture contents and temperatures. This is usually done by fitting moisture loss data for drying of a thin slice of food sample of known thickness at fixed temperature and significant ambient air velocity (to ensure internal mass transfer resistance dominates) with analytical solution of 1D diffusion equation with fixed boundary concentration. However, such a technique does not work for meat products undergoing denaturation of protein matrix, as transport occurs due to both temperature and moisture gradients and moisture is expelled from the matrix in liquid form also. In this study, a diffusivity of 10^{-7} m^2/s is used, which was determined by van der Sman (2007) by minimizing the error norm between predicted and observed results. For sensitivity analysis, the process was also simulated at moisture diffusivity of 10^{-6} and 10^{-8} m^2/s. The primary effect of diffusivity is on spatial moisture profiles (Figure 6.12a), with increase in diffusivity leading to lower moisture gradients. Total moisture loss increased by 10 % with an order of magnitude increase in moisture diffusivity (Figure 6.12b). The increase in moisture loss was entirely due to increase in drip loss as evaporation loss is independent

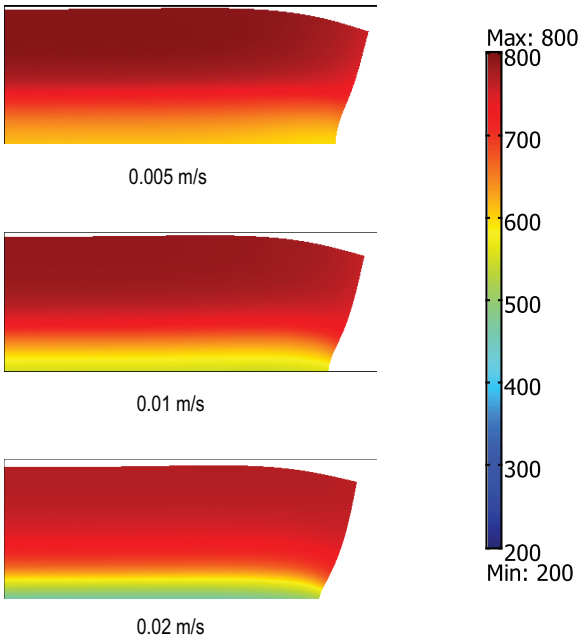

(a)

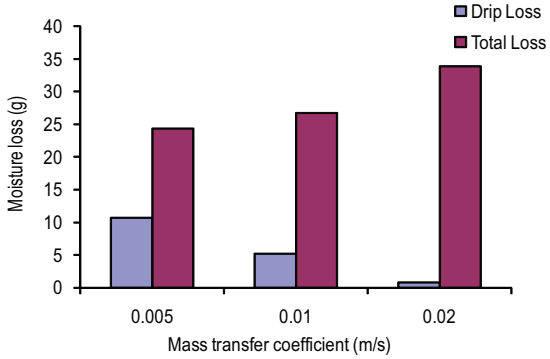

(b)

Figure 6.11: a) Contours of moisture concentration (kg/m^3) and (b) total moisture loss and drip loss, after 15 minutes of heating for mass transfer coefficient, h_m = 0.005, 0.01 and 0.02 m/s. Drip loss decreases while the evaporation loss increases with increase in mass transfer coefficient.

of surface concentration for high moisture materials.

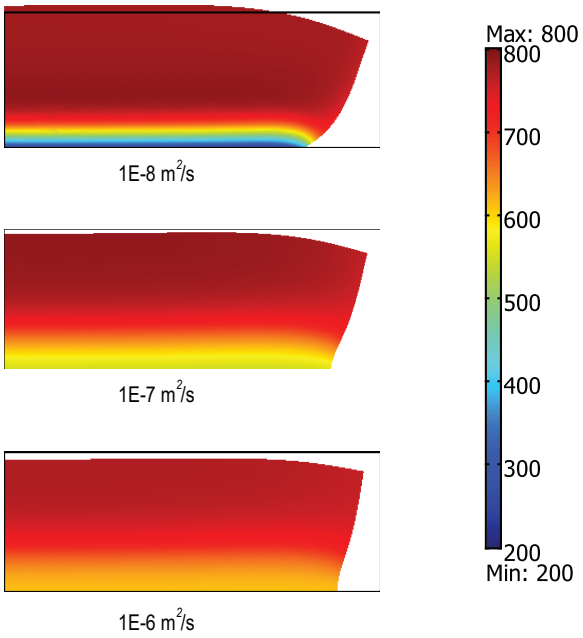

(a)

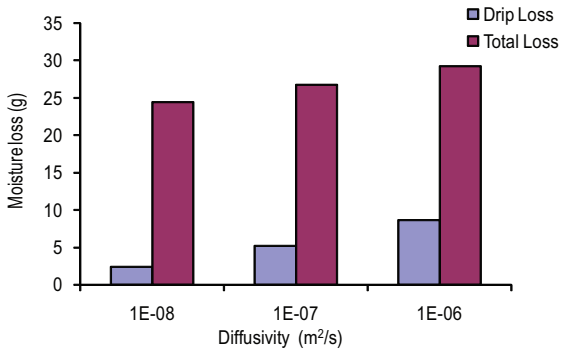

(b)

Figure 6.12: a) Contours of moisture concentration (kg/m^3) and (b) total moisture loss and drip loss, after 15 minutes of heating for moisture diffusivity, $D_{w,c_w} = 10^{-8}, 10^{-7}$ and 10^{-6} m^2/s. Lower diffusivity leads to larger moisture gradients and lower drip loss.

6.6.4 Equilibration Time for Change in Water Holding Capacity

In this study, it is assumed that the time-scale of protein denaturation (and, thus, change in water holding capacity) is much smaller than the relevant time-scales of the heating process, and, thus, change in the water holding capacity is given by the change in patty temperature (Figure 6.2). However, the recommendation for determining water holding capacity is too keep the samples (even if thin) in a water bath for 20 minutes, which means that the time-scale for change in water holding capacity can be in minutes. However, little data for kinetics of change in water holding capacity is available. To explore the effect of time-scale of change in water holding capacity, first order kinetics is assumed:

$$\frac{c_{w,eq} - c_{w,eq,\infty}(T)}{c_{w,0} - c_{w,eq,\infty}(T)} = e^{-t/\tau} \tag{6.22}$$

Simulations were performed for three values of time constant, $\tau = 1, 3, 6$ minutes. Moisture losses (total and drip) after 15 minutes of heating for the three values of τ and $\tau = 0$ (instant equilibrium, used in the simulations) are plotted in Figure 6.13. It can be seen that the drip losses decrease with increase in the value of τ, reducing to 0 for $\tau = 6$ minutes as water holding capacity reduces at a lesser rate as compared to $\tau = 0$. Since evaporation losses dominate in this process, the effect on total moisture loss is small. However, τ can play a controlling role in processes where evaporation is small such as boiling.

To summarize the inferences from sensitivity analysis, heat transfer coefficient, mass transfer coefficient, moisture diffusivity and time-scale of protein denaturation all play a role in the patty cooking process. Heat transfer coefficient affects energy delivered to the surface, which, in turn affects near surface moisture concentration and temperature. Mass transfer coefficient changes the nature of moisture loss, with lower mass transfer coefficient meaning more drip loss. Diffusivity and time-scale of protein denaturation

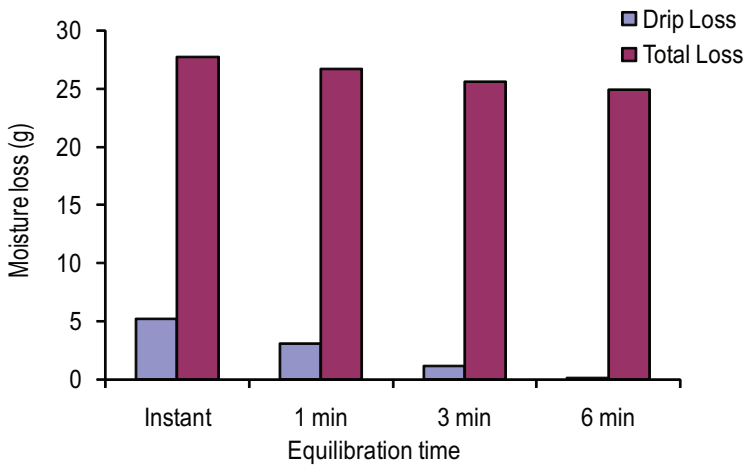

Figure 6.13: Total moisture loss and drip loss, after 15 minutes of heating for 4 different values of time-constant for kinetics of protein denaturation, τ = 0, 1, 3, 6 minutes. Drip loss decreases with increase in time-constant, while the evaporation loss remains unaffected.

affect drip losses by changing the surface moisture content and equilibrium moisture content respectively.

6.7 Example of Model Application in Process Design

As an example of application of the model developed in this study to process design, three different ways of hamburger patty cooking are simulated– 1) single-sided contact-heating without flip (as discussed till now), 2) double-sided contact-heating (with both the sides heated with $h = 400$ W/m^{2}K at plate temperature of 120°C), and 3) single-sided contact-heating with flipping after every 5 minutes (boundary conditions are exchanged between top and bottom surface after every 5 minutes). Figure 6.14 plots time taken for the cold point temperature to reach 72°C and total moisture loss till that time, for the three processes. Cold point temperature dictates food safety with a temperature of 72°C ensuring sufficient microbial destruction and can be treated as a design

constraint. Total moisture loss is a quality parameter which needs to be minimized to preserve meat juices. Thus, moisture loss and time taken can be treated as variables to be optimized. With this understanding, single-sided heating without flip performs the worst as it leads to most moisture loss. This process also takes the most time. Double-sided contact heating preserves the most moisture and takes least time, while single-sided heating with flipping is stands between the other two on both counts. Here, the primary advantage of simulation over experiments lies in the fact that it is not always possible to easily experimentally measure cold-point temperatures, especially for non-standard shapes and complex heating methods such as combination heating in a oven.

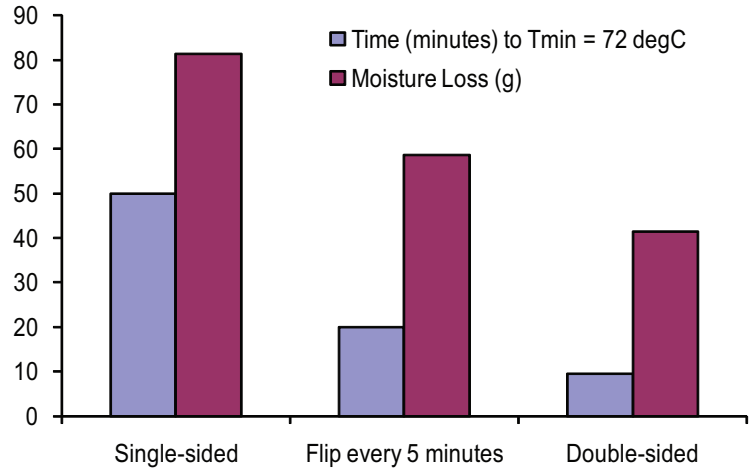

Figure 6.14: Time taken for the cold-point to reach 72°C and total moisture loss till that time for three different scenarios of patty cooking.

6.8 Conclusions

A deformable porous-media based model has been used to simulate single-sided contact-heating of hamburger patties. Since the meat stays rubbery during the process, local vol-

ume change at any point has been shown to be equal to the volume of moisture loss. The model predictions (moisture history, diameter change and point-temperature histories) are validated using experimental data. Sensitivity analysis on various parameters has been performed to reveal their respective contributions to transport. Since the resistance to heat transfer is mainly internal, heat transfer coefficient primarily affects moisture and temperature values near the surface. For moisture transport, mass transfer coefficient and moisture diffusivity both play a significant role– the former affects the nature of moisture loss and the latter affects moisture gradients and drip loss. Time-scale of protein denaturation can affect the drip loss through change in equilibrium moisture concentration. The fundamental basis of the model that does away with empirical parameters, makes its extension to other thermal processes of meat and to thermal processing of other biological materials easier and, thus, it can be an important tool in making safety, quality and product design related predictions.

BIBLIOGRAPHY

[1] Bengtsson NE, Jakobsson B, Dagerskog M.Cooking of Beef by Oven Roasting - Study of Heat and Mass-Transfer. *Journal of Food Science*.1976;41(5):1047-1053.

[2] Chau KV, Snyder GV. Mathematical-Model for Temperature Distribution of Thermally Processed Shrimp, *Transactions of the ASAE*. 1988;31(2):608-612.

[3] Fowler AJ, Bejan A. The Effect of Shrinkage on the Cooking of Meat. *International Journal of Heat and Fluid Flow*. 1991;12(4):375-383.

[4] Pan Z, Singh RP, Rumsey, TR. Predictive modeling of contact-heating process for cooking a hamburger patty. *Journal of Food Engineering*. 2000;46(1):9-19.

[5] Sebastian P, Bruneau D, Collignan A, Rivier M. Drying and smoking of meat: Heat and mass transfer modeling and experimental analysis. *Journal of Food Engineering*. 2005;70(2):227-243.

[6] Shilton N, Mallikarjunan P, Sheridan, P. Modeling of heat transfer and evaporative mass losses during the cooking of beef patties using far-infrared radiation. *Journal of Food Engineering*. 2002;55(3):217-222.

[7] Wang L, Singh RP. Finite element modeling and sensitivity analysis of double-sided contact-heating of initially frozen hamburger patty. *Transactions of the ASAE*. 2004;47(1):147-157.

[8] Kondjoyan A, Rouaud O, McCann MS, Havet M, Foster A, Swain M, Daudin JD. Modelling coupled heat-water transfers during a decontamination treatment of the surface of solid food products by a jet of hot air. I. Sensitivity analysis of the model and first validations of product surface temperature under constant air temperature conditions. *Journal of Food Engineering*. 2006;76(1):53-62.

[9] van der Sman RGM. Soft condensed matter perspective on moisture transport in cooking meat. *AIChE Journal*. 2007;53(11):2986-2995.

[10] Dhall A, Datta AK. Transport in Deformable Food Materials: A Poromechanics Approach in preparation

[11] Vujosevic L, Lubarda VA. Finite-strain thermoelasticity based on multiplicative decomposition of deformation gradient. *Theoretical and Applied Mechanics*. 2002;28-29:379-399.

[12] USDA Nutrition Database http://www.nal.usda.gov/fnic/foodcomp/search/. Accessed July 31, 2010.

[13] Ni H, Datta AK. Moisture, oil and energy transport during deep-fat frying of food materials, *Food and Bioproducts Processing*. 1999;77(C3):194-204.

[14] Choi Y, Okos MR. Thermal properties of liquid foods – review. In: *Okos MR (editor). Physical and Chemical Properties of Food* Saint Joseph, Michigan: American Society of Agricultural Engineers, 1986:35-77.

[15] Hashin Z. Large Isotropic Elastic Deformation of Composties and Porous Media. *International Journal of Solids and Structures*. 1985;21(7):711-720.

[16] Dagerskog M. Pan Frying of Meat Patties 1. Study of Heat and Mass-Transfer. *Lebensmittel-Wissenschaft & Technologie-Food Science and Technology*. 1979;12(4):217-224.

[17] Housova J, Topinka P. Heat Transfer During Contact Cooking of Minced Meat Patties. *Journal of Food Engineering*. 1985;4(3):169-188.

[18] Ikediala JN, Correia LR, Fenton GA, BenAbdallah N. Finite element modeling of heat transfer in meat patties during single-sided pan-frying. *Journal of Food Science*. Jul-Aug 1996;61(4):796-802.

[19] Pan Z, Singh RP. Heating surface temperature and contact-heat transfer coefficient of a clam-shell grill. *Lebensmittel-Wissenschaft Und-Technologie-Food Science and Technology*. 2002;35(4):348-354.